LASER EVAPORATIVE HEATING IN RELATION TO MACHINING

BY

SAAD BIN MANSOOR

A Thesis Presented to the

DEANSHIP OF GRADUATE STUDIES

KING FAHD UNIVERSITY OF PETROLEUM & MINERALS

DHAHRAN, SAUDI ARABIA

In Partial Fulfillment of the
Requirements for the Degree of

MASTER OF SCIENCE

In

MECHANICAL ENGINEERING

NOVEMBER 2005

In the name of Allah, most Gracious, most Merciful.

KING FAHD UNIVERSITY OF PETROLEUM AND MINERALS
DHAHRAN 31261, SAUDI ARABIA

DEANSHIP OF GRADUATE STUDIES

This thesis, written by **SAAD BIN MANSOOR** under the direction of his thesis advisor and approved by his thesis committee, has been presented to and accepted by the Dean of Graduate Studies, in partial fulfilment of the requirements for the degree of **MASTER OF SCIENCE IN MECHANICAL ENGINEERING**.

Thesis Committee

Dr. Bekir. S. Yilbas (Thesis Advisor)

Dr. Habib I. Abualhamayel (Thesis Co-Advisor)

Dr. Ahmet Z. Sahin

Dr. Shahzada Z. Shuja

Dr. Luai M. Al-Hadhrami

Dr. Faleh A. Al-Sulaiman
Department Chairman

Dr. Mohammad A. Al-Ohali
Dean of Graduate Studies

٢٩ ذو الحجة ١٤٢٦ هـ
Date 29 - 01 - 2006

عمادة الدراسات العليا
DEANSHIP OF GRADUATE STUDIES

Dedicated to

my parents Lubna & Mansoor

and brothers Ahmed & Umair

ACKNOWLEDGEMENT

All praise belongs to **Allah**, glorified is He and exalted. Who caused this work to be completed successfully. Who gave me the opportunity, strength and persistence to work on it. And Who helped me in the most difficult of times. I'm happy to have had an opportunity to glorify His name in the sincerest way through this small accomplishment and pray to Him to accept my efforts.

I would like to acknowledge the role of the King Fahd University of Petroleum & Minerals in extending a generous financial assistance to me and for providing a wonderful environment, academic and otherwise, which made my stay at KFUPM a memorable experience.

My deep appreciation goes to my thesis advisor Dr. Bekir S. Yilbas for his constant help and guidance and for is compassionate attitude.

Very special thanks to Mr. Ovaisullah, Dr. Arif, Dr. Qutub and Dr. Mahmood Sarhan. They extended their help to me in very difficult times.

Dr. Shuja helped me considerably during my thesis and I had fruitful discussions with him regarding the FLUENT 6.2 package. I appreciate his assistance.

I'm grateful to Dr. Rached for helping me with the FLUENT 6.2 package or else my work might have been delayed.

Thanks to my parents and brothers for their moral and financial support. Their emotional support was invaluable during my stay at KFUPM.

I would also like to recognize the support of my relatives Naveed and Saqib and those friends with whom I spent considerable time here at KFUPM, (in alphabetical order) Abbas, Syed Hafeez, Abdul Qaiyum, Abid, Adnan S., Adnan Y., Aamir, Aiman, Ahmed, Ahmer, Aminuddin, Arshed M., Arshed R., Basha, Basharat, Bilal, Faisal, Hasan, Imran A., Imran N., Iqtedar, Itrat, Jawad, Kashif, Khawar, Kamran, Moinuddin, Mudassir, Munib, Naeem, Ovaisullah, Saad, Sajid, Salman, Samivullah, Shiraz, Zeeshan A., Zeeshan M. and specially Juned. I spent an excellent time with them.

TABLE OF CONTENTS

LIST OF TABLES

LIST OF FIGURES

THESIS ABSTRACT

Name: Saad bin Mansoor

Title: Laser Evaporative Heating in Relation to Machining

Major Field: Mechanical Engineering

Date of Degree: November 2005

Laser pulse heating and phase change process taking place in the region irradiated by a laser beam are considered. A numerical method is employed to predict the temperature field, recessing velocities of evaporating and melting surfaces. An experiment is conducted to compare the cavity size obtained from the experiment with the prediction. The predicted recession velocity of the evaporating surface is compared with the results of one-dimensional closed form solution. The influence of laser pulse intensity on the recession velocity, the size of the mushy zones and resulting cavity formation in time and its shape are computed. Heating situation is simulated through a numerical scheme employing finite difference method. The grid independent tests are carried out to secure grid independent solutions. The study is extended to include the vapor ejection from the temporally developing cavity due to evaporating surface. A numerical scheme employing a control volume approach is used in solution. The vapor jet is considered to expand into the stagnant water, which is situation observed in laser shock processing of the surfaces. Since the actual vapor front density is not known and not provided in the open literature, two extreme densities are introduced in the simulations.

خلاصة الرسالة

الاسم: سعد بن منصور
عنوان الرسالة: التسخين التبخيري باستخدام أشعة الليزر في عملية تشغيل المعادن
التخصص: الهندسة الميكانيكية
تاريخ التخرج: نوفمبر ٢٠٠٥

في هذه الدراسة تمت دراسة عملية التسخين بواسطة أشعة الليزر المتقطعة و ايضا عملية تغير الطور في المنطقة التي اسقطت عليها أشعة الليزر. تم أستخدام طريقة عددية للتنبؤ بمجال درجة الحرارة وسرعة الارتداد للأسطح المنصهرة والمتبخرة. تم عمل تجربة معملية لمقارنة حجم التجويف الناتج في التجربة مع القيم التي تم التنبؤ بها. و تمت مقارنة سرعة الارتداد للسطح المتبخر مع حل مضبوط آحادي البعد. تم حساب تأثير كثافة أشعة الليزر المسقطة علي سرعة الارتداد ، حجم الأسطح المتأثرة وتكون التجويف مع مرور الزمن وشكله. تم عمل محآكاة لموضع التسخين عن طريق برنامج عددي باستخدام طريقة الفرق المحدد. تم عمل امتداد للدراسة لتشمل البخار المقذوف من التجويف المتكون لحظيا نتيجة للسطح المتبخر ولحل هذا الجزء استعمل برنامج عددي يستخدم طريقة الحجم المحدد. تم اعتبار أن نافورة البخار تتمدد داخل الماء الراكد اعلي السطح المسقطة عليه أشعة الليزر وهو ما تم ملاحظته عند اصتطدام الأشعة مع تلك الأسطح. وحيث أن كثافة البخار الامامي غير معلومة ولاتوجد معلومات عنها في الدراسات السابقة فقد تم استخدام قييمتين مختلفتين تماما في عملية المحآكاة.

CHAPTER 1

INTRODUCTION

In 1960, the scientific world was electrified by news of the world's first laser action. Only five years later, at a rate surpassing the accelerating pace of modern technology, industry had harnessed the laser. On December 14, 1965, Western Electric announced the first use of laser light in a mass production application: a laser system had been developed for piercing holes in diamond dies for drawing wire.

Since then, the laser has proven to be an effective tool in numerous other industrial applications, and increasing numbers of engineers are encountering this new technology in their work. Lasers in industry are being used to measure process parameters and to scribe, drill, evaporate, and weld a wide variety of materials in a wide variety of applications. As a result, more and more engineers are finding that they need reliable

information on subjects such as interferometry, thermal processing, holography, detection, and laser safety procedures.

The laser is a unique source of radiation capable of delivering intense coherent electromagnetic fields in the spectral range between the ultra-violet and the far infrared. This laser beam coherence in manifested in two ways: (1) it possesses good temporal coherence qualities since it is highly monochromatic, and (2) it is spatially coherent – as evidenced by the nearly constant phase wavefront and directionality of the emitted light. The temporal coherence of the laser is a measure of the ability of the beam to produce interference effects as a result of differences in path lengths and is, therefore, important for such applications as interferometry and holography. The spatial coherence is particularly important for power applications where it provides the capability of focusing all the laser's available output energy into an extremely small spot size. Thus, power densities, which are unattainable with any other source of light, can be attained.

Spatial and temporal coherence are properties that have long been recognized as indispensable for various industrial and laboratory applications. Long before the advent of the laser, light possessing various degrees of coherence could be obtained by filtering ordinary light. However, the filtering process resulted in an output beam of such low intensity as to render such techniques useless in most practical applications. It remained for the laser, with its inherent properties of coherence and high intensity, to demonstrate the applicability of optical electromagnetic radiation to numerous new technologies.

The special characteristics of laser radiation are directly attributable to the phenomenon of stimulated emission and to the feedback mechanism provided by the cavity structure. Such a laser system consists of an active medium (lasing material), which in this case is gas, but may consist of a solid or a liquid. A power supply pumps energy into the active medium, exciting the active atoms and rendering amplification possible. The laser, however, normally functions as an oscillator rather than an amplifier and is consequently a source of coherent light rather than an amplifier of existing light signals. To achieve oscillation, mirrors are placed perpendicular to the axis of the active medium to form an optical resonant cavity. Stimulated emission in the active medium results in the required amplification, whereas the mirrors supply the feedback required for regenerative action and oscillation. These features combine to differentiate the lasers from other sources of light and lead to the singularly intense light typical of lasers.

The word laser is actually a contraction of the phrase ‘light amplification by stimulated emission of radiation.’ This phrase describes a process by means of which a collimated, monochromatic and coherent beam of light is obtained. This beam of light can then be used for varying purposes. One such purpose is laser machining. Laser beams can be used to concentrate great amounts of power in a very short space. This property can be used effectively for industrial and commercial purposes in the form of laser machining of metals and other materials. Specifically we can perform cutting, drilling, welding and marking operations on metals. We shall be concerned about laser drilling in this document.

Lasers are widely used in industry as machine tools due to their precision of operation, low cost, localized processing, and high speed of operation. In laser machining applications, a laser beam is used as a heat source, increasing temperature rapidly to the melting and evaporation temperature of the substrate material. Since the arrangements of the optical setting for the laser beam is very precise, the localized heating can be controlled easily. Laser machining can be categorized into two groups based on the type of processing being involved during the machining such as drilling, cutting, welding, alloying and others. Moreover, the laser processing can be pre or post treatment operations such as duplex treatment for coatings and scribing after coatings. In order to optimize the laser machining process and reduce the experimental time and cost, the model studies receive considerable attention. Moreover, the model studies give insight into the physical processes that take place during the heating process and being easier to accomplish as compared to experimental studies. The measurement of physical properties during laser workpiece interaction is difficult and costly since, the process is involved with high temperature, short duration, and localized heating

From the modelling point of view, the laser machining can be classified into two categories: i) laser conduction limited heating, and ii) laser non-conduction limited heating. In the laser conduction limited heating situation, substrate surface is heated up to the melting temperature of the substrate material; in this case, substrate remains in the solid state during the process. One of the laser conduction limited applications is the laser quenching of the surfaces. In the laser non-conduction limited heating situation, substrate surface under goes a phase change during the processing, i.e. melting and subsequent

evaporation is resulted. The laser drilling, cutting, and welding are typical examples of laser non-conduction limited heating situations.

In laser machining process, the end-product quality is very important from the manufacturing point of view. Consequently, the optimization studies improve laser cutting process considerably. The quality assessment of the end product, such as drilled hole, cut surface, etc., can be possible through examining the geometric features of the laser machined section. One of the methods associated with the quality assessment is the factorial analysis. In this case, the affecting factors are varied at randomly or with increments to generate the random blocks. Through the statistical testing of the measurable responses, the significant levels of the affecting parameters can be identified.

When high power laser beam is focused onto the substrate surface, the beam energy is partially absorbed by the substrate material. Depending on the focused beam diameter at the surface, laser power intensity (combining the laser output energy and pulse length), and reflectivity of the surface, substrate material undergoes solid heating, melting and evaporation. In the case of evaporation process, the evaporating front detaches from the liquid surface generating a recoil pressure across the vapor-liquid interface. As the evaporation of the surface progresses, the recoil pressure increases considerably influencing the evaporation rate. As the heating progresses further, the liquid surface recesses towards the solid bulk forming the cavity in the substrate material. Depending on the pulse length and power intensities, the liquid ejection from the cavity occurs, which is particularly true for the long pulses (~ ms pulse lengths); however, the surface ablation

without liquid ejection takes place for short pulses (~ ns pulse lengths). Moreover, the liquid ejection improves the material removal rates from the cavity. In the case of laser shortpulse processing, the recoil pressure increases substantially due to high rates of momentum exchange during the evaporation process. In this case, high pressure at the vapor/liquid interface acts as a pressure force generating a surface stresses at the liquid/solid interface. This, in turn, results in a pressure wave propagating into the substrate material. Depending on the magnitude of pressure wave, the plastic deformation through dislocations in the surface region of the substrate material takes place. The depth of deformed region is limited with the interaction of loading (plastic wave) and unloading (elastic wave) waves., i.e. as the loading phase is completed (when the evaporation is completed, the recoil pressure diminishes), unloading wave (elastic wave) from the liquid/solid interface initiates. Since the unloading wave travels faster than the loading wave, both waves meet at some depth below the surface. It should be noted that the wave motion in the substrate material is complicated and requires comprehensive investigation.

Drilling is the process by which a hole can be created in a material or in the ground. Usually in industry one needs to make a hole in a metal sheet or in a metal part. The hole can be a through-hole or a blind-hole. Traditionally, drilling process can be accomplished by means of a rapidly rotating drill bit, which is forced against the metal surface and is designed to remove the metal through its rotating action as it penetrates into the metal sheet or part. Another method to accomplish drilling is to use a high-powered laser and point it to the desired area on the metal surface. The laser beam gets absorbed in the metal and heats it up to a point that the metal melts and subsequently evaporates. In this

way a hole can be created. There are advantages and disadvantages of both methods. Some of the pros and cons of the laser drilling process are listed below.

Advantages

- Faster than any conventional method.
- Minimal mechanical force on work piece.
- Processing of high alloy metals without difficulty.
- Very small holes can be laser drilled in production. A focused spot can be as small as 0.1mm (0.004”) in diameter.
- No tool cost or wear.
- Angled holes and difficult access holes can be drilled.
- Low dimensional variability.
- Low distortion.

Limitations

- Laser holes are tapered to some extent (approximately 1% of the drill depth).
- Cannot drill a blind hole to a precise depth.
- Adherent metal to be removed from exit hole.
- Slower processing of large holes due to trepanning.
- Thermal shock to metal.

Laser drilling process can be studied experimentally or theoretically. There are various parameters involved in laser drilling which have to be adjusted and fine-tuned in order to

yield acceptable machining characteristics. The optimal values of these parameters depend on the specific drilling operation being performed. These values can either be found by extensive experimentation or by a rigorous theoretical approach to the problem. We shall be concerned with the theoretical approach.

Laser drilling as stated before is accomplished essentially by heating the metal to a point that it melts and then evaporates leaving behind a cavity, which grows with time and approximates the desired hole. We would like to model this whole process mathematically. Once the relevant physics is cast into the shape of a system of partial differential equations and accompanying initial/boundary conditions we can attempt to obtain a solution either analytically or numerically. Most often than not the system of equations is too complex to yield to an exact analytical solution. The only practical choice left is then to solve it numerically on a digital computer. The task is not easy but holds the promise of a reasonable solution. The disadvantage is that during the numerical solution of the system of equations the various important parameters have to be kept constant. Consequently, for each set of parameter values we have to solve the system of equations numerically. We can term it as a simulation. That is, we are simulating the whole laser drilling process and are researching the affect of various parameter values on the machining characteristics.

CHAPTER 2

LITERATURE SURVEY

2.1 Introduction

The research papers in this literature survey are classified according to the nature of the problem they address. They are arranged into the classes Conduction Limited and Non-Conduction Limited. The class Conduction Limited pertain to research papers in which the problem is limited to a consideration of conduction heat transfer and no consideration is given to the phase change phenomenon. In contrast the class Non-Conduction Limited include research papers in which the problem being dealt includes both conduction and latent heat transfers.

2.2 Conduction Limited Heating

Shuja [1] investigated the influence of the workpiece speed on the resulting temperature profiles during the gas-assisted laser heating process. He considered three-dimensional situation and governing equations of flow and energy were solved numerically using the control volume approach. He introduced low Reynolds number k-ε model to account for the turbulence effect due to convective cooling. He showed that the workpiece speed had a significant effect on the resulting temperature profiles; specifically, an increase in the workpiece speed resulted in a decrease of the maximum temperature attained at the workpiece surface.

Qiu et al. [2] studied nanosecond laser heating of gold films both theoretically and experimentally. They used a two-step radiation heating model to characterize transient temperatures of the electron and lattice systems. Microstructures and morphology of films before and after laser pulse heating were characterized with optical and electron microscopes. They showed that in the nanosecond regime electrons and the lattice were in thermal equilibrium and the classical Fourier heat conduction model was applicable. They also found that the thermal stress played a significant role in laser-film interaction for thin films, which could lead to structure changes of films at a temperature much lower than the melting point whereas structure change in thick films were mainly due to melting.

Qiu et al. [3] studied the size effect, due to both surface scattering and grain-boundary scattering, on the thermal conductivity of a material and on the energy exchange between electrons and material lattice during nonequilibrium laser heating. They developed a simple formula to predict the influence of film thickness, grain size, interface scattering parameters and the electron and lattice temperatures on the effective thermal conductivity of metal thin films. They developed a three-energy model to characterize the energy exchange between electrons and the lattice. They showed that the size effect reduced the effective thermal conductivity and increased the electron-phonon energy exchange rate.

Yilbas et al. [4] studied the thermal integration process during the pulse laser heating of metals. They considered two cases. In the first case, the effect of a high intensity pulse followed by a series of pulses having the same pulse length and repetition rate but different power intensities was accommodated. In the second case, a high pulse intensity followed by a series of pulses with the same intensity and pulse length but different repetition rates was considered. The heat transfer mechanism was modelled by an electron-kinetic-theory approach. They showed that thermal integration was possible for repetitive pulse heating and that the second case gave an improved thermal integration process.

Grigoropoulos et al. [5] studied the pulsed laser heating of thin silicon layers. They incorporated the effect of the change of material complex refractive index due to thermal gradients across the heat affected zone during transient heating at the nanosecond scale. They also included the effect of wave interference. Thin film optics theory was used to

rigorously account for the above effects. They presented results for the induced temperature field in thin silicon films by pulsed ruby and Nd:Yag laser light.

Yilbas et al. [6] studied mathematically the laser successive pulse heating of a workpiece surface. They used a 3-dimensional mathematical model based on the electron-kinetic theory approach. They solved the resulting integro-differential equation numerically to obtain the temperature profiles. They showed that the gain of energy by lattice site atoms through successive electron-phonon collisions was considerable in the surface vicinity. They also found out that the oscillations in surface temperature occurred in response to repetitive pulse frequency and concluded that it was less likely that the temperature profile followed the pulse profile due to the occurrence of conduction losses and motion of the slab.

Yilbas et al. [7] considered laser heating of silicon. They solved the heat transfer equations based on a three-dimensional form of electron kinetic theory approach. They used finite differences to solve the equations using a step input laser pulse with a Gaussian distribution. They compared their predictions with the results from the Fourier heating model. They showed that the temperature rise in the surface vicinity depended on the electron lattice site atom collisions. As the heating progresses, the internal energy gain dominated the conduction losses in this region. They also showed that the electron kinetic theory predictions and the Fourier theory results became similar as the laser pulse length increased.

Chen et al. [8] considered extensions to the dual-hyperbolic two temperature and hot-electron blast models to investigate the deformation in metal films subjected to ultrashort laser heating. They derived a new set of fully coupled, transient thermoelasticity equations based on the assumption of uniaxial strain but three-dimensional stress. They then solved these numerically. They showed that two potential material removal mechanisms could be identified, thermal (melting) and non-thermal (high stress). They showed that non-thermal damage could be a dominating mechanism in ultrashort laser-material ablation. They showed that the major driving force for non-thermal damage was the hot-electron blast force, generated by non-equilibrium hot electrons. They found that for Gold films thicker than 200 nm, a thin layer of material near the heated surface could be removed while damage could initiate from the middle region and then extending over the entire film if a Gold film of 50 nm thickness or less was employed.

Yilbas [9] considered laser short-pulse heating of Gold, Copper and Gold-Copper assembly. He modelled the energy transport inside the substrate material using an electron kinetic theory approach, which included thermomechanical coupling. Since stress levels exceeded the plastic limit of the substrate material, elasto-plastic analysis was employed. He found that 0.5 μm Gold layer did not result in temperature gradient change across the Gold-Copper interface. He showed that the plastic region was formed in the surface region of the substrate material, which extended up to almost 20 nm below the surface.

Naqvi et al. [10] considered time exponentially varying pulse laser heating of four and two layer assemblies. They used a four layer assembly of Gold-Chromium-Gold-Silicon and a two layer assembly of Gold-Silicon. They used elasto-plastic analysis to compute the stress levels in the substrate material and obtained the temperature field numerically using a control volume approach. They showed that stress levels higher than the yielding limit of the substrate material occurred in the surface region, which resulted in a plastic zone in this region. They found that the size of the plastic zone extended towards the solid bulk as the heating progresses.

Oane et al. [11] studied temperature fields in pulsed laser heated solids in relation to laser cleaning of surfaces. They developed an analytical procedure to study the temperature fields for a deeper knowledge of the laser-thin film substrate interaction.

Shao et al. [12] studied the heat generation and temperature field in a multilayer device consisting of thin and weakly absorbing materials subject to pico-second to nano-second pulsed-laser heating. They considered interference effects due to internal reflection and refraction. They used a tracking method based on electromagnetic optics and wave optics to determine the two-dimensional electrical and magnetic fields. These were used to calculate the heat generation and the accompanying temperature distribution. They applied this method to ZnSe interference filter subject to inclined laser incidence on its side. They showed that there was strong localized heating in a narrow region along the side where laser power was incident. This produced several high power spots aligned

obliquely to the side surface. They also showed that the pure absorption model was not valid for even small incident angles.

Shen et al. [13] considered the laser heating problem with nonlinear boundary conditions due to time-dependent absorptance. They solved the problem analytically using eigenfunction expansion method. They applied their results to calculate the heating of an aluminium plate. They showed that the nonlinearity between temperature and laser power density was magnified with an increase of the laser power density because the absorptance increased greatly with a considerable temperature rise. They showed that the rate of change of surface temperature was greater and less time was required to initiate melting in the case of temperature dependent absorptance. They also concluded that the effect of temperature-dependent absorptance was greatest at the surface and became more effective as the heating process approached the melting temperature.

Shuja et al. [14] investigated the effect of the assist gas jet on the thermal integration due to repetitive pulsed laser heating. They solved two-dimensional axisymmetric flow and energy equations numerically using a control volume approach. Turbulence was incorporated by using the low Reynolds number k-ε model and variable transport properties for the assist gas and solid substrate were taken into account. They also extended the study to include two gas jet velocities and three laser pulse types. They showed that thermal integration in the solid substrate was possible for a low-intensity power ratio of the repetitive pulses and the influence of the assist gas jet on the temperature profiles was almost insignificant.

Shuja et al. [15] considered three-dimensional laser gas-assisted heating of a moving stainless-steel workpiece. They solved the flow and energy equations numerically using a control volume approach taking into account turbulence by means of the low-Reynolds k-ε model. They carried out the simulations for three different workpiece speeds. They showed that the workpiece movement affected considerably the temperature rise inside the solid substrate. They also showed that the convective cooling effect of the impinging gas jet was more pronounced as the radial distance along the workpiece surface increased.

Jimenez et al. [16] studied growth of oxide films when a laser beam was shined on and heated a metallic layer deposited on a glass substrate in normal atmospheric environment. They used a three-dimensional heat diffusion model to make theoretical predictions about the dependence of oxide layer thickness on the laser power density. They showed that the predictions of the three-dimensional model were in good agreement with experiments. They also showed that surface cooling occurred between consecutive laser pulses and that the oxide track surface profile closely followed the spatial laser profile indicating the negligible importance of heat diffusive effects in the growth of oxide films by laser heating.

Kapitskii et al. [17] studied the role of convection in forming temperature and velocity fields in the gaseous medium in relation to the studies of kinetics of chemical reactions by the method of homogeneous laser pyrolysis. They developed a mathematical model

and calculated the nonsteady three-dimensional convection in a horizontal cylindrical reactor. They incorporated volumetric heating of the medium on the axis of the reactor by a continuous CO_2 laser. They compared their results with temperature field calculation based on the solution of the heat conduction equation and with experimental data.

Handa et al. [18] studied the pulsed laser heating of coated and laminated materials in relation to industrial characterization of bonded interface. They used a dynamic finite-element model to predict the transient stress and strain distribution in the material under pulsed surface heating. They studied the acoustic wave propagation and the elastic deformation of the layer.

Yilbas [19] studied laser short-pulse heating of Gold, Copper and Lead. He examined the material responses to laser short-pulse heating due to electron kinetic, two-temperature and one-temperature theories in detail. He studied the differences between the collisional and diffusional heating mechanisms and the conditions for the convergence of conduction mechanisms. He showed that the predictions from the electron kinetic theory differed from those of the one-temperature model in the surface vicinity of the substrate during the early heating duration. As the heating progressed both models predicted similar temperature profiles. He also showed that the electron kinetic theory and the two-temperature model predictions were in good agreement.

Yilbas et al. [20] investigated laser heating of titanium during laser gas assisted heating. They used the Fourier heat transfer model for solid heating and flow equations for the gas

jet impingement to describe the problem. Turbulence was incorporated via adopting the low-Reynolds number k-ε model. Nitrogen diffusion coefficient into the solid substrate was calculated using previous experimental results. They showed that the temperature rise in the solid substrate was considerable at the onset of laser pulse but as the heating progressed the temperature rise attained almost a steady value. They showed that the cooling effect of the impinging gas was minimal in the heating cycle. The nitrogen diffusion depth was found to be only 10 nm in the central region of the heated spot and did not extend considerably into the solid substrate in the axial direction.

Tian et al. [21] studied a heat transfer in a stationary fused silica rod heated by a CO_2 laser. He developed a model, which assumed fused silica to be opaque or semitransparent to laser irradiation. The radiative heat transfer from fused silica was modelled using the zonal method and the spectral dependence of the fused silica absorption coefficient in semitransparent wavelengths was approximated by a two-band model. The radiative source term was calculated by means of the weighted-sum-of-gray-gas method. They solved the resulting governing equation numerically. They discussed the importance of modelling the effects of laser energy penetration below the fuse silica surface during heating and the importance of radiative heat transfer in fused silica. They showed that a temperature difference of 25 K occurred if the Rosseland diffusion model was used in place of the zonal method.

Chen et al. [22] studied the ultrashort laser pulse interaction with a metal film. They developed a model to study the axisymmetric, dual-hyperbolic, two-temperature model to

investigate the two-temperature thermal response of a metal film. They modelled the laser heating as a volumetric heat source and incorporated temperature-dependent thermophysical properties in their model. They solved the resulting non-linear coupled differential equations through a fourth-order accurate finite difference algorithm. They calculated the electron and lattice temperature fields and examined the suitability of using a one-dimensional, two-temperature model for predicting the damage threshold fluence.

Shuja et al. [23] studied three-dimensional laser heating of steel substrate when subjected to impinging gas. They solved the governing flow and energy equations numerically by means of the control volume approach. The gas jet was assumed to impinge to the workpiece and was coaxial to the laser beam. To introduce turbulence the authors tested the k-ε model with and without corrections and the Reynolds stress model under conditions of constant heat flux from the solid wall and selected the low-Reynolds number k-ε model. Four gas jet velocities were considered. They showed that the impinging gas jet velocity had a considerable effect on the resulting gas side temperature. Also as the radial distance from the heated spot centre increased, the temperature at the surface decreased rapidly. They also showed that the assisting gas jet velocity did not influence the temperature profiles inside the solid substrate considerably.

Reich et al. [24] gave an overview of the computational modelling of laser induced heating. They describe recent efforts to simulate the heating of an enclosed container using a laser. They discussed the requirements of model complexity to achieve good results, relative to test data.

Yilbas et al. [25] investigated unsteady laser heating of a solid in relation to laser hardening of metallic surfaces. He examined the time unsteady analysis of the conduction limited process for a time dependent laser pulse power intensity. He showed that the conditions for thermal integration to occur required a minimum pulse rate of 100 kHz and in the limit the solution obtained reduced to that obtained for a step input.

Iwamoto et al. [26] studied energy transfer and surface modification of a metal surface theoretically in relation to pulsed laser heating. They assumed a Gaussian distribution in the radial direction. He showed that the peak deformation was proportional to the laser power.

Kalyon et al. [27] studied the laser heating process in relation to obtaining a desired temperature at the surface. They formulated the desired temperature at the surface and predicted the discrete step input intensity profiles. They introduced the ratio (k) of the desired surface temperature to steady value and the rise time of irradiance corresponding to the desired surface temperature. They developed a functional relation between the desired temperature and the variables k and t_r. They showed that as the dimensional rise time (t_r) decreased, while the temperature ratio (k) increased, partial steady heating of the surface was possible. Also as t_r increased, steady heating of the surface became impossible for all (k) values.

Shuja et al. [28] studied stress field in a steel workpiece in relation to the laser repetitive pulse heating of steel with assisting gas. They considered a two-dimensional axisymmetric case and solved the governing flow and energy equations using the control volume approach. The stress equations were solved using the finite element method. Turbulence was accounted for via the low-Reynolds number k-ε model. Temperature and stress fields corresponding to two repetitive pulse types and variable properties of workpiece were examined. They showed that the radial stress component was compressive while its axial counterpart is tensile. Also, the temporal behaviour of the equivalent stress almost followed the temperature field in the workpiece. They showed that one of the two pulse types resulted in higher equivalent stress in the workpiece.

Tzou et al. [29] analyzed the lagging behaviour in a double-layered thin film subjected to femtosecond pulsed laser heating. They used the dual-phase-lag model to describe the microstructural interaction effect and the fast-transient effect of thermal inertia. They put major emphasis on the appropriate thermal properties of the padding layer. They showed that thermal diffusivity and the two phase lags in the padding layer had profound effect.

Tokarev et al. [30] studied analytical modelling to the time-dependent pulsed laser heating. They obtained analytical solutions for the spatial and temporal temperature fields. Heat conduction equation was considered with a solid-melt phase boundary. The phase boundary was treated as a moving heat source of negative intensity. They showed that the short pulse effects could be essential even for nanosecond irradiation, when high enough pulse intensities were used and melting without vaporisation took place during

the first picosecond of laser heating. They also compared their results with measurements on silicon with nanosecond excimer laser radiation.

Qiu et al. [31] studied heat transfer mechanisms during ultrafast laser heating from a microscopic point of view. They modelled the heating process by the deposition of radiation energy, the transport of energy by electrons and the heating of the material lattice through electron-phonon interactions. A new macroscopic model governing the electron and lattice temperatures and the heat flux was developed from the microscopic transport process of electrons, characterized by the Boltzmann equation. They solved the model, evaluating the scattering term from quantum mechanical considerations. They showed that during ultrafast laser heating the inelastic scattering process became important and the relaxation time approximation was not generally valid. Also, the predictions agreed with the experimental data during subpicosecond laser heating.

Liu et al. [32] investigated the interaction of ultrashort laser pulses with planar metal targets. Theoretical analysis was carried out and energy flux in the process of femtosecond laser pulse heating was examined. They derived the electron temperature as a function of time from a one-dimensional two-temperature diffusion model and also the range of ultrashort laser duration and an expression of the highest electron temperature.

Yilbas et al. [33] studied gas-assisted nano-second pulse laser heating of a stationary surface. They conducted a numerical and theoretical investigation where in the governing flow and energy equations were solved via the control volume approach. Low Reynolds

number k-ε model accounted for turbulence effects. They ran the simulations for two gas jet velocities. An analytical solution accommodating the convection losses was also derived to validate the numerical predictions. They showed that temperature profiles predicted from the simulations agreed well with the analytical solutions. Also, the impinging gas jet velocity had no significant effect on the temperature distribution. They showed that as the heating progresses, equilibrium heating initiated, in which case the internal energy gain of the solid increased at an almost constant rate.

Smith et al. [34] investigated ultrashort pulse laser heating of metal films. They conducted a theoretical analysis and solved the Parabolic Two Step (PTS) heat conduction model taking into account non-equilibrium heating. They derived an analytical expression for the laser power that caused the film temperature to exceed a critical value and also presented an equation, which could be used to calculate the thermal damage threshold value for non-equilibrium heating. They showed that in non-equilibrium heating, the predicted peak lattice temperature was significantly lower and occurred at some time after the deposition of energy, which could be orders of magnitude greater than the pulse duration.

Yilbas et al. [35] compared the predictions of one-equation (Fourier heating model), two-equation, and kinetic theory models in relation to short-pulse laser heating. Three different pulses of lengths 1 ns, 0.1 ns and 0.01 ns were used. They described the physical significance of the predictions and discussed the discrepancies among the results. They showed that all the models predicted similar temperature profiles in the substrate for a

nanosecond laser pulse. As the pulse length shortened, the one-equation model predicted excessive temperature rise in the surface vicinity, whereas the two-equation and kinetic theory model predicted similar temperature profiles. They showed that in these cases electron temperature rised rapidly while the lattice temperature increase slowed down.

Al-Nimr [36] investigated a perturbation technique to simplify the generalised governing equations of the parabolic two-step model in relation to laser heating of thin metal films. He used the perturbation technique to eliminate the coupling between the electron and the lattice energy equations when the temperature difference between the electron and the lattice was a small, perturbed quantity. He derived a mathematical criterion to determine the conditions in which electron and lattice were in thermal equilibrium. He showed that five dimensionless parameters control the state of thermal equilibrium between the lattice and the electron.

Longtin et al. [37] investigated the thermal aspects of saturable absorption during high-intensity laser heating of liquids. They used a microscopically based theoretical model of the radiation absorption and heating process and compared its solutions with experiment for a contemporary saturable absorbing liquid.

Hosseini et al. [38] investigated the temperature and stress distribution at the interface of an elastic layer and a rigid foundation under a thermal shock in relation to pulsed laser heating. They used a boundary element method to calculate the effective stress and temperature fields. The pulse duration used was of the order of the characteristic time for

heat to diffuse across the layer thickness. The generalised thermoelasticity assumption based on the Lord and Shulman model was considered and the results were compared with the classical coupled and uncoupled models. They also studied the effect of pulse duration and layer thickness on the effective stress and temperature distribution of the layer using the classical theory of thermoelasticity. They showed that for the same maximum surface temperature rise, a shorter pulsed laser induced much stronger effective stress wave front. Also, the layer thickness had minor effect on the effective stress distribution.

Yilbas et al. [39] studied electron-kinetic theory, Fourier theory (one-equation model) and a two-equation model in relation to sub-nanosecond laser heating pulses. They solved the governing equations numerically for gold and chromium substrates. The effect of laser pulse intensity on the temperature rise was also considered. The predictions were validated for a triangular pulse and a silicon substrate. They showed that electron kinetic theory and two-equation model both predicted lower temperatures in the surface vicinity at early heating times. However, as the pulse heating progresses, the predictions of both models converged to the result of a one-equation model.

Yilbas et al. [40] studied the laser pulse heating of substrate analytically. They obtained a closed form solution for the temperature rise inside the substrate. Heating and cooling cycles of the heating process were also accommodated. The influence of pulse length on the resulting temperature profiles was investigated by keeping the energy content of all pulses constant. They showed that the rate of surface rise in the heating cycle and its

decay rate in the cooling cycle were high for short pulses. The closed form solution agreed well with the numerical predictions.

Yilbas [41] studied a three-dimensional laser heating process based on the electron kinetic theory approach. He obtained the temperature profiles from the kinetic theory and compared them with those obtained from the Fourier theory. The convergence of three-dimensional to one-dimensional heating was also investigated. Further, the results were also compared with the two-equation model for a one-dimensional case and the study was extended to include two different laser pulse lengths. He showed that three-dimensional heating approached its one-dimensional counterpart for the Gaussian intensity profile. As the pulse length shortens the Fourier theory predicted higher temperatures in the surface region of the substrate as compared to that predicted from the electron kinetic theory. Also, he showed that the temperature profiles obtained from the two-equation model and the kinetic theory were almost identical for the pulse length employed.

Khan et al. [42] investigated the stress field generated in a sheet metal in relation to laser heating. The problem was formulated analytically and solved using a finite element method. They showed that the laser scanning speed influenced considerably the temperature and stress fields in the sheet metal. Increasing the laser scanning speed reduced temperature in the region away from the centre of the laser heat source. They further showed that the stress components were compressive in the region close to the source; however, it became tensile in the region away from the heat source.

Yilbas et al. [43] studied the cooling rate of Ti-14Al-21Nb alloy subjected to laser pulse heating. They conducted a theoretical study based on Fourier analysis to predict the cooling rate of after laser pulse irradiation. They further, carried out an experiment to measure the cooling rate. The study was extended to include experimental investigation into metallurgical changes due to laser pulse.

Tian et al. [44] studied the CO_2 laser heating of glass rods. They calculated the temperature field in the glass rod by solving the governing equations using the control volume approach. The glass was assumed to be opaque at the laser beam wavelength of 10.6 μm. The dependence of absorption coefficient on wavelength and temperature was accounted for in the model. To analyze the radiation heat transfer, a diffusion approximation was incorporated in the model. The authors studied the effect of laser power, laser focus, the moving speed and the radius of the glass rod on the temperature distribution. They showed that with careful choice of these parameters a CO_2 laser might be used as a heat source for glass rod annealing or coating with stringent temperature constraints.

Com-Nogue et al. [45] studied the influence of various processing parameters in relation to laser hardening of 12% Cr steels. They carried out an experimental investigation in which two 12% Cr steels were used and the effect of laser beam shape, absorption coating nature, laser power and the travel speed were examined. A 5 kW CO_2 laser was used in the hardening trials. They also determined the residual stresses in the steel resulting from the hardening and compared their behaviour to the hardening of a carbon

steel and a low-alloy steel. In addition to the experiments a numerical solution of the heat conduction equation was also obtained and correlated with the experiments.

Yilbas [46] considered laser shortpulse heating of gold with variable properties. A theoretical analysis was conducted to examine the problem. The model was based on electron kinetic theory approach and a non-equilibrium energy transport was considered. The resulting integro-differential equations were reduced to partial differential equations using a Fourier transform method and these were further reduced to two differential equations similar to those of the two-equation model. The author correlated the coefficients of the differential equations. He showed that the variable properties resulted in higher lattice site and lower electron temperatures as compared to those corresponding to constant properties case.

Grimes et al. [47] studied the laser heating of metal surfaces by femtosecond pulses. They conducted experiments by shining a metallic surface with an intense, obliquely incident p-polarised laser field with $L\lambda^2$ approximately greater than 10^{14} $W\mu m^2$. They showed that a vacuum heating contribution to absorption of laser pulses existed. They showed that this was an important absorption mechanism for both discrete surfaces and density gradients of scale length L approximately less than electron quiver amplitude.

Yilbas et al. [48] studied laser pulse heating of a metallic substrate with convective boundary condition at the surface. A time exponentially varying laser pulse was employed and an analytical closed form solution was obtained using the Laplace

transformation method. They showed that the analytical solution became identical to that obtained for a step input pulse intensity when the pulse parameters (β and γ) were set to zero. The effect of Biot number on the temperature profiles became significant for Bi greater than or equal to 0.202. Moreover, they showed that the pulse parameter (β/γ) had considerable influence on the temperature profiles, in which case, temperature attained low values as β/γ became high.

Arnold et al. [49] studied the laser-induced free-electron heating in wide-gap solids. They examined a microscopic theory for the interaction of intense laser radiation at visible and near-infrared wavelengths with free electrons in a wide-band-gap solid. A numerical integration of the governing Boltzmann transport equation was carried out based on Monte Carlo method. Free-electron mediated energy transfer from the laser field to the solid and the electron-multiplication rate due to band-to-band ionisation as a function of laser intensity for SiO_2 was calculated. The authors treated the interaction of the laser radiation with the free electrons both within the standard classical approximation and quantum mechanically using second-order perturbation theory. They used the steady state Monte Carlo results in rate equations to make a direct comparison to experimental laser-induced heating data.

Chen et al. [50] studied various thermal transport models in relation to laser short-pulse heating of metallic materials. They conducted a numerical study in which they solved three two-temperature (dual-hyperbolic, hyperbolic, parabolic), two one-temperature (thermal wave and Fourier conduction) and one ultrafast thermomechanical models. A

finite difference method was used for the heat conduction equations and a combined finite-difference/finite-element method for solving the coupled thermomechanical equations. They showed that for pure metals the hyperbolic two-temperature model should be used for short-pulse (≤ 1ns) laser heating, while Fourier's law be used for long-pulse (> 1 ns) laser heating. For alloys, the dual-hyperbolic two-temperature model be used for short-pulse (≤ 10 ns) laser heating. Moreover they showed that, due to high strain rate caused by nanosecond- and shorter- pulse lasers, a coupled thermomechanical model should be considered for more accurately predicting the lattice field.

Zhao at al. [51] investigated the rapid CO_2 laser heating of silica glass. They conducted a numerical simulation in which a three dimensional heat transport model was considered. Temperature dependent glass thermophysical properties were also accounted for and change in the glass fictive temperature was investigated. They showed that the laser processing results in an increase in fictive temperature in the local laser affected zone. The fictive temperature was elevated by about 1000 K, was uniform to about 5% over the laser affected zone and transitions abruptly to the surrounding untreated glass value outside the laser affected zone. They showed that the thermal penetration depth could be determined from the thermophysical model.

Brantov et al. [52] investigated nonlocal heat wave propagation from laser-heated skin layer of an overdense plasma into a cold target. Their model accounted for the heat flux delocalisation and include collisional, frequency dependent and nonlocal effects. They tested their formula for the nonlocal heat flux in Fokker-Planck simulation of the hotspot

relaxation. They showed that good agreement was observed between kinetic simulations and the analytical model. They showed that thermal transport inhibition and large extent of the heat wave front occurred as compared to the classical Spitzer-Harm theory predictions.

Lu [53] studied the laser heating of a substrate by multi-beam irradiation. He derived a general model for the calculation of the temperature profile induced by the multi-beam laser in a semi-infinite substrate. He applied his model to calculate 2-beam irradiation induced temperature rise in the substrate. He showed that the double- Gaussian beam had advantages of narrow temperature profile and low heat flow intensity. Also, flatly topped temperature profiles could be obtained by converting the Gaussian laser beam.

Yilbas et al. [54] investigated the laser picosecond heating of silver using the electron kinetic theory approach. They solved the governing equations numerically and incorporated thermomechanical coupling in the equations. Temperature and stress fields were calculated. They showed that electron temperature well in excess of lattice site temperature occurred in the surface vicinity of the substrate material. Although the lattice site temperature was low, stress levels as high as 300 MPa were computed in the region heated by the laser beam. In addition they showed that thermal expansion of the surface at the irradiated spot centre reached 0.5 nm after 4 ns of the heating period.

Yilbas et al. [55] considered laser gas-assisted heating of steel in relation to heating and elastic response of the material and wave analysis. They solved the relevant governing

equations of flow and heat transfer numerically by means of a control volume approach while finite element and spectral element methods were used for the stress and wave equations. The normal component of the thermal stress was taken as the source of load for the flexural wave generation in the material. The wave characteristics were analyzed at four locations at the workpiece surface. They showed that the normal component of the stress was tensile. The dispersion effect of the workpiece material, interference of the reflected beam and partial overlapping of second mode of the travelling wave enable to identify a unique pattern in the travelling wave in the substrate.

Yilbas [56] studied entropy production in the electron and lattice subsystems and their coupling through thermal communication in relation to laser short-pulse heating of metallic substrates. He considered the ballistic behaviour of the electrons in the electron subsystem and obtained temperature fields. He showed that entropy production during thermal communication of electron and lattice subsystems was higher than those corresponding to electron and lattice subsystems.

Yilbas [57] studied laser short-pulse heating of gold-chromium two-layer assembly. The governing equations were solved numerically through the finite difference method. Heating period of the order of picoseceonds was examined due to which non-equilibrium energy transport occurred. Electron kinetic theory was employed while elasto-plastic analysis was carried out when modelling the thermomechanical response of the substrate materials. Thermomechanical coupling was also taken into account. He showed that the

temperature attained considerably high values across the gold-chromium interface, which in turn resulted in excessive stress levels in this region.

Shuja et al. [58] studied gas jet-assisted laser heating of a moving steel substrate with finite thickness. They conducted a theoretical investigation in which the relevant governing equations were solved numerically. Three-dimensional flow and energy equations were considered with variable properties of the gas. Turbulence was accounted for by means of the low Reynolds number k-ε model. Control volume approach was used and the simulations were performed for three different assisting gas jet velocities. The workpiece speed was kept constant. They showed that the effect of the assisting gas jet velocity on the surface temperature was more pronounced in the cooling cycle than in the heating cycle of the laser heating process. Also, the workpiece movement affected the location of the maximum temperature at the surface, which moved away from the initially irradiated spot centre in the direction of motion of the workpiece.

Kozlov [59] studied analytically the laws for the development of spatial temperature fields in a semiinfinite nontransparent body subjected to surface laser heating. He assumed that the laser beam was Gaussian and that the power was such that it neither disintegrates the material nor it caused a nonlinear variation of the thermophysical properties in the vicinity of the heated spot. He proposed a number of methods for determining the thermophysical characteristics of the body and also its absorptance for known values of the thermophysical properties.

Jiang [60] examined the modelling of energy coupling of CO_2 laser material interaction. He investigated several available models that described the effect of the different parameters such as refractive index, wavelength, angle of incidence, polarization, temperature, power, surface roughness and surface coating on the energy coupling phenomenon. He devised a generic methodology, which was used to de-couple, classify and recategorise the parameters and presented a process of creating a general model that combines the influences of selected crucial parameters.

Zheng et al. [61] investigated the thermopiezoelectric response of a piezoelectric thin film in relation to laser heating. They devised a theoretical model to study the problem. Transient temperature field of a two-dimensional composite media was analytically obtained by employing an integral transform technique. Analytical thermopiezoelectric fields were obtained by means of potential functions method. For a PZT-6B thin film deposited on substrate of a single crystal MgO, they showed that the temperature field was primarily controlled by the characteristic beam radius and maximum incident flux. The radial stress was shown to be much higher than normal and tangential stress.

Chen et al. [62] studied the thermomechanical response of metal films under the action of ultrashort-pulsed laser heating. They developed a micro-scale, ultrafast, axisymmetric thermoelasticity model and solved it numerically. The model covered the dual-hyperbolic two-step heating process in heat transport, the coupling effect between lattice temperature and strain rate and hot-electron blast effect in momentum transfer. The resulting coupled, transient thermoelasticity equations were solved by means of a non-conventional finite-

difference algorithm. A Gaussian laser pulse was assumed. They presented results including the hot-electron blast force, lattice temperature and thermal stresses. In addition they examined the credibility of the simplified one-dimensional model.

Takahashi et al. [63] studied a kinetic model of gas heating of laser-produced plasmas in atmospheric air. They developed a kinetic model for laser-induced breakdown and gas heating in an N_2/O_2 gas mixture. Particle densities, electron energy, electron rate coefficient, vibrational temperature, gas temperature and other plasma parameters were calculated. Gas temperature was calculated from the potential differences in all chemical reactions. They showed that the electron density of 10^{23} per m^3 is the threshold of electrical breakdown and gas heating, and that the electron-ion recombination and the collisional de-excitation of vibrationally excited N_2 had a strong effect on the gas heating.

Shuja et al. [64] studied gas assisted laser repetitive pulse heating of steel in relation to the thermoelastic displacement of the metal surface. They calculated the strain in the surface vicinity and the thermoelastic displacement of the surface for two pulse types. The correlation between the surface temperature and the surface displacement was explored. They showed that the surface displacement follows the frequency of the temperature profiles, however the rise and fall of the rates of the surface displacement differ considerably from those of the temperature field. This was more pronounced for the repetitive pulses with long cooling periods. In addition, the spatial resolution of the surface displacement differs from the spatial resolution of the surface temperature across the irradiated surface.

Yilbas [65] considered laser step-input pulse heating of gold substrate. He studied the thermal response of electron and lattice subsystems to four different intensity pulses with the same energy content. The modelling was based on the electron kinetic theory approach so as to account for the nonequilibrium energy transport in the substrate material. He showed that electron temperature rised rapidly in the heating cycle while lattice temperature rise was gradual, which was more pronounced for laser short pulse lengths. In the cooling cycle, electron temperature decay rate differed from the rate of lattice site temperature rise due to the specific heat ratios of electron and lattice sites.

Ho et al. [66] investigated the modelling of nonlinear laser heating of semiconductors. He considered a new theoretical framework and incorporated the dynamical behaviour of semiconductors, the temperature-carrier coupling, the generation and recombination of defects, the diffusion of defects, the diffusion of impurities by defect-dopant pair mechanism and chemical reaction between species. They applied this model to n-type silicon irradiated by a nanosecond pulsed Nd:YAG laser and examined the dynamical evolution of laser-semiconductor interaction process by calculating the carrier, defect and impurity concentration profiles.

Shuja et al. [67] studied the laser pulse heating of steel surfaces incorporating the effect of an impinging gas and variable properties. They solved 2-dimensional axisymmetric flow and energy equations numerically using a control volume approach. Turbulence was accounted for via the low Reynolds number k-ε turbulence model. Variable properties for

both the solid and gas were assumed. Air was considered as an assisting gas coaxial with the laser beam. The results were compared to the analytical solution from the literature. They showed that the assisting gas jet had some influence on the temperature profiles, however this effect was minimum at the irradiated spot centre but it amplified considerably in the gas side. In addition, consideration of variable properties resulted in lower surface temperature as compared to constant properties case.

Grum et al. [68] investigated temperature profiles, heating and quenching rates during laser melt hardening of cast iron. They used a mathematical model to determine the temperature profiles in gray and nodular iron and the depth of the modified layer. They critically assessed the mathematical results and compared them to experiment. They showed that the predicted microstructural changes from the temperature profiles on heating and cooling were confirmed by microhardness measurements. In addition they showed that in some heat treatment conditions, deviations occurred between the mathematical model and experimental results.

Tian et al. [69] studied laser heating of moving glass rods. They considered a heat transfer model to calculate the temperature field in moving glass rods. Conduction and radiation heat transfer in radial and axial directions were accounted for. Radiation heat transfer was modelled through the Rosseland diffusion approximation. The spectral property of the glass was simulated through a two-band model. They showed that glass rods of sufficiently large optical thickness should be treated as a semitransparent medium for radiative transfer and that it was reasonably accurate to assume it to be opaque to CO_2

laser irradiation. The resulting temperature profile was shown to be strongly dependent on the size and power of the laser beam. They further showed that the diameter and the speed of the moving glass rods were also important in determining the temperature field. The convective heat transfer coefficient between the glass rod and the environment had little effect.

Hoogers et al. [70] studied laser-induced disordering of clean and adsorbate covered rhodium surfaces by LEED and by laser-induced thermal desorption (LITD) of deuterium. They conducted experimental analysis in which excimer laser pulses of 120 ns duration and intensities between 35 and 85 MW/cm^2 were applied. They showed that Rh{111} was more resistant to disordering than Rh{332}, which was consistent with a decrease in the activation energy for disordering due to steps from 59 to 39 kJ/mol. They estimated onset temperatures for disordering as 954 K and 700 K. In addition they showed that there was no protective effect for adsorbate monolayers of oxygen and carbon monoxide.

2.3 Non-Conduction Limited Heating

Yilbas et al. [71] studied the laser heating mechanism initiating the drilling process. The study included conduction and convection effects and assumes a steady-state evaporation process. They conducted a laser drilling experiment while monitoring the surface evaporation process. Also using a model, they predicted the maximum temperature

attained inside the material, nucleation, explosion process and drilling efficiency. The results for the vapour front velocity were compared with those of the previous experiments.

Yilbas [72] studied the laser induced heating of an aluminium workpiece. He developed a heat transfer model, which incorporated the temporal variation of CO_2 laser output pulse, phase change process and temperature dependent thermal properties of the workpiece. He solved the heat transfer equations numerically also accounting for the surface reflectivity. He showed that the time corresponding to maximum temperature could be predicted by proper selection of pulsed parameters. He also showed that the ability of the material to follow the laser pulse profile depended upon the pulse shape.

Yilbas et al. [73] examined a heat transfer model to study laser induced interaction mechanism. They used steady state and time dependent heating modes to predict temperature profiles inside the workpiece material. They estimated the time for the surface temperature to reach 90% of its steady state value. They also conducted experiments, measuring the surface temperature of the irradiated spot to validate their theoretical predictions. They found that during the use of a pulsed laser, as the heating progresses the drilling velocity rised while the liquid depth and time to reach steady state fall.

Cole et al. [74] studied the laser melting of Silicon. They solved the heat equation for the melting process numerically. They used different values of the thermal conductivity and

melting temperature for the amorphous Silicon compared to that of crystalline Silicon. They showed that the predictions were in good agreement with experimental results for melting thresholds and melt depths. They predicted that the maximum melt depths were attained when pulses of constant energy density applied were not dependent on the pulse duration for various amorphous and crystalline silicon combinations. They showed that the melting thresholds for both crystalline Silicon and Silicon with amorphous surface layers increased with increasing pulse length.

Mancini [75] studied laser ablation using a hydrodynamic model. The model, which they used, took into account the phenomena of heating, thermal conduction, hydrodynamics and atomic kinetics. They computed the ionization balance, plasma formation and expansion and the attenuation of the laser light as it traveled through the plasma.

Linford [76] considered the interaction physics of intracavity laser heated particles. He studied the case of a moderate power, high repetition rate Nd:YAG laser oscillator producing low energy optical pulses. The particles he considered were contaminants that inadvertently became attached to intracavity optical surfaces lying within the beam line of the laser. He conducted computer simulations to calculate the behaviour of a variety of dielectric, refractory and metallic particles when irradiated with small diameter, high intensity intracavity laser radiation. He showed that due to small laser beam diameters, contaminating intracavity particles larger than 5 μm could effect the dynamics of Nd:YAG laser oscillation, causing mode changes, delaying the achievement of peak laser power and reducing performance. He showed that significant heating of the particles

might occur during the relatively short oscillation build-up time. He predicted ablation, melting and vaporisation of small diameter particles under these conditions. He calculated steady-state conditions for high repetition rate operation, which means that the asymptotic particle and substrate temperature depend upon the thermal properties of the optical substrates. He determined operating regimes for which laser heated particle damage does not occur.

Arif et al. [77] studied laser short pulse heating of copper. They employed the electron kinetic theory approach to model the nonequilibrium heating process while thermomechanical coupling is introduced in the energy transport equation to account for the thermomechanical response of the substrate material. They numerically calculated the stress field due to temperature gradient in the laser irradiated region by using a thermo-elastic and thermo-elasto-plastic analyses. They showed that the temperature gradient is higher in the region next to the surface vicinity inside the substrate material. They showed that equivalent stress levels attain high values in the vicinity of the surface, which in turn results in a plastic zone.

Zhavyi et al. [78] studied liquid-solid phase transitions induced in monocrystalline GaAs by two laser beam irradiation. They modelled the problem on the basis of a one-dimensional Stefan problem and solved it numerically using finite difference technique. They considered two variants of combined irradiation by Q-switched ruby and CW Nd:YAG lasers. In the first variant nanosecond radiation from a ruby laser induces the surface melting of a GaAs wafer and “switches on” the absorption of additional CW

intensive radiation directed from the backside of the wafer. In the second variant two laser beams are directed from one side. They showed that the motion of the liquid-solid interface could be controlled by changing the intensity of CW radiation. They showed that because of strong temperature dependence of optical absorption in solid GaAs, a heat wave moving forward toward Nd:YAG laser radiation could arise near the liquid-solid interface in opposite geometry and screen the melt from the CW laser beam. They also showed that in the case of a one-sided geometry the time dependence of melting depth has a nonmonotone character; the crystallization process can be terminated and the melting develops again.

Jimenez et al. [79] studied oxide thin film growth on titanium films using laser heating. Films previously deposited on a glass substrate were heated by Nd:YAG laser pulses in air. The samples were moved at a constant speed of 2 mm/s to create oxide tracks. The micro-topographic analysis of the tracks was performed by a microprofiler. They also solved an analytical equation describing the oxidation rate. They showed that the surface temperature gradient has much effectiveness on the film growth process. They also showed that thermo-oxidation reactions took place at the Ti film surface that reached an estimated temperature of 1160 K due to action of the first pulse. The analytical results were in agreement with the experimental data for film thickness in the high laser intensity region.

Yilbas et al. [80] considered short pulse laser heating of steel and related Fourier and electron kinetic theory models. They solved the governing equations of heating

numerically with appropriate boundary conditions and calculated the recession and vapour front velocities, vapour pressure and recoil pressure for different laser power intensities. They also modelled the elastic-plastic wave propagation in the solid substrate. They showed that the rapid rise of surface temperature occurred at high laser power intensities and the recoil pressure generated at the surface substantiated resulting in elastic-plastic wave propagation in the solid substrate. They showed that a plastic region of the order of 0.9 μm was developed in the surface vicinity of solid substrate and the time required for this deformation was in the order of 25 ns.

Muhammad Sami et al. [81] studied the heat transfer mechanisms relevant to pulsed laser heating. They used the Kinetic theory approach and calculated the temperature profiles numerically for different pulses. They considered conduction, convection due to melting and evaporation in their heat transfer model. They also carried out a comparison between various temperature profiles.

Kostyukov et al. [82] studied collisional and collisionless heating in a cluster plasma in the framework of nanoplasma model. They identified an efficient autoresonant regime of collisionless heating and analyzed it. They derived a simple analytic expression for the threshold of the transition from a collisional regime to a collisionless regime. They showed that the collisionless regime of absorption was dominant for the last stage of laser-cluster interaction.

Kaplan [83] studied absorption mechanism in laser materials processing. He developed a mathematical model to calculate the absorptivity and the resulting temperature field as a function of space and time during pulsed laser heating of a plane surface. He modelled the temperature dependence of the absorptivity treating Au/Ni-galvanized Cu-substrate as an electronic material.

Kalyon et al. [84] investigated the laser pulse heating process with a time exponentially varying pulse shape. They obtained a closed form solution for the temperature rise. They took into account evaporation of the surface. They used the Laplace transform technique to obtain the analytical solution. The effects of the boundary conditions at the surface and pulse parameters on the temperature profiles were examined. They showed that the surface temperature profile was very sensitive to the convective boundary condition at the surface. They showed that as the convective cooling of the surface proceeded, oscillation in the temperature profiles was observed around the evaporation temperature. Also as the power intensity profile moved towards the pulse beginning, the peak surface temperature increased.

Cote et al. [85] studied gun steel using laser pulse heating in air, argon, oxygen, nitrogen and hydrogen. They observed surface roughening, melting and oxidation-induced composition changes on the steel surface. They also performed computer modelling of laser pulse process for the specimen configuration used in the experiments. They showed that comparisons of laser pulse heating experiments with actual data offered new perspective on gun bore degradation mechanisms.

Volkert et al. [86] studied phase transformations during pulsed laser heating of phase change media. They carried out analytic and finite element modelling. Through modelling they identified the issues that were relevant to optimizing the performance of these structures for use in high density, high speed optical data storage systems. They concluded that the approach provided the understanding to suggest specific means of optimization. They presented guidelines for media optimization and about areas that posed the most serious limitation.

Yilbas [87] studied laser heating process based on an electron-kinetic theory approach. He derived governing equations for a 3-dimensional model based on the electron-kinetic theory approach and took into account phase change and conduction effects. The laser heat source was assumed to be moving with a constant speed. He then solved the governing integro-differential heat transfer equation numerically. In addition he conducted experiments to measure the surface temperature of the workpiece substrate. He showed that the rapid increase in temperature occurred in the surface vicinity due to successive temperature electron-lattice site atom collisions. He showed that, as the depth of melting increased during heating, the temperature remained almost constant at the melting temperature of the substrate in the surface vicinity. He showed that the theoretical predictions were in good agreement with the experiments.

Li et al. [88] studied two different models of heat sources in relation to laser melting of Al_2O_3-based refractory. They calculated the thermal fields by solving the three-

dimensional quasi-steady heat conduction equations using the Green function method and thereby predicted the melt cross-sections of the refractory. The laser heating was modelled both by a volumetric heat source and by a surface heat source. They showed that the predicted melt depths and widths using a volumetric heat source model were in excellent agreement with the experimental data. Further, the predicted cross-sectional profiles melt/solid interfaces were consistent with the experimental results for smaller melt cross-sections. They also showed that the increase in the size of melt cross-section increased the discrepancy between the theoretical and experimental data.

Mazukhin et al. [89] considered nonequilibrium laser heating and melting of silicon. They studied the mathematical model of nonequilibrium laser heating and phase transformations induced by nanosecond pulse laser irradiation at 1.06 μm. They considered the complex dynamics of the radiation absorption, the electron-hole plasma development, the heat diffusion and the radiation transfer. They conducted simulations and showed that the radiation absorption process was self-regenerative. They also showed that significant overheating of plasma occurred and that an overheated metastable region formed in the solid phase.

Shen at al. [90] studied mathematical modelling of laser induced heating and melting in solids. They developed an analytical method for treating the problem and applied it to aluminium, titanium, copper and fused quartz. They obtained the time needed to melt and vaporise and the effects of the laser power density on the melt depth for the four metals. They also calculated the depth profile and time evolution of the temperature in

aluminium before and after melting. They showed that the calculated melt depth evolution of fused quartz induced by 1.06 μm laser irradiation was in good agreement with the experimental results.

Yilbas et al. [91] investigated 3-dimensional laser heating of semi-infinite steel subjected to repetitive pulsation. They considered an electron kinetic theory approach to model the problem and derive the governing equations. The resulting integro-differential equations were solved numerically. The model took into account conduction and phase change processes and the laser beam was considered as scanning the surface with a constant velocity. Repetitive pulses were used such that the ratio of successive pulse intensity to the first pulse intensity was kept constant and the cooling period between two consecutive pulses was also kept constant. Three ratios were considered to investigate the effect of power intensity ratio on the resulting temperature profiles. Conditions for the thermal integration and isothermal heating were also introduced. They showed that the temperature profiles did not follow the pulse profile and that thermal integration was possible for the low power intensity ratio considered.

Yilbas [92] investigated the heat transfer mechanism taking place during Nd:YAG laser irradiation of steel workpieces. His study included conduction, phase change and convection. He assumed a Gaussian profile for the laser output intensity in space and incorporated time-dependence resembling the actual laser output pulse. Computations were carried out to obtain theoretical predictions. Mass removal from the irradiated spot was modelled using momentum and continuity equations and temperature dependent

thermal properties were taken into account. He further carried out experimental measurements of surface temperature and evaporating surface velocities. Optical and streak photography techniques were employed. He showed that surface temperatures and evaporating front velocities were in good agreement with the experimental results.

Bashenko et al. [93] investigated the effect of concentrated heating by a CO_2 laser on the variation of the structure and properties of the surface layer of workpieces of low-machinability materials subject to cutting. They considered the power of the laser of up to 3 kW and employed finite element method and experiments on 3 different nickel alloys for their investigations. They used the experimental results to formulate the model of the process of laser-assisted machining of the strain-hardened materials and to classify the nature of laser heating required in machining materials of various grades. They showed that the reduction of the energy capacity of the process of cutting austenitic strain-hardened materials was due to the hardening of the surface layer of the workpiece.

Yilbas et al. [94] studied the laser material removal by evaporation and radial ejection of liquid during laser machining process. They conducted a mathematical analysis and solved the time unsteady problem. They predicted nucleation explosions during the process.

Yilbas et al. [95] developed a 3-D laser heating model including phase change process. They developed the mathematical model and solved it numerically. The model considered the probability of electron and lattice site atom collisions during conduction

heating process, and the probability of vacancy and molecular collisions during the phase change process. The collision probability of each species was considered when describing the conduction, melting and evaporation processes in laser pulse heating. They showed that the 3-D model gave lower surface temperatures as compared to results obtained from 1-D model.

Peng et al. [96] studied two mathematical models in relation to laser induced surface melting experiments involving Ti alloy. They used analytical and numerical procedures to obtain solutions to the models. Both models were based on different assumptions and had different applicabilities. They presented a comparison between the two models and the advantages and limitations of the analytical and numerical modelling procedures.

Koc et al. [97] studied the laser heating process including evaporation through the electron-kinetic theory approach. A numerical procedure was adopted to solve the resulting governing equations. The transport of energy was described in the model on the basis of electron-phonon and molecule-phonon collisions. The study considered three different heating pulses and the resulting temperature distributions inside and at the surface of the substances were computed. Also, the first and second law efficiencies of the melting process were included which would give the pulse shape for improved melting efficiency. They showed that the temperature distribution in the vicinity of the surface depended on the electron distribution and on the number of collisions taking place in the region. And that the Fourier theory results gave a lower surface temperature than predicted from this study.

Balandin et al. [98] investigated interference effects in relation to laser pulse heating of multilayer structures. They solved the heat–diffusion equation numerically taking into account current phase transitions and interference of heating radiation reflected from layers and phase boundaries. The periodical change of reflectivity versus the thickness of one or several layers and the effect of radiation absorption and heating were also investigated. The authors compared the results of computer modelling with experimental data.

Yilbas et al. [99] considered laser heating of steel using the Fourier heating model taking into account phase change. They solved the governing equations numerically using a control volume approach. The thermal stresses generated in the solid region of the substrate were also calculated. To ensure grid independent results the authors also conducted grid independence tests. Further, they also carried out an experiment to validate the cavity profile as predicted from the simulations. They showed that the predicted cavity profile agreed well with the experimental results. The temperature profile decayed sharply in the liquid region close to the cavity wall. In addition they showed that the equivalent stress reached its maxima at two locations in the radial direction, and as the heating progressed the magnitude of the second peak of equivalent stress reduced.

Dutta et al. [100] investigated heat transfer, fluid flow and mass transfer in relation to a single-pass laser surface alloying process. They developed a transient model for the

problem and solved it numerically through a control volume approach. Phase change processes were also accounted for and were modelled using a fixed-grid, enthalpy-porosity technique. The model was used to predict the species concentration distribution inside the molten pool during alloying and in the entire cross-section of the solidified alloy. The authors also conducted a parametric study with regard to laser power, scanning speed and powder feed rate to assess their influence on geometry and dynamics of the pool, cooling rates and species concentration distribution inside the substrate.

Kalyon et al. [101] studied the laser pulse heating process in relation to a time exponentially varying pulse. They conducted a theoretical analysis and obtained an analytical closed form solution for the temperature rise. Evaporation from the surface was taken into account and the effect of pulse parameters on the temperature profiles was examined. They showed that the closed form solution derived from the present study reduced to a previous analytical solution with recession velocity set to zero. In addition they showed that the predictions of the numerical simulations and the closed form solution were in good agreement.

Chung et al. [102] considered scanning laser-induced melting, vaporisation and resolidification in metals subjected to step heat flux input. They developed a 1-D physical model based on Stefan problem with appropriate boundary conditions and obtained numerical solutions. The beam power was assumed constant. The effects of varying beam diameter, scan speeds and substrate temperatures on process variables were investigated for Nickel. They also derived relations for the time to initiate melting, to initiate

vaporisation, to reach maximum melting depth, for melt resolidification, and for maximum melting and vaporisation depths. Lastly, surface temperatures were compared with approximate closed form solutions.

Cho et al. [103] studied the laser beam welding of Ti-6Al-4V alloy in relation to the residual stresses developed in it. They predicted the residual stresses by means of a process model. The model validation was done by means of processing trials. Characterisation of the heat transfer during welding and the observation of the fusion zone enabled the development of a suitable thermal model. They showed that predictions with regard to the residual stresses were in agreement with the experiments.

Yeo et al. [104] considered three-dimensional variable-property modelling of laser full-penetration welding. They included in their model the effects of welding speed, Marangoni convection, natural convection, surface heat loss and temperature dependent material properties. They showed that the welding speed and the Marangoni convection played critical roles in determining the welding characteristics. Also a comparison of the variable-property modelling to a 3-D constant-property counterpart showed that the variable-property effects were appreciable. They also showed a method to use the modelling results to estimate the keyhole radius or to predict the welding energy efficiency.

Coelho et al. [105] investigated thermal modelling of high-speed laser cutting of superposed thermoplastic films. They developed a theoretical model describing the

temperature distribution in thin film thermoplastics material and solved the heat conduction equation analytically by the Green function method. Heating and cooling thermal stress evolution was also accounted for. They applied the predicted engineering parameters to the cutting of superposed high- and low- density polyethylene samples and validated them experimentally. They showed that proper modelling and an introduction of a reflective substrate under the samples improved the process efficiency and allowed cutting operations of up to 20 m/s and cut with welding of up to 14 m/s.

Fischer et al. [106] studied the modelling of near infrared pulsed laser sintering of metallic powders. He described a model for the above stated problem and solved it numerically. Experimental validation was performed with a pulsed Nd:YAG laser on titanium powder. He showed that the model predictions were in good agreement with the experiments.

Yagnik et al. [107] studied pulsed laser surface heating of UO_2. Theoretical and experimental analysis was carried out. They heated solid uranium dioxide targets in vacuum to 3700 K. The target surface temperature was then compared to results obtained from a 1-D heat transport model of the problem that accounted for conduction and melting in the solid and ablation and radiation from the surface. Vaporisation of UO_2 was assumed to be congruent. The theoretical model also took into account temporal and spatial characteristics of the laser beam as well as temperature-dependent physical and thermodynamic properties of UO_2. Post-irradiation microscopic examination was also carried out of the target surface for model validation and tests were performed to asses

qualitatively the attenuation of laser light and thermal radiation from the surface by the vapour blow-off from the target. They showed that this last effect was not of significance.

McMasters et al. [108] investigated the penetration of the laser flash beyond the surface of the material being heated. They conducted a theoretical study in which three different heat transfer models were considered. Each model has different assumptions about the initial temperature distribution inside the material. Parameter estimation was performed using the data from a previous experimental research. The material used was carbon bonded carbon fibre (CBCF).

Potente at al. [109] studied the heating and joining of thermoplastics during laser transmission welding. They conducted an experimental and theoretical study. Two parts were joined together through laser heating of one of the surfaces of the opaque part, which was in contact with the transparent part. The laser passed through the transparent part, which was subsequently heated by conduction heat transfer. They showed that if the opaque laser absorbing part had a high absorption constant the process could be readily described by a physico-mathematical model. They compared the experimental and theoretical results and showed that by introducing a correction factor it was also possible to successfully model the low absorption constant case.

Wang et al. [110] investigated laser heating assisted cutting of ceramics by metals. They used finite element numerical analysis to solve the mathematical models and calculated temperature distributions resulting from simultaneous laser heating and metal cutting.

They showed that the high temperature in the cutting area is caused by the superposition of the temperature distribution of laser heating and metal cutting. The temperature in the cutting area was shown to be related to the distance between the laser heating point and the cutting point, the cutting speed and the thermophysical characteristics of the material being cut.

Yilbas et al. [111] considered nitrogen diffusion onto titanium as a result of laser heating. They conducted a transient heat transfer analysis based on the Fourier theory and obtained a closed form solution taking into account the phase change process. Nitrogen concentration inside the substrate was computed using a previously obtained diffusion coefficient. They considered five different pulse lengths with the same energy content to investigate the effect of laser parameters on the diffusion. They showed that the influence of the pulse length on the nitrogen concentration was considerable and its effect on the diffusion coefficient was significant.

Minko et al. [112] studied metal surface defects resulting from laser heating of the metal surface. They experimentally studied the appearance of microcraters, microparticles and continuity breaks of characteristic sizes 1-10 μm under the action of laser monopulses of the duration of 40 ns to 300 ns. They also developed a model of initial destruction of materials and generation of condensed particles based on an exclusive thermal action of laser radiation and the natural inhomogeneity of the solid.

Tiwari et al. [113] investigated laser-aided heating and evaporation of metallic particles. They developed a theoretical model of particle heating and their phase transitions in relation to laser heating. They also discussed the conversion of liquid droplets to the gaseous state. They showed that the temperature rise of the particle was uniform due to the predominance of thermal conduction. As the temperature rised, heating rate increased due to increase in electron-phonon collisional frequency.

Sonti et al. [114] studied the modelling heat flow in deep-penetration laser welds in aluminium alloys. They developed a two-dimensional finite-element nonlinear transient heat–conduction model and used it to simulate deep-penetration keyhole laser welds in aluminium alloys. The weld thermal profiles were calculated in an arbitrary reference plane as the laser beam approached and passed the plane. Three-dimensional quasi-steady-state shapes of the weld pools were then determined from the thermal profiles. They showed that the predicted weld bead shape and dimensions were in good agreement with the experimental results. It was showed that the model predicted large mushy zones for aluminium laser welds during solidification, which was directly related to the probability of porosity formation by increased bubble entrapment. This agreed well with the experimental finding of large amounts of porosity in laser welds in aluminium alloys.

CHAPTER 3

MATHEMATICAL ANALYSIS

The problem discussed in this thesis consists of two distinct parts. The mathematical analysis of these parts is considerably different. Let us discuss the solution procedure one-by-one.

3.1 Laser Heating of the Substrate Material

Let us first consider the solution procedure of a 2D melting problem. We start from a solid body whose temperature is rising with time in a nonuniform manner. Energy is provided by a nonuniform volumetric heat source inside the body, which causes the temperature to rise in the body. Due to the nonuniform nature of the heat source the temperature distribution inside the body becomes also nonuniform. As heating

progresses, a time is reached when the temperature at some parts of the body reaches melting temperature of the substrate material and the material converts into a liquid phase. One can tackle this problem in the following manner. Start solving the unsteady heat conduction equation in the solid phase. In the time step, in which some parts of the body reach or exceed the melting point, the boundary between solid and potential liquid regions should be determined. Since a fixed rectangular grid is chosen in the solution domain, there are regions where the solid-liquid interface will pass through the individual cells. In this case, all such cells make up a so-called ‘mushy zone’ in which they are in partly solid and partly liquid phases. In this scenario, the usual heat conduction equation cannot be solved in these regions, but instead a ‘quality’ equation should be considered. The quality of a mushy zone (cell) can range from 0 to 1. A quality of 0 designates a solid cell and a quality of 1 designates a liquid cell. Therefore, in the newly demarcated region calculate the quality of the cells by solving the quality equation. There will be cells whose quality will be in between 0 and 1. All such cells make up the ‘mushy zone’. There will be cells whose quality will be equal to or greater than 1. All such cells make up the liquid region. Calculate the boundaries of these two regions. In the liquid region one should solve the heat conduction equation to obtain the temperature field. This procedure is repeated in the next time step. In this way one can proceed in time to determine the region where phase change takes place. As simulation progresses the time step will be reached in which the temperature of some parts of the liquid region will reach or exceed the boiling point of the substrate material. At this point, we start calculating the boundary of the liquid and the potential vapour regions. In the potential vapour region we

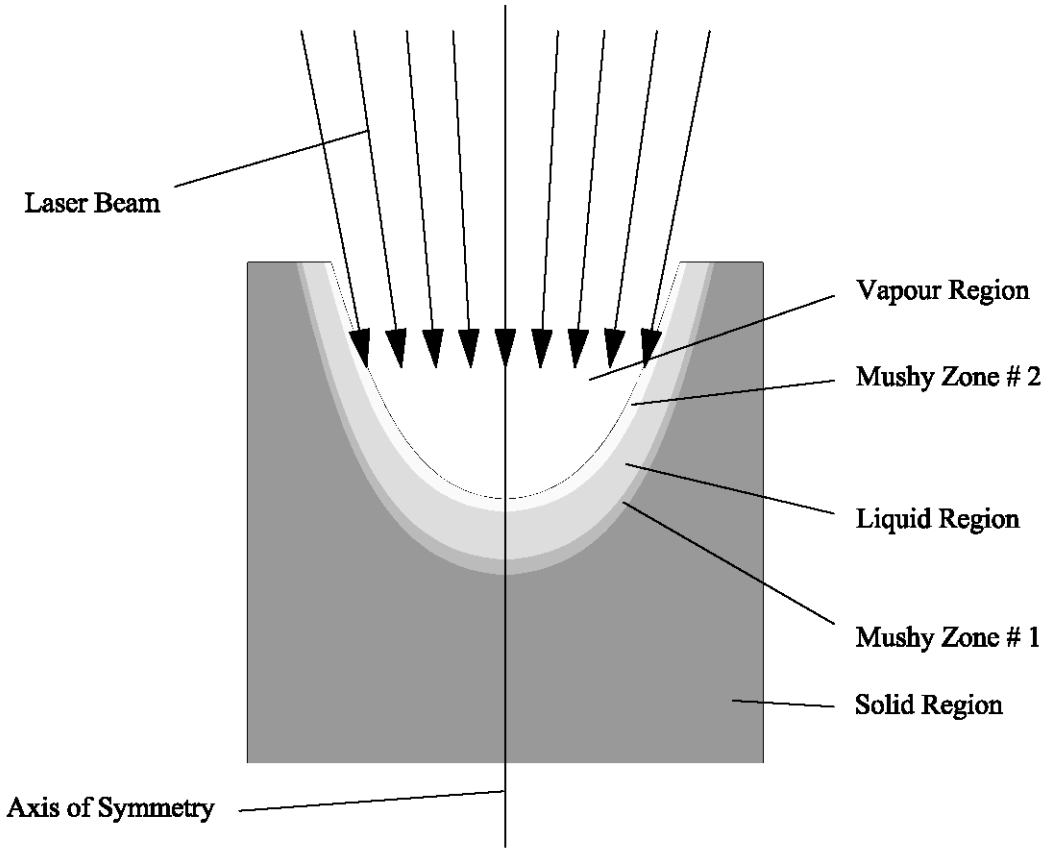

Figure 3.1 - Schematic of a laser drilling process.

can then calculate the quality of each cell to determine whether it has fully converted to vapour phase or not. There will be cells whose quality will be in between 0 and 1. All such cells make up the second ‘mushy zone’ region. There will be cells whose quality will be equal to or greater than 1. All such cells make up the vapour region. One should calculate the boundaries of these two regions. The boundary between the second mushy zone and the vapour region actually defines the cavity shape. This procedure is repeated for all future time steps. In this way the cavity shape can be predicted.

For modelling a laser drilling operation, one approach is to assume the laser heating by means of a volumetric heat source, which is spatially and temporally distributed in the workpiece. The magnitude of the volumetric heat source depends on the laser surface intensity, the laser beam absorption depth and the reflectance of the laser beam from the surface. Let us now list the major assumptions of the mathematical model employed in the analysis.

- Fourier’s law of heat conduction is applicable in the solid and liquid regions.
- The problem is 2D axisymmetric.
- The material is a pure substance with single melting and evaporation temperatures.
- Laser absorption is modelled by a volumetric heat source in the metal.
- Thermo-physical properties of the metal are constant.
- The vapour does not interact with the laser beam.
- Liquid movement and expulsion are negligible.

- Insulated boundary conditions at the upper surface.
- Solid and liquid phases have the same absorption coefficient.
- Material has a certain absorption depth for the laser radiation.
- Laser beam intensity has Gaussian distribution.
- There is no ionization of the emerging gas front.
- There is no multiple reflection phenomena from the surface.
- Laser pulse is time exponentially varying resembling the actual laser pulse intensity.

Mathematical details of the problem are presented in the next section. We have three distinct stages. In stage 1 the temperature anywhere in the solid region is below melting point. In stage 2 the temperature anywhere in the liquid is below evaporation temperature. In stage 3 we have three distinct phases, solid, liquid and vapour.

3.1.1 Stage 1: No melting; solid phase exists only; no mushy zone

The transient heat transfer equation for a solid substrate at constant properties irradiated by a laser beam is presented below.

Solid Phase:

In the solid phase, the Fourier heat conduction equation is used. This is due to that the length and the time scales considered in the analysis are larger than interatomic spacing and electron relaxation time. Therefore, the heat diffusion equation is:

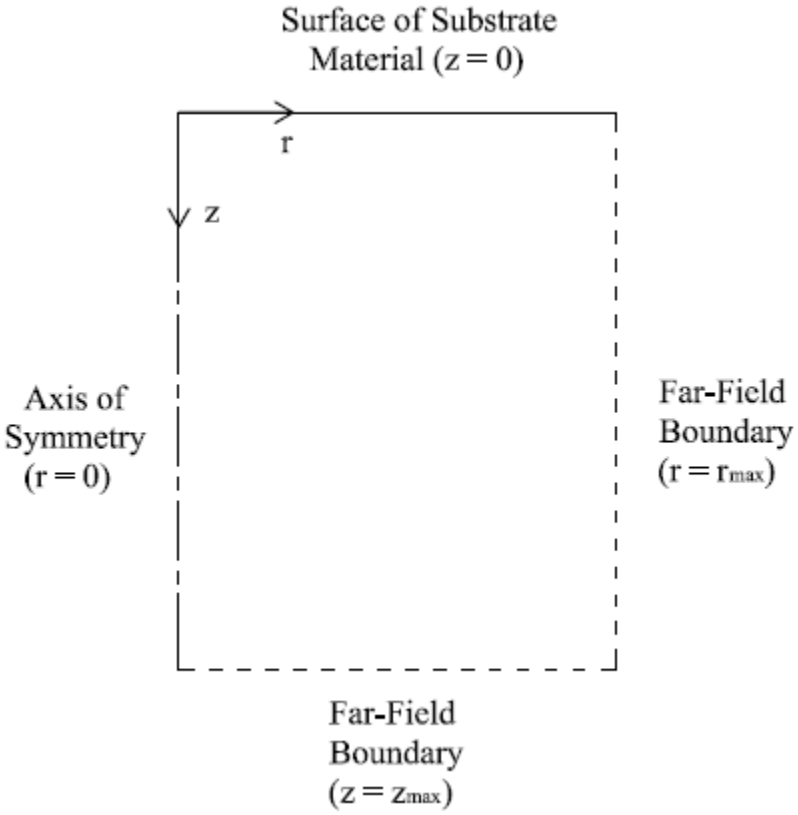

Figure 3.2 - Solution domain for an axisymmetric laser heating of a substrate material.

$$\rho_s Cp_s \frac{\partial T_s}{\partial t} = k_s \left[\frac{1}{r} \frac{\partial}{\partial r} \left(r \frac{\partial T_s}{\partial r} \right) + \frac{\partial^2 T_s}{\partial z^2} \right] + S \qquad (3.1)$$

where T_s is the temperature in the solid phase and the time dependent laser source term S is:

$$S = I_o(t) \delta (1 - r_f) e^{(-\delta z)} e^{-(r/a)^2}$$

However, peak power intensity at the workpiece surface can be formulated to resemble the actual laser pulse. In this case, the following equation is adopted for peak power intensity.

$$I_o = \left[cp_1 (t/cp_5) + cp_2 (t/cp_5)^2 + cp_3 (t/cp_5)^3 \right] \exp\left(cp_4 (t/cp_5) \right)$$

Initial Condition:

Initially material is considered at uniform ambient temperature, which is 300 K.

$$T_s(z, r, t) = 300\ K \quad at\ t = 0$$

Boundary Conditions:

At a depth of infinity, temperature is assumed to be reduced to initial temperature (300K).

$$T_s(z, r_{\max}, t) = 300\ K$$

$$T_s(z_{\max}, r, t) = 300\ K$$

At symmetry axis, temperature is assumed to be maximum due to axis-symmetry heating situation.

$$\left.\frac{\partial T_s}{\partial r}\right|_{\substack{z=z \\ r=0 \\ t=t}} = 0$$

At the surface, convective boundary is assumed with $h \cong 10^2\ \ W/\left(m^2 K\right)$ and T_o is the temperature at infinity, which is 300 K.

$$-k_s \left.\frac{\partial T_s}{\partial z}\right|_{\substack{z=0 \\ r=r \\ t=t}} = h\left(T_{surface} - T_o\right)$$

Here, I_o, δ, r_f and a are the laser power intensity, reciprocal of the absorption depth, reflectance and the Gaussian parameter, respectively. cp_1, cp_2, cp_3, cp_4 and cp_5 are curve fit constants. The numerical values of the different parameters are:

$I_o = 10^{13}\left(Wm^{-2}\right)$

$\delta = 6.17\times10^{6}\left(m^{-1}\right)$

$r_f = 0.5$

$a = \frac{2r_o}{3}(m)$

$r_o = 1.25\times10^{-5}(m)$

$cp_1 = 0.0105771617002674$

$cp_2 = 0.0118181307770856$

$cp_3 = 750.004377930276$

$cp_4 = 10.1106779350279$

$cp_5 = 2.71e\text{-}008$

In the time step in which the temperature, in some cells, reach or exceed the melting point we have to start calculating the phase change boundaries as well as the quality in the mushy zone. In the cells where the quality, x_m reaches or exceeds 1 an unsteady heat conduction equation is also to be solved for the concerned cells. The quality equation is derived by means of the energy method. Consider a differential element in a substrate material, which is subjected to a melting process and let x_m be the mass fraction of the liquid present in the element, then the energy content (ΔU) of the differential element with volume $(\Delta \forall)$ at the melting temperature T_m can be written as:

$$\Delta U = \rho_m \Delta \forall \left[x_m \left(L_m + Cp_m \left(T_m - T_{ref} \right) \right) + Cp_s \left(1 - x_m\right)\left(T_m - T_{ref} \right) \right]$$

where

$$x_m = \frac{m_m}{m_m + m_s}$$

Here, T_{ref} , x_m, m_m and m_s are the reference temperature for enthalpy, quality of liquid, mass of liquid and mass of solid in the element, respectively. After assuming that specific heat of melt is the same as solid at the melting temperature $\left(Cp_s = Cp_m \text{ at } T = T_m\right)$, the above equation reduces to:

$$\Delta U = \rho_m \Delta \cancel{V} \left[x_m L_m + Cp_m \left(T_m - T_{ref} \right) \right]$$

For a unit volume, it reduces to:

$$\frac{\Delta U}{\Delta \cancel{V}} = \Delta u = \rho_m \left[x_m L_m + Cp_m \left(T_m - T_{ref} \right) \right]$$

Differentiation with time yields:

$$\frac{\partial u}{\partial t} = \rho_m L_m \frac{\partial x_m}{\partial t} \qquad (3.2)$$

since $Cp_m\left(T_m - T_{ref}\right) =$ const.

It is important to note that in conduction equation (3.1) $\rho_s Cp_s T_s$ is also the enthalpy per unit volume i.e.

$$\rho_s Cp_s \frac{\partial T}{\partial t} = \frac{\partial u}{\partial t}$$

Substituting eq. (3.2) into (3.1) gives the energy equation for the differential element subjected to the phase change process (melting):

$$\rho_m L_m \frac{\partial x_m}{\partial t} = k_m \left[\frac{1}{r} \frac{\partial}{\partial r} \left(r \frac{\partial T}{\partial r} \right) + \frac{\partial^2 T}{\partial z^2} \right] + S \qquad (3.3)$$

Equation (3.3) is applicable for the differential elements (cells defined by nodes in the substrate material) when temperature becomes melting temperature of the substrate material $T = T_m$ and $0 \le x_m \le 1$, i.e., a mushy zone. Consequently, here temperature of the cells with $0 \le x_m \le 1$ is set to melting temperature $(T = T_m)$. When the value x_m exceeds 1, $(x_m > 1)$ and equation (3.3) is not applicable for the differential element under consideration. In this case, equation (3.1) is used to determine the temperature rise in the liquid heating with the liquid thermal properties employed, i.e., the liquid heating initiates and continues till the temperature reaches the evaporation temperature. It is important to note that inside the mushy zone terms like $\frac{\partial T}{\partial r}$ and $\frac{\partial T}{\partial z}$ are zero, because temperature is

constant, but equation (3.3) is valid at mushy zone/solid and mushy zone/liquid interfaces where these terms are not generally zero.

Let us now discuss the time step in which the temperature in some cells reach or exceed the boiling point. In this case again a mushy zone arises whose constituent cells are part vapour and part liquid. Eq. (3.3) is valid in this second mushy zone when the appropriate thermophysical properties are used in it. The appropriate equation is:

$$\rho_b L_b \frac{\partial x_b}{\partial t} = k_b \left[\frac{1}{r} \frac{\partial}{\partial r} \left(r \frac{\partial T}{\partial r} \right) + \frac{\partial^2 T}{\partial z^2} \right] + S \qquad (3.4)$$

Equation (3.4) is applicable for the range $T = T_b$ and $0 \le x_b \le 1$ in the mushy zone (partially liquid and partially vapour). Consequently, temperature of the cells with $0 \le x_b \le 1$ is set to boiling temperature $(T = T_b)$. It should be noted that x_m is replaced with x_b, which represents the fraction of vapour phase in the differential element.

3.1.2 Stage 2: Melting has started but not evaporation; liquid and solid phases exist; one mushy zone exists

In the second stage three distinct regions exist; solid, solid-liquid mushy zone and liquid. Three different differential equations are to be solved, one in each phase. In the solid and the liquid phases the unsteady heat conduction with heat generation is to be solved, each equation incorporating the appropriate thermophysical properties. In the solid-liquid

mushy zone eq. (3.3) is to be solved. It is to be noted that these regions are not fixed in space but move with time. So that in each time step, before solving eq. (3.3) and eq. (3.5), the boundaries of these regions have to be calculated according to the following criterion.

$T_s \geq T_m \quad \rightarrow \quad$ *Solid-liquid mushy zone*

$x_m \geq 1 \quad \rightarrow \quad$ *Liquid region*

In addition, it should be mentioned that within this stage 2 there would be a time duration in which only the solid and solid-liquid mushy zone will exist. The relevant equations along with the boundary conditions are listed below:

Solid Phase:

Since the length and time scales are larger than the interatomic spacing, therefore the heat diffusion equation is used:

$$\rho_s Cp_s \frac{\partial T_s}{\partial t} = k_s \left[\frac{1}{r} \frac{\partial}{\partial r} \left(r \frac{\partial T_s}{\partial r} \right) + \frac{\partial^2 T_s}{\partial z^2} \right] + S \qquad (3.1)$$

Boundary Conditions:

At a depth of infinity, temperature is assumed to be reduced to initial temperature (300K).

$$T_s(z, r_{\max}, t) = 300\ K$$

$$T_s(z_{\max}, r, t) = 300\ K$$

At symmetry axis, temperature is assumed to be maximum due to axi-symmetric heating situation.

$$\left.\frac{\partial T_s}{\partial r}\right|_{\substack{z=z \\ r=0 \\ t=t}} = 0$$

At the surface, convective boundary is assumed with $h \cong 10^2\ \ W/(m^2 K)$ and T_o is the temperature at infinity, which is 300 K.

$$-k_s \left.\frac{\partial T_s}{\partial z}\right|_{\substack{z=0 \\ r=r \\ t=t}} = h(T_{surface} - T_o)$$

At the solid and solid-liquid mushy zone boundary, the temperature is understood to be the melting temperature.

$$T_s(z, r, t) = T_m \text{ at solid and solid} - \text{liquid mushy zone interface}$$

Solid-Liquid Mushy Zone:

In the solid-liquid mushy zone the quality (x_m) is calculated by means of the following equation.

$$\rho_m L_m \frac{\partial x_m}{\partial t} = k_m \left[\frac{1}{r} \frac{\partial}{\partial r} \left(r \frac{\partial T}{\partial r} \right) + \frac{\partial^2 T}{\partial z^2} \right] + S \qquad (3.3)$$

Initial Condition:

Initially the substrate material is all solid, therefore the quality x_m at every node is 0.

$$x_m(z, r, t) = 0 \quad at\ t = t_m$$

where t_m is the time at which melting starts in the solid substrate.

Boundary Conditions:

At symmetry axis, the quality x_m is assumed to be maximum due to axi-symmetric heating situation.

$$\left. \frac{\partial x_m}{\partial r} \right|_{\substack{z=z \\ r=0 \\ t=t}} = 0$$

At the surface the gradient in the z-direction is assumed to be zero.

$$\left.\frac{\partial x_m}{\partial z}\right|_{\substack{z=0 \\ r=r \\ t=t}} = 0$$

At the solid and solid-liquid mushy zone boundary, the quality is 0.

$$x_m(z,r,t) = 0 \; at \; solid \; and \; solid-liquid \; mushy \; zone \; interface$$

At the liquid and solid-liquid mushy zone boundary, the quality is 1.

$$x_m(z,r,t) = 1 \; at \; liquid \; and \; solid-liquid \; mushy \; zone \; interface$$

Liquid Phase:

Since the length and time scales are larger than the interatomic spacing, therefore the heat diffusion equation is used:

$$\rho_l Cp_l \frac{\partial T_l}{\partial t} = k_l \left[\frac{1}{r} \frac{\partial}{\partial r} \left(r \frac{\partial T_l}{\partial r} \right) + \frac{\partial^2 T_l}{\partial z^2} \right] + S \qquad (3.5)$$

where T_l is the temperature in the liquid phase.

Initial Condition:

Initially the liquid phase is at a uniform temperature, which is the melting temperature $T_m = 1811\,K$.

$$T_l(z,r,t) = T_m \quad at\ t = t_{sl}$$

where t_{sl} is the time at which the solid-liquid mushy zone starts converting into the liquid phase.

Boundary Conditions:

At symmetry axis, the temperature T_l is assumed to be maximum due to axi-symmetric heating situation.

$$\left.\frac{\partial T_l}{\partial r}\right|_{\substack{z=z \\ r=0 \\ t=t}} = 0$$

At the surface, convective boundary is assumed with $h \cong 10^2\ \ W/(m^2 K)$ and T_o is the temperature at infinity, which is 300 K.

$$-k_l \left.\frac{\partial T_l}{\partial z}\right|_{\substack{z=0 \\ r=r \\ t=t}} = h(T_{surface} - T_o)$$

At the liquid and solid-liquid mushy zone boundary the temperature is taken to be the melting temperature.

$T_l(z,r,t) = T_m$ *at liquid and solid – liquid mushy zone interface*

3.1.3 Stage 3: Initiation of evaporation; vapour, liquid and solid phases exist; two mushy zones exist

In the third stage all three phases exist as well as two mushy zones. Five differential equations are to be solved, one in each region along with the appropriate initial and boundary conditions. Again it should be stated that liquid-vapour mushy zone and the vapour region move with time so that before calculating the quality and temperature in these regions respectively, their boundaries should be calculated according to the following criterion.

$T_l \geq T_b$ $\rightarrow$ *Liquid-vapour mushy zone*

$x_b \geq 1$ $\rightarrow$ *Vapour region*

As in the second stage, the third stage also consists of a time duration in which only the solid, solid-liquid mushy zone, liquid and liquid-vapour mushy zone regions exist and there is no vapour region. The relevant equations along with the boundary conditions are listed below.

Solid Phase:

Since the length and time scales are larger than the interatomic spacing, therefore the heat diffusion equation is used:

$$\rho_s Cp_s \frac{\partial T_s}{\partial t} = k_s \left[\frac{1}{r} \frac{\partial}{\partial r} \left(r \frac{\partial T_s}{\partial r} \right) + \frac{\partial^2 T_s}{\partial z^2} \right] + S \qquad (3.1)$$

Boundary Conditions:

At a depth of infinity, temperature is assumed to be reduced to initial temperature (300K).

$$T_s(z, r_{\max}, t) = 300\ K$$

$$T_s(z_{\max}, r, t) = 300\ K$$

At symmetry axis, temperature is assumed to be maximum due to axi-symmetric heating situation.

$$\left. \frac{\partial T_s}{\partial r} \right|_{\substack{z=z \\ r=0 \\ t=t}} = 0$$

At the surface, convective boundary is assumed with $h \cong 10^2\ \ W/(m^2 K)$ and T_o is the temperature at infinity, which is 300 K.

$$-k_s \left.\frac{\partial T_s}{\partial z}\right|_{\substack{z=0 \\ r=r \\ t=t}} = h\left(T_{surface} - T_o\right)$$

At the solid and solid-liquid mushy zone boundary the temperature is taken to be the melting temperature.

$$T_s(z,r,t) = T_m \text{ at solid and solid} - \text{liquid mushy zone interface}$$

Solid-Liquid Mushy Zone:

In the solid-liquid mushy zone the quality (x_m) is calculated by means of the following equation.

$$\rho_m L_m \frac{\partial x_m}{\partial t} = k_m \left[\frac{1}{r}\frac{\partial}{\partial r}\left(r\frac{\partial T}{\partial r}\right) + \frac{\partial^2 T}{\partial z^2}\right] + S \qquad (3.3)$$

Boundary Conditions:

At symmetry axis, the quality x_m is assumed to be maximum due to axi-symmetric heating situation.

$$\left.\frac{\partial x_m}{\partial r}\right|_{\substack{z=z \\ r=0 \\ t=t}} = 0$$

At the surface the gradient in the z-direction is assumed to be zero.

$$\left.\frac{\partial x_m}{\partial z}\right|_{\substack{z=0 \\ r=r \\ t=t}} = 0$$

At the solid and solid-liquid mushy zone boundary, the quality is 0.

$$x_m(z,r,t) = 0 \; at \; solid \; and \; solid-liquid \; mushy \; zone \; interface$$

At the liquid and solid-liquid mushy zone boundary, the quality is 1.

$$x_m(z,r,t) = 1 \; at \; liquid \; and \; solid-liquid \; mushy \; zone \; interface$$

Liquid Phase:

Since the length and time scales are larger than the interatomic spacing, therefore the heat diffusion equation is used:

$$\rho_l Cp_l \frac{\partial T_l}{\partial t} = k_l \left[\frac{1}{r} \frac{\partial}{\partial r} \left(r \frac{\partial T_l}{\partial r} \right) + \frac{\partial^2 T_l}{\partial z^2} \right] + S \qquad (3.5)$$

Boundary Conditions:

At symmetry axis, the temperature T_l is assumed to be maximum due to axi-symmetric heating situation.

$$\left.\frac{\partial T_l}{\partial r}\right|_{\substack{z=z \\ r=0 \\ t=t}} = 0$$

At the surface, convective boundary is assumed with $h \cong 10^2 \ \ W/\left(m^2 K\right)$ and T_o is the temperature at infinity, which is 300 K.

$$-k_l \left.\frac{\partial T_l}{\partial z}\right|_{\substack{z=0 \\ r=r \\ t=t}} = h\left(T_{surface} - T_o\right)$$

At the liquid and solid-liquid mushy zone boundary the temperature is taken to be the melting temperature.

$$T_l(z,r,t) = T_m \ \textit{at liquid and solid} - \textit{liquid mushy zone interface}$$

At the liquid and liquid-vapour mushy zone boundary the temperature is taken to be the evaporation temperature.

$$T_l(z,r,t) = T_b \ \textit{at liquid and liquid} - \textit{vapour mushy zone interface}$$

Liquid-Vapour Mushy Zone:

In the liquid-vapour mushy zone the quality (x_b) is calculated by means of the following equation.

$$\rho_b L_b \frac{\partial x_b}{\partial t} = k_b \left[\frac{1}{r} \frac{\partial}{\partial r} \left(r \frac{\partial T}{\partial r} \right) + \frac{\partial^2 T}{\partial z^2} \right] + S \qquad (3.4)$$

Initial Condition:

Initially the cells in the vapour-liquid mushy zone are all liquid, therefore the quality x_b at those nodes is 0.

$$x_b = 0 \quad at\ t = t_b$$

where t_b is the time at which evaporation starts in the liquid region.

Boundary Conditions:

At symmetry axis, the quality x_m is assumed to be maximum due to axi-symmetric heating situation.

$$\left. \frac{\partial x_b}{\partial r} \right|_{\substack{z=z \\ r=0 \\ t=t}} = 0$$

At the surface the gradient in the z-direction is assumed to be zero.

$$\left.\frac{\partial x_b}{\partial z}\right|_{\substack{z=0 \\ r=r \\ t=t}} = 0$$

At the liquid and liquid-vapour mushy zone boundary, the quality is 0.

$$x_b(z,r,t) = 0 \; at\ liquid\ and\ liquid-vapour\ mushy\ zone\ interface$$

At the vapour and liquid-vapour mushy zone boundary, the quality is 1.

$$x_b(z,r,t) = 1 \; at\ vapour\ and\ liquid-vapour\ mushy\ zone\ interface$$

The thermo-physical properties used during the simulations are given in Tables 3.1 & 3.2.

Solid Phase	Liquid Phase	Vapour Phase
$k_s = 63\left(Wm^{-1}K^{-1}\right)$	$k_l = 37\left(Wm^{-1}K^{-1}\right)$	$k_v = 0.9k_l\left(Wm^{-1}K^{-1}\right)$
$\rho_s = 7860\left(kgm^{-3}\right)$	$\rho_l = 6891\left(kgm^{-3}\right)$	$\rho_v = \rho_l/15\left(kgm^{-3}\right)$
$Cp_s = 420\left(Jkg^{-1}K^{-1}\right)$	$Cp_l = 824\left(Jkg^{-1}K^{-1}\right)$	$Cp_v = 1.1Cp_l\left(Jkg^{-1}K^{-1}\right)$

Table 3.1 - Thermo-physical properties in the solid and liquid regions of the substrate material.

Solid-Liquid Mushy Zone	Liquid-Vapour Mushy Zone
$L_m = 247112\left(Jkg^{-1}\right)$	$L_b = 6213627\left(Jkg^{-1}\right)$
$T_m = 1811\left(K\right)$	$T_b = 3134\left(K\right)$
$k_m = k_l x_m + k_s\left(1 - x_m\right)$	$k_b = k_v x_b + k_l\left(1 - x_b\right)$
$\rho_m = \rho_l x_m + \rho_s\left(1 - x_m\right)$	$\rho_b = \rho_v x_b + \rho_l\left(1 - x_b\right)$
$Cp_m = Cp_l x_m + Cp_s\left(1 - x_m\right)$	$Cp_b = Cp_v x_b + Cp_l\left(1 - x_b\right)$

Table 3.2 - Thermo-physical properties in the solid-liquid and liquid-vapour regions of the substrate material.

3.2 Transiently Developing Jet In Relation To Laser Heating

In the second part of the problem, the vapour jet coming out of the cavity is modelled using FLUENT 6.2. The output of the previous simulations i.e., the time-varying cavity shape, mass flux/velocity of the vapour and the temperature distribution at the substrate surface are now inputs to the FLUENT simulations. Three, main, fluid dynamic/mass transfer models are used which are:

1. The Reynolds Averaged Navier-Stokes equations comprising of the continuity equation, the radial and axial momentum conservation equations and the energy conservation equation for an unsteady, incompressible, axisymmetric, turbulent flow.
2. The Standard k-ε turbulence model to calculate the turbulent viscosity.
3. The Species transport model to account for the mass transfer of the vapour jet from the cavity into the ambient water.

The relevant governing equations and associated boundary conditions are presented in the next section. It should be noted that all the unknown quantities are time-averaged since the RANS equations are being used.

3.2.1 Continuity Equation

$$\frac{1}{r}\frac{\partial(rV_r)}{\partial r}+\frac{\partial V_z}{\partial r}=0 \qquad (3.6)$$

3.2.2 r-momentum Equation

$$\frac{\partial(\rho V_r)}{\partial t}+\frac{1}{r}\frac{\partial(\rho r V_r^2)}{\partial r}+\frac{\partial(\rho V_r V_z)}{\partial z}=-\frac{\partial p}{\partial r}+\frac{2}{r}\frac{\partial}{\partial r}\left(\mu_{eff} r\frac{\partial V_r}{\partial r}\right)+\frac{\partial}{\partial z}\left(\mu_{eff}\frac{\partial V_r}{\partial z}\right)+\frac{\partial}{\partial z}\left(\mu_{eff}\frac{\partial V_z}{\partial z}\right)-2\mu_{eff}\frac{V_r}{r^2} \quad (3.7)$$

3.2.3 z-momentum Equation

$$\frac{\partial(\rho V_z)}{\partial t}+\frac{1}{r}\frac{\partial(\rho r V_r V_z)}{\partial r}+\frac{\partial(\rho V_z^2)}{\partial z}=-\frac{\partial p}{\partial z}+\frac{1}{r}\frac{\partial}{\partial r}\left(\mu_{eff} r\frac{\partial V_z}{\partial r}\right)+2\frac{\partial}{\partial z}\left(\mu_{eff}\frac{\partial V_z}{\partial z}\right)+\frac{1}{r}\frac{\partial}{\partial r}\left(\mu_{eff} r\frac{\partial V_r}{\partial z}\right) \quad (3.8)$$

where, effective viscosity $\left(\mu_{eff}\right)$ is :

$$\mu_{eff} = \mu + \mu_t$$

and

$$\mu_t = \frac{\rho C_\mu K^2}{\varepsilon}$$

and

$$C_\mu = 0.09$$

3.2.4 Energy Equation

$$\frac{\partial(\rho E)}{\partial t}+\frac{1}{r}\frac{\partial(rV_r\rho E)}{\partial r}+\frac{\partial(V_z\rho E)}{\partial z}=\frac{1}{r}\frac{\partial}{\partial r}\left(rk_{eff}\frac{\partial T}{\partial r}\right)+\frac{\partial}{\partial z}\left(k_{eff}\frac{\partial T}{\partial z}\right)$$
$$+\left[\frac{1}{r}\frac{\partial}{\partial r}\left(rh_{vapour}\left(\rho D+\frac{\mu_t}{Sc_t}\right)\frac{\partial Y_{vapour}}{\partial r}\right)+\frac{\partial}{\partial z}\left(h_{vapour}\left(\rho D+\frac{\mu_t}{Sc_t}\right)\frac{\partial Y_{vapour}}{\partial z}\right)\right]$$
$$+\left[\frac{1}{r}\frac{\partial}{\partial r}\left(rh_{air}\left(\rho D+\frac{\mu_t}{Sc_t}\right)\frac{\partial Y_{air}}{\partial r}\right)+\frac{\partial}{\partial z}\left(h_{air}\left(\rho D+\frac{\mu_t}{Sc_t}\right)\frac{\partial Y_{air}}{\partial z}\right)\right] \quad (3.9)$$

where,

$E=Y_{air}h_{air}+Y_{vapour}h_{vapour}$, after neglecting the contribution of kinetic energy.

$$h_{vapour}=\int_{T_{ref}}^{T}Cp_{vapour}\,dT=Cp_{vapour}\left(T-T_{ref}\right)$$

$$h_{air}=\int_{T_{ref}}^{T}Cp_{air}\,dT=Cp_{air}\left(T-T_{ref}\right)$$

where effective conductivity $\left(k_{eff}\right)$ is:

$$k_{eff}=k+k_t$$

and

$$k_t = Cp\frac{\mu_t}{\mathrm{Pr}_t}$$

and,

$$D = 2.88\times10^{-5}\left(m^2/s\right)$$

and

$$Sc_t = 0.7$$

and

$$\mathrm{Pr}_t = 0.85$$

and

$$T_{ref} = 298.15\,K$$

3.2.5 Turbulence Kinetic Energy Equation, K

$$\frac{\partial(\rho K)}{\partial t}+\frac{1}{r}\frac{\partial(\rho r V_r K)}{\partial r}+\frac{\partial(\rho V_z K)}{\partial z}= \frac{1}{r}\frac{\partial}{\partial r}\left(\frac{\mu_{eff}}{\sigma_K} r\frac{\partial K}{\partial r}\right)+\frac{\partial}{\partial z}\left(\frac{\mu_{eff}}{\sigma_K}\frac{\partial K}{\partial z}\right)-\rho\varepsilon+P_K \tag{3.10}$$

where,

$$P_K=\mu_{eff}\left[2\left\{\left(\frac{\partial V_z}{\partial r}\right)^2+\left(\frac{\partial V_r}{\partial r}\right)^2+\left(\frac{V_r}{r}\right)^2\right\}+\left(\frac{\partial V_z}{\partial r}+\frac{\partial V_r}{\partial z}\right)^2\right]$$

3.2.6 Rate of Dissipation Equation, ε

$$\frac{\partial(\rho\varepsilon)}{\partial t}+\frac{1}{r}\frac{\partial(\rho r V_r\varepsilon)}{\partial r}+\frac{\partial(\rho V_z\varepsilon)}{\partial z}=\frac{1}{r}\frac{\partial}{\partial r}\left(\frac{\mu_{eff}}{\sigma_\varepsilon} r\frac{\partial\varepsilon}{\partial r}\right) +\frac{\partial}{\partial z}\left(\frac{\mu_{eff}}{\sigma_\varepsilon}\frac{\partial\varepsilon}{\partial z}\right)-C_1\frac{\varepsilon}{K}P_K-C_2\rho\frac{\varepsilon^2}{K} \tag{3.11}$$

where,

$$P_K=\mu_{eff}\left[2\left\{\left(\frac{\partial V_z}{\partial r}\right)^2+\left(\frac{\partial V_r}{\partial r}\right)^2+\left(\frac{V_r}{r}\right)^2\right\}+\left(\frac{\partial V_z}{\partial r}+\frac{\partial V_r}{\partial z}\right)^2\right]$$

and

$$\sigma_K = 1, \qquad \sigma_\varepsilon = 1.3, \qquad C_1 = 1.44, \qquad C_2 = 1.92$$

3.2.7 Species Transport Equation

The species mass fraction (Y) can be determined from the transport equation, i.e.:

$$\frac{\partial(\rho Y_{vapour})}{\partial t} + \frac{1}{r}\frac{\partial(rV_r \rho Y_{vapour})}{\partial r} + \frac{\partial(V_z \rho Y_{vapour})}{\partial z} = \left[\frac{1}{r}\frac{\partial}{\partial r}\left(r\left(\rho D + \frac{\mu_t}{Sc_t}\right)\frac{\partial Y_{vapour}}{\partial r}\right) + \frac{\partial}{\partial z}\left(\left(\rho D + \frac{\mu_t}{Sc_t}\right)\frac{\partial Y_{vapour}}{\partial z}\right)\right] \tag{3.12}$$

For water,

$$Y_{water} = 1 - Y_{vapour} \tag{3.13}$$

3.2.8 Initial and Boundary Conditions:

The solution domain and boundary conditions are shown in figure (3.3).

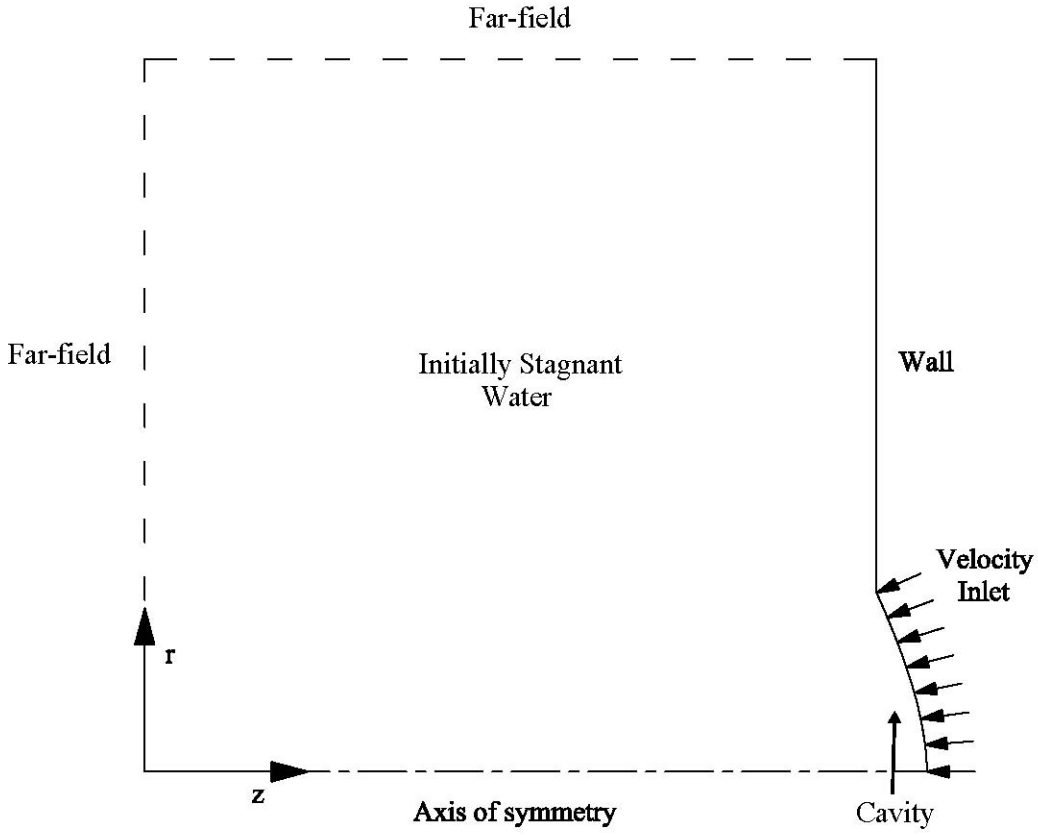

Figure 3.3 - Solution domain for an axisymmetric transient turbulent vapour jet emanating from the cavity and emerging into initially stagnant water.

Initial Conditions

Initially the ambient water is stagnant, therefore the z- and r-direction velocity components are zero.

$$V_z(z,r,0)=0$$

$$V_r(z,r,0)=0$$

The temperature is considered to be uniform and equal to 300K.

$$T(z,r,0)=300\ K$$

The turbulent kinetic energy and its rate of dissipation are understood to be unity throughout the domain.

$$K(z,r,0)=1$$

$$\varepsilon(z,r,0)=1$$

The vapour mass fraction is zero whereas the water mass fraction is unity throughout the domain.

$$Y_{vapour}(z,r,0)=0$$

Symmetry Axis: $(\mathbf{r = 0})$

At the symmetry axis all the unknown quantities are considered to be maximum accept the r-direction velocity, which is zero.

Axial velocity component is symmetric about $r = 0$, $\left.\frac{\partial V_z}{\partial r}\right|_{\substack{z=z \\ r=0 \\ t=t}} = 0$

Radial velocity component is zero at $r = 0$, $V_r(z, 0, t) = 0$

Temperature is symmetric about $r = 0$, $\left.\frac{\partial T}{\partial r}\right|_{\substack{z=z \\ r=0 \\ t=t}} = 0$

Turbulent Kinetic Energy has symmetric distribution about $r = 0$, $\left.\frac{\partial K}{\partial r}\right|_{\substack{z=z \\ r=0 \\ t=t}} = 0$

Rate of dissipation of TKE has symmetric distribution about $r = 0$, $\left.\frac{\partial \varepsilon}{\partial r}\right|_{\substack{z=z \\ r=0 \\ t=t}} = 0$

Vapour mass fraction has symmetric distribution about $r = 0$, $\left.\frac{\partial Y_{vapour}}{\partial r}\right|_{\substack{z=z \\ r=0 \\ t=t}} = 0$

Outflow: $(\mathbf{z = 0})$

At the outflow boundary perpendicular to the z-axis the normal derivatives of all the unknown quantities are considered to be zero accept the r-direction velocity, whose value is zero as required from the continuity equation.

Normal derivative of the axial velocity component is zero, $\left.\frac{\partial V_z}{\partial z}\right|_{\substack{z=0 \\ r=r \\ t=t}} = 0$

Radial velocity component is zero, $V_r(0, r, t) = 0$

Normal derivative of the temperature is zero, $\left.\frac{\partial T}{\partial z}\right|_{\substack{z=0 \\ r=r \\ t=t}} = 0$

Normal derivative of the turbulent kinetic energy is zero, $\left.\frac{\partial K}{\partial r}\right|_{\substack{z=0 \\ r=r \\ t=t}} = 0$

Normal derivative of the rate of dissipation of TKE is zero, $\left.\frac{\partial \varepsilon}{\partial r}\right|_{\substack{z=0 \\ r=r \\ t=t}} = 0$

Normal derivative of the vapour mass fraction is zero, $\left.\frac{\partial Y_{vapour}}{\partial r}\right|_{\substack{z=0 \\ r=r \\ t=t}} = 0$

Outflow: $(\mathbf{r} = \mathbf{r_{max}})$

At the outflow boundary perpendicular to the r-axis the normal derivatives of all the unknown quantities are considered to be zero accept the z-direction velocity, whose value is zero as required from the continuity equation.

Radial velocity component is zero, $V_z\left(z, r_{\max}, t\right) = 0$

Normal derivative of the axial velocity component is zero, $\left.\frac{\partial V_r}{\partial r}\right|_{\substack{z=z \\ r=r_{\max} \\ t=t}} = 0$

Normal derivative of the temperature is zero, $\left.\frac{\partial T}{\partial r}\right|_{\substack{z=z \\ r=r_{\max} \\ t=t}} = 0$

Normal derivative of the turbulent kinetic energy is zero, $\left.\frac{\partial K}{\partial r}\right|_{\substack{z=z \\ r=r_{\max} \\ t=t}} = 0$

Normal derivative of the rate of dissipation of TKE is zero, $\left.\frac{\partial \varepsilon}{\partial r}\right|_{\substack{z=z \\ r=r_{\max} \\ t=t}} = 0$

Normal derivative of the vapour mass fraction is zero, $\left.\frac{\partial Y_{vapour}}{\partial r}\right|_{\substack{z=0 \\ r=r_{\max} \\ t=t}} = 0$

Wall: $\mathbf{z = f(r,t)}$

The surface of the substrate material including the cavity acts like a wall in the solution process and hence a no-slip and a no temperature jump boundary conditions are considered. At the cavity surface the vapour mass fraction is considered to be one, whereas the water mass fraction is considered to be zero. As evaporation initiates, the cavity formation starts. The cavity not only expands along the axial direction with increasing time but also in the radial direction. The maximum radius at any time, of the cavity is denoted by $r_{\max}$. The depth of the cavity along the radial direction at any time determines it shape, which can be represented as a function of radial coordinate and time. Thus the function $z = f(r,t)$ below gives the depth of the cavity below the substrate surface along the radial direction at any time instant. It is to be noted that this function is only valid for $0 \le r \le r_{\max}$, where $r_{\max}$ itself is a function of time.

$$f(r,t) = \left[c\left((r/\Delta r)^2 - r_{\max}^2 \right) + d\left((r/\Delta r)^3 - r_{\max}^3 \right) \right] (\rho_l / \rho_v) \Delta z$$

$$c = cc_3 + cc_2 (t/\Delta t) + cc_1 (t/\Delta t)^2$$

$$\left.\begin{aligned} cc_1 &= 4.4499 \times 10^{-6} \\ cc_2 &= -0.0026726 \\ cc_3 &= -0.15077 \end{aligned}\right\} \text{Curve-fit constants}$$

$$d = cd_3 + cd_2\left(t/\Delta t\right) + cd_1\left(t/\Delta t\right)^2$$

$$\left.\begin{aligned} cd_1 &= -1.7974\times10^{-7} \\ cd_2 &= 0.00011187 \\ cd_3 &= 0.0062477 \end{aligned}\right\} \text{Curve-fit constants}$$

The maximum radius $r_{\max}$ of the cavity at any time step is given as,

$$r_{\max} = cr_5 + cr_4\left(t/\Delta t\right) + cr_3\left(t/\Delta t\right)^2 + cr_2\left(t/\Delta t\right)^3 + cr_1\left(t/\Delta t\right)^4$$

$$\left.\begin{aligned} cr_1 &= -2.5982\times10^{-9} \\ cr_2 &= 2.0455\times10^{-6} \\ cr_3 &= -0.00059955 \\ cr_4 &= 0.086871 \\ cr_5 &= 7.7763 \end{aligned}\right\} \text{Curve-fit constants}$$

$$\Delta z = 3.2415\times10^{-8}\ m$$

$$\Delta r = 8.3333\times10^{-7}\ m$$

$$\Delta t = 6\times10^{-11}\ s$$

At the cavity surface the axial velocity component is calculated from the function $z = f(r,t)$. Beyond r_{max} the velocity is zero.

$$V_z(z,r,t) = \frac{\rho_l}{\rho_v}\frac{\partial f}{\partial t}\frac{\partial f/\partial r}{\sqrt{1+(\partial f/\partial r)^2}}, \qquad 0 \le r \le r_{max}, z = f(r,t)$$

$$= 0, \qquad r > r_{max}$$

At the cavity surface the radial velocity component is calculated from the function $z = f(r,t)$. Beyond r_{max} the velocity is zero.

$$V_r(z,r,t) = -\frac{\rho_l}{\rho_v}\frac{\partial f}{\partial t}\frac{1}{\sqrt{1+(\partial f/\partial r)^2}}, \qquad 0 \le r \le r_{max}, z = f(r,t)$$

$$= 0, \qquad r > r_{max}$$

The temperature at the cavity surface is the evaporation temperature $T_b = 3134\,K$, for $0 \le r \le r_{max}$. However beyond r_{max} the temperature declines sharply at the wall and is obtained from the MATLAB simulation discussed earlier.

$$T(z,r,t) = 3134, \qquad 0 \le r \le r_{max}, z = f(r,t)$$

$$= 2834\exp\left(\text{-}btemp\left((r/\Delta r) - r_{max}\right)^2\right) + 300, \qquad r > r_{max}$$

$$btemp = ctemp(t/\Delta t)^2 + dtemp(t/\Delta t) + etemp$$

$$\left.\begin{aligned} ctemp &= 1.0370442955011\times10^{-6} \\ dtemp &= -3.39682806506743\times10^{-5} \\ etemp &= 0.0241815719639816 \end{aligned}\right\} \text{Curve-fit constants}$$

The default value for turbulent kinetic energy all along the wall is taken to be unity.

$$K(z,r,t) = 1\ (m/s)^2$$

The default value for the rate of dissipation of TKE all along the wall is taken to be unity.

$$\varepsilon(z,r,t) = 1\ (m/s)^2$$

The vapour mass fraction is unity at the cavity surface and zero beyond $r_{\max}$.

$$\begin{aligned} Y_{vapour}(z,r,t) &= 1, && 0 \le r \le r_{\max}, z = f(r,t) \\ &= 0, && r > r_{\max} \end{aligned}$$

CHAPTER 4

NUMERICAL METHOD AND ALGORITHM

4.1 Introduction

The mathematical analysis described in the previous chapter for the case of laser heating of the substrate material results in partial differential equations that do not yield to an analytical solution due to mathematical difficulties involved. Due to this reason some other method of solution is required. To solve these equations, numerical methods can be employed, which are able to handle problems of high degree of complexity. In this chapter we shall describe the methodology for solution of the differential equations, and the associated algorithms required for its implementation on a computer programming language. For the two different parts of the problem the methodologies adopted are distinct and have to be discussed separately. For the first part a computer program has been developed in MATLAB to solve the governing equations. Outputs from this solution phase consists of the cavity shape at each time step, its recession velocity which can be calculated from the expression for the time-dependent cavity shape and the

temperature distribution at the surface of the substrate material. These outputs become the inputs for the second solution phase, in which the governing equations are solved using the commercial CFD package FLUENT 6.2. Each solution phase is described separately. But before explaining the specific methodologies, the workings of a related numerical solution are discussed below.

A preliminary idea about the workings of a finite difference based numerical method can be obtained by considering a planar, steady state heat flow situation in a metal without heat generation. The continuous temperature field satisfies the Laplace equation and the solution is uniquely determined by specifying the boundary conditions, for e.g., Dirichlet B.C.s. To obtain a numerical solution to this problem two important steps have to be accomplished. The first step is the discretisation of the continuous domain into a fixed number of points. Since there are infinite points in a continuum and a numerical solution procedure can give you the temperature at only a finite number of points, therefore it is necessary to represent your continuous domain by a fixed number of points. Careful selection of points is important to get a meaningful solution. In the second step, the governing partial differential equation has to be discretised. Since our domain is now discrete instead of continuous, therefore we need a difference equation instead of a differential equation. This difference equation is derived from the original differential equation by substituting finite difference approximations of the second-order derivatives in the original differential equation. Applying this difference equation to each point of the discretised domain excluding the points constituting the boundary, one obtains a relation between the temperature at that point and the temperatures at the neighbouring points.

This relation is actually a linear algebraic equation. In this way all the unknown temperatures are related to each other by means of a system of simultaneous, linear algebraic equations. The boundary conditions enter into those algebraic equations, which represent temperatures of points next to the points constituting the boundary of the domain. This system of equations can then be solved numerically to obtain the temperatures. Gauss-Seidel iterative procedure is one popular method.

4.2 Laser Heating of the Substrate Material

4.2.1 Numerical Method

Several techniques of numerical analysis exist. Among them the most famous are finite difference, finite volume, finite element, spectral and pseudo-spectral methods. For the solution of the laser heating problem, finite difference method was used. Before proceeding to the finite difference method, it is appropriate to define basic properties of numerical solutions that determine their level of accuracy. These properties include:

- Convergence
- Consistency
- Stability

Convergence is the property of a numerical method to produce a solution, which approaches the exact solution as the grid spacing; control volume size or element size is reduced to zero.

Consistency is the property of a numerical method to produce systems of algebraic equations, which can be demonstrated to be equivalent to the original governing partial differential equations as the grid spacing tends to zero.

Stability is associated with the growth or damping of errors as the numerical method proceeds and hence it describes whether or not the dependent variable is bounded. For transient analysis, the dependent variable is unstable if the solution oscillates with amplitude that increases with time. If a technique is not stable, even round-off errors in the initial data can cause wild oscillations or divergence.

4.2.2 Finite Difference Method

The particular approach that we have chosen here for the discretisation of the differential equations is the Finite Difference Method. This choice also affects the domain discretisation details. As mentioned in the Sec. 4.1.1, the domain is first discretised into a finite number of representative points. Secondly, the governing differential equations are discretised and converted to equivalent difference equations. After carefully implementing the boundary conditions a system of linear, simultaneous, algebraic equations is obtained. The solution of this system is then attempted by means of the

Gauss-Seidel iterative procedure. Domain discretisation and the discretisation of the governing equations are discussed in the sections below.

4.2.3 Domain Discretisation

Let us first quickly have an overview of the problem. The laser beam is shining on the metal surface at a point. Actually, this point is a spot with a very small diameter. The laser gets absorbed in the metal surface to a certain depth. Due to this action, uneven heating of the substrate material occurs, with high temperatures occurring in the spot vicinity. Mathematically, this phenomenon can be modelled as an axisymmetric heat conduction problem, the lasing action being replaced by a nonuniform volumetric heat generation inside the substrate material. The axis of symmetry passes through the spot centre and is actually the z-axis. The radial r-axis is perpendicular to this z-axis. The spot centre is the origin of the coordinate system. Since the laser spot has radial symmetry, therefore we need only to consider a 2-dimensional problem, i.e., determination of the temperature field on $\theta = 0$ plane. This means that a heat conduction problem is to be solved on a rectangular domain with z- and r- directions as the coordinate axes. The heat source is designed such that it decays exponentially along the z- and r-axes as one moves from the origin. Along the r-axis the profile is actually Gaussian as shown in Figure 4.1.

As mentioned, we are concerned with a rectangular domain. The maximum distance in the radial direction is $r_{\max} = 8.333 \times 10^{-5}\ m$ and the maximum distance in the axial direction is $z_{\max} = 6.483 \times 10^{-6}\ m$. At first, the edges of the domain coinciding with the

coordinate axes are discretised. The number of divisions in the r- and z- directions are $nr = 100$ and, $nz = 200$ respectively. Once this is done the coordinates for other points of the discretised domain can be found by drawing lines parallel to coordinate axes through each node on the r- and z- axes as shown in Figure 4.2. In this way we obtain a mesh representing our continuous domain.

4.2.4 Discretisation of the Governing Equations

The relevant model equations are (3.1), (3.3), (3.4) and (3.5). These equations contain four main variables, T_s, T_l, x_m and x_b. In actual numerical implementation we treat T_s and T_l as the same variable since solid and liquid do not exist simultaneously at a grid point. Where they do, they are described by means of the quality. So we need to discretise only three equations. These equations contain the following generic derivative terms, $\frac{\partial T}{\partial t}$, $\frac{1}{r}\frac{\partial}{\partial r}\left(r\frac{\partial T}{\partial r}\right)$, $\frac{\partial^2 T}{\partial z^2}$ and $\frac{\partial x}{\partial t}$. For a grid point C, E and W are its r-direction neighbours, while N and S are its z-direction neighbours as shown in Figure 4.3. For temporal derivatives first-order backward differences are used whereas for spatial derivatives second-order central differences have been employed. These selections lead to an implicit scheme. If we set *p* as the time index, *i* as the r-coordinate index and j as the z-coordinate index then the discretised form of these terms are,

$$\frac{\partial T}{\partial t} \approx \frac{T_{i,j}^{p} - T_{i,j}^{p-1}}{\Delta t}$$

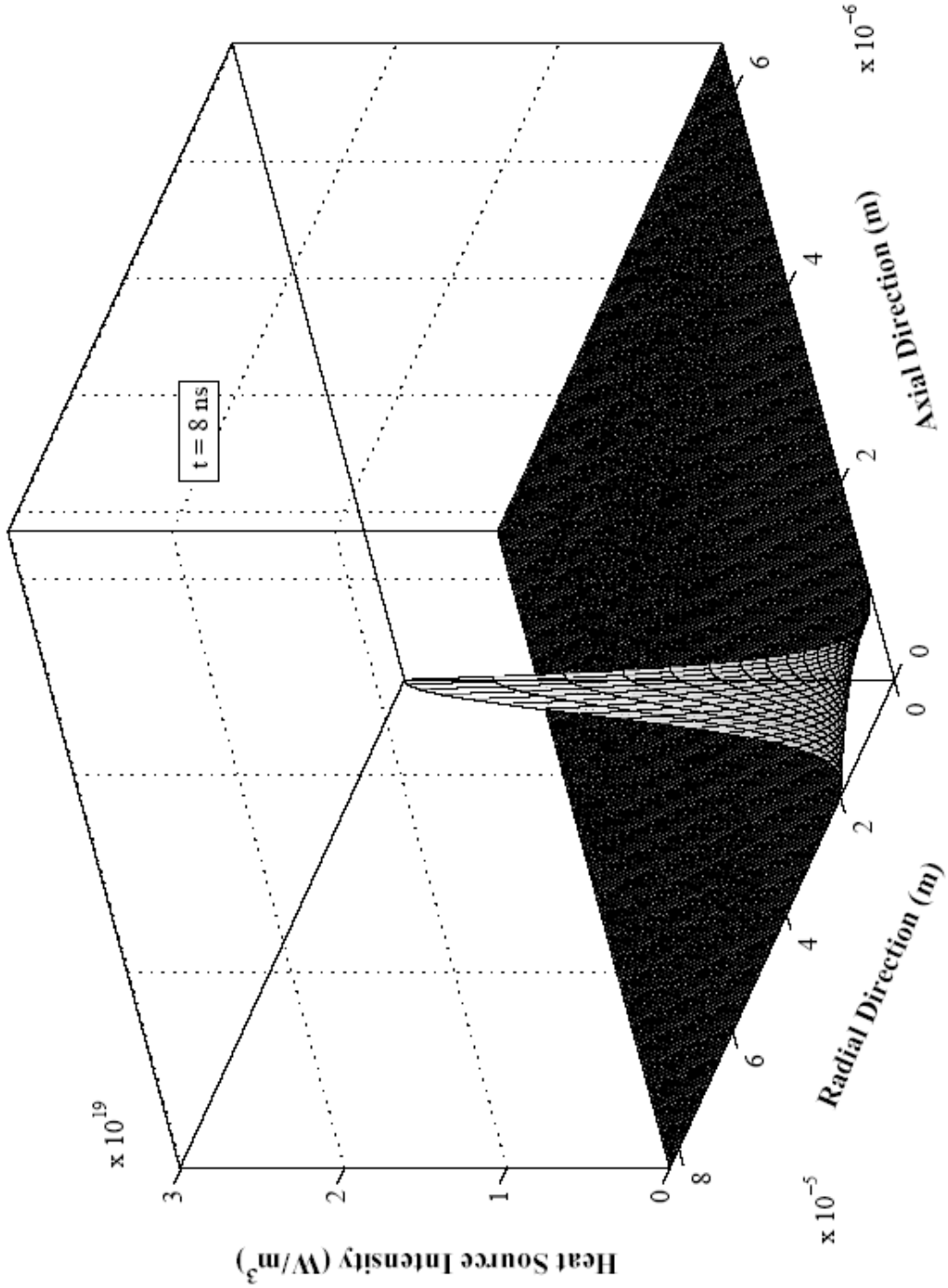

Figure 4.1 - Heat source intensity distribution inside the substrate material at t = 8 ns.

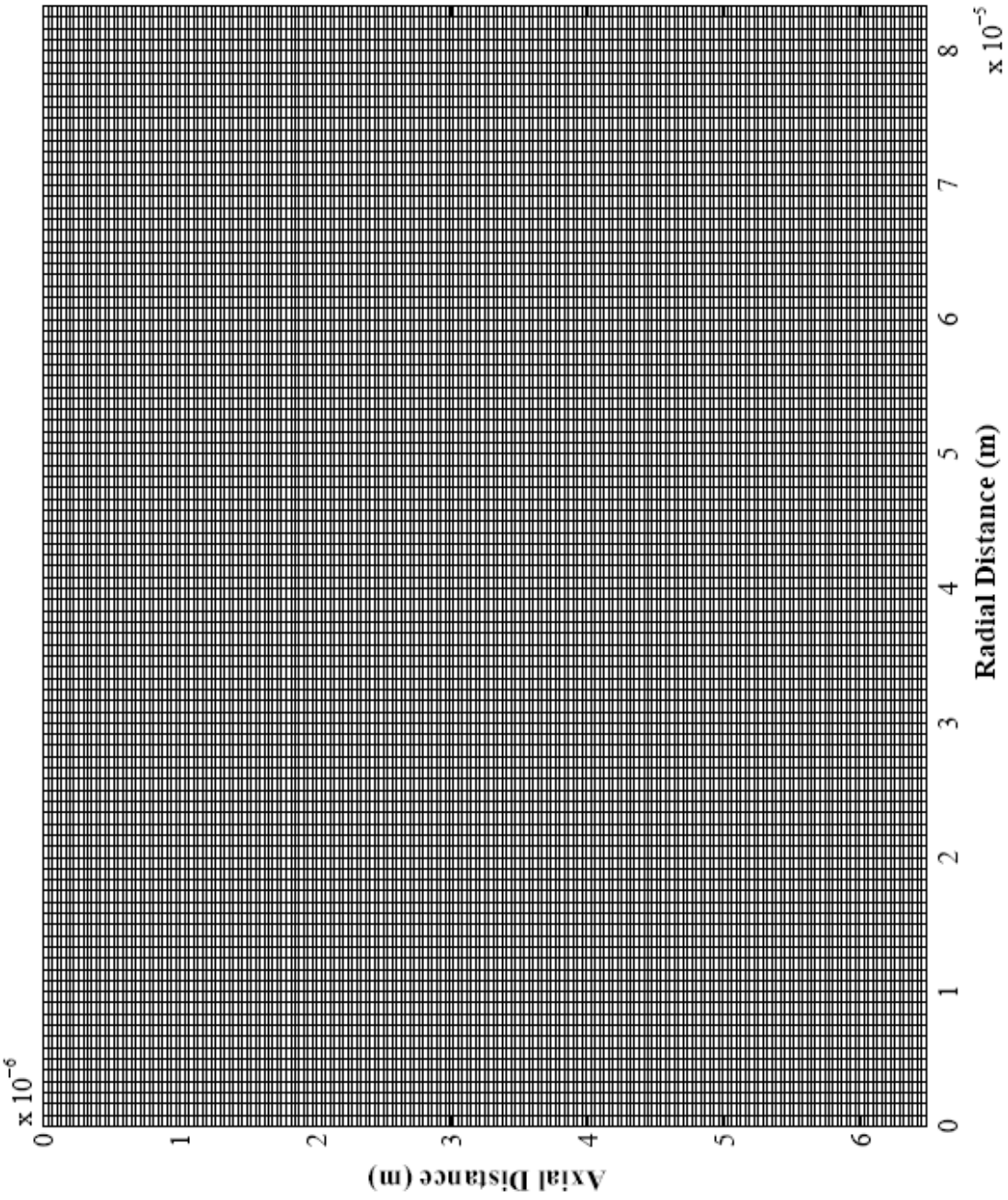

Figure 4.2 - Computational grid for an axisymmetric laser heating of a substrate material.

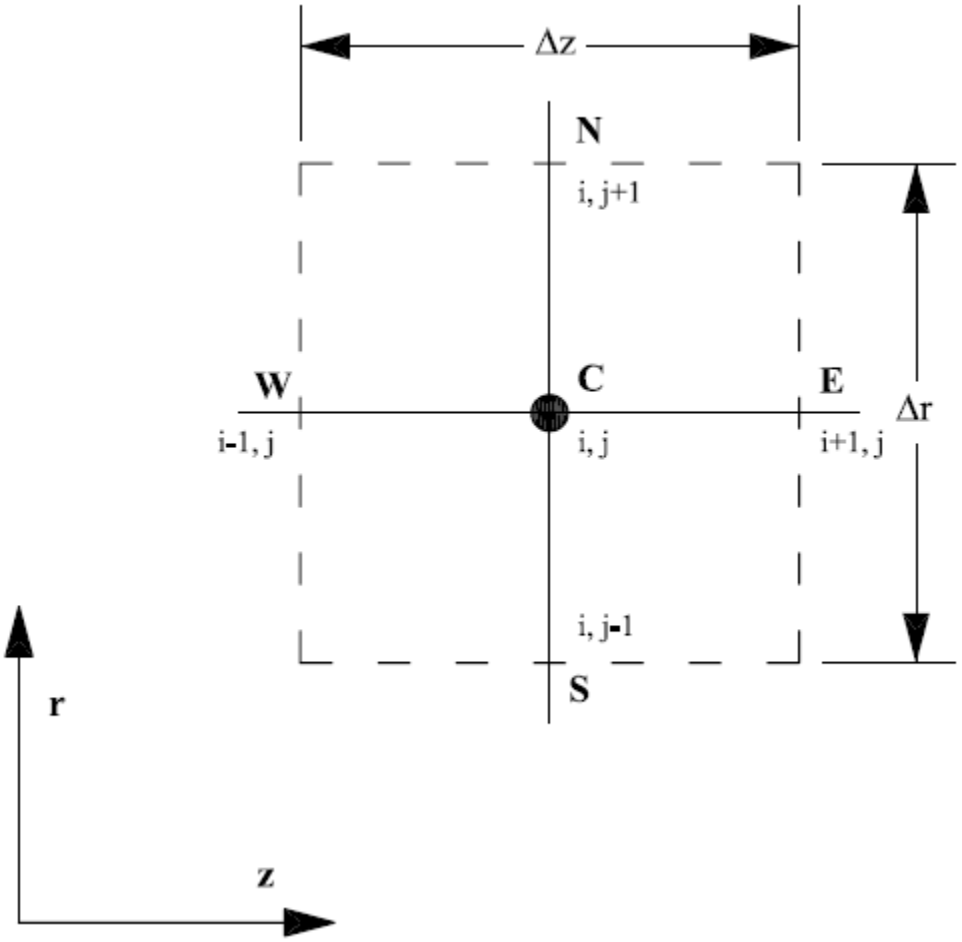

Figure 4.3 - An internal grid point with neighbours for an axisymmetric laser heating of a substrate material.

$$\frac{1}{r}\frac{\partial}{\partial r}\left(r\frac{\partial T}{\partial r}\right) \approx \frac{1}{r_i}\left(\frac{r_{i+\frac{1}{2}}\left(T^p_{i+1,j}-T^p_{i,j}\right)-r_{i-\frac{1}{2}}\left(T^p_{i,j}-T^p_{i-1,j}\right)}{(\Delta r)^2}\right)$$

$$\frac{\partial^2 T}{\partial z^2} \approx \frac{T^p_{i,j+1}-2T^p_{i,j}+T^p_{i,j-1}}{(\Delta z)^2}$$

$$\frac{\partial x}{\partial t} \approx \frac{x^p_{i,j}-x^{p-1}_{i,j}}{\Delta t}$$

Substituting these approximations in the differential equations, we obtain for eqs. (3.1) and (3.5),

$$\rho Cp\left(\frac{T^p_{i,j}-T^{p-1}_{i,j}}{\Delta t}\right)=k\left[\frac{1}{r_i}\left(\frac{r_{i+\frac{1}{2}}\left(T^p_{i+1,j}-T^p_{i,j}\right)-r_{i-\frac{1}{2}}\left(T^p_{i,j}-T^p_{i-1,j}\right)}{(\Delta r)^2}\right)+\left(\frac{T^p_{i,j+1}-2T^p_{i,j}+T^p_{i,j-1}}{(\Delta z)^2}\right)\right]+S^p_{i,j}$$

simplifying we obtain,

$$a_C T^p_{i,j} = a_E T^p_{i+1,j} + a_W T^p_{i-1,j} + a_N T^p_{i,j+1} + a_S T^p_{i,j-1} + T^{p-1}_{i,j} + a_H S^p_{i,j} \qquad (4.1)$$

where,

$$a_E = \frac{\alpha \Delta t\left(r_i + 0.5\Delta r\right)}{r_i\left(\Delta r\right)^2}$$

$$a_W = \frac{\alpha \Delta t\left(r_i - 0.5\Delta r\right)}{r_i\left(\Delta r\right)^2}$$

$$a_N = a_S = \frac{\alpha \Delta t}{\left(\Delta z\right)^2}$$

$$a_H = \frac{\Delta t}{\rho Cp}$$

$$a_C = 1 + a_E + a_W + a_N + a_S$$

for eq. (3.1),

$$\rho = \rho_s \qquad Cp = Cp_s \qquad \alpha = \frac{k_s}{\rho_s Cp_s}$$

and for eq. (3.5),

$$\rho = \rho_l \qquad Cp = Cp_l \qquad \alpha = \frac{k_l}{\rho_l Cp_l}$$

For equation (3.3) we obtain,

$$\rho_m L_m \left(\frac{x_{mi,j}^{\ p} - x_{mi,j}^{\ p-1}}{\Delta t} \right) = k_m \left[\frac{1}{r_i} \left(\frac{r_{i+\frac{1}{2}} \left(T_{i+1,j}^{p} - T_{i,j}^{p} \right) - r_{i-\frac{1}{2}} \left(T_{i,j}^{p} - T_{i-1,j}^{p} \right)}{(\Delta r)^2} \right) + \left(\frac{T_{i,j+1}^{p} - 2T_{i,j}^{p} + T_{i,j-1}^{p}}{(\Delta z)^2} \right) \right] + S_{i,j}^{p}$$

simplifying we obtain,

$$x_{mi,j}^{\ p} = b_E T_{i+1,j}^{p} - b_C T_{i,j}^{p} + b_W T_{i-1,j}^{p} + b_Z \left(T_{i,j+1}^{p} - 2T_{i,j}^{p} + T_{i,j-1}^{p} \right) + b_H S_{i,j}^{p} + x_{mi,j}^{\ p-1} \qquad (4.2)$$

where,

$$b_E = \frac{\alpha_m Cp_m \Delta t (r_i + 0.5\Delta r)}{L_m r_i (\Delta r)^2}$$

$$b_W = \frac{\alpha_m Cp_m \Delta t (r_i - 0.5\Delta r)}{L_m r_i (\Delta r)^2}$$

$$b_C = b_E + b_W$$

$$b_N = b_S = \frac{\alpha_m Cp_m \Delta t}{L_m (\Delta z)^2}$$

$$b_H = \frac{\Delta t}{\rho_m L_m}$$

and finally for equation (3.4) we obtain,

$$\rho_b L_b \left(\frac{x_{bi,j}^{\ p} - x_{bi,j}^{\ p-1}}{\Delta t} \right) = k_b \left[\frac{1}{r_i} \left(\frac{r_{i+\frac{1}{2}} \left(T_{i+1,j}^{\ p} - T_{i,j}^{\ p} \right) - r_{i-\frac{1}{2}} \left(T_{i,j}^{\ p} - T_{i-1,j}^{\ p} \right)}{(\Delta r)^2} \right) + \left(\frac{T_{i,j+1}^{\ p} - 2T_{i,j}^{\ p} + T_{i,j-1}^{\ p}}{(\Delta z)^2} \right) \right] + S_{i,j}^{\ p}$$

simplifying we obtain,

$$x_{bi,j}^{\ p} = c_E T_{i+1,j}^{\ p} - c_C T_{i,j}^{\ p} + c_W T_{i-1,j}^{\ p} + c_Z \left(T_{i,j+1}^{\ p} - 2T_{i,j}^{\ p} + T_{i,j-1}^{\ p} \right) + c_H S_{i,j}^{\ p} + x_{bi,j}^{\ p-1} \qquad (4.3)$$

where,

$$c_E = \frac{\alpha_b C p_b \Delta t (r_i + 0.5\Delta r)}{L_b r_i (\Delta r)^2}$$

$$c_W = \frac{\alpha_b C p_b \Delta t (r_i - 0.5\Delta r)}{L_b r_i (\Delta r)^2}$$

$$c_C = c_E + c_W$$

$$c_N = c_S = \frac{\alpha_b Cp_b \Delta t}{L_b (\Delta z)^2}$$

$$b_H = \frac{\Delta t}{\rho_b L_b}$$

For all equations,

$$S_{i,j}^{p} = I_o(t)\delta(1-r_f)\exp(-\delta z_j)\exp(-r_i^2/a^2) \qquad (4.4)$$

the functional form of $I_o(t)$ is given in chapter 3.

4.2.5 Boundary Conditions

Let us represent the variables T_s, T_l, x_m and x_b by means of the variable φ. Then the various boundary conditions are discussed below with reference to figure (3.2),

At the symmetry axis $(r = 0)$ we have,

$$\frac{\partial \varphi}{\partial r} = 0$$

if $i = 1$ corresponds to points on the symmetry axis then the discretised form of the boundary condition becomes,

$$\frac{\varphi_{2,j} - \varphi_{1,j}}{\Delta r} = 0$$

or,

$$\varphi_{2,j} = \varphi_{1,j}$$

At the surface $(z = 0)$ we have,

$$\frac{\partial \varphi}{\partial z} = 0$$

if $j = 1$ corresponds to points on the symmetry axis then the discretised form of the boundary condition becomes,

$$\frac{\varphi_{i,2} - \varphi_{i,1}}{\Delta z} = 0$$

or,

$$\varphi_{i,2} = \varphi_{i,1}$$

At the right most boundary $\left(r = r_{\max}\right)$ we have,

$$T_{nr+1,j} = 300$$

$$x_{m\,nr+1,j} = 0$$

$$x_{b\,nr+1,j} = 0$$

where $i = nr + 1$ corresponds to points on the boundary $r = r_{\max}$.

At the bottom $\left(z = z_{\max}\right)$ we have,

$$T_{i,nz+1} = 300$$

$$x_{bi,nz+1} = 0$$

$$x_{bi,nz+1} = 0$$

where $j = nz + 1$ corresponds to points on the boundary $z = z_{\max}$.

4.2.6 Stability and Other Considerations

Since we are using first-order backward differences for time derivatives, therefore our discretised equations constitute what is called an implicit scheme. In the absence of convection terms, which is the case in hand, this scheme is unconditionally stable with respect to the size of the time step Δt , given that the spatial steps Δr and Δz are fixed.

During the laser heating of the substrate it is to be noted that when evaporation starts, the metal vapour is ejected out into the water and leaves behind a cavity. The laser beam is now focused on the deformed surface of the substrate, which constitutes the cavity. This aspect has to be accommodated in the solution procedure. In this case the heat source distribution has to be modified so that its peak value always occurs at the substrate surface. The appropriate modifications are,

$$S_{i,j}^{p} = I_o(t)\delta(1-r_f)\exp\left(-\delta\left(z_j - zc_i\right)\right)\exp\left(-r_i^2/a^2\right), \quad (0 \le r \le r_{\max}, z \ge zc_i)$$

$$S_{i,j}^{p} = I_o(t)\delta(1-r_f)\exp\left(-\delta z_j\right)\exp\left(-r_i^2/a^2\right), \qquad (r > r_{\max})$$

where zc_i is the depth of the cavity, which varies with r_i until $r = r_{\max}$ where $zc = 0$. In the cavity itself heat generation term has no meaningful definition since it has been assumed that the vapour does not interact with the laser beam.

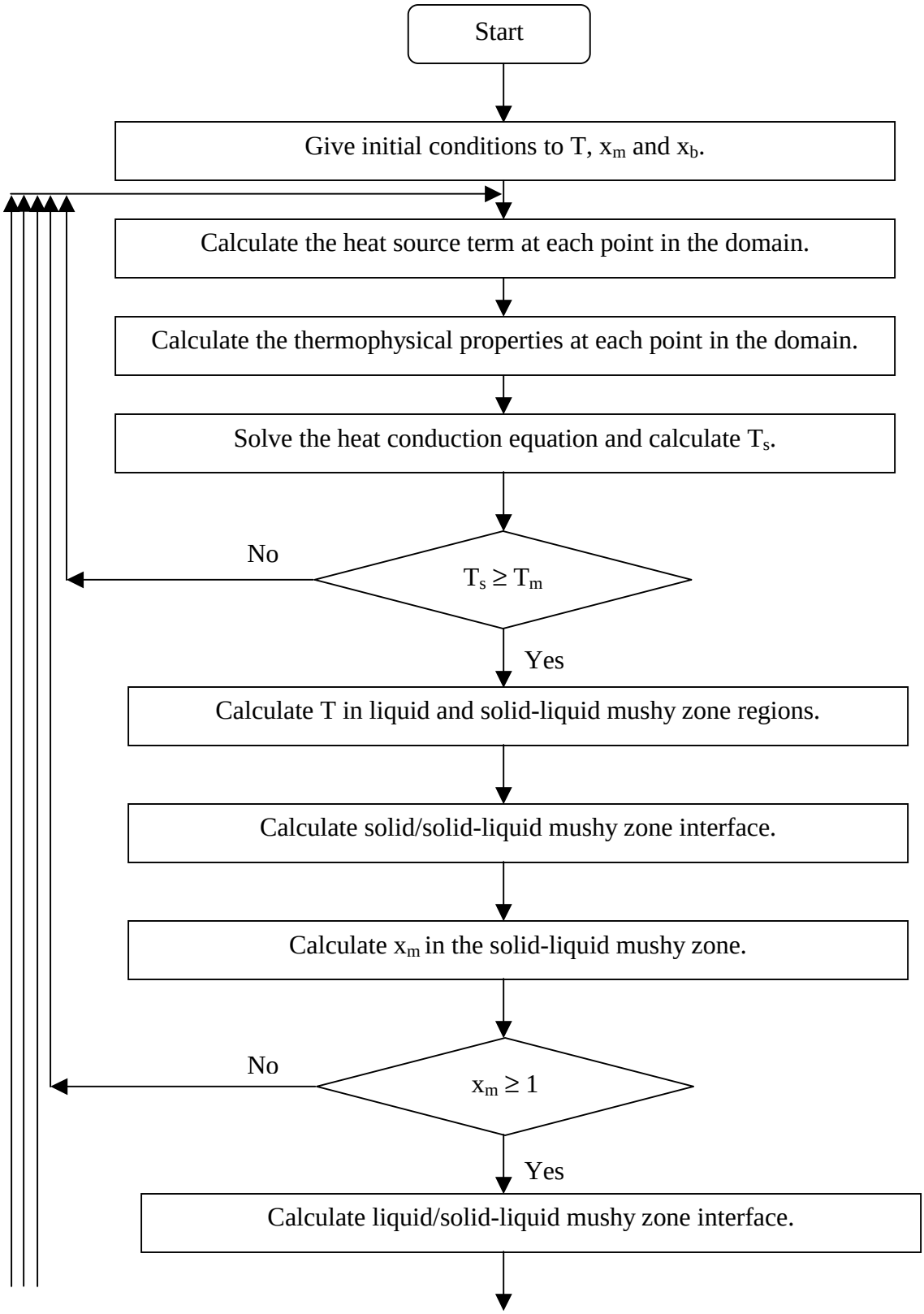
Start
Give initial conditions to T, x_m and x_b.
Calculate the heat source term at each point in the domain.
Calculate the thermophysical properties at each point in the domain.
Solve the heat conduction equation and calculate T_s.
No
$T_s \geq T_m$
Yes
Calculate T in liquid and solid-liquid mushy zone regions.
Calculate solid/solid-liquid mushy zone interface.
Calculate x_m in the solid-liquid mushy zone.
No
$x_m \geq 1$
Yes
Calculate liquid/solid-liquid mushy zone interface.

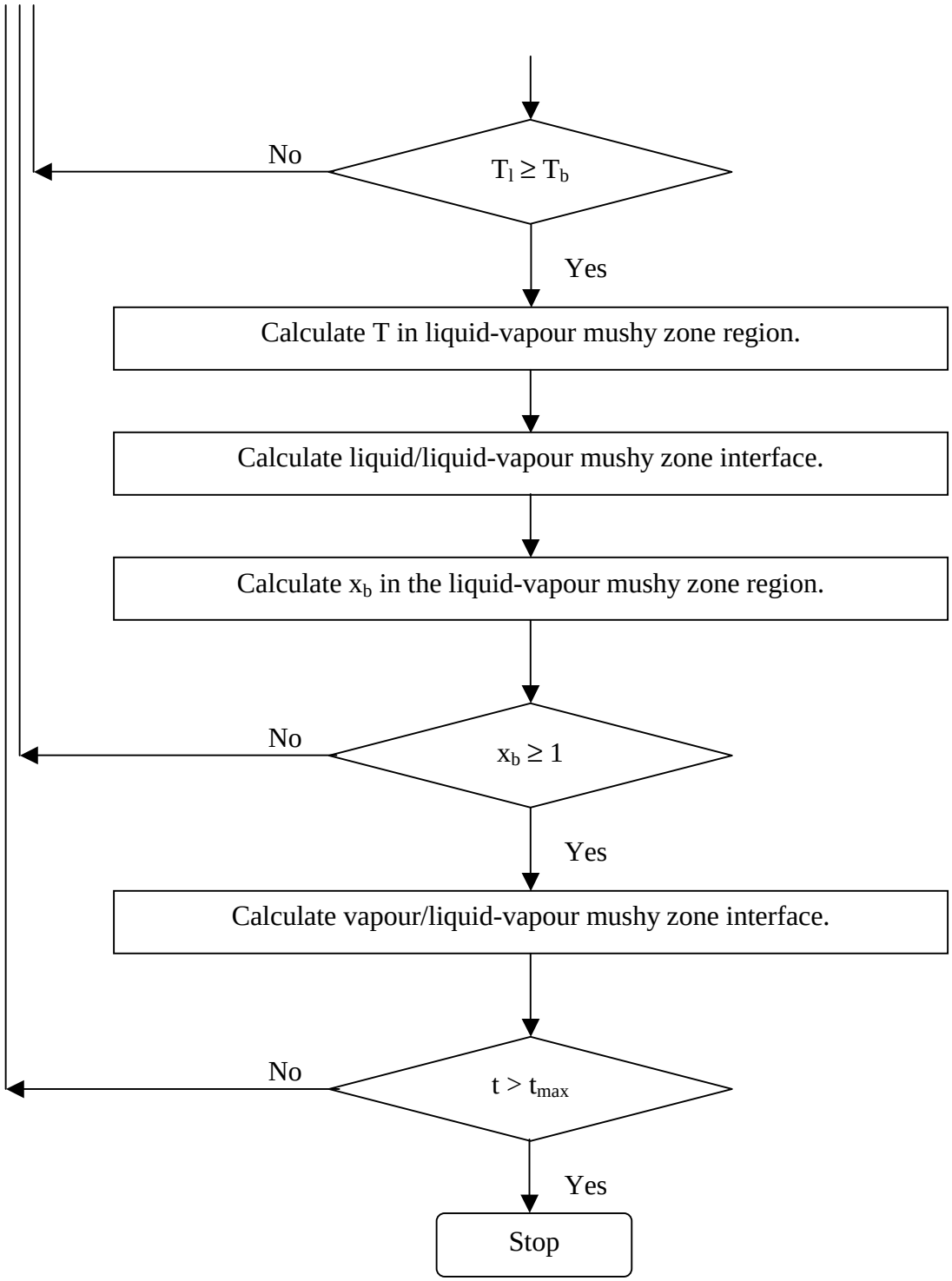

Figure 4.4 - Algorithm for the solution of phase change problem in MATLAB.

4.3 Transiently Developing Jet in Relation to Laser Heating

4.3.1 Numerical Method

In this solution phase FLUENT 6.2 is used to solve the governing equations. It is to be noted that the transport equations are now convection-diffusion equations. For momentum transport these are non-linear partial differential equations and therefore further consideration has to be given towards their numerical solution.

The property of convergence as discussed in section 4.2.1 is usually very difficult to establish theoretically and in practice Lax's Theorem is used, which states that for linear problems a necessary and sufficient condition for convergence is that the method is both consistent and stable. In CFD methods this theorem is of limited use since the governing equations are non-linear. In such problems consistency and stability are necessary conditions for convergence, but not sufficient.

The inability to prove conclusively that a numerical solution scheme is convergent or not, is perhaps somewhat unsatisfying from a theoretical standpoint, but there is no need to be too concerned since the process of making the mesh spacing very close to zero is not feasible on computing machines with a finite representation of numbers. Round-off errors would swamp the solution long before a grid spacing of zero is actually reached. In CFD, there is a need of codes that produce physically realistic results with good accuracy in simulations with finite (sometimes quite coarse) grids. Patankar [115] has formulated

rules, which yield robust finite volume calculation schemes. The three crucial properties of robust methods include:

- Conservativeness
- Boundedness
- Tranportiveness

Conservativeness is the property of a numerical scheme, which is associated with the consistent expressions for fluxes of the fluid property through the cell faces of adjacent control volumes.

Boundedness is akin to stability and requires that in a linear problem without sources the solution be bounded by maximum and minimum boundary values of the flow variable. Boundedness can be achieved by placing restrictions on the magnitude and signs of the coefficients of the algebraic equations. Although flow properties are non-linear it is important to study the boundedness of a finite volume scheme for closely related but linear problems.

Finally all flow processes contain effects due to convection and diffusion. In diffusive phenomena, such as heat conduction, a change of temperature at one location affects the temperature in more or less equal measure in all directions around it. Convective phenomenon involves influencing exclusively in the flow direction so that a point only experiences effects due to changes at upstream locations. Transportiveness must account

for the directionality of influencing in terms of the relative strength of diffusion to convection.

Conservativeness, boundedness and transportiveness are now commonly accepted as alternatives for the more mathematically rigorous concepts of convergence, consistency and stability [116].

4.3.2 The Finite Volume Method

In this method, the calculation domain is divided into a number of non-overlapping control volumes such that there is one control volume surrounding each grid point. The differential equation is integrated over each control volume. Profiles (such as step-wise and piecewise-linear), expressing the variation of field variable (temperature, pressure, velocity, species mass fraction, etc.) between the grid points, are used to evaluate the required integrals. The result is the discretisation equation containing the values of field variable for a group of grid points. The discretisation equation thus obtained in this manner express the conservation principle of the field variable for the finite control volume, just as the differential equation expresses it for an infinitesimal control volume.

4.3.3 Discretisation

All the relevant partial differential equations, which are used to model the flow in this section, can be written in a general form.

$$\frac{\partial}{\partial t}(\bar{\rho}\varphi)+\frac{\partial}{\partial x_j}\left(\bar{\rho}\bar{u}_j\varphi-\Gamma_\varphi\frac{\partial\varphi}{\partial x_j}\right)=\bar{S}_\varphi \qquad (4.5)$$

The finite difference counterpart of this general partial differential equation (4.5) is derived by supposing that each variable is enclosed in its own control volume and then by integrating the partial differential equation (4.5) over the control volume with some suitable assumption of field-variable profile within the control volume.

For the purpose of solution the flow domain is overlaid with a number of grids whose centre points or nodes denote the location at which all variables except velocities are calculated. The latter are computed at locations midway between the two pressure points. Thus the normal velocity components are directly available at the control volume faces, where they are needed for the scalar transport convection-diffusion computations. The nodes of a typical grid cluster for two dimensions are labeled as P, N, S, E and W. This is shown in Figure 4.4.

The integration of each term in Eq. (4.5) can be obtained with reference to the control volume for a typical node P with its four nearest neighbours, N, S, E and W in the spatial domain and P_o in the time domain. The integration yields,

$$\int_t^{t+\Delta t}\left\{\int_{CV}\left(\frac{\partial}{\partial t}(\bar{\rho}\varphi)-\bar{S}_\varphi\right)d\forall+\oint_{CS}\left[\hat{n}.\left(\rho\bar{u}_j\varphi-\Gamma_\varphi\nabla\varphi\right)\right]dA\right\}dt=0 \qquad (4.6)$$

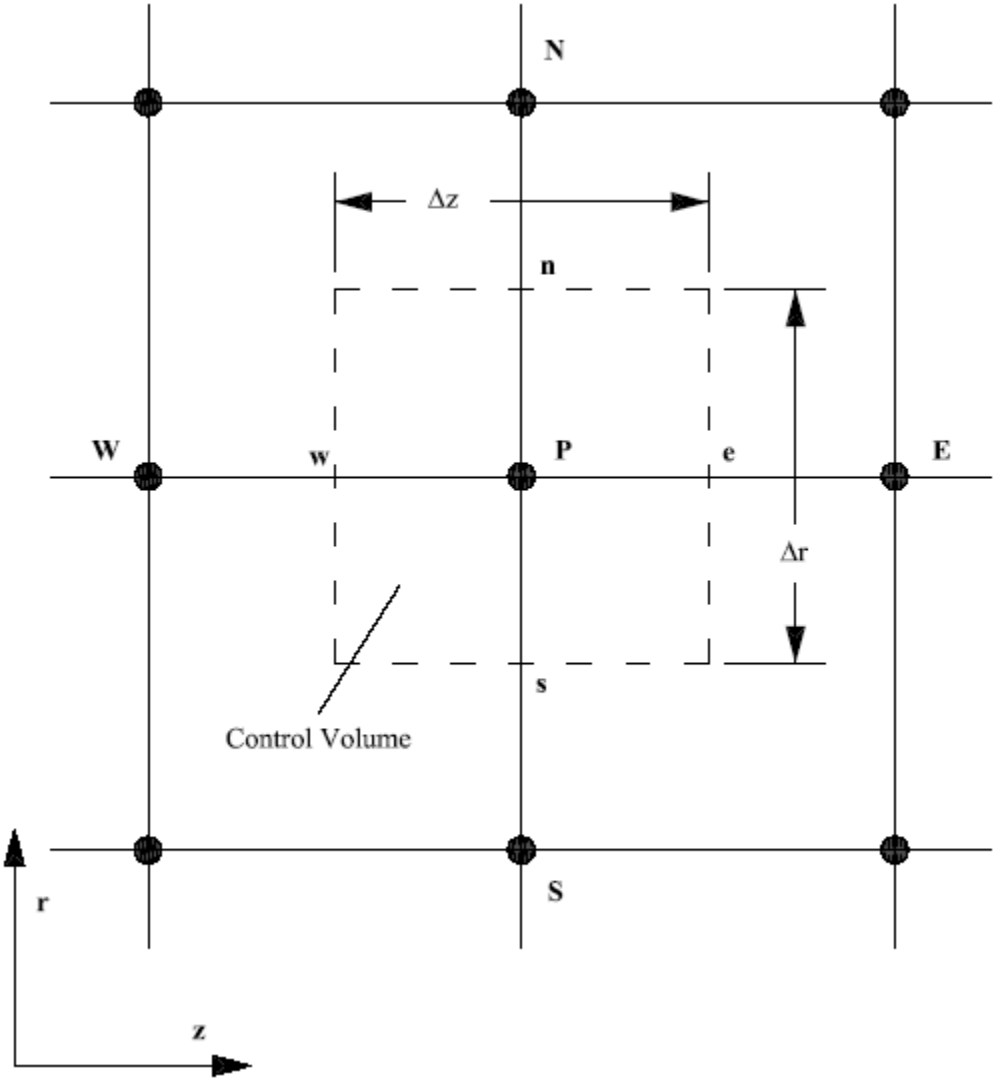

Figure 4.5 - Control volume for the two- dimensional situation.

Divergence theorem gives,

$$\int_t^{t+\Delta t}\left\{\int_{CV}\left(\frac{\partial}{\partial t}(\bar{\rho}\varphi)-\bar{S}_\varphi\right)d\forall+\oint_{CV}\left[\frac{\partial}{\partial x_j}\left(\bar{\rho}\bar{u}_j\varphi-\Gamma_\varphi\frac{\partial\varphi}{\partial x_j}\right)\right]d\forall\right\}dt=0 \quad (4.7)$$

or

$$\int_t^{t+\Delta t}\left\{\left(\frac{\partial}{\partial t}(\bar{\rho}\varphi)-\bar{S}_\varphi\right)\Delta\forall+\left[\left(\bar{\rho}\bar{u}_j\varphi-\Gamma_\varphi\frac{\partial\varphi}{\partial x_j}\right)\Delta A_j\right]_{L_1}^{L_2}\right\}dt=0 \quad (4.8)$$

or

$$\int_t^{t+\Delta t}\left\{\left(\frac{\partial}{\partial t}(\bar{\rho}\varphi)-\bar{S}_\varphi\right)\Delta\forall+\left[J_j\Delta A_j\right]_{L_1}^{L_2}\right\}dt \quad (4.9)$$

Where L_1 denotes w or s, L_2, e or n and J_j the total flux (convection plus diffusion) across the face $'j'$.

If $\bar{S}_\varphi$ is independent of time then Eq. (4.9) becomes

$$\left[\frac{\overline{\rho}_P\varphi_P - \overline{\rho}_P^o\varphi_P^o}{\Delta t} - \overline{S}_\varphi\right]\Delta\forall + J_e - J_w + J_n - J_s = 0 \qquad (4.10)$$

where J_e, J_w, J_n and J_s are the integrated total fluxes over the control volume faces; i.e., J_e stands for $J_x\Delta A_x$ over the interface e, and so on. Where the superscript *'o'* is used for old values (i.e., the values at previous time step).

The linearization of the source term gives

$$\overline{S}_\varphi = S_o + S_P\varphi_P \qquad (4.11)$$

Now Eq. (4.10) becomes

$$\left(\frac{\overline{\rho}_P\varphi_P - \overline{\rho}_P^o\varphi_P^o}{\Delta t}\right)\Delta\forall + J_e - J_w + J_n - J_s = \left(S_o + S_P\varphi_P\right)\Delta\forall \qquad (4.12)$$

Now integration of the continuity equation (3.6) in a similar manner to Eq. (4.5) gives

$$\int_t^{t+\Delta t}\left\{\int_{CV}\left[\frac{\partial\overline{\rho}}{\partial t} + \frac{\partial}{\partial x_j}\left(\overline{\rho u}_j\right)\right]d\forall\right\}dt = 0 \qquad (4.13)$$

or

$$\int_t^{t+\Delta t}\left\{\frac{\partial\overline{\rho}}{\partial t}\Delta\forall+\left[\overline{\rho}\overline{u}_j\Delta A_j\right]_{L_1}^{L_2}\right\}dt=0 \qquad (4.14)$$

or

$$\int_t^{t+\Delta t}\left\{\frac{\partial\overline{\rho}}{\partial t}\Delta\forall+\left[F_j\Delta A_j\right]_{L_1}^{L_2}\right\}dt=0 \qquad (4.15)$$

or

$$\left(\frac{\overline{\rho}_P-\overline{\rho}_P^{o}}{\Delta t}\right)\Delta\forall+F_e-F_w+F_n-F_s=0 \qquad (4.16)$$

where F_j is the mass flux through the face $'j'$; F_e, F_w, F_n and F_s are the mass flow rates through the faces of the control volume; i.e., F_e stands for $F_x\Delta A_x$ over the interface e, and so on.

Multiplying Eq. (4.16) by φ_P, subtracting the resulting equation from Eq. (4.12) and noting that;

$$J_e-F_e\varphi_P=a_E\left(\varphi_P-\varphi_E\right) \qquad (4.17)$$

$$J_w-F_w\varphi_P=a_W\left(\varphi_W-\varphi_P\right) \qquad (4.18)$$

$$J_n - F_n\varphi_P = a_N\left(\varphi_P - \varphi_N\right) \tag{4.19}$$

$$J_s - F_s\varphi_P = a_S\left(\varphi_S - \varphi_P\right) \tag{4.20}$$

one can develop the following algebraic equation [115]:

$$a_P\varphi_P = a_E\varphi_E + a_W\varphi_W + a_N\varphi_N + a_S\varphi_S + b \tag{4.21}$$

where

$$a_P = a_E + a_W + a_N + a_S + a_P^o - S_P\Delta\forall \tag{4.22}$$

$$a_P^o = \frac{\overline{\rho}_P^o\Delta\forall}{\Delta t} \tag{4.23}$$

$$b = a_P^o\varphi_P^o + S_o\Delta\forall \tag{4.19}$$

$$a_E = D_e A\left(\left|P_e\right|\right) + \left[\left[-F_e, 0\right]\right] \tag{4.20}$$

$$a_W = D_w A\left(\left|P_w\right|\right) + \left[\left[F_w, 0\right]\right] \tag{4.21}$$

$$a_N = D_n A(|P_n|) + [[-F_n, 0]] \qquad (4.22)$$

$$a_S = D_s A(|P_s|) + [[F_s, 0]] \qquad (4.23)$$

and P_e, P_w, P_n and P_s are the Peclet numbers: i.e., P_e stands for $\frac{F_e}{D_e}$ and so on; D_e, D_w, D_n and D_s are the diffusion conductances i.e., D_e stands for $\frac{\Gamma_e \Delta y}{(\delta x)_e}$ and so on. The values of $A(|P|)$ are given in [115] for different schemes. In the present study, first order upwind scheme is employed for which $A(|P|)$ is unity.

Equation (4.21) is written for each of the variables $\bar{u}$, $\bar{v}$, k, ε, $\bar{\rho}$, $\bar{Y}_i$ and $\bar{T}$ at every cell. Although the control volumes adjacent to the boundary are treated differently from the interior ones and need different algebraic formulation, it is possible to have a unified formulation to calculate the field variable in the near boundary region through the use of source term [116].

4.3.4 Computation of the Flow Field

The solution of the general transport equation (4.5) presents two new problems:

- The convective term Eq. (4.5) contains non-linear inertia terms.
- The continuity, momentum, energy, species and turbulence equations, represented by Eq. (4.5) are intricately coupled because every velocity component appears in each equation. The most complex issue to resolve is the role played by pressure. It

appears in the momentum equations, but there is evidently no transport equation for pressure.

If the pressure gradient is known, the process of obtaining and solving discretised equations for velocities from momentum equations is similar to that for any other scalar (e,g. temperature, species mass fraction, etc.) and developed schemes such as central differencing, upwind, hybrid schemes, etc. are applicable. In general purpose flow computations the pressure field is calculated as a part of the solution so its gradient is normally not known beforehand. If the flow is compressible, the continuity equation may be used as a transport equation for density and the pressure may be obtained from the density and temperature by using the equation of state. However, if the flow is incompressible the density is constant and hence by definition not linked to the pressure. In this case coupling between pressure and velocity introduces a constraint on the solution of the flow field: if the correct pressure field is applied in the momentum equations the resulting velocity field should satisfy continuity. Both the problems associated with the non-linearities in Eq. (4.5) and the pressure velocity linkage can be resolved by adopting an iterative solution strategy such as *SIMPLE (Semi-Implicit Method for Pressure-Linked Equations)* algorithm of Patankar and Spalding [116].

Before outlining the algorithm it is very important to explain the grid staggering, which is the first step to the SIMPLE algorithm. The finite volume method starts as always with discretisation of the flow domain and of the general transport equation (4.5). First there is a need to decide where to store the velocities. It seems logical to define these at the same

locations where the scalar variables, such as pressure, temperature, etc. are defined. However, if the velocities and pressure are both defined at the nodes of an ordinary control volume, a highly nonuniform pressure field may act like a uniform field in the discretised momentum equations [116]. For instance, if velocities and pressure are both defined at the nodes of an ordinary control volume and the pressure gradient terms in the momentum equations are discretised by central differencing scheme in a uniformly discretised flow field, it is found that all the discretised pressure terms in axial and radial directions are zero at all nodal points even though the pressure field exhibits spatial oscillation in both directions of a two dimensional flow field [116]. As a result this pressure field would give the same (zero) momentum source in the discretised equations as a uniform pressure field. This behaviour is obviously non-physical.

It is clear that, if velocities are defined at the scalar nodes (at which scalars such as pressure and temperature are defined), the influence of pressure is not properly represented in the discretised momentum equations. A remedy for this problem is to use a staggered grid for the velocity components. The idea is to evaluate scalar variables such as pressure, density, temperature, species concentration, turbulence kinetic energy and turbulence dissipation at ordinary nodal points but to calculate velocity components on staggered grids centered around the cell faces. The arrangement for two-dimensional flow calculation with staggered grid arrangement is shown in Figure 4.5. In Figure 4.5 unbroken lines (grid lines) are numbered by means of capital letters …, I-1, I, $I+1$, … and …, J-1, J, $J+1$, … in the axial and radial directions respectively whereas the dashed lines that construct the scalar cell faces are denoted by lower case letters …, i-1,

i, $i+1$, … and …, j-1, j, $j+1$, … in the axial and radial directions respectively. A subscript system based on this numbering allows us to define the locations of grid nodes and cell faces with precision. Scalar nodes, located at the intersection of two grid lines are identified by two capital letters for e.g., point P in Figure 4.5 is denoted by (I,J). The axial velocities are stored at the e- and w-cell faces of a scalar control volume. These are located at the interaction of a line defining a cell boundary and a grid line and are therefore defined by a combination of a lower case letter and a capital for e.g., the w-face of the cell around point P is identified by (i,J). For the same reasons the storage locations for the radial velocities are combinations of a capital and a lower case letter for e.g., the s-face is given by (I,j).

The staggering of the velocity avoids the unrealistic behaviour of the discretised momentum equation for spatially oscillating pressures. A further advantage of the staggered grid arrangement is that it generates velocities at exactly the locations where they are required for the scalar transport-convection-diffusion computations. Hence no interpolation is needed to calculate velocities at the scalar (e.g., pressure and temperature) cell faces.

4.3.5 The SIMPLE Algorithm

The discretised momentum equations for $\bar{u}$ and $\bar{v}$ using Eq. (4.21) are,

$$a_{i,J}\bar{u}_{i,J} = \sum a_{nb}\bar{u}'_{nb} + (\bar{p}_{I-1,J} - \bar{p}_{I,J})A_{i,J} + b_{i,J} \qquad (4.29)$$

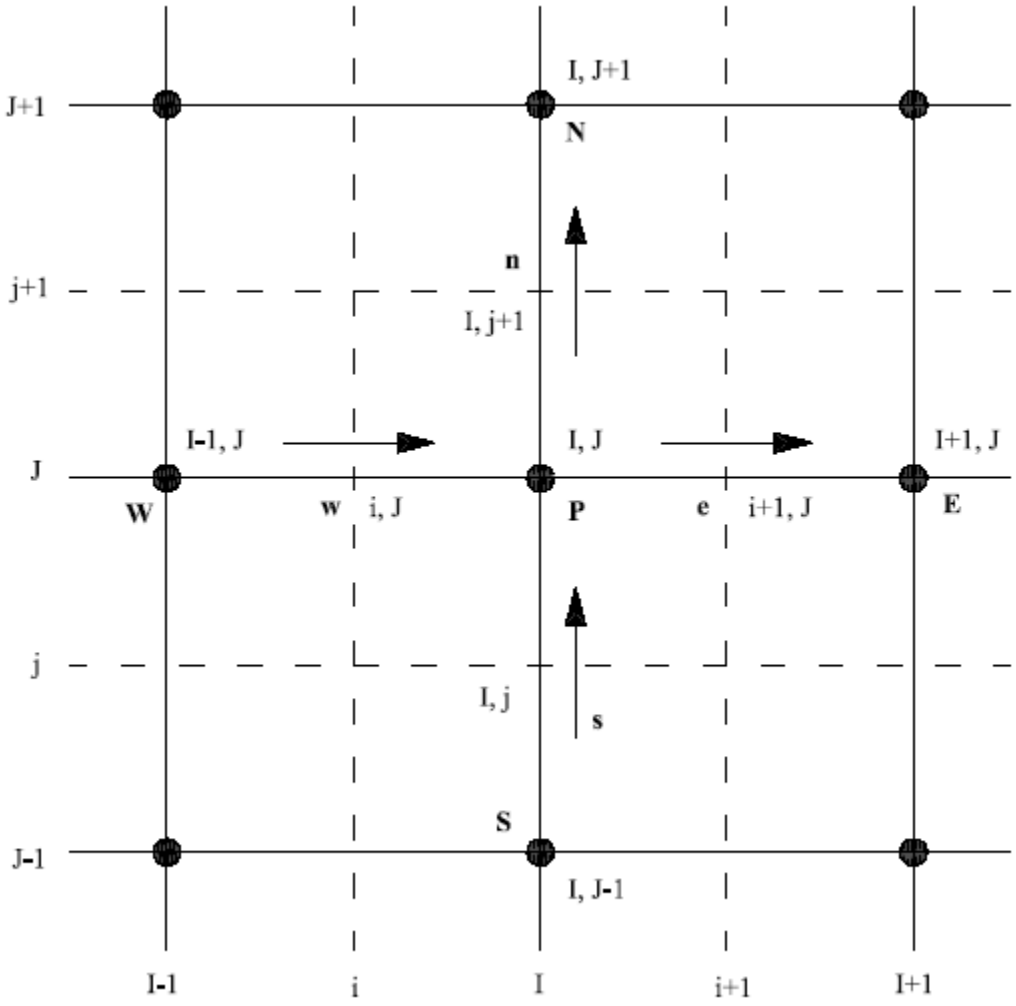

Figure 4.6 - Staggered grid arrangement for velocity components.

$$a_{I,j}\bar{v}_{I,j} = \sum a_{nb}\bar{v}'_{nb} + \left(\bar{p}_{I,J-1} - \bar{p}_{I,J}\right)A_{I,j} + b_{I,j} \qquad (4.30)$$

To initiate the *SIMPLE* calculation process the coefficients are calculated from the so-called guessed velocity components and then the pressure field p^* is guessed [116]. Discretised momentum equations (4.29) and (4.30) are solved using the guessed pressure field to yield velocity components $\bar{u}^*$ and $\bar{v}^*$ as follows,

$$a_{i,J}\bar{u}^*_{i,J} = \sum a_{nb}\bar{u}^*_{nb} + \left(\bar{p}^*_{I-1,J} - \bar{p}^*_{I,J}\right)A_{i,J} + b_{i,J} \qquad (4.31)$$

$$a_{I,j}\bar{v}^*_{I,j} = \sum a_{nb}\bar{v}^*_{nb} + \left(\bar{p}^*_{I,J-1} - \bar{p}^*_{I,J}\right)A_{I,j} + b_{I,j} \qquad (4.32)$$

If $\bar{p}'$ is the correction pressure and $\bar{p}^*$ the guessed pressure then the correct pressure field $\bar{p}$ is,

$$\bar{p} = \bar{p}^* + \bar{p}' \qquad (4.33)$$

Similarly if $\tilde{u}'$ and $\tilde{v}'$ are the velocity corrections and $\tilde{u}^*$ and $\tilde{v}^*$ the guessed velocities then the correct velocities $\tilde{u}$ and $\tilde{v}$ are,

$$\bar{u} = \bar{u}^* + \bar{u}' \qquad (4.34)$$

$$\bar{v} = \bar{v}^{*} + \bar{v}' \tag{4.35}$$

After subtracting Eqs. (4.31) and (4.32) from (4.29) and (4.30), respectively using correction formulae (4.33 - 4.35), omitting the terms $\sum a_{nb}\bar{u}'_{nb}$ and $\sum a_{nb}\bar{v}'_{nb}$ from the equations resulting from subtraction and then using again Eqs. (4.34) and (4.35), the following expressions for correct velocities at nodes $w\,(i, J)$ and $s\,(I, j)$ are obtained,

$$\bar{u}_{i,J} = \bar{u}^{*}_{i,J} + d_{i,J}\left(\bar{p}'_{I-1,J} - \bar{p}'_{I,J}\right) \tag{4.36}$$

$$\bar{v}_{I,j} = \bar{v}^{*}_{I,j} + d_{I,j}\left(\bar{p}'_{I,J-1} - \bar{p}'_{I,J}\right) \tag{4.37}$$

Similar expressions for velocities $\bar{u}_{i+1,J}$ and $\bar{v}_{I,j+1}$ exist,

$$\bar{u}_{i+1,J} = \bar{u}^{*}_{i+1,J} + d_{i+1,J}\left(\bar{p}'_{I,J} - \bar{p}'_{I+1,J}\right) \tag{4.38}$$

$$\bar{v}_{I,j+1} = \bar{v}^{*}_{I,j+1} + d_{I,j+1}\left(\bar{p}'_{I,J-1} - \bar{p}'_{I,J+1}\right) \tag{4.39}$$

where

$$d_{i,J} = A_{i,J} / a_{i,J} \tag{4.40}$$

$$d_{I,j} = A_{I,j} / a_{I,j} \tag{4.41}$$

$$d_{i+1,J} = A_{i+1,J} / a_{i+1,J} \tag{4.42}$$

$$d_{I,j+1} = A_{I,j+1} / a_{I,j+1} \tag{4.43}$$

Using correct velocity in the discretised continuity equation the following discretised equation for the pressure correction $\overline{p}'$ is obtained,

$$a_{I,J}\overline{p}'_{I,J} = a_{I+1,J}\overline{p}'_{I+1,J} + a_{I-1,J}\overline{p}'_{I-1,J} + a_{I,J+1}\overline{p}'_{I,J+1} + a_{I,J-1}\overline{p}'_{I,J-1} + b'_{I,J} \tag{4.44}$$

where

$$a_{I,J} = a_{I+1,J} + a_{I-1,J} + a_{I,J+1} + a_{I,J-1} \tag{4.45}$$

$$a_{I+1,J} = (\overline{\rho} dA)_{i+1,J} \tag{4.46}$$

$$a_{I-1,J} = (\overline{\rho} dA)_{i,J} \tag{4.47}$$

$$a_{I,J+1} = (\overline{\rho} dA)_{I,j+1} \tag{4.48}$$

$$a_{I,J-1} = \left(\bar{\rho} dA\right)_{I,j} \tag{4.49}$$

$$b'_{I,J} = \left(\bar{\rho}\bar{u}^{*} A\right)_{i,J} - \left(\bar{\rho}\bar{u}^{*} A\right)_{i+1,J} + \left(\bar{\rho}\bar{v}^{*} A\right)_{I,j} - \left(\bar{\rho}\bar{v}^{*} A\right)_{I,j+1} \tag{4.50}$$

As soon as the starred velocity components are obtained the pressure correction equation (4.44) is solved for $\bar{p}'$ at all scalar nodes. Once the pressure correction field is known, the correct pressure field may be obtained using formula (4.33) and correct velocity components through formulae (4.36 - 4.39).

Afterwards, the discretisation equations for the scalar variables, such as temperature, species mass fraction and turbulence quantities are solved if they influence the flow field through fluid properties, source terms, etc. If a particular scalar variable does not influence the flow field, it is better to calculate it after a converged solution for the flow field has been obtained.

If the solution is not converged the correct pressure $\bar{p}$ is treated as a new guessed $\bar{p}^{*}$ and the corrected velocity components as new guessed velocity components, but not the starred values, and the whole procedure is repeated over and over until converged solution is obtained.

The pressure correction equation is susceptible to divergence [116] unless some under-relaxation is used during the iterative process and therefore new (improved) pressures $\bar{p}^{new}$ are obtained with,

$$\bar{p}^{new} = \bar{p}^{*} + \alpha_{\bar{p}} \bar{p}' \tag{4.51}$$

where $\alpha_{\bar{p}}$ is the pressure under-relaxation factor.

The velocities $\bar{u}^{*}$, $\bar{v}^{*}$ and $\bar{u}$, $\bar{v}$ are also under-relaxed as follows,

$$\bar{u}^{*\,new} = \alpha_{\bar{u}} \bar{u}^{*} + (1 - \alpha_{\bar{u}}) \bar{u}^{n-1} \tag{4.52}$$

$$\bar{v}^{*\,new} = \alpha_{\tilde{v}} \bar{v}^{*} + (1 - \alpha_{\tilde{v}}) \bar{v}^{n-1} \tag{4.53}$$

$$\bar{u}^{new} = \alpha_{\tilde{u}} \bar{u} + (1 - \alpha_{\tilde{u}}) \bar{u}^{n-1} \tag{4.54}$$

$$\bar{v}^{new} = \alpha_{\tilde{v}} \bar{v} + (1 - \alpha_{\tilde{v}}) \bar{v}^{n-1} \tag{4.55}$$

$\alpha_{\bar{u}}$ and $\alpha_{\bar{v}}$ are under relaxation factors for x and y velocity components. $\bar{u}^{*}$ and $\bar{v}^{*}$ are the velocity components obtained from solving the momentum equations (4.31) and (4.32) whereas $\bar{u}$ and $\bar{v}$ are the corrected velocity components obtained from velocity

correction formulae (4.36 - 4.39). $\bar{u}^{n-1}$ and $\bar{v}^{n-1}$ are the velocity components obtained in the previous iteration.

The pressure correction equation is also affected by velocity under-relaxation and it can be shown that the d-terms of pressure correction equation (4.44) will be multiplied by the velocity under-relaxation. The second terms of the velocity correction formulae (4.36 – 4.39) will also be multiplied by the velocity under-relaxation. The complete steps followed can be well described by the flow chart (Figure 4.6).

4.3.6 Grid Details and Computation

Along the radial direction fine uniform grid spacing is allocated at the inlet while gradually increasing spacing is considered away from it. Along the axial direction, again fine uniform grid spacing is used inside and near the cavity while the grid spacing gradually increases away from it. The number of grid points in the radial direction is 300 while 215 grid points are used in the axial direction. The actual computational grid is shown in Figure 4.7. Grid independence test result for velocity is shown in Figure 4.8. It maybe observed that for 215×300, 265×370 and 265×370 grid points the results are almost in agreement.

Eight variables are computed at all grid points. These are the two velocity components, local pressure, two turbulence quantities, temperature and two mass fractions.

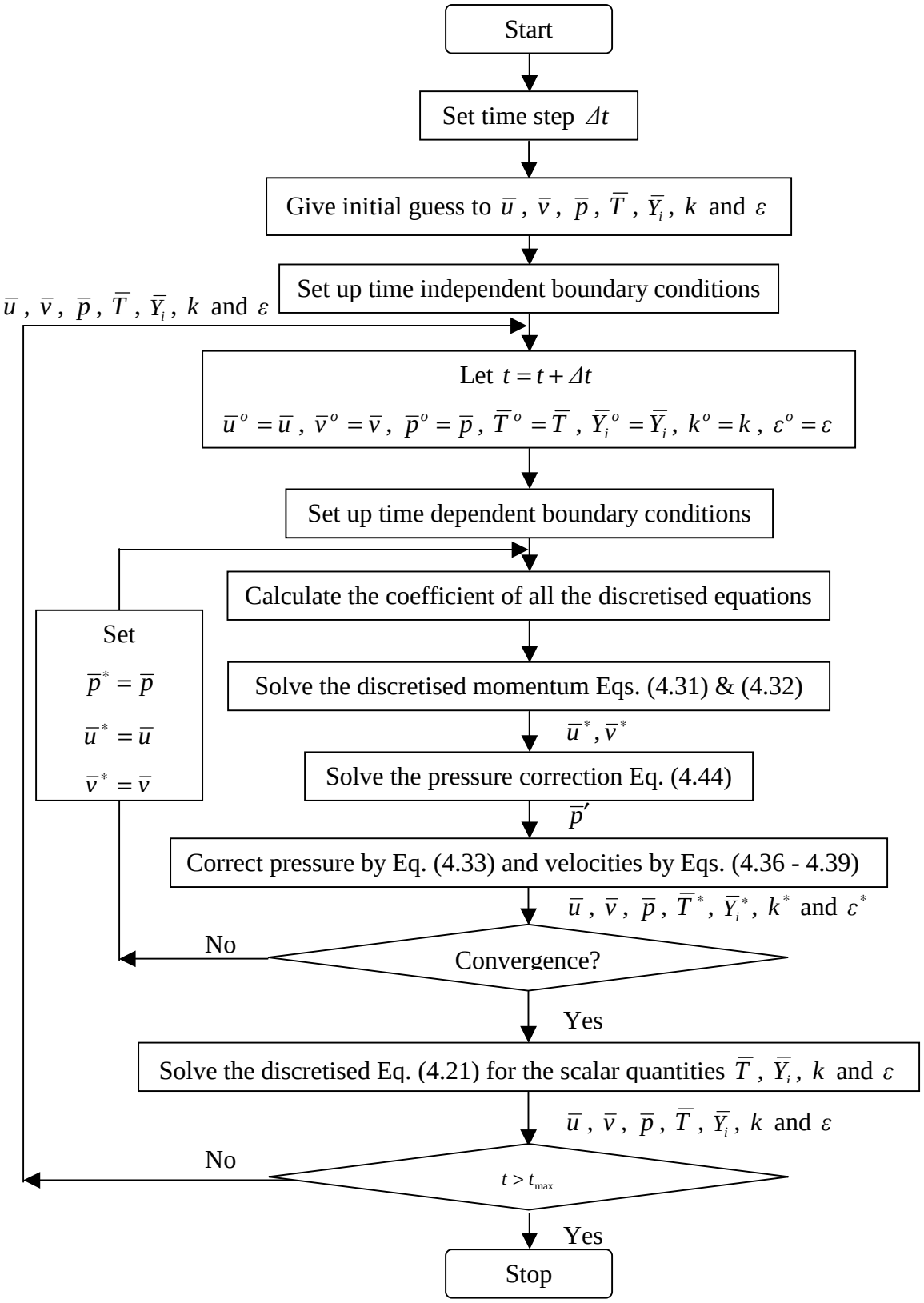

Figure 4.7: The SIMPLE Algorithm.

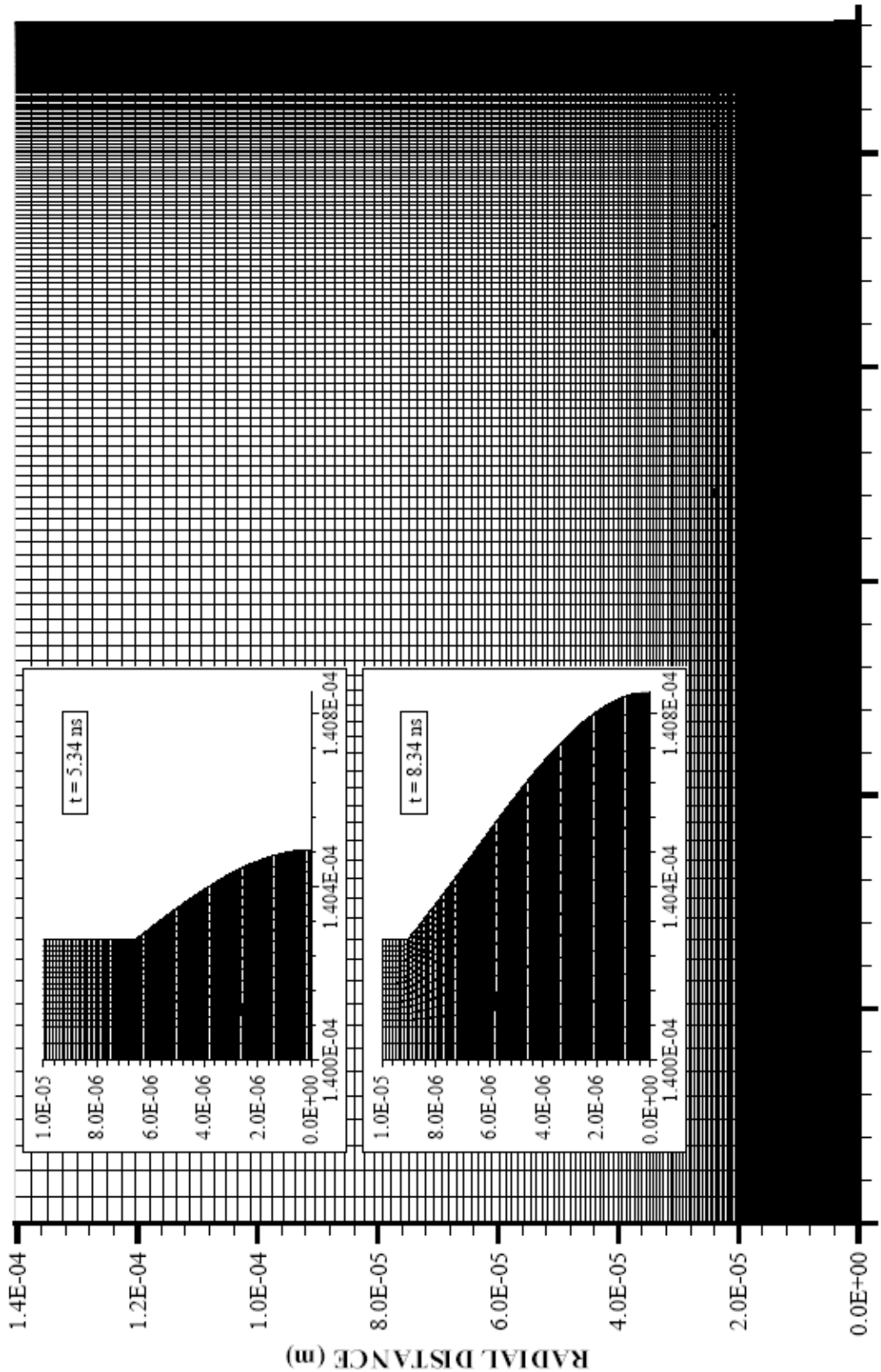

Figure 4.8 – Computational grid for an axisymmetric transient turbulent vapour jet emanating from the cavity.

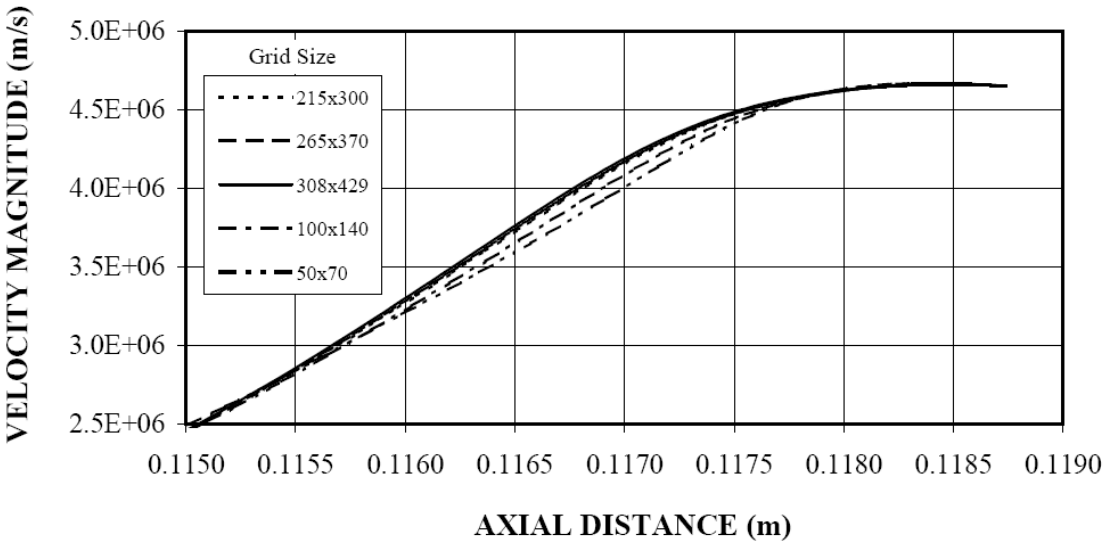

Figure 4.9 - Grid independence test for velocity magnitude along the symmetry axis.

CHAPTER 5

RESULTS AND DISCUSSIONS

5.1 Laser Heating of the Substrate Material

Laser non-conduction limited heating of a steel surface is considered. The cavity formation at the surface during the heating pulse is modelled using an energy method. The mushy zones between vapour-liquid and liquid-solid, interfaces are predicted, numerically. The propagation of the solid-liquid and the liquid-vapour interfaces are also predicted as the heating progresses. Further, the laser pulse peak intensity is varied to investigate the effect of peak intensity on the evaporation and melting processes. The

pulse shape used in the simulation resembles the actual laser pulse shape used in the experiment as shown in figure (5.1). The spatial distribution of the pulse intensity is assumed to be Gaussian with its $1/e$ points correspond to 8.3×10^{-6} m.

Figure (5.2) shows temperature contours in the substrate surface for different heating situations while figures (5.3a & 5.3b) shows temperature distribution along the z-axis inside the substrate material for four different heating periods and three radial locations. Evaporation of the surface in the region of the irradiated spot centre initiates at early heating periods and as the time period progresses, the cavity is formed in the surface vicinity of the substrate material. The cavity depth reaches slightly above 1 μm along the axial direction (z-axis) and 10 μm along the radial direction (r-axis). The rate of extension of cavity in the axial direction is higher than its counterpart corresponding to the radial direction. This is due to the laser power intensity distribution across the irradiated spot, which is Gaussian. In this case, energy absorbed from the irradiated field is unidirectional, which is along the axial direction, and energy absorbed in the irradiated spot centre is high. This in turn results in higher temperature gradients in the axial direction then that of the radial direction. Since the temperature gradient is the driving force for diffusional energy transport inside the substrate material; consequently, energy transfer towards the solid bulk enhances due to contribution of diffusional energy transport along the axial direction. This improves the rate of cavity extension in the axial direction. When examining figure (5.4a & 5.4b), solid heating, solid-liquid phase change and super heating of liquid are evident at low heating periods (6 ns) and at axial depth

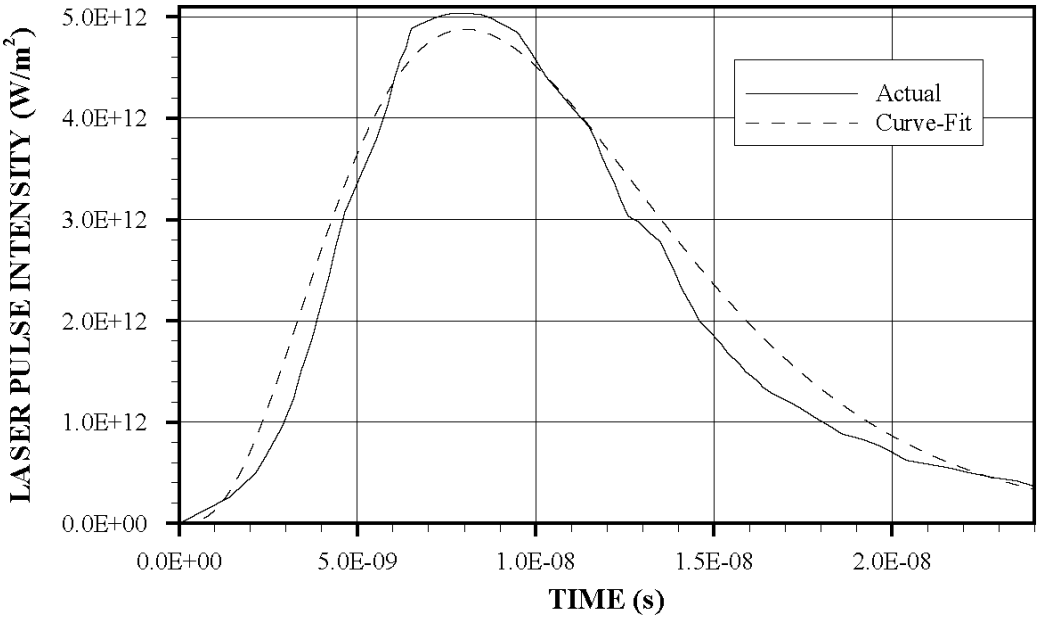

Figure 5.1 - Temporal variation of laser pulse intensity used in the simulations and obtained from the measurement.

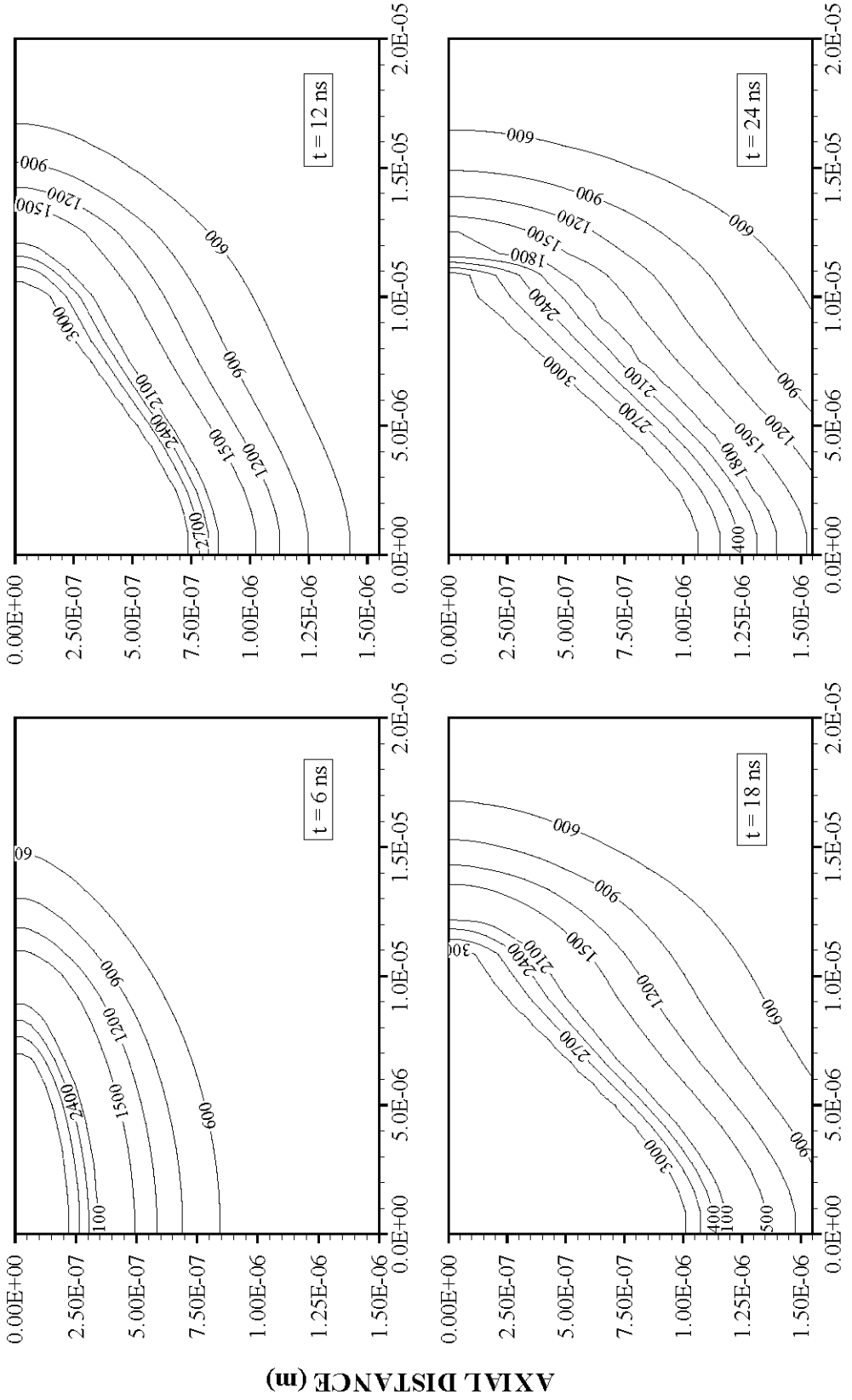

Figure 5.2 - Contour plots of temperature distribution for three different heating durations.

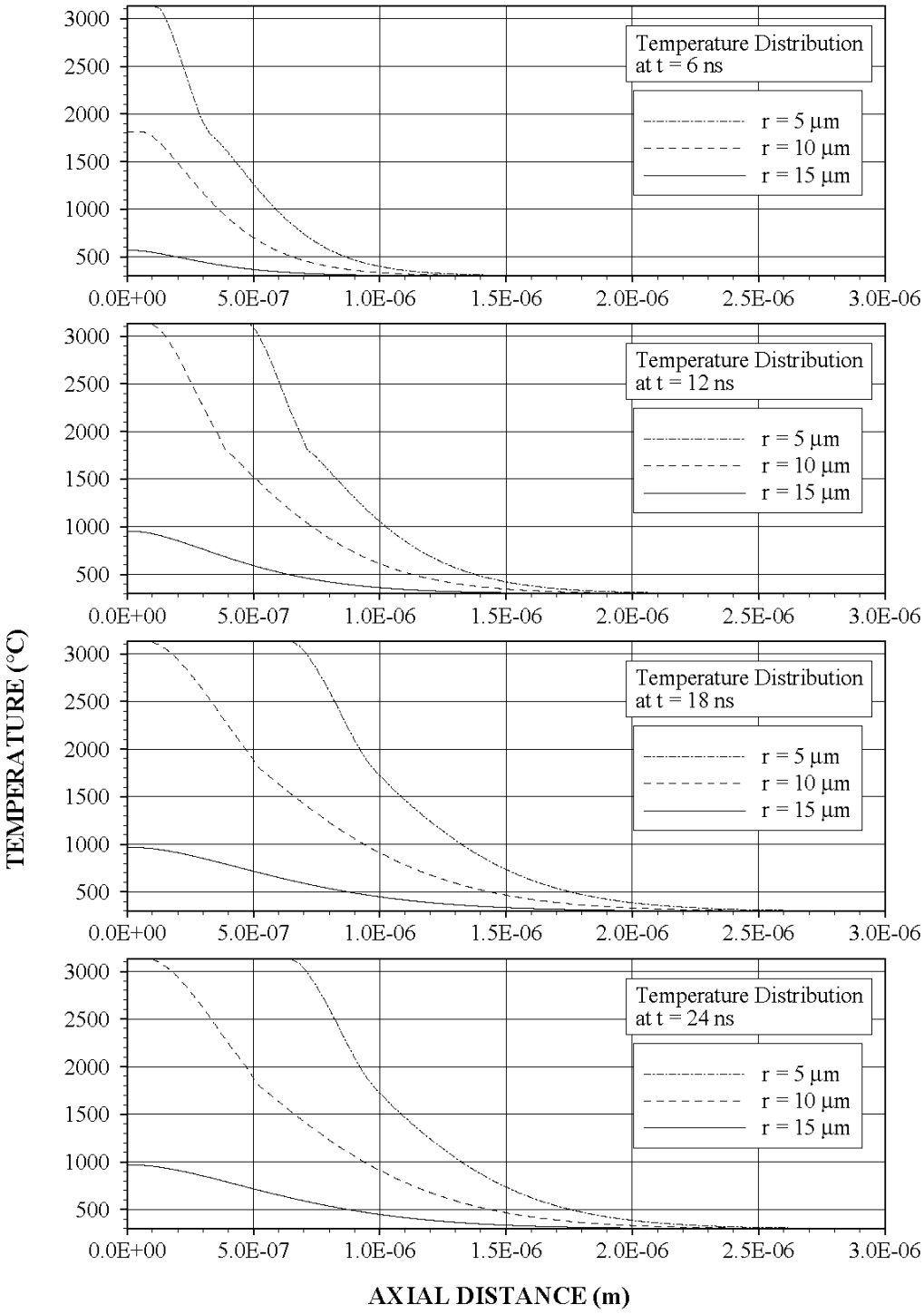

Figure 5.3a - Temperature variation along the axial distance for different radial locations and heating durations.

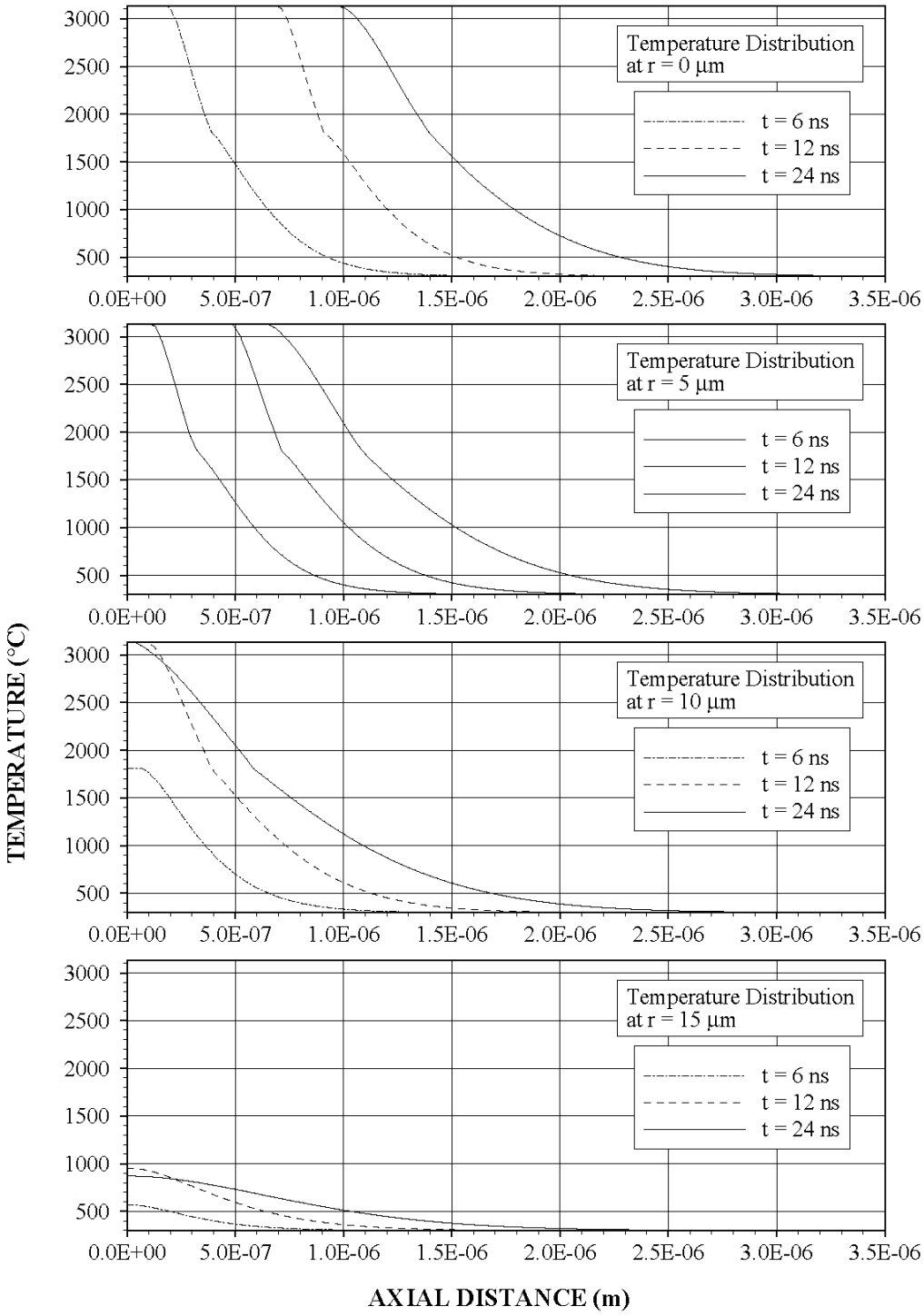

Figure 5.3b - Temperature variation along the axial distance for different radial locations and heating durations.

close to the surface region (z = 0.32 μm). As the heating period progresses, temperature across the radial direction becomes smooth and constant temperature region due to phase change becomes invisible. This indicates that progressing the heating duration reduces the size of the mushy zone, i.e. constant temperature zone in the radial direction becomes negligible such that mushy zone thickness is limited with a fraction of μm. In the case of temperature distribution in the axial direction (figure (5.3a & 5.3b)), the existing of mushy zone is not visible due to considerably small size of the mushy zone along the axial direction. Moreover, temperature in the solid phase decays sharply in the region of the mushy zone. As the depth below the surface increases towards the solid bulk, temperature decay becomes gradual. This occurs because of the energy balance attained between internal energy gain from the irradiated field, and diffusional energy transfer to solid bulk from the surface region due to temperature gradient. High rate of energy gain from the irradiated field enhances temperature rise in the vicinity of the surface and temperature gradient next to the surface vicinity becomes high enhancing the diffusional energy transport. Figure (5.5) shows three-dimensional plot of mass fraction of liquid (x_m) in the solid-liquid interface for different heating periods while figures (5.6a & 5.6b) and (5.7a & 5.7b) show mass fraction of liquid in the mushy zone along the axial and radial directions for different heating periods. It should be noted that $x_m = 1$ represents the saturated liquid region while $x_m = 0$ corresponds to a solid region. The mass fraction of vapour in the liquid-vapour mushy zone is not presented in figures (5.6) and (5.7). Moreover, the solid-liquid mushy zone is limited by $0 \leq x_m \leq 1$. The depth of the mushy zone is low in the early heating period and extends in the radial direction. The size of

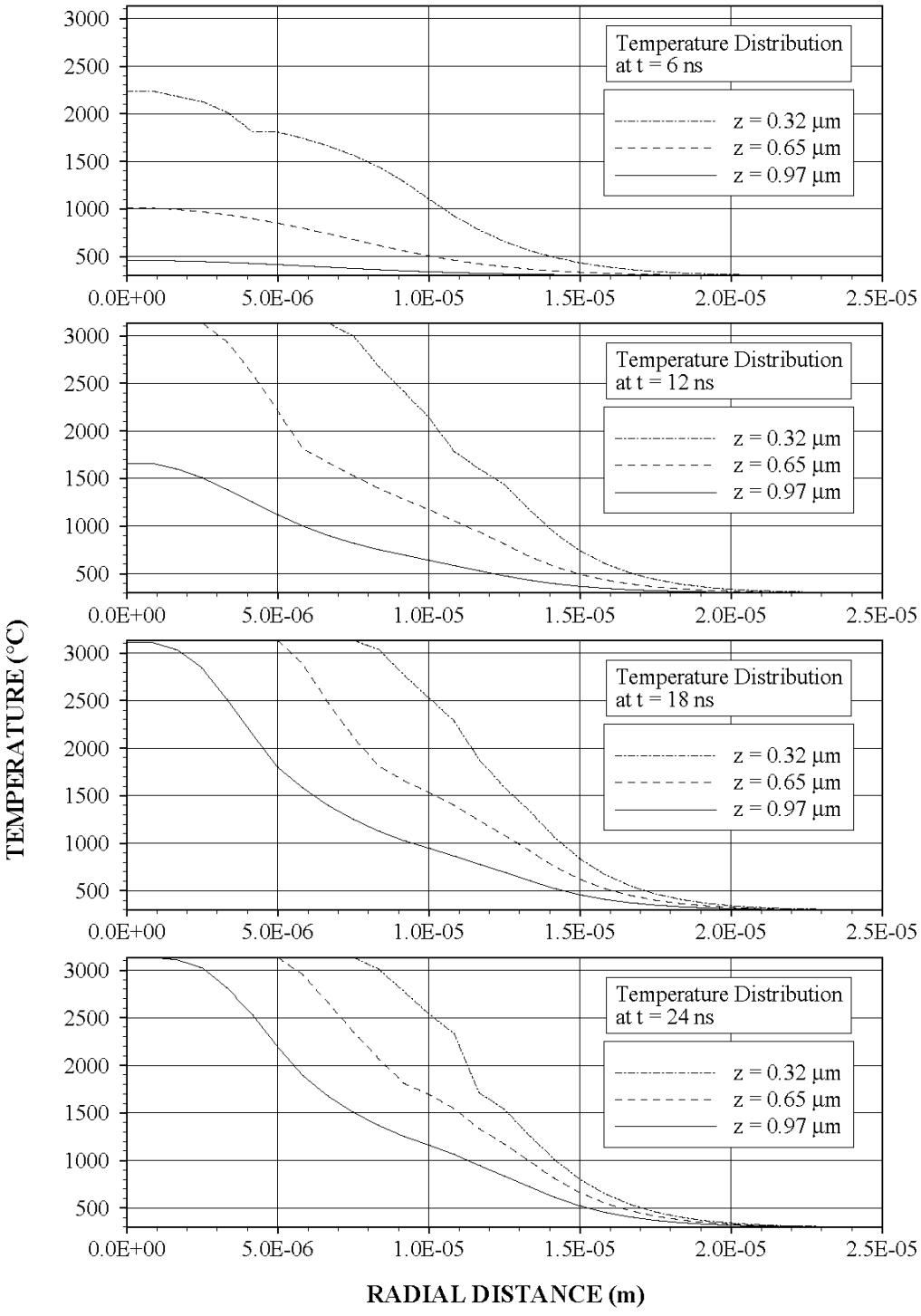

Figure 5.4a - Temperature variation along the radial distance for different axial locations and heating durations.

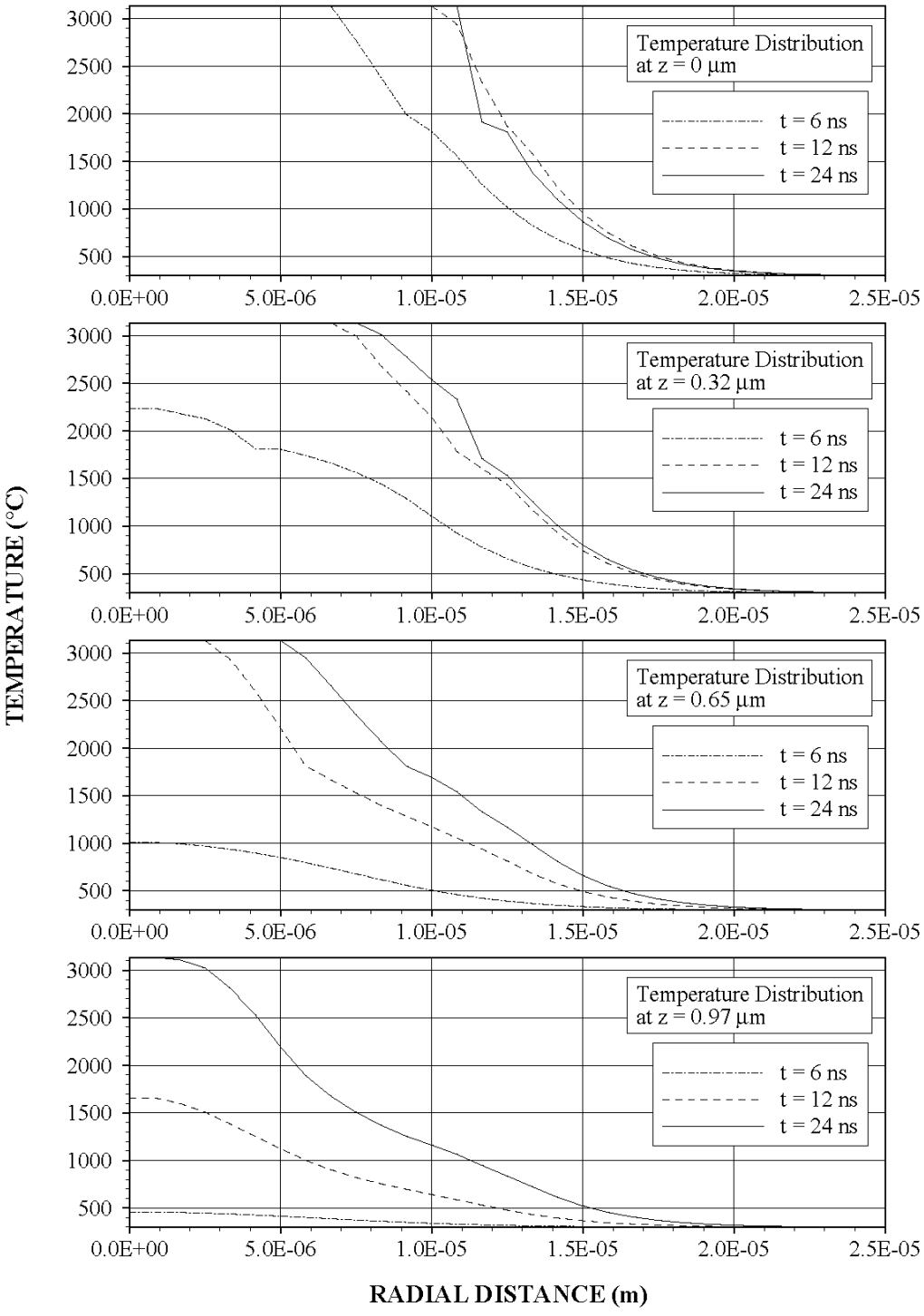

Figure 5.4b - Temperature variation along the radial distance for different axial locations and heating durations.

mushy zone is higher towards the edge of the melt zone in the radial direction than that corresponding to the axial direction at the centre of the irradiated region. This is because of the high magnitude of axial temperature gradient at the centre of the irradiated region. Consequently high temperature gradient in the liquid zone enhances the rate of energy transport by conduction to the solid-liquid mushy zone. In this case, the size of mushy zone reduces while the size of liquid region extends. This enhances the cavity formation in the axial direction. As the heating period increases, the size of solid-liquid mushy zone increases slightly. However, this increase is not significant. This indicates that the rate of energy transfer to solid-liquid mushy zone from the liquid region is almost the same as the rate of energy diffused from the mushy zone to solid substrate. This is more pronounced at long heating periods (t = 24 ns). The solid-liquid mushy zone variation in the radial direction (figure (5.7)) shows that in the early heating period (t = 6 ns), the size of the mushy zone is larger than that corresponding to the other heating periods, particularly in the surface region. As the heating period increases, the depth of mushy zone becomes considerably small; in which case, x_m decays sharply in a short distance next to the liquid region. This may be explained through the amount of energy absorption from the irradiated field. In the early heating period, the depth of liquid region is less and the absorbed energy is considerable across the mushy zone. This enhances the solid phase turning into a mushy zone at solid-liquid interface. It should be noted that energy absorbed from the irradiated field varies exponentially along the depth in the axial direction (Lambert's law). Consequently large amount of energy is absorbed from the irradiated fields in the surface vicinity of the substrate material than in the region next to

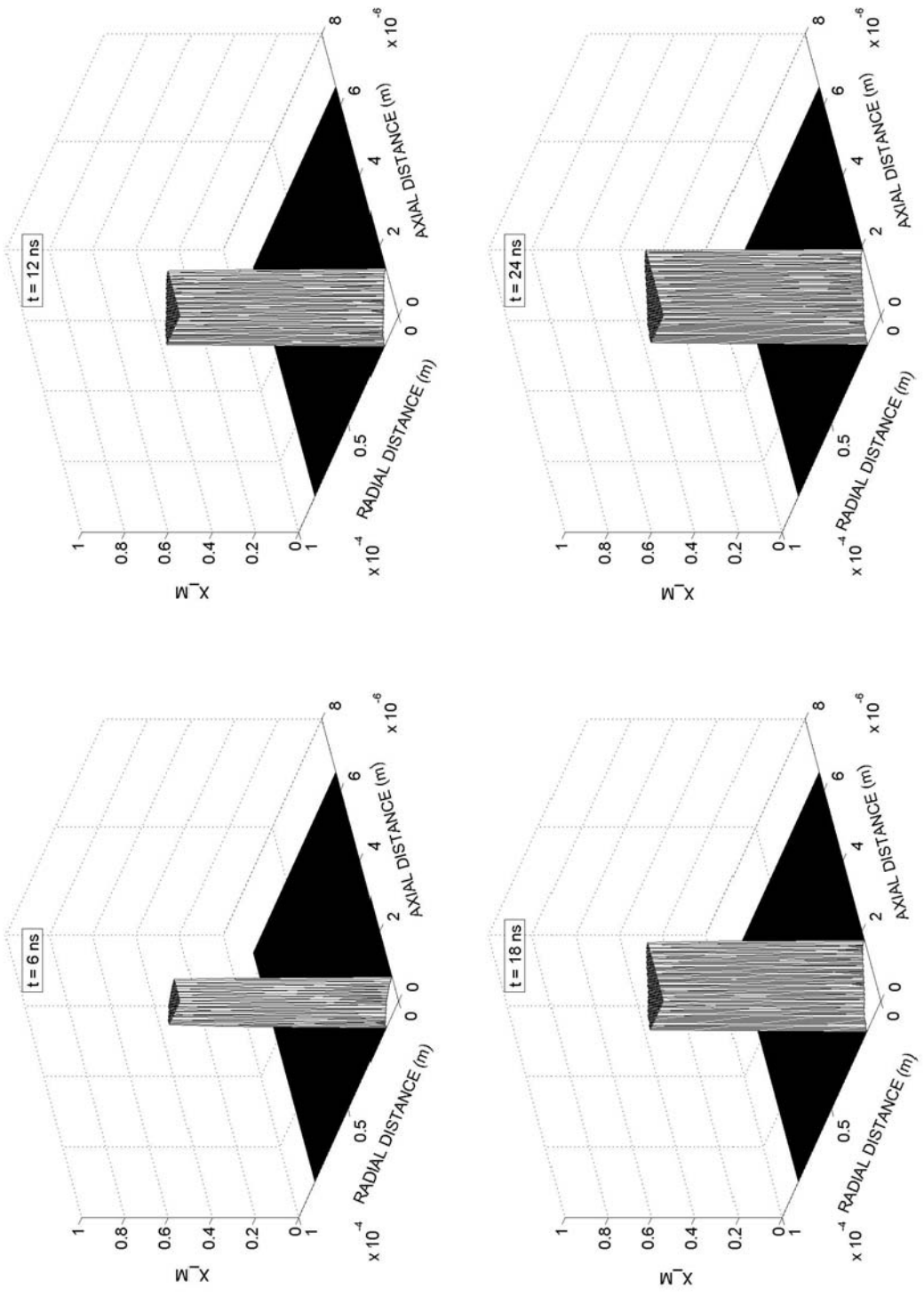

Figure 5.5 - Three-dimensional view of Solid-Liquid interface inside the substrate material for three heating durations.

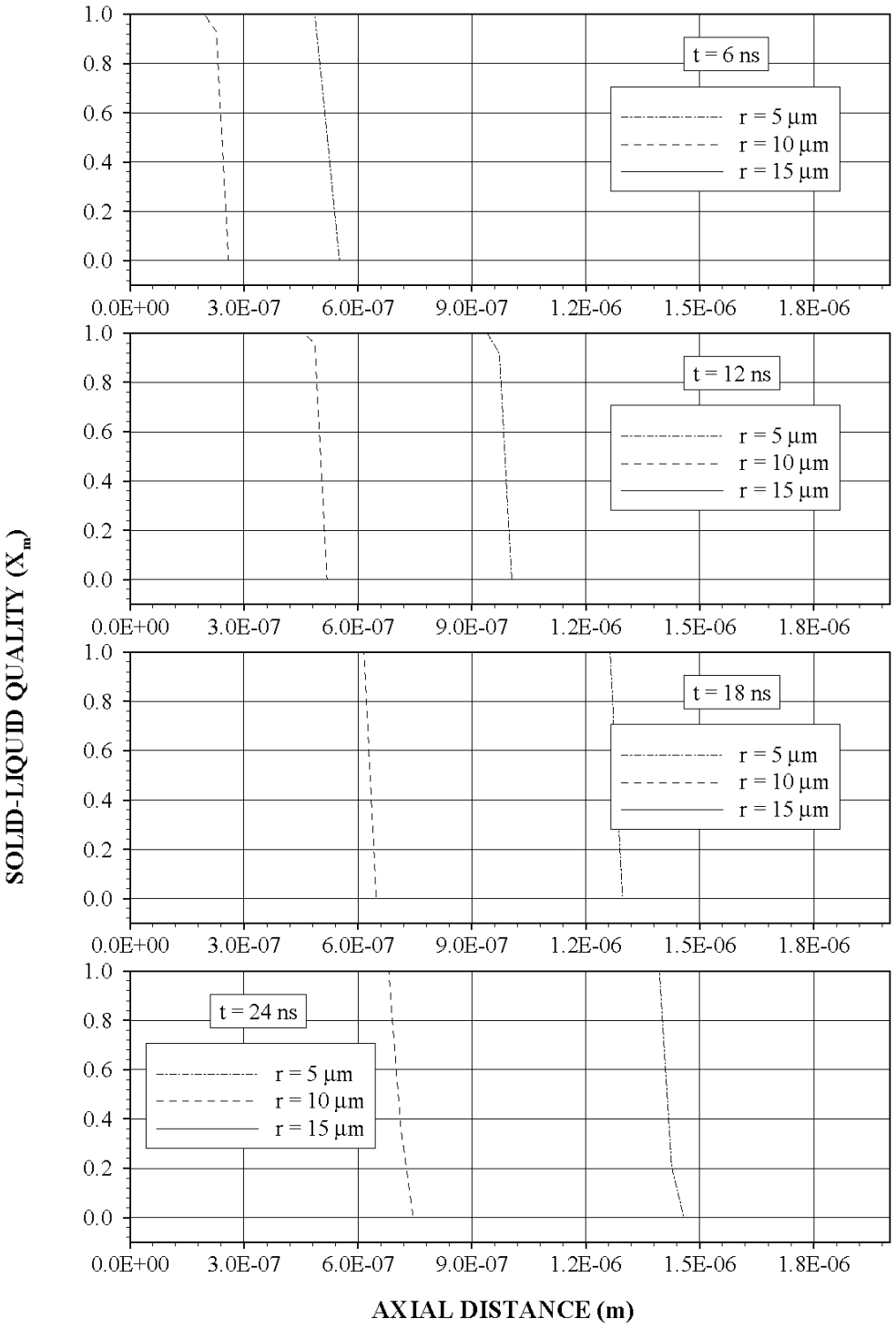

Figure 5.6a - Solid-Liquid Quality (x_m) variation along the axial distance for different radial locations and heating durations.

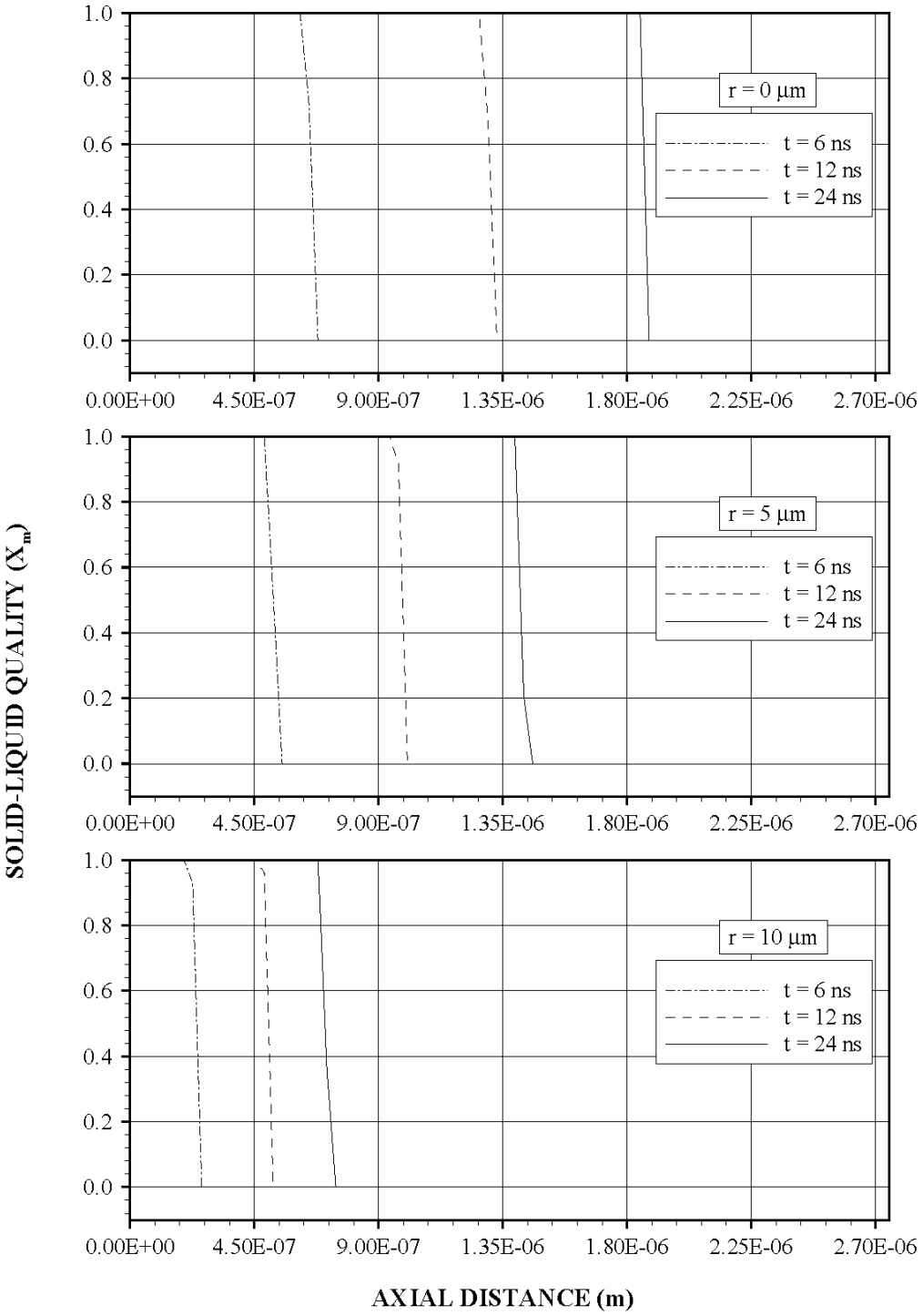

Figure 5.6b - Solid-Liquid Quality (x_m) variation along the axial distance for different radial locations and heating durations.

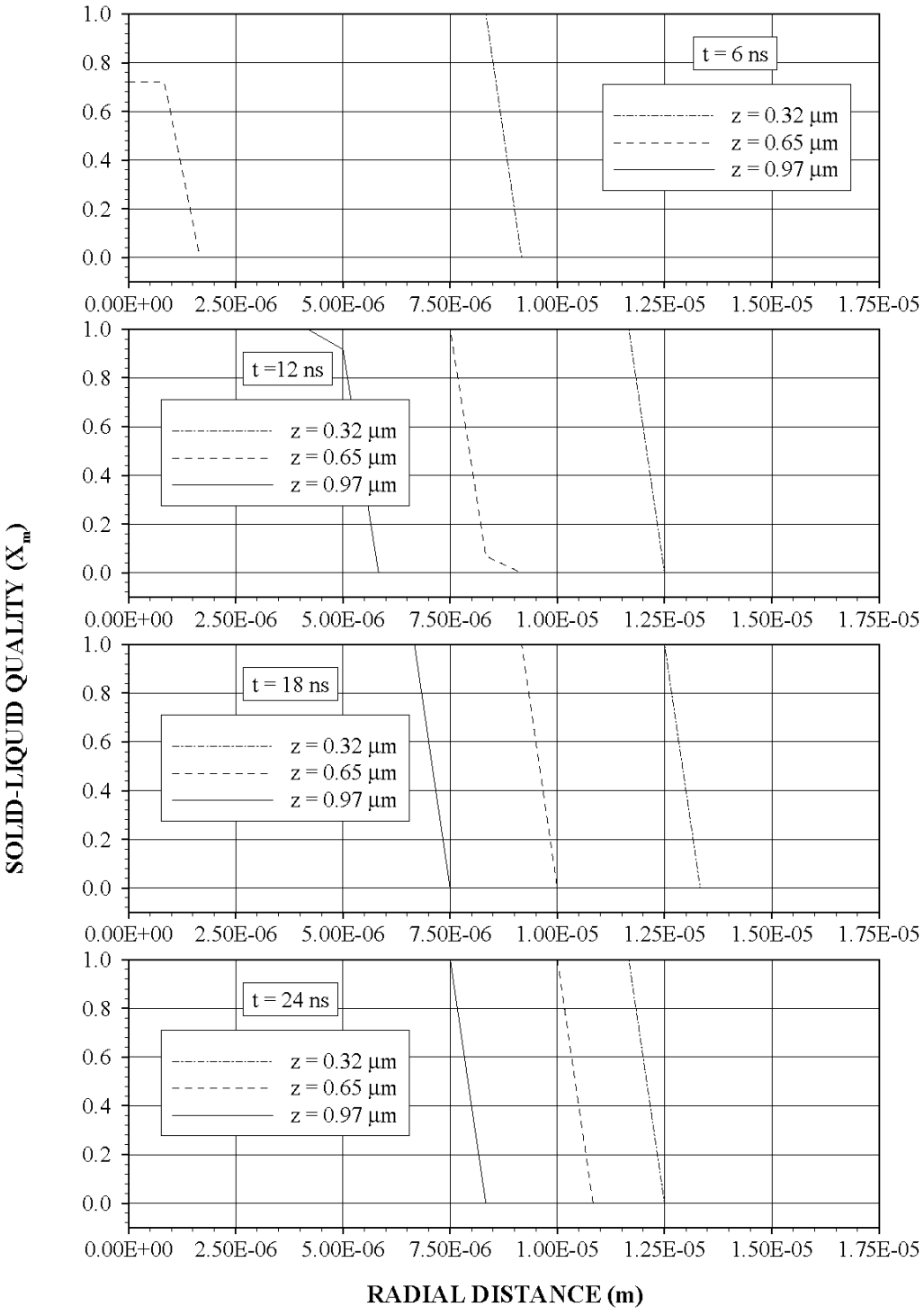

Figure 5.7a - Solid-Liquid Quality (x_m) variation along the radial distance for different axial locations and heating durations.

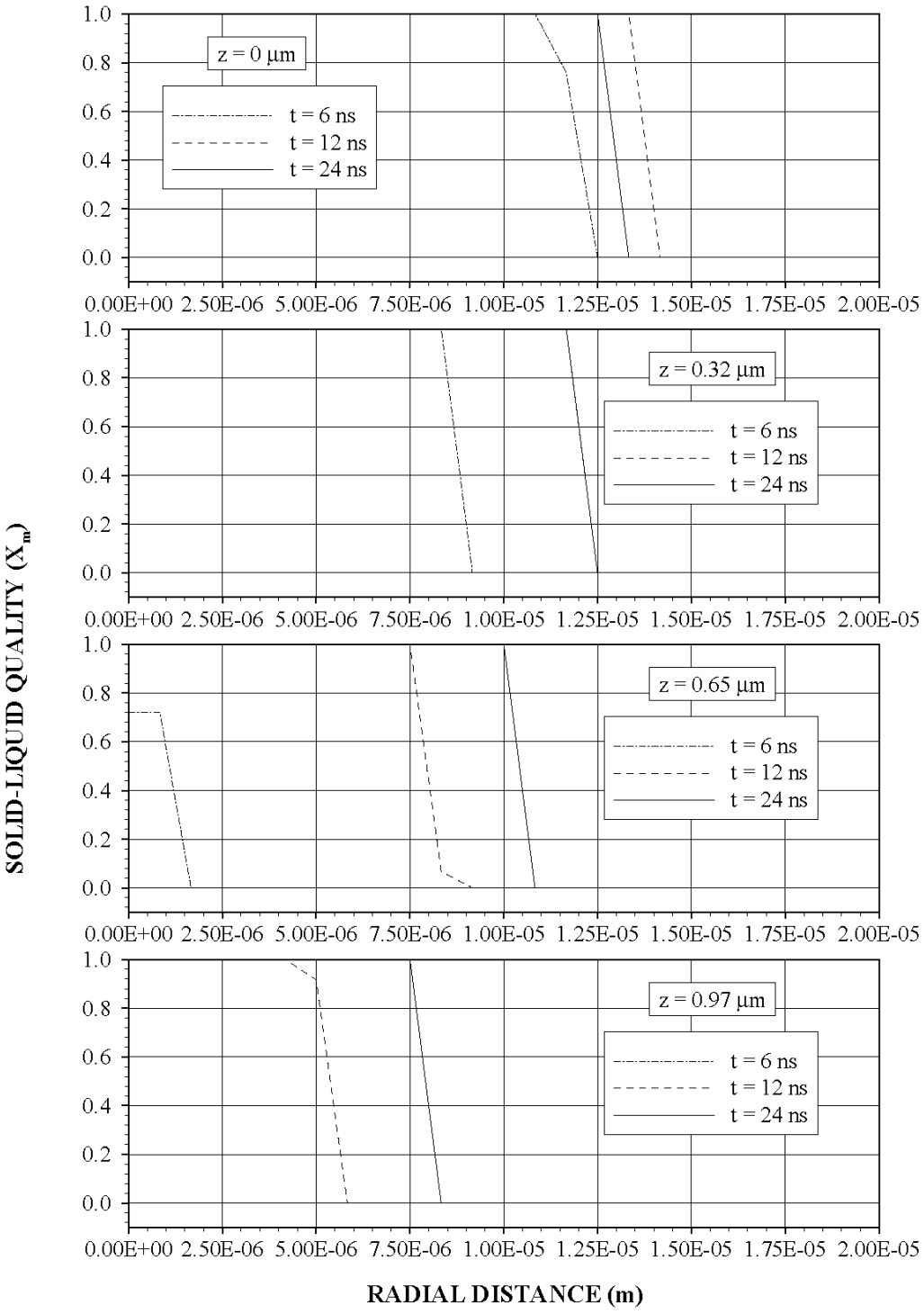

Figure 5.7b - Solid-Liquid Quality (x_m) variation along the radial distance for different axial locations and heating durations.

the surface vicinity. As the heating period progresses, liquid layer thickness becomes large and the large amount of energy is absorbed in this region resulting in rapid rise of liquid region depth. This in turn suppresses energy gain from the irradiated field enhancing the solid-liquid mushy zone size. In the case of figure (5.7), in which radial distribution of x_m is shown for different heating periods. The gradient of x_m, (dx_m/dr) is low in the early heating period as the heating period increases, it becomes high, particularly in the surface region. As the depth below the surface increases (z = 0.97 μm), (dx_m/dr) remains low upto t = 12 ns and beyond this time it attains high values and remains the same with progressing time.

Figure (5.8) shows three-dimensional plot of mass fraction of vapour (x_b) in the vapour-liquid mushy zone for different heating periods while figures (5.9a & 5.9b) and (5.10a & 5.10b) show variation of x_b along axial and radial direction for different heating periods. The behaviour of x_b in the radial direction is similar to that corresponding to x_m, provided that the location of x_m and x_b isotherms differs. It should be noted that $x_b = 1$ represents the surface of the cavity. Moreover, in the analysis, the surface at $x_b = 1$ varies with time. Consequently, the free surface of the workpiece is moved to the surface where $x_b = 1$ and the lower power intensity at the free surface of the workpiece is adjusted accordingly. $x_b = 0$ represents the liquid surface under the liquid-vapour mushy zone in the substrate material. Although the maximum energy absorbed from the irradiated field takes place at the free surface of the workpiece, the rate of evaporation is limited because of the high value of latent heat of evaporation. Since, the laser pulse intensity varies with time during the heating process (figure (5.1)), the rate of evaporation and, the depth of the cavity vary

with time. However, as the heating period progresses, the progression of the cavity depth and the thickness of the liquid-mushy becomes steady.

Figure (5.11a) shows the cavity shape obtained from predictions and the experiment while figure (5.11b) shows SEM micrograph of the cavity cross section. It can be observed that the cavity profile predicted from the model agrees well with the experimental data.

Figure (5.12) shows temporal variation of temperature at different at depths below the surface and two radial locations. Temperature at the surface rises rapidly to reach melting and evaporation temperatures. Moreover, the rate of temperature rise at some depth below the surface is lower than that of the surface. This is because of the amount of laser power absorbed by the substrate material, which is highest in the surface vicinity (Lambert's law). Temperature remains the same during the melting process. However, duration of constant temperature increases slightly as the depth below the surface increases. This is more pronounced at radial location $r = \frac{r_o}{2}$. This is because of the spatial distribution of the laser power intensity at the workpiece surface, which is Gaussian, i.e. as radial distance from the symmetry axis increases, the power intensity reduces. The low duration of constant temperature during melting at large depths below the surface suggests that less energy is absorbed from the irradiated field in this region. Consequently, less rate of energy available for melting is responsible for slow melting process at some depth below the surface. Moreover, the rate of rise of temperature in the

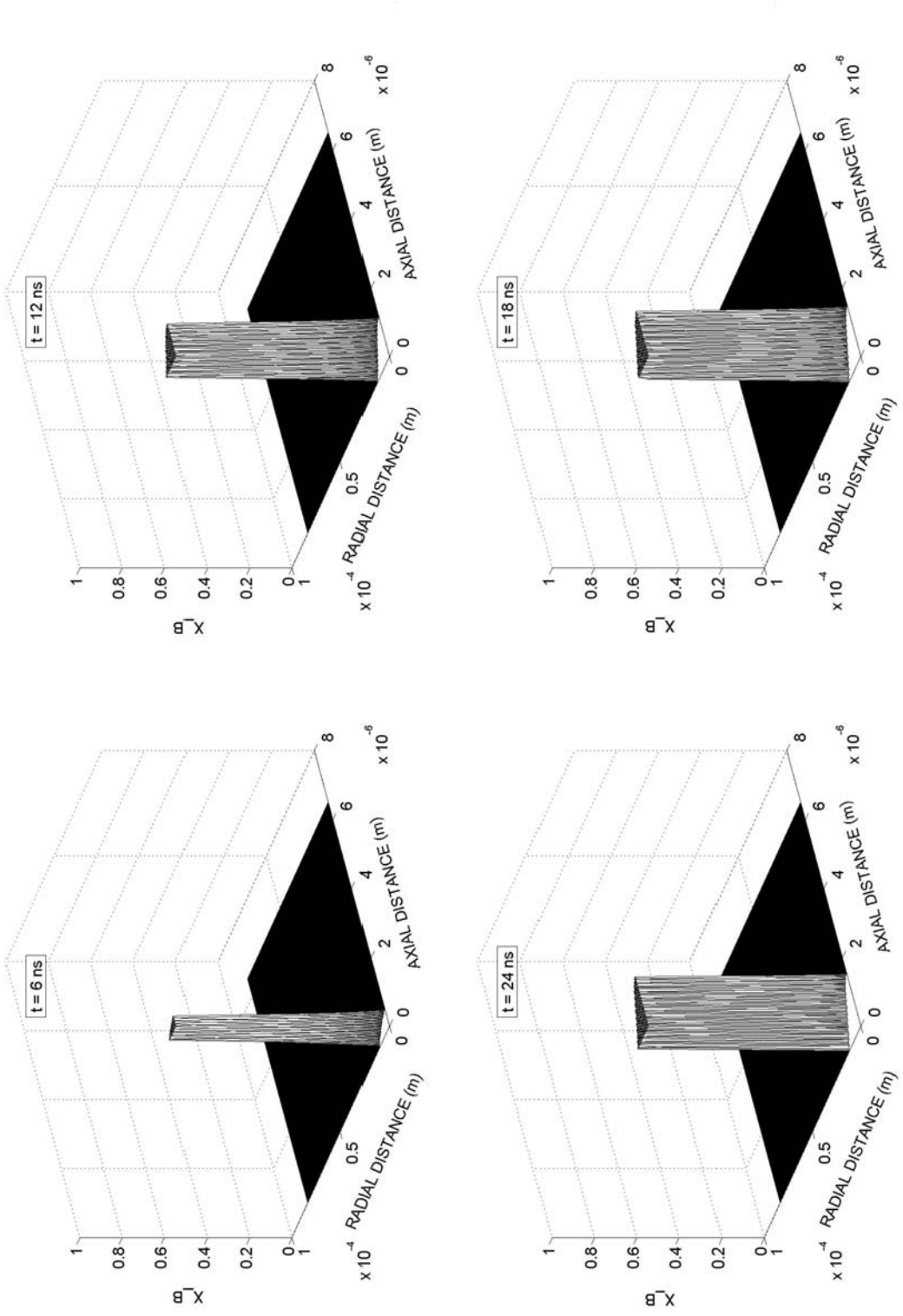

Figure 5.8 - Three-dimensional view of Liquid-Vapour interface inside the substrate material for three heating durations.

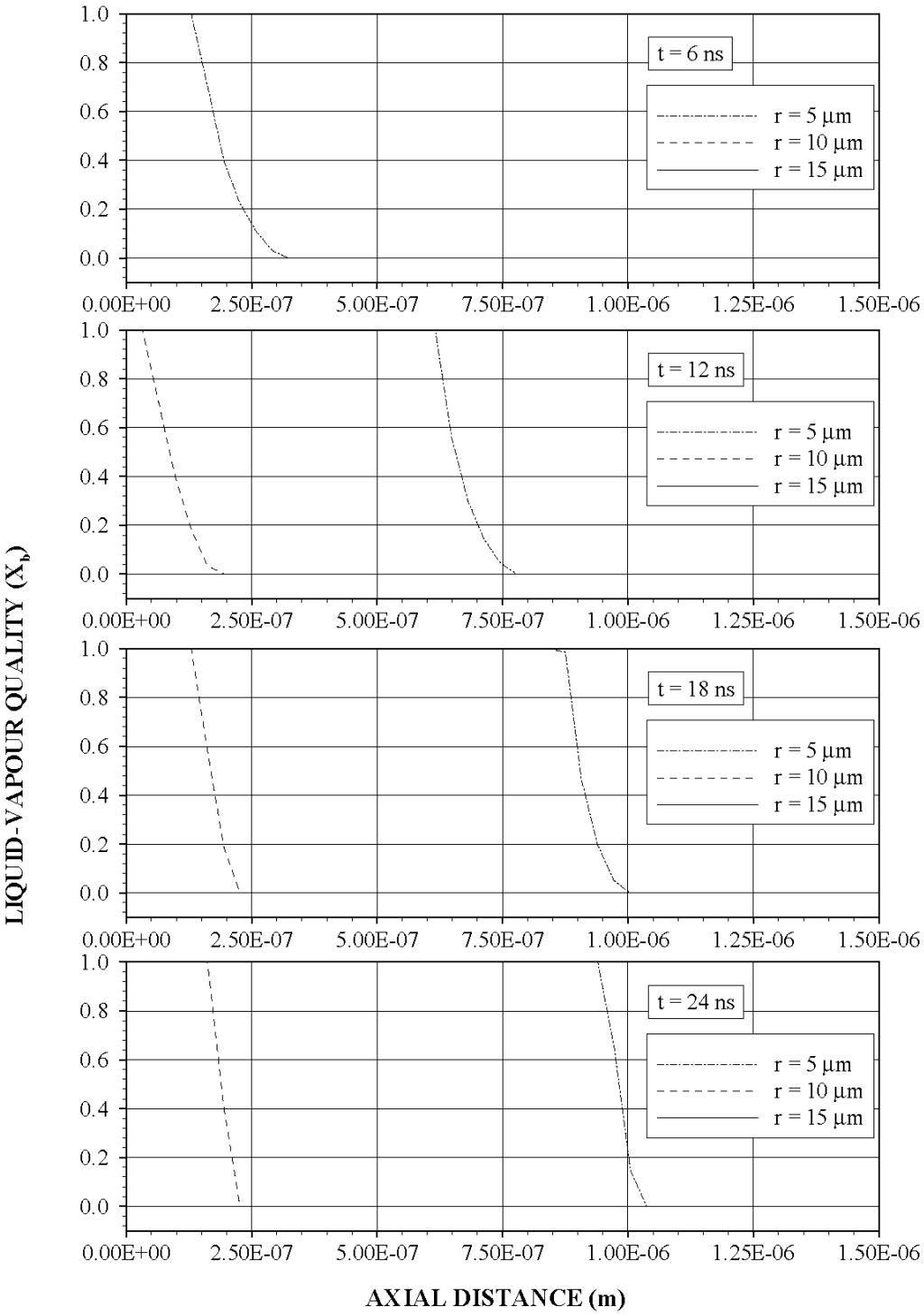

Figure 5.9a - Liquid-Vapour Quality (x_b) variation along the axial distance for different radial locations and heating durations.

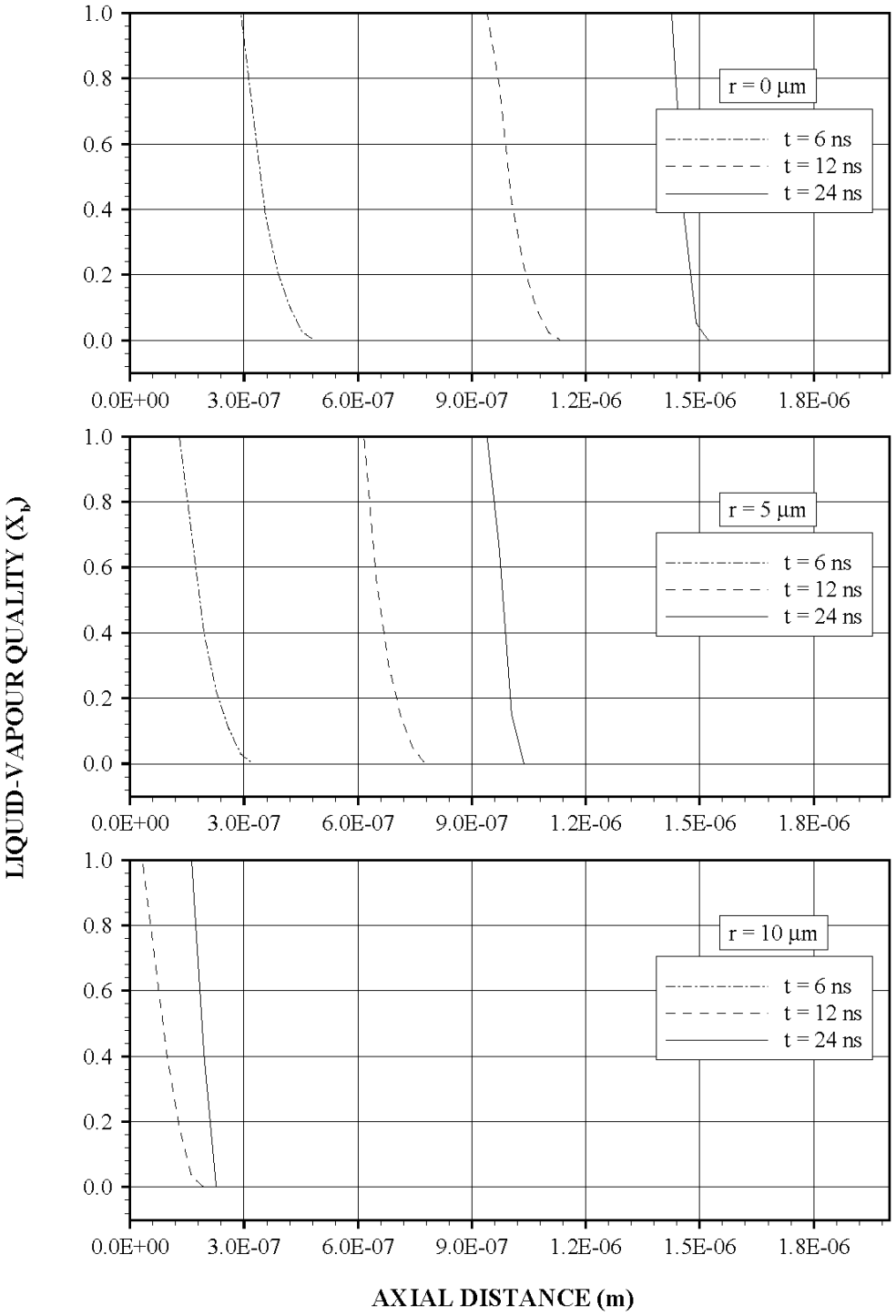

Figure 5.9b - Liquid-Vapour Quality (x_b) variation along the axial distance for different radial locations and heating durations.

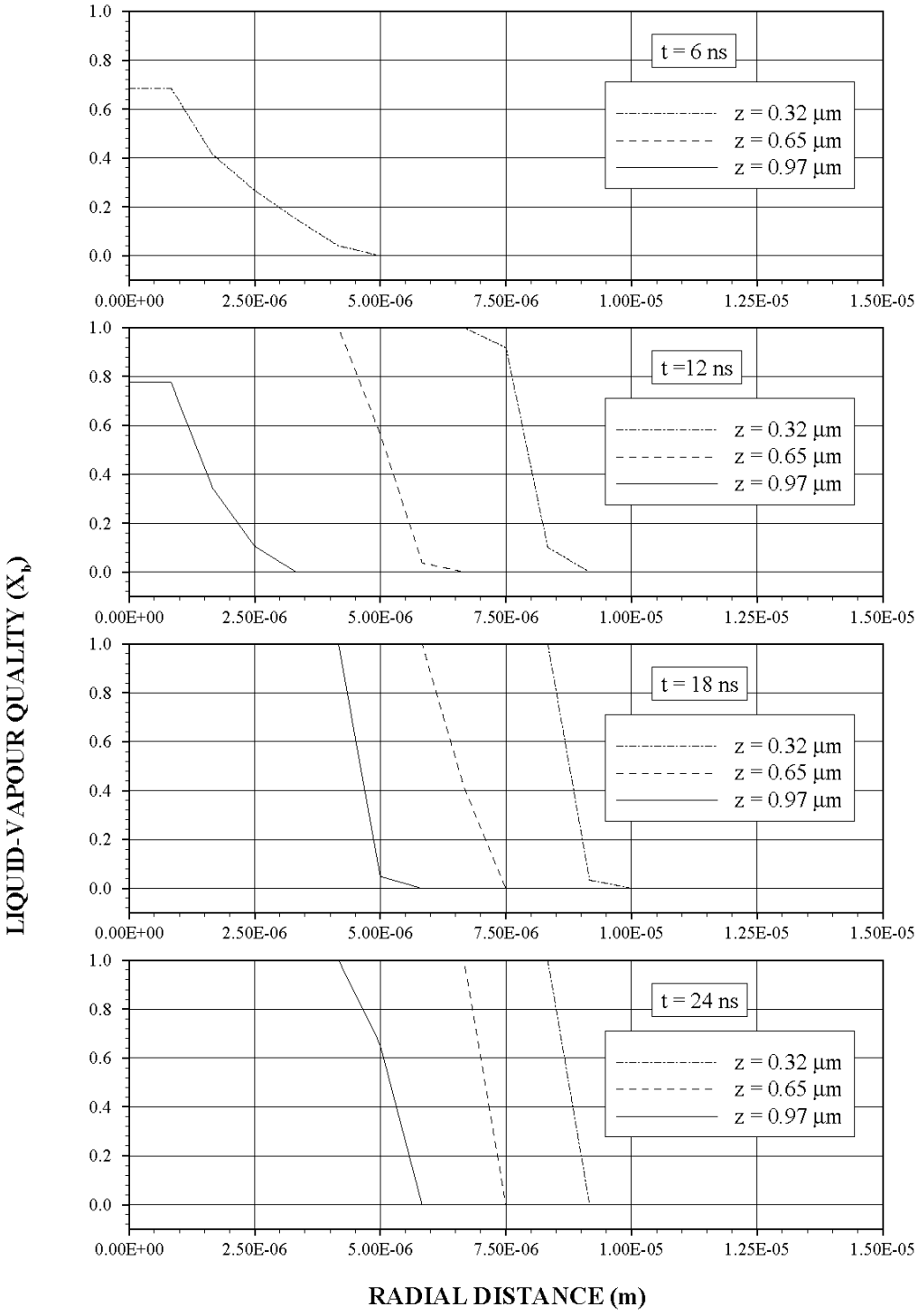

Figure 5.10a - Liquid-Vapour Quality (x_b) variation along the radial distance for different axial locations and heating durations.

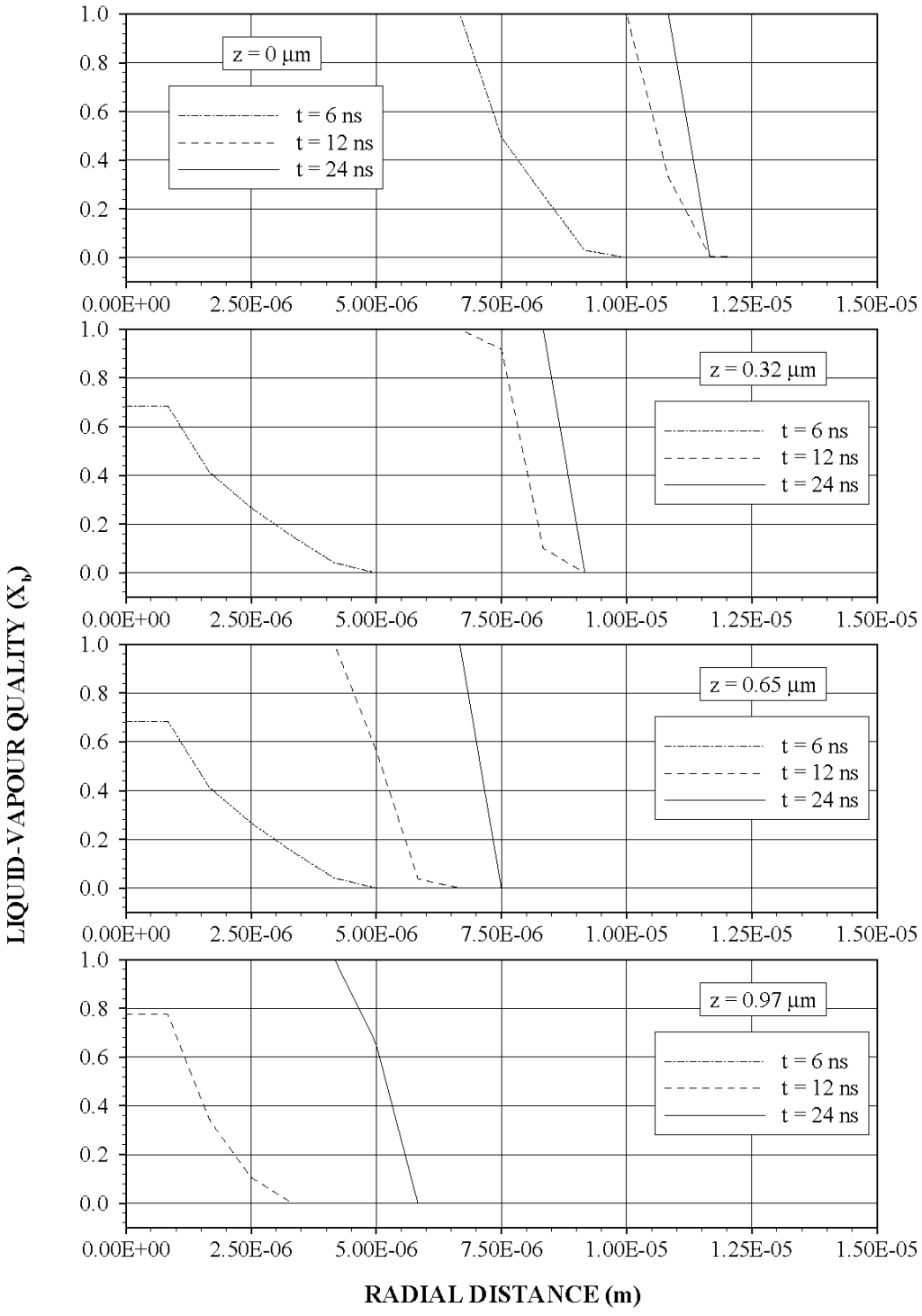

Figure 5.10b - Liquid-Vapour Quality (x_b) variation along the radial distance for different axial locations and heating durations.

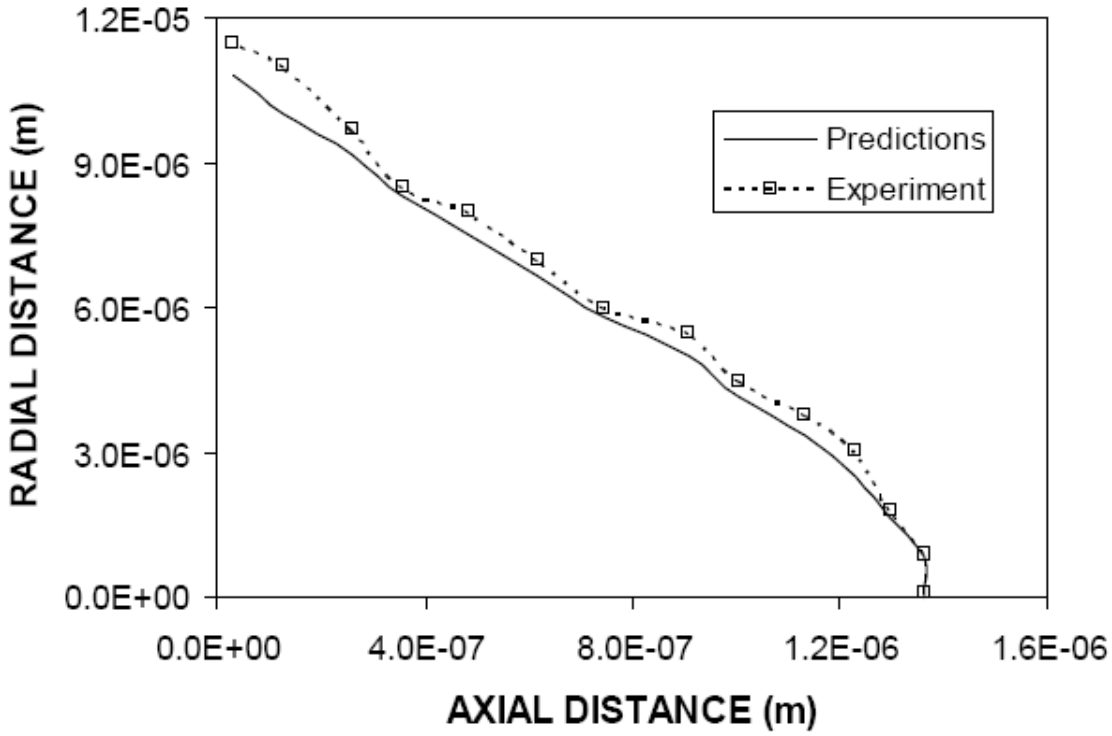

Fig 5.11a - Cavity shape predicted from the experiment and obtained from the experiment for a single pulse irradiation.

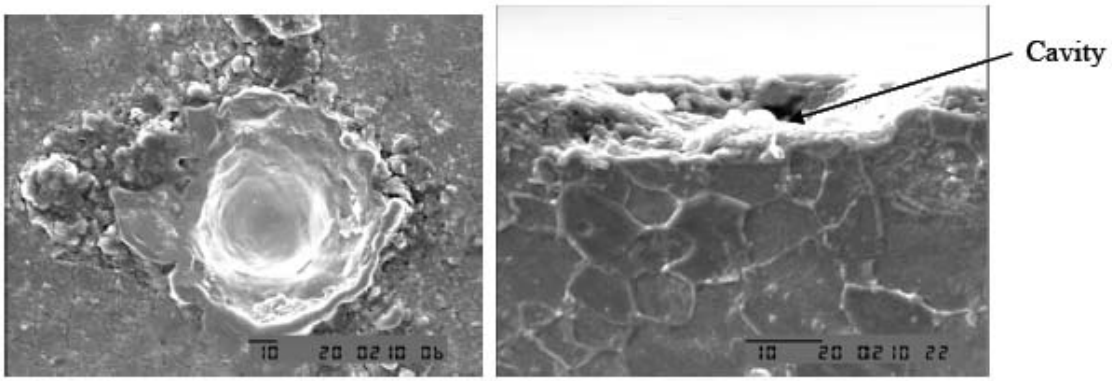

Fig 5.11b - SEM micrograph of laser formed cavity for a single pulse laser irradiation.

melting region (before initiation of melting) is less than that corresponding to immediately after the completion of the melting. This indicates that although the location of melting point is the same inside the substrate material, the low temperature gradient in the melting region suppresses the diffusional energy transport in this region before melting. Once the melting is completed the temperature gradient increases and the contribution of diffusional energy transport enhances the rise of temperature in this region.

Figure (5.13) shows three-dimensional view of laser produced cavity inside the substrate material for different heating periods while Figure (5.14) shows the cross-sectional view of the cavity formed at different heating periods, i.e. the liquid-vapor and solid-liquid mushy zones as well as liquid and solid zones are shown. The cavity surface extends almost steadily in space and cavity size gradually increases after 19.5 ns, then it remains almost the same with progressing time. This is because of the laser beam energy which reduces gradually with time after 20 ns of the heating duration (figure (5.1)). In the case of figure (5.14), the mushy zone at liquid-vapor interface is thicker than the mushy zone at solid-liquid interface for all heating periods. This is because of the latent heat of evaporation, which is considerably higher than the latent heat of fusion (Table 5.1). Moreover, the liquid layer thickness remains almost uniform along the radial direction in the early heating period (t = 6.54 ns). As the heating period progresses, the liquid layer thickness becomes large towards the edge of the cavity in the radial direction, particularly when the heating period corresponds to the high power intensity ($10.92 \text{ ns} \le t \le 15.23 \text{ ns}$). In this case, high power intensity in the region of the

symmetry axis enhances the evaporation rate and the liquid phase evaporates at a high rate reducing the liquid layer thickness in this region. Moreover, the thickness of the mushy zone at liquid-vapor interface reduces significantly as the heating period progresses. This indicates that the high intensity reduces the size of the mushy zone at liquid-vapor interface. It should be noted that the heating duration is short (few nanoseconds) and the liquid layer thickness is small (fraction of micrometer); therefore, liquid flow in the cavity can be neglected and the effects of liquid motion on the heat transfer characteristics should be negligible in the cavity.

Figure (5.15) shows temporal variation of liquid-vapour quality at different axial locations. The cavity shape corresponds to the liquid-vapour interface for a given heating duration, provided that the quality $x_b = 0$, i.e. liquid phase exists solely at interface. In the case of liquid-vapour quality (x_b), it changes sharply with progressing time in the surface region ($z = 0$ and $z = 9.72 \times 10^{-9}$ m). The rapid change in (x_b) in the early heating period is associated with the laser output beam power, which rises rapidly at the surface and as the depth from the surface increases to the absorption depth $\left(z = \frac{1}{\delta}\right)$, the amount of laser irradiated power being absorbed by the substrate material reduces significantly. The absorption of beam power in the substrate material reduces exponentially with increasing depth from the surface (Lambert's law). Consequently, less absorbed energy gives rise to less energy available for the phase change process. This, in turn, enhances the depth of the mushy zone and lowers the rate of change of x_b with

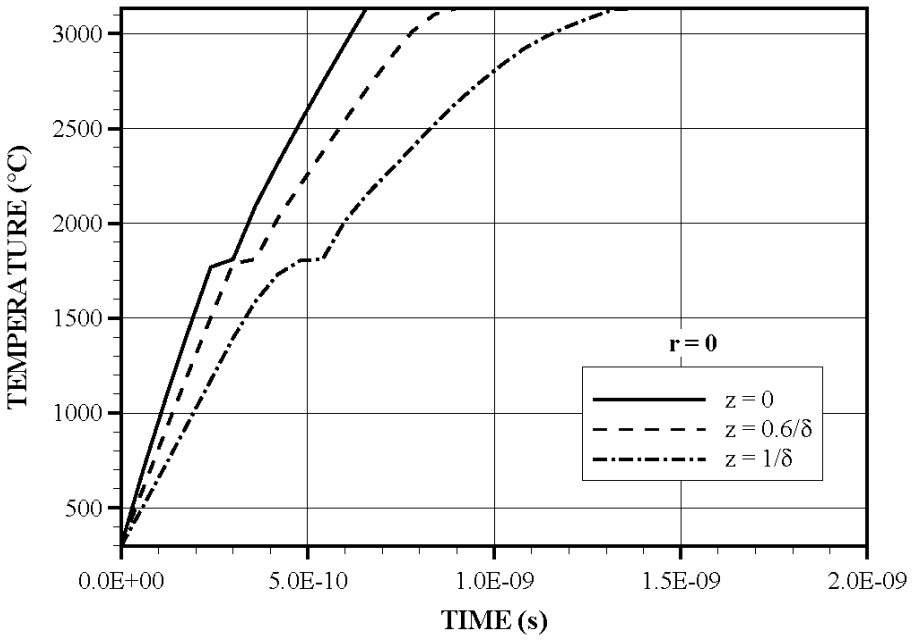

a) Radial location is at symmetry axis (r = 0).

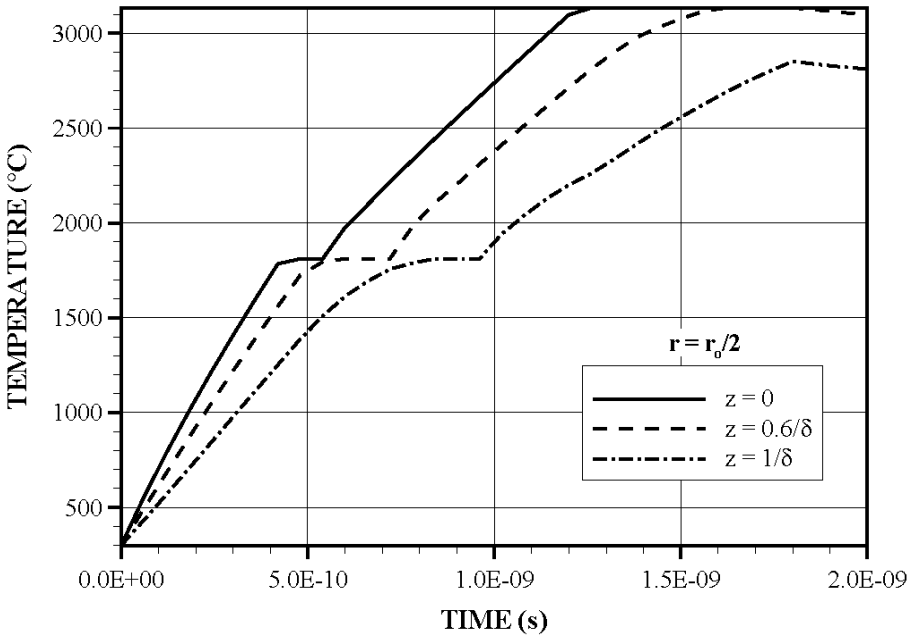

b) Radial location is at r = r_o/2.

Figure 5.12 - Temporal distribution of temperature at radial locations a) at symmetry axis and b) at r= r_o/2.

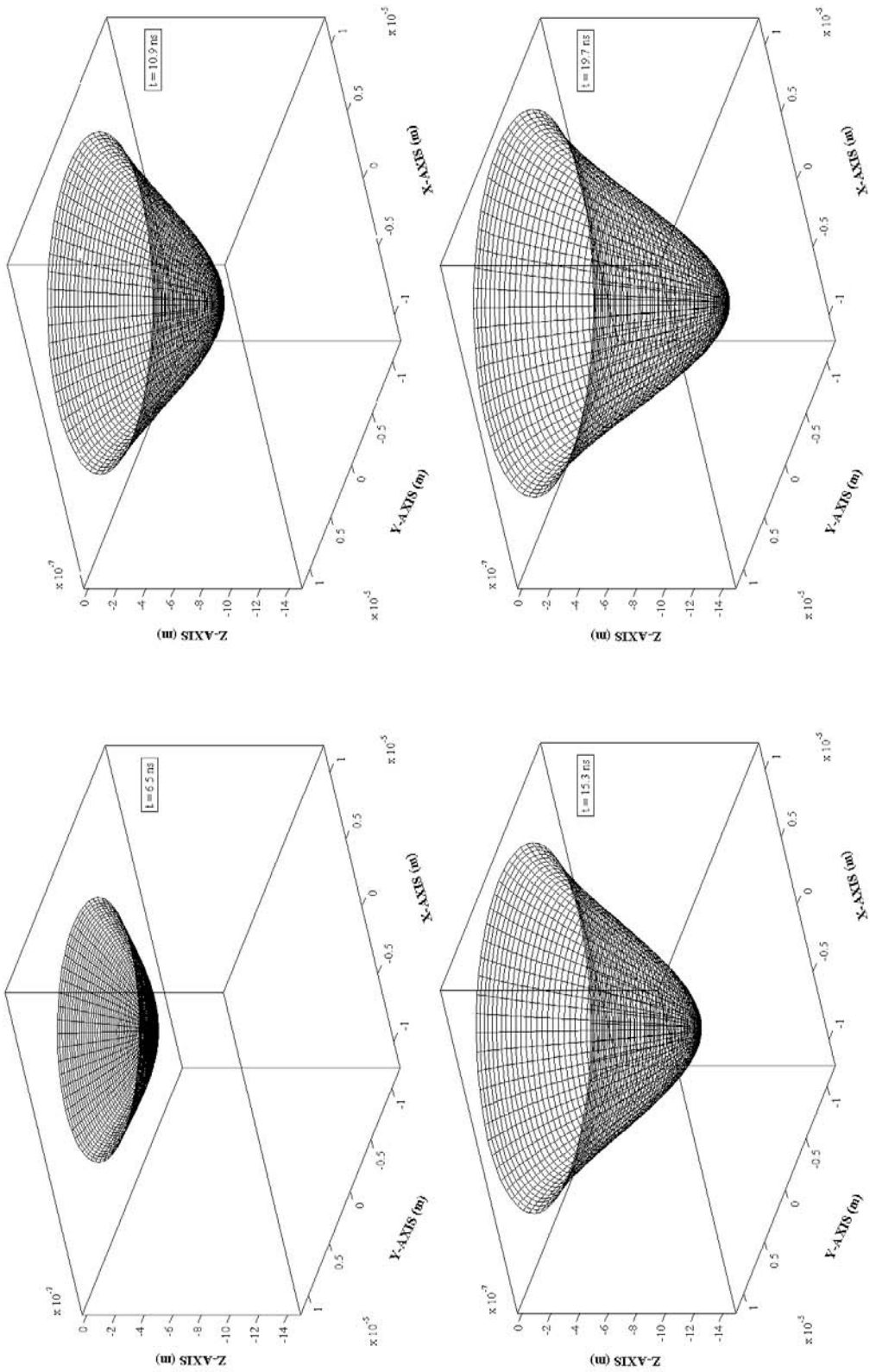

Figure 5.13 - Three-dimensional view of the cavity at different time durations.

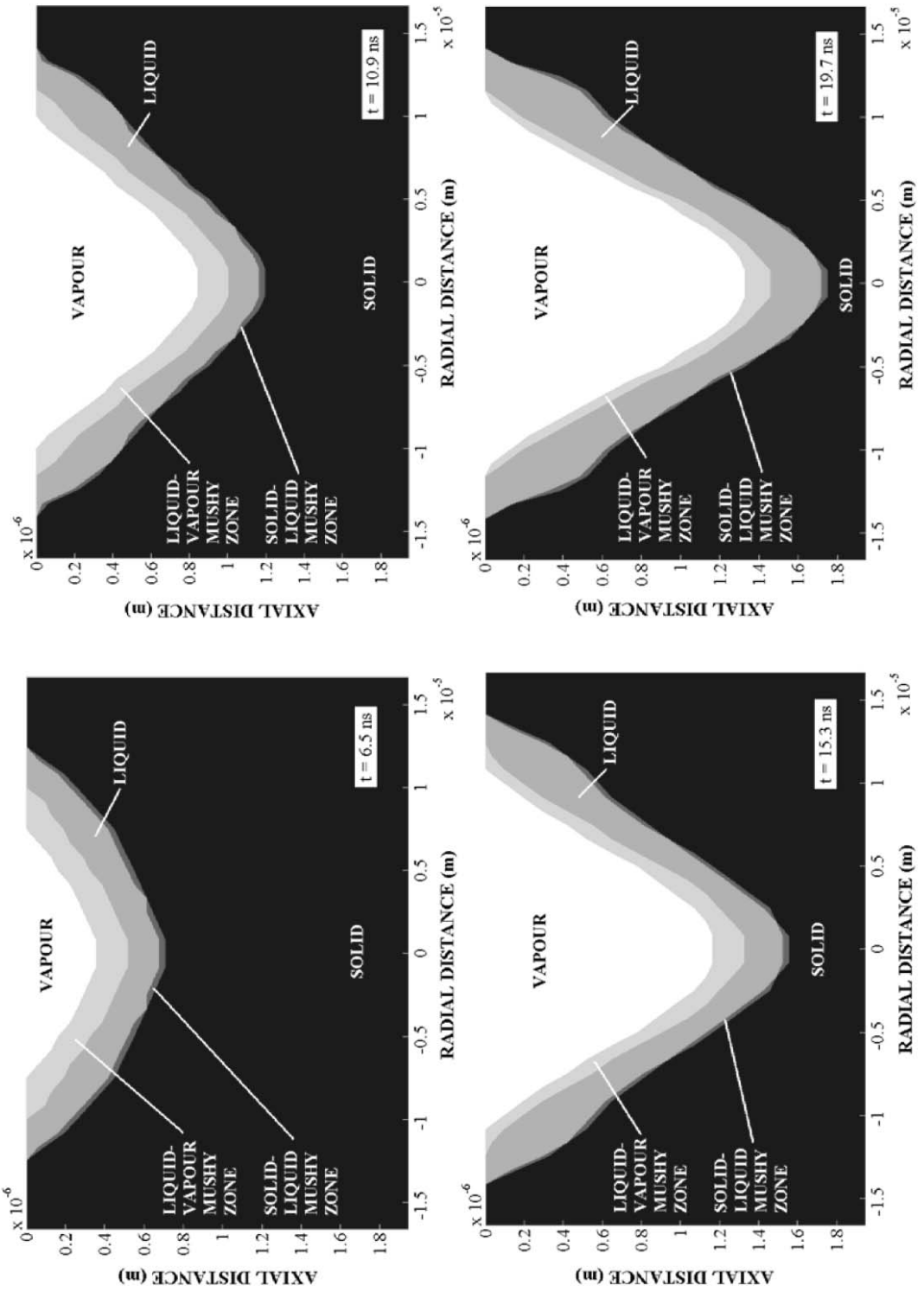

Figure 5.14 - Cross-sectional view of cavity for different heating periods.

progressing heating time. It should be noted that the energy gain at some depth below the surface is governed by the absorption of irradiated energy and diffusional energy transport due to temperature gradient in the surface region. Although energy gain by the absorption of irradiated energy reduces at a depth $z = \frac{1}{\delta}$, the diffusional energy transport from the surface region to the depth $z = \frac{1}{\delta}$ contributes the phase change process significantly. In this case, phase change process continues and depth of mushy zone at vapour-liquid interface extends towards the liquid zone. When the radial location changes from the symmetry axis to $\frac{r_o}{2}$ (r_o being the irradiated spot radius), the rise of liquid-vapour quality differs than that corresponding to symmetry axis. In this case, the rate of rise of the quality becomes small at $r = \frac{r_o}{2}$. The time shift for the rise of liquid-vapour quality at $r = \frac{r_o}{2}$ is due to time required for temperature to rise the boiling temperature in the liquid layer in the cavity.

Figure (5.16) shows the temporal variation of quality of solid-liquid (x_m) in the mushy zone at different axial locations in the substrate material and two radial locations. The rise of solid-liquid quality is rapid, particularly in the surface region along the symmetry axis where radial location is $r = 0$. The rapid rise of the quality is due to high rate of energy gain of the substrate material from the irradiated field in the surface region. Moreover, as the depth below the surface increases to absorption depth, the quality rises rapidly with progressing time. This suggests that energy transport by conduction is high along the symmetry axis resulting in considerably high rate of energy transferring to this region from the surface vicinity. The rate of solid-liquid quality rise is almost the same at

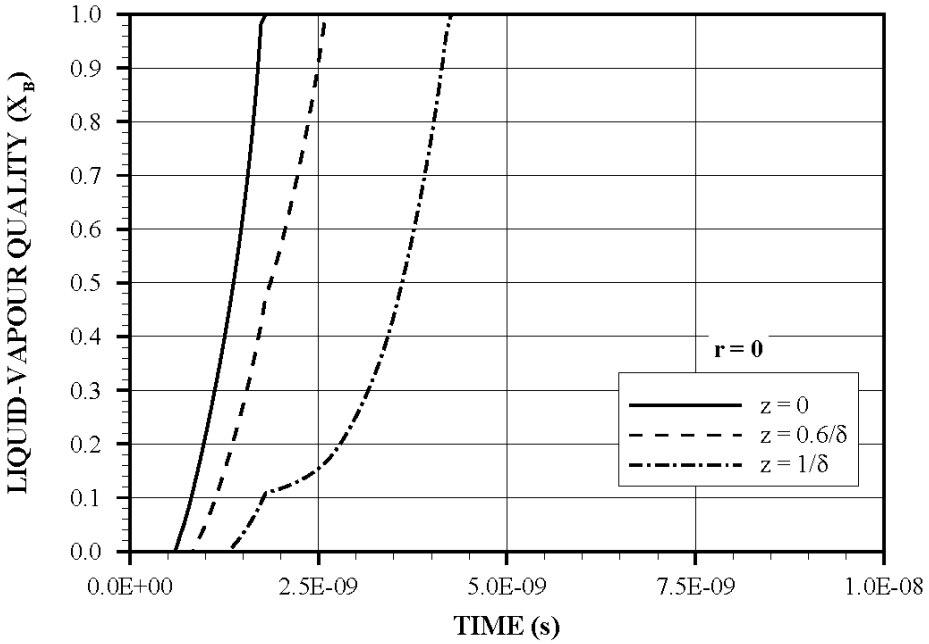

a) Radial location is at symmetry axis (r = 0).

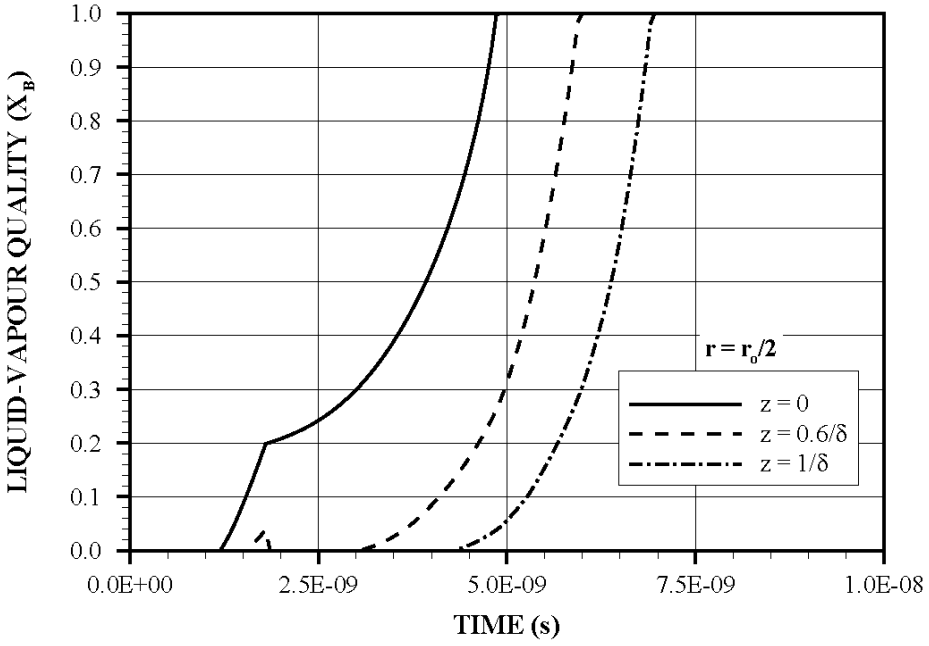

b) Radial location is at r = r_o/2.

Figure 5.15 - Temporal distribution of liquid-vapour quality (x_b) at radial locations a) at symmetry axis and b) at r = r_o/2.

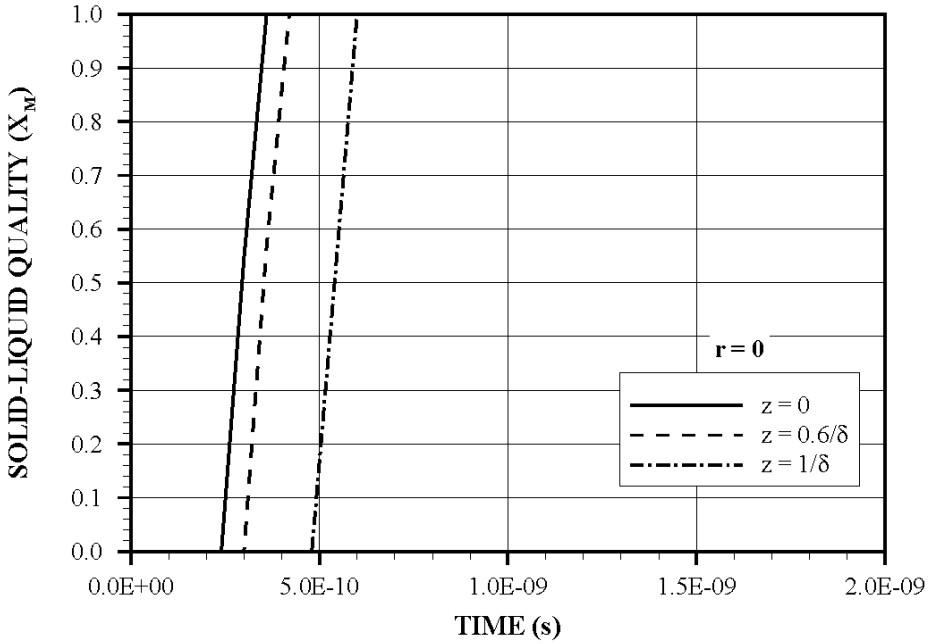

a) Radial location is at symmetry axis (r = 0).

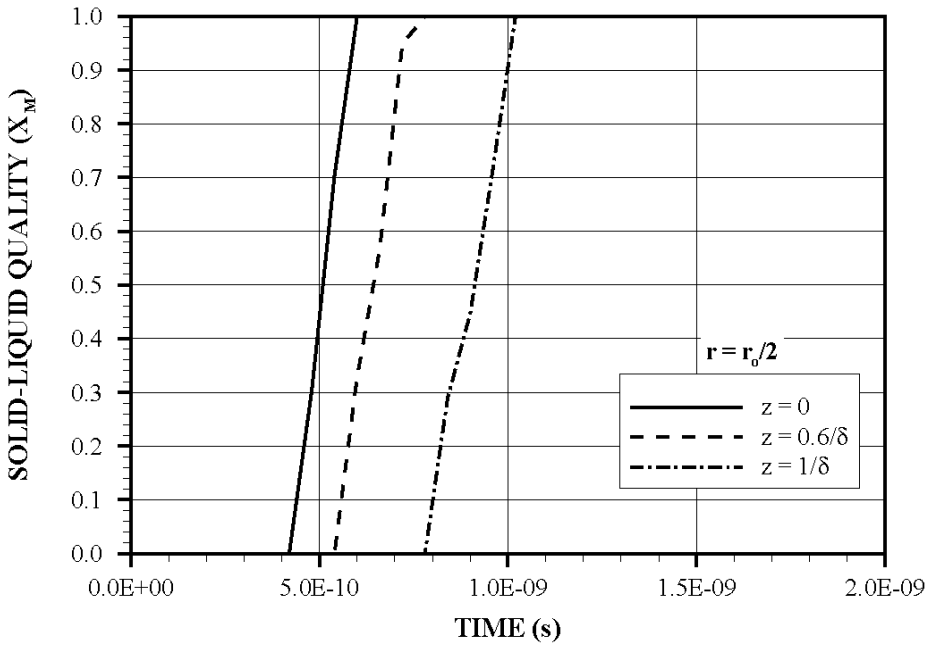

b) Radial location is at r = r_o/2.

Figure 5.16 - Temporal distribution of solid-liquid quality (x_m) at radial locations a) at symmetry axis and b) at r= r_o/2.

different depths below the surface, which suggests that high rate of energy transport, takes place via diffusion into the bulk of the substrate material. In the case of radial location at $r = \frac{r_o}{2}$, the solid-liquid quality behaves similar to that corresponding to the symmetry axis, provided that the rate of the rise of quality is smaller for $r = \frac{r_o}{2}$ than that of at the symmetry axis. This is because of the amount of energy absorbed by the substrate material at $r = \frac{r_o}{2}$, which is less than at the symmetry axis ($r = 0$) due to Gaussian distribution of the laser pulse intensity at the workpiece surface.

Figure (5.17) shows recession velocity of the surface in the radial direction for different heating periods. The solid surface of the workpiece is defined when the quality in solid-liquid mushy zone is zero; consequently, time variation of solid surface (recession of the solid surface) during the heating period defines the recession velocity of the solid surface. In the early heating period, recession velocity of the surface is high; however its size in the radial direction is small due to amount of melt during the early heating period which is less despite the fact that the rate of melting is high. As the time progresses, the size of melt in the radial direction extends and the recession velocity increases substantially. It should be noted that at 10.92 ns of the heating pulse, laser power intensity is high, which in turn results in high rate of energy gain of the substrate material via absorption from the irradiated field. Moreover, as the heating period progresses further ($t \geq 15.3\,\text{ns}$), the size of recessing surface in the radial direction increases; although, the recession velocity of the surface decreases. The enhancement of the size of the recessing surface in the radial direction is due to energy absorbed from the irradiated field (power intensity distribution

at the surface is Gaussian with the spot radius $r_o = 25$ μm) and the diffusional energy transport in the radial direction from symmetry axis to the edge of the heated spot. The attainment of low recession velocity at the surface for long heating period can be explained in terms of temporal variation of laser power intensity, which reduces considerably for heating periods $t \geq 15.3$ ns.

Figure (5.18) shows temporal variation of recession velocity of the evaporating surface at different locations in the radial direction. Temporal variation of recession velocity follows almost the temporal variation of the laser pulse, provided that the rise and decay rates of the recession velocity differ than that of the laser pulse. This is true for all radial locations. As the radial location increases to $r = \frac{r_o}{2}$, the decay rate of recession velocity differs than that of other radial locations for the heating periods of $t \geq 1.5 \times 10^{-8}$ s. This is because of the radial heat diffusion, which becomes less as the radial location from the irradiated spot centre increases, lowering the energy available for phase change in this region, i.e. the rate of solid surface recession becomes less.

Figure (5.11a) shows the cavity shapes predicted and obtained from the experiment while figure (5.19) shows the recession velocity of the evaporating surface predicted from the present study and the one-dimensional analytical solution [101]. The recession velocity predicted agrees with the one-dimensional closed form solutions, provided that some small discrepancies occur between both results. This can be explained in terms of the affects of the radial heat conduction and spatial distribution of the laser beam intensity,

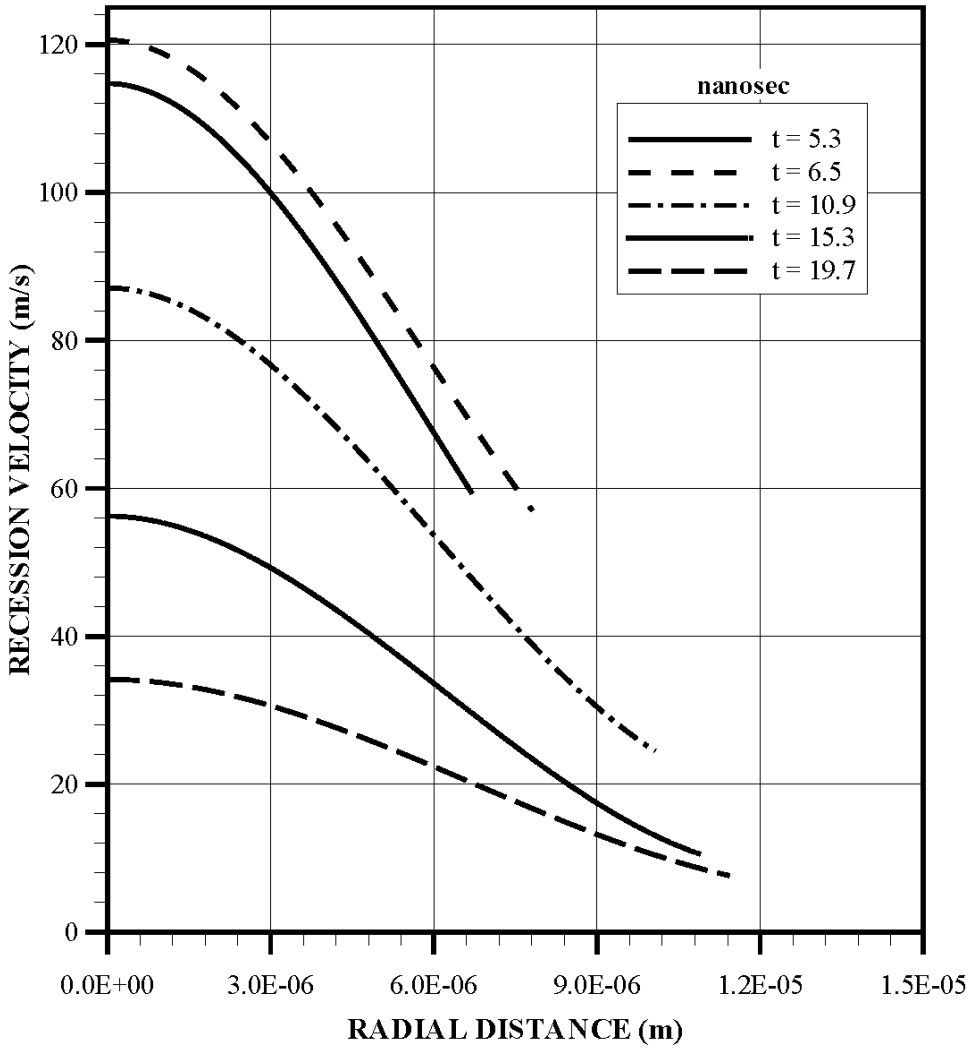

Figure 5.17a - Recession velocity of liquid-vapour interface along the radial distance at different time durations.

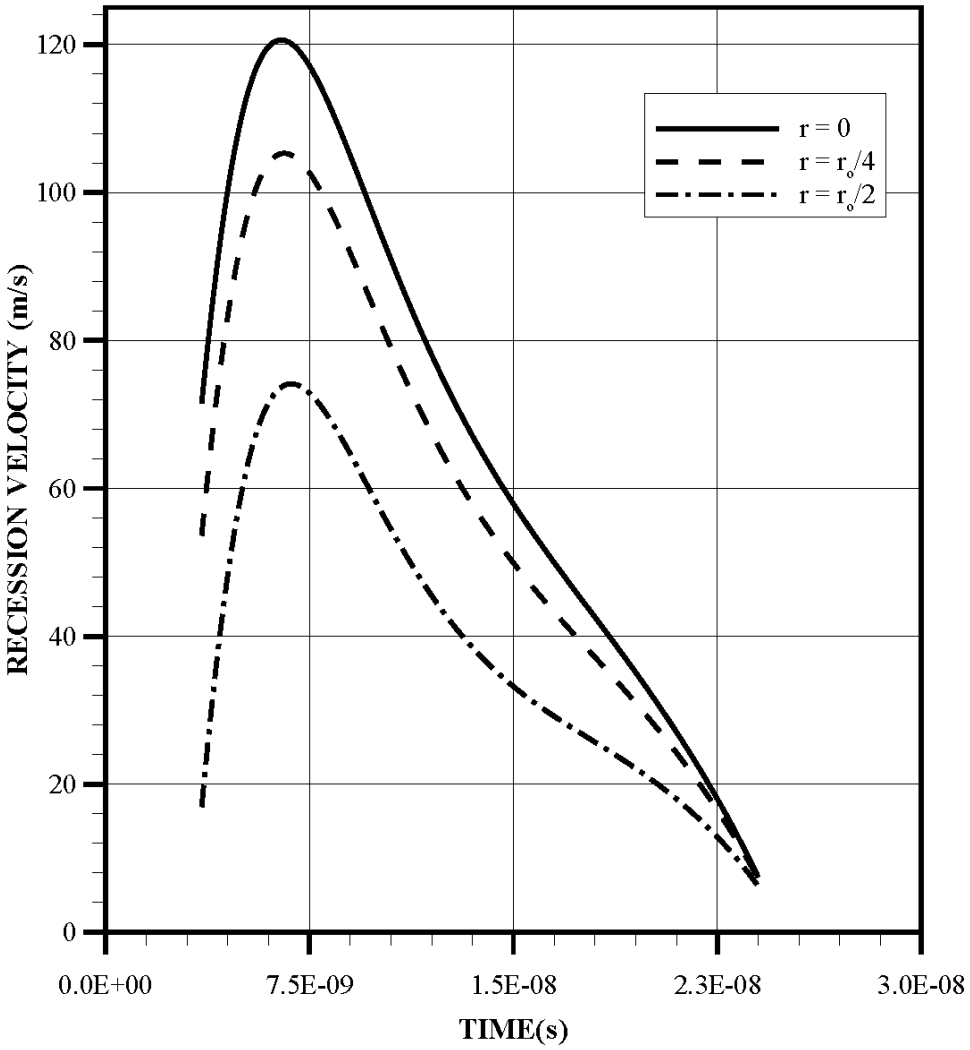

Figure 5.17b - Temporal variation of the recession velocity of liquid-vapour interface at different radial locations.

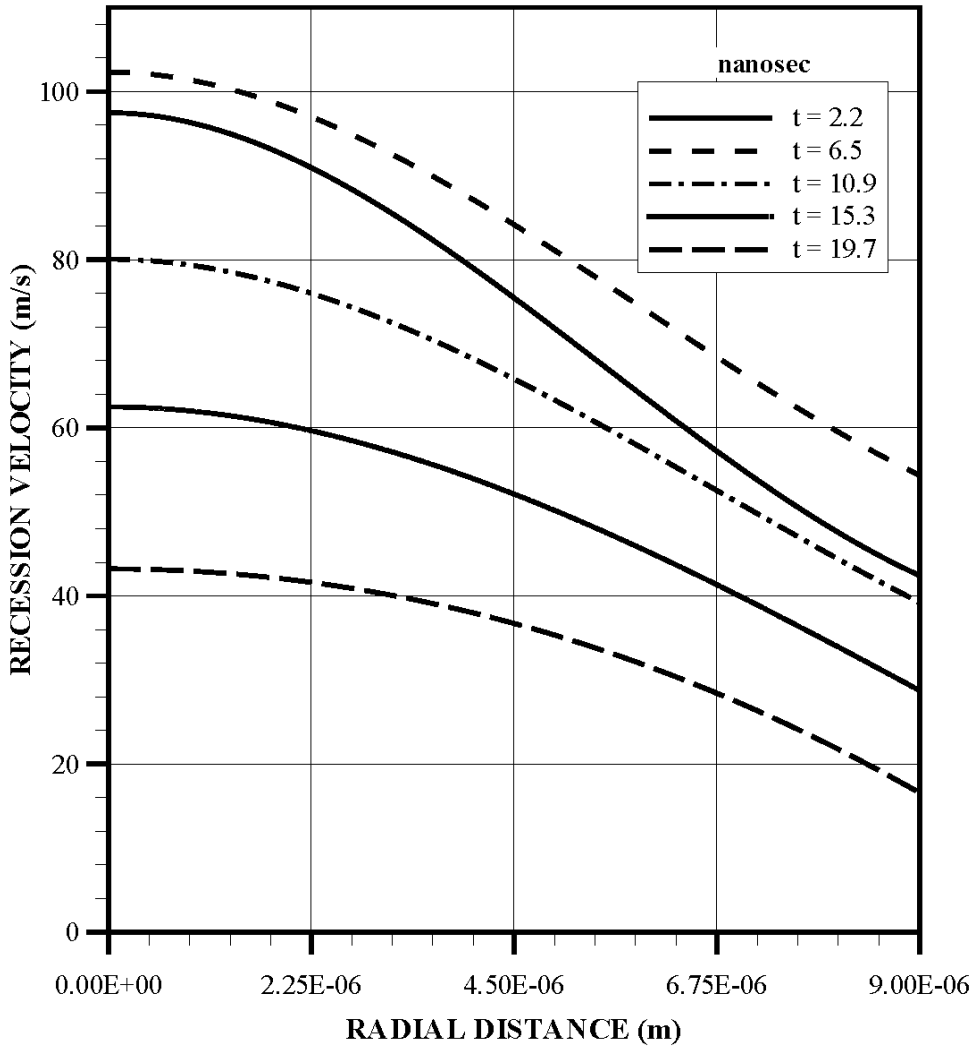

Figure 5.18a - Recession velocity of solid-liquid interface along the radial distance at different time durations.

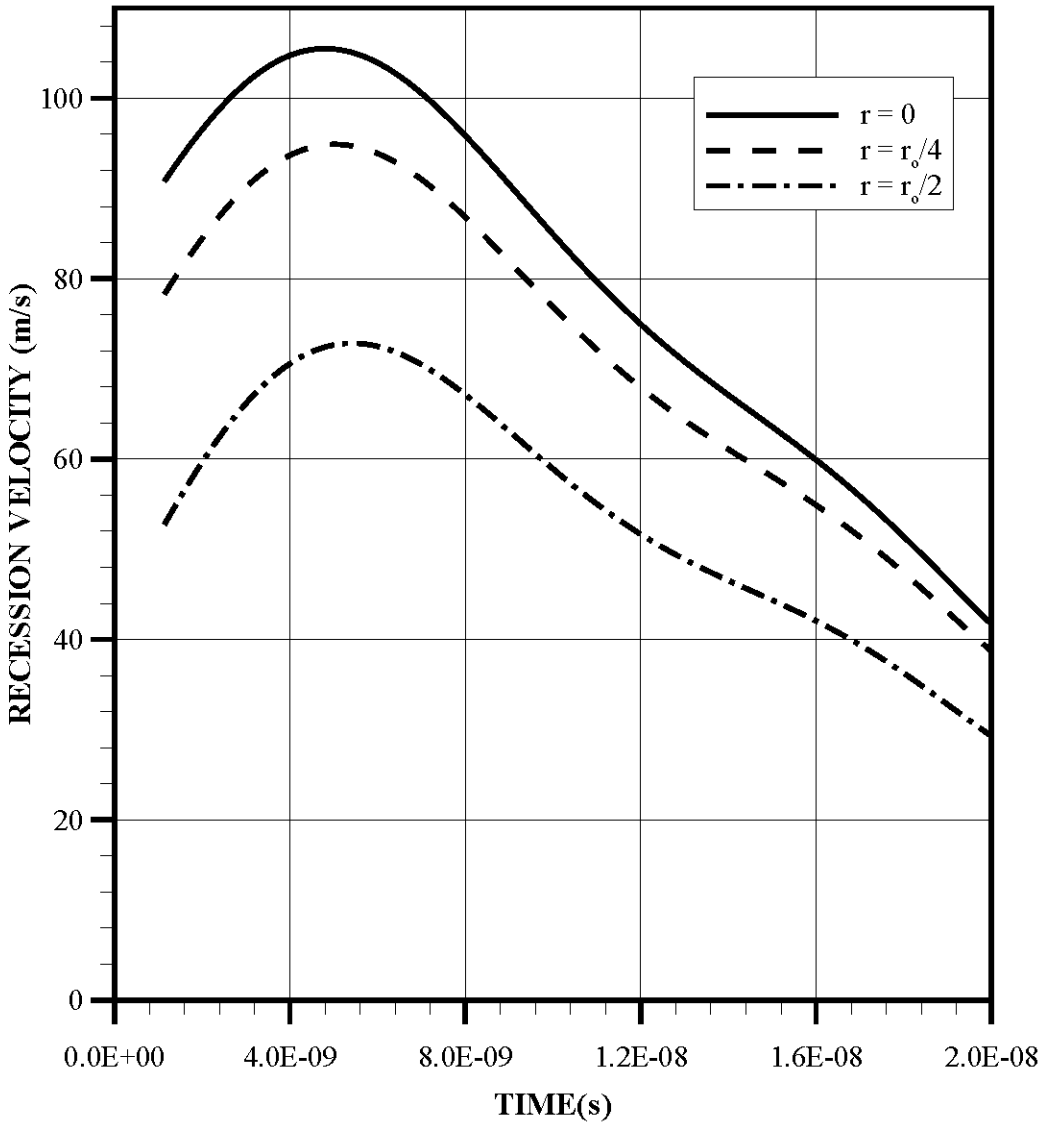

Figure 5.18b - Temporal variation of the recession velocity of solid-liquid interface at different radial locations.

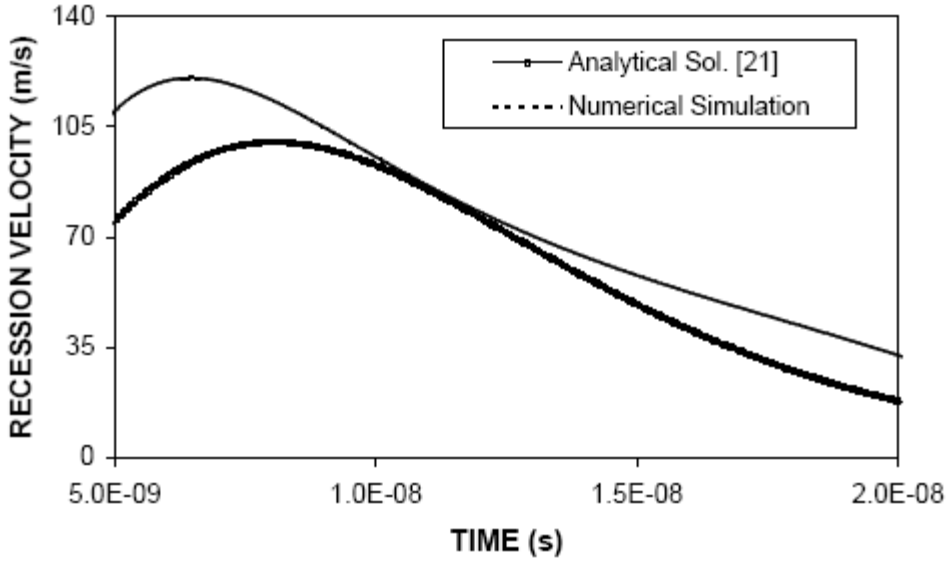

Figure 5.19 - Comparison of recession velocity obtained from present predictions along the symmetry axis and one-dimensional analytical solution [101].

which are accommodated in the present model while omitted in the one-dimensional analysis. Moreover, it is evident that the cavity shape predicted agrees well with the experimental results. Consequently, the evaporative heating model introduced in the present study has a sound base to predict the physical processes involving during the laser heating of solid substrates.

Figure (5.20) shows laser pulse intensity distributions used in the simulations and employed in the experiment. The pulse intensity distributions accommodated in the simulations almost follow the actual pulse intensity used in the experiment. It should be noted that the spatial distribution of the pulse intensity is Gaussian and its $1/e$ points correspond to 8.3×10^{-6} m.

Figure (5.21) shows temperature distribution inside the substrate material along the symmetry axis for different laser peak power intensities. Temperature profiles in the liquid zone (where $T_b \geq T \geq T_m$) have almost the same gradient for all power intensities. However, in the solid ($T < T_m$), temperature gradient for high power intensity becomes slightly less than that corresponding to other power intensities. This occurs because of the rate of heat transfer, which is high in the solid for high power intensities, i.e. lowering the temperature gradient in this region. It should be noted that as temperature reaches the evaporation temperature of the substrate material the melt surface recesses towards the substrate material and the depth of melt recession is determined at a location where

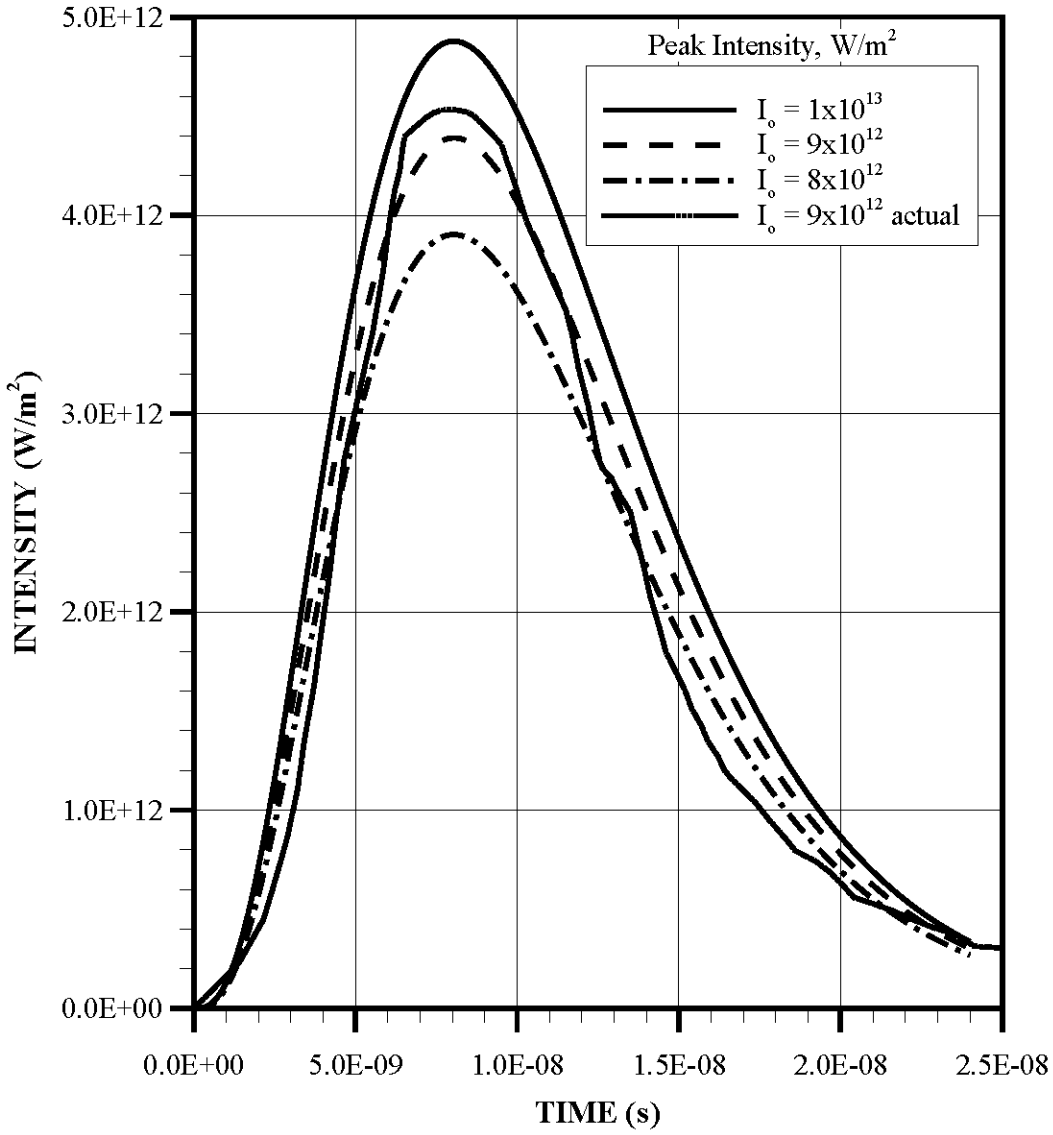

Figure 5.20 - Temporal distribution of laser pulse intensity for three different peak intensities and actual pulse intensity obtained from experiment.

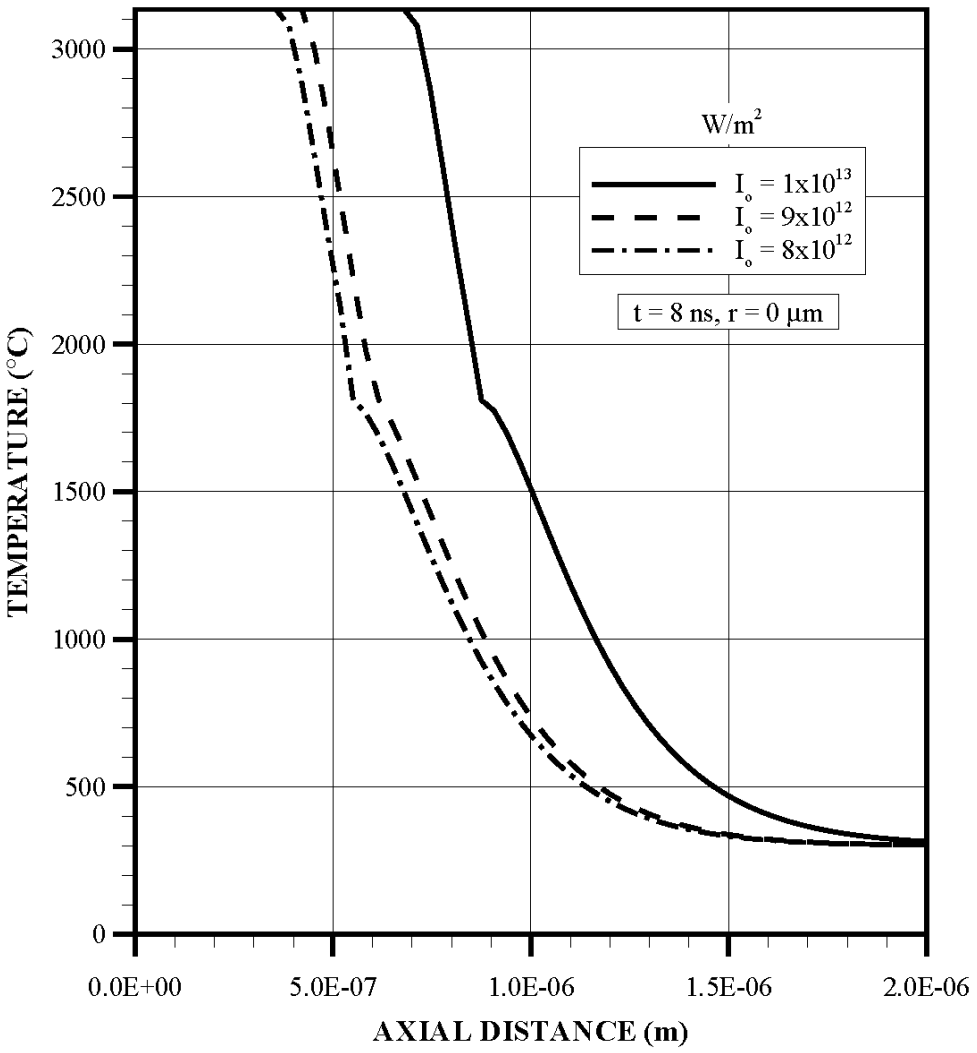

Figure 5.21 - Temperature distribution along the symmetry axis at the instant of peak intensity for different laser pulse intensities.

temperature becomes the same as the evaporation temperature. The depth of evaporated surface increases significantly as the power intensity increases, i.e. increase in power intensity from $8x10^{12}$ to $9x10^{12}$ W/m^2 results in almost 15% increase in depth of evaporated surface; however, when increased from $9x10^{12}$ to $1x10^{13}$ W/m^2 the evaporated surface increases almost 40%. This occurs because of the threshold power intensity required for the evaporation process. As the power intensity increases beyond the threshold, the rate of evaporation accelerates significantly [117].

Figure (5.22) shows, three dimensional view of the cavities formed after the evaporation process for different laser power intensities at 8 ns heating duration. The cavity surface corresponds to the temperature of evaporation. The size of the cavity enhances significantly as the intensity increases from $9x10^{12}$ W/m^2 to 10^3 W/m^2. Moreover, the increase in the size is more pronounced along the symmetry axis, i.e. the depth of the cavity increases more than the radial enlargement of the cavity. Figure (5.23) shows the cross-sectional view of the cavity with the phases developed. In general, the size (depth and width) of the liquid-solid mushy zone is significantly smaller than that corresponding to vapour-liquid mushy zone. This occurs because of the spatial distribution of the volumetric heat source accommodated in equation (1), which is Gaussian with high magnitude in the surface region. It should be noted that power intensity absorbed by the substrate material decays exponentially inside the substrate material with increasing depth (Lambert's law). In this case, the magnitude of volumetric heat source in the surface region becomes higher than that corresponding to some depth below the surface. Consequently, high magnitude of heat source in the surface region enhances the rate of

evaporation in this region. However, the latent heat of evaporation is higher than the latent heat of fusion (Table 5.1); in which case, the size of vapour-liquid mushy zone increases due to large value of latent heat of evaporation. The depth of the cavity extends more along the symmetry axis than that which occurs at some distance away from the symmetry axis in the radial direction. This is because of the laser power intensity distribution across the surface, which is Gaussian, i.e. along the radial axis power intensity reduces exponentially so that the amount of volumetric heat source available at radial locations away from the symmetry axis becomes less. This, in turn, results in low rate of evaporation in this region, i.e. the width of cavity remains almost unaltered with progressing heating. Figure (5.11a & 5.11b) shows the cavity predicted and obtained experimentally at the end of the heating pulse.

Figure (5.24) shows recession velocity of the liquid-solid surface towards the solid bulk for three power intensities and at different heating periods. The recession velocity is high in the early heating period and as the heating duration progresses, it reduces. Moreover, as the distance in the radial direction increases, it also decays. The attainment of high recession velocity in the early heating period can be explained in terms of heat transfer and the progressing of the phase changes with progressing time. In this case, the rate of evaporation is high while the depth of liquid layer is small in the early heating period and as the heating duration progresses, energy absorbed from the irradiated field is transferred to the formation of liquid layer above the solid phase. In addition, liquid heating (super heating) reduces the energy available at the solid surface to enhance the melting process.

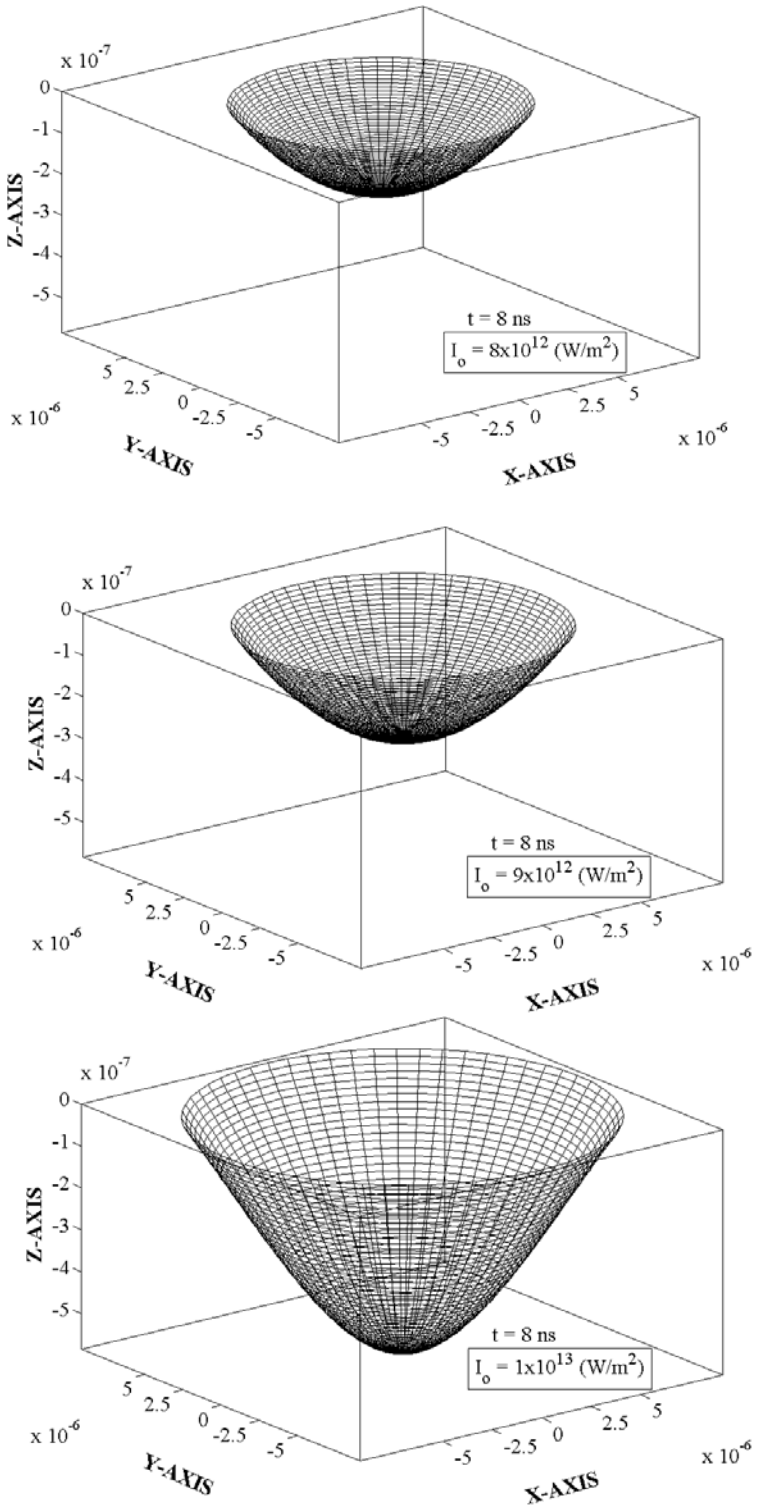

Figure 5.22 - Three-dimensional view of the cavity at the instant of peak intensity for different laser pulse intensities.

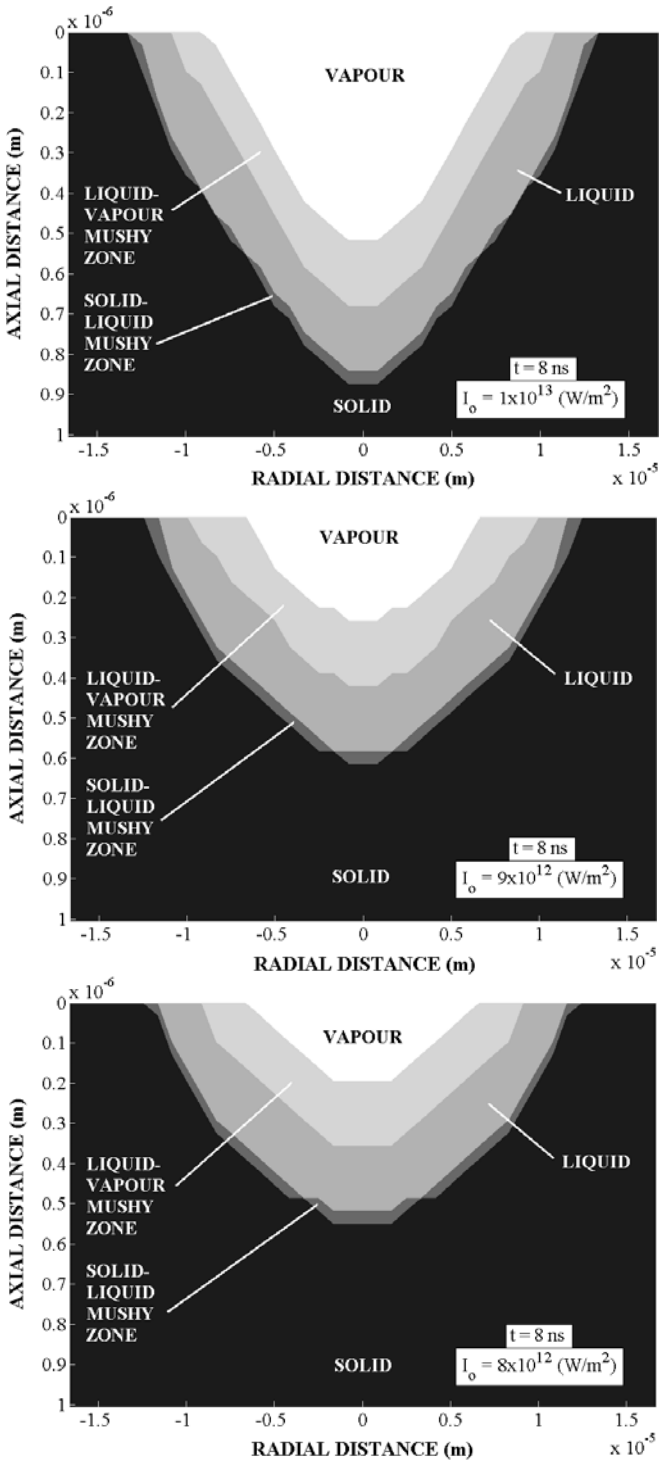

Figure 5.23 - Cross-sectional view of laser produced cavity and the vapour and liquid phases, and mush zones.

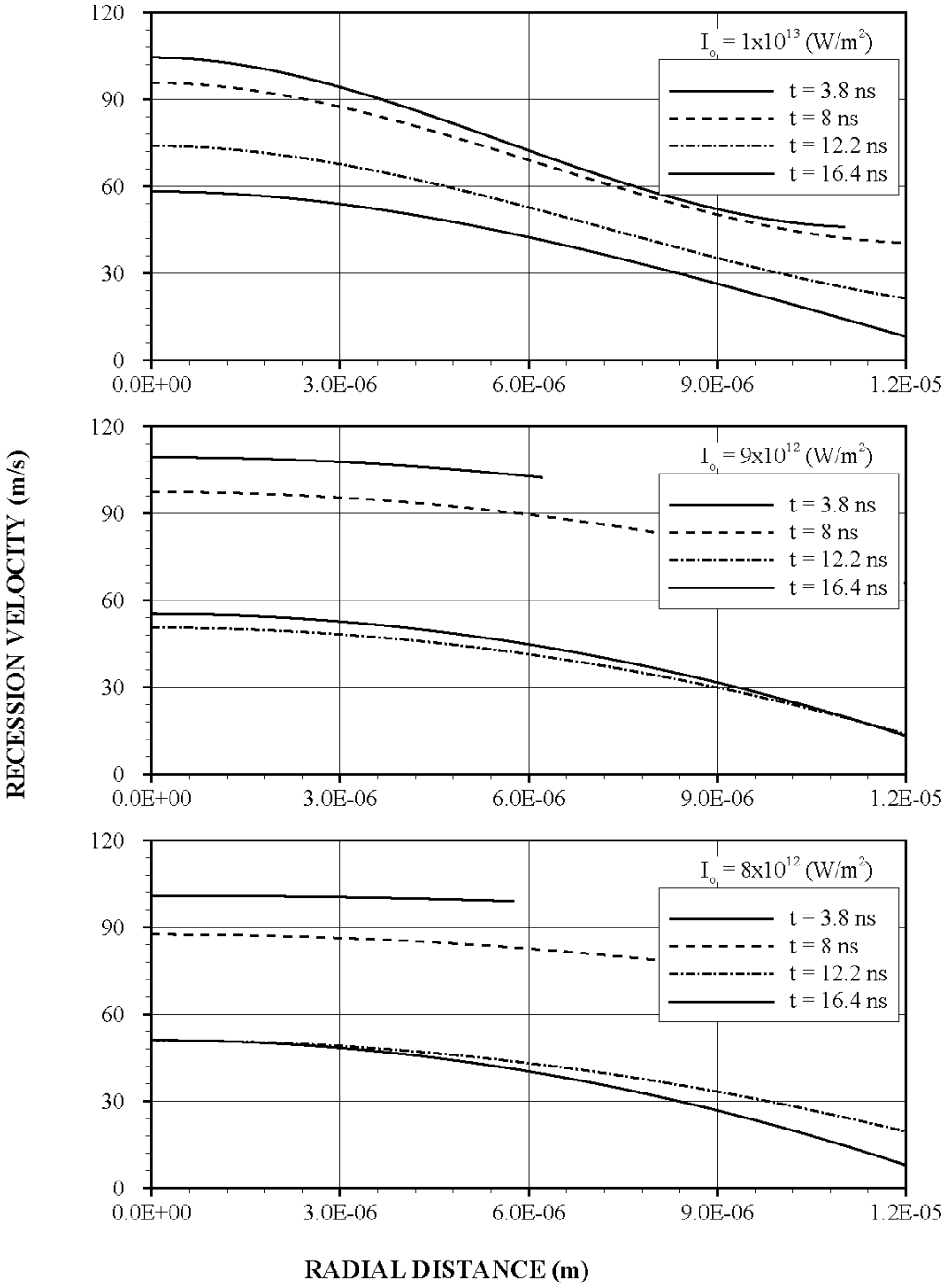

Figure 5.24 - Recession velocity of iquid-solid interface along the radial distance at different time durations and laser pulse intensities.

The recession velocity of the liquid-solid surface terminates at some location in the radial direction due to the energy available in this region, which becomes less than the threshold energy for the phase change. This is more pronounced in the early heating period. This suggests that as the time progresses, the radial heat conduction enhances the phase change in the region of the outer edge of the cavity. Moreover, increasing power intensity does not alter the magnitude of recession velocity significantly, particularly in the early heating period.

Figure (5.25) shows recession velocity of the liquid-vapour phase for different power intensities at different heating durations. Recession velocity attains higher values in the early heating period, as the time progresses it reduces. This is because of the evaporation rate, which is high in the early heating period, i.e. energy absorbed by the substrate material in the surface region, enhances the evaporation rate while liquid formation is small in the early heating period [118]. The decrease in the recession velocity along the radial axis is associated with the radial distribution of laser power intensity, which decays exponentially with increasing radial distance. When comparing the recession velocity of the vapour-liquid surface with the recession velocity of the liquid-solid surface (figure (5.24)), recession velocity of the vapour-liquid surface is higher than that corresponding to liquid-solid surface, despite the fact that the latent heat of evaporation is higher than the latent heat of fusion (Table 5.1). This is because of the amount of energy absorbed in the surface region, which is considerably higher than at some depth below the surface where melting takes place.

Figure (5.26) shows the quality in the liquid-solid mushy zone for different laser power intensities at three depths below the surface. It should be noted that the quality is defined by the amount of liquid in the liquid-solid mixture in the mushy zone. The slope of quality does not vary for all power intensities. However, as the depth increases, the variation of quality with depth becomes gradual. This indicates that the phase change across the mushy zone (liquid-solid) is gradual due to less absorbed energy available in this region. Moreover, sharp variation in the quality at small distance in the radial direction indicates that the size of the liquid-solid mushy zone is small and the amount of liquid in the mushy zone changes almost linearly in the radial direction.

Figure (5.27) shows the quality in the vapour-liquid mushy zone for different laser power intensities at different depths below the surface. Due to the high rate of evaporation at the surface and the amount of irradiated energy absorbed in the surface region (which is high), the quality reduces gradually in the radial direction in the mushy zone. Moreover, as the distance from the surface increases, slight variation in the quality occurs as the distance increases towards the radial direction, which indicates that the width of the mushy zone is slightly large at some depth below the surface, i.e. due to less irradiated energy available in this region suppresses the rate of evaporation; therefore, the size of mushy zone becomes large in this region.

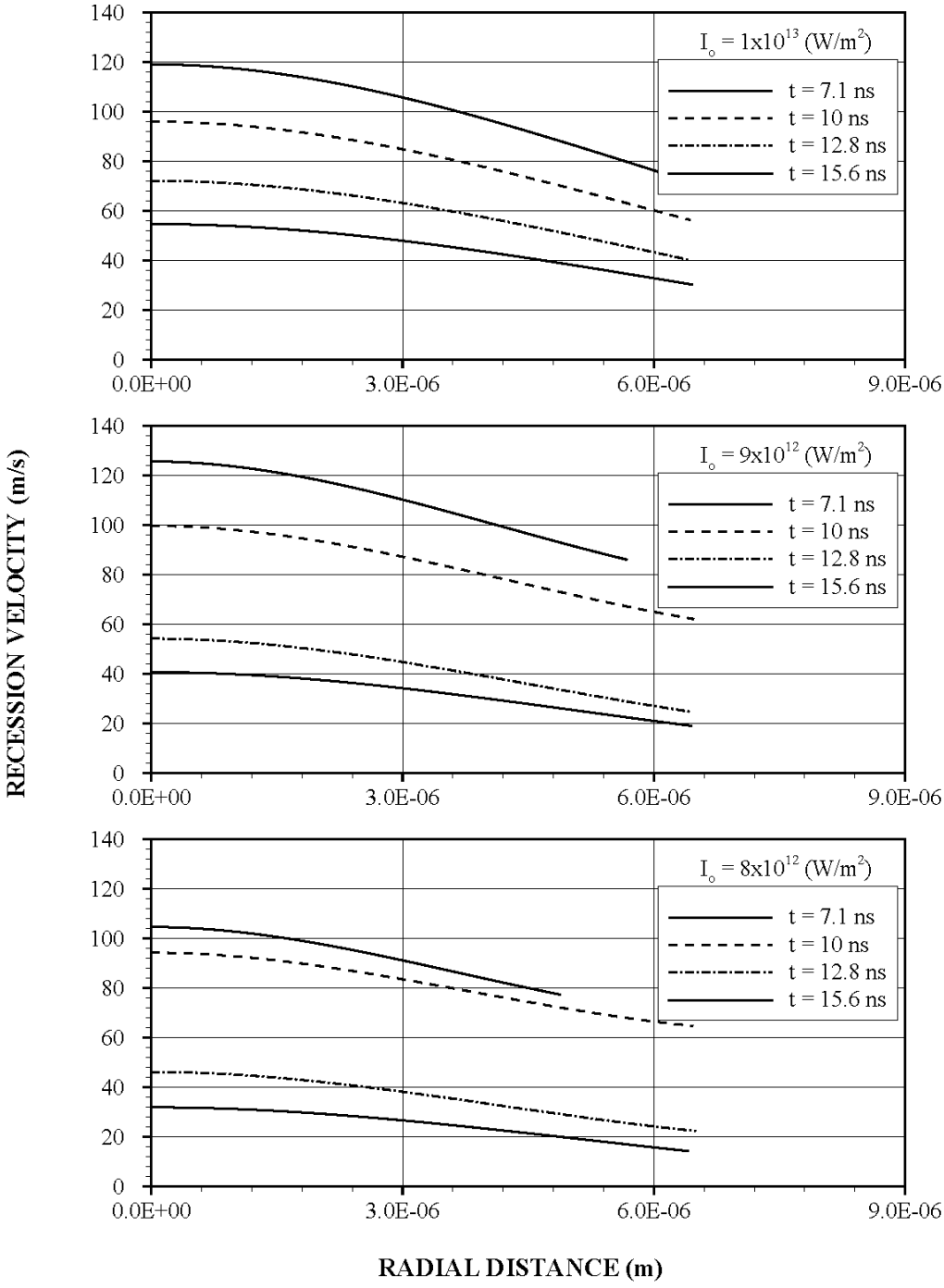

Figure 5.25 - Recession velocity of vapour -liquid interface along the radial distance at different time durations and laser pulse intensities.

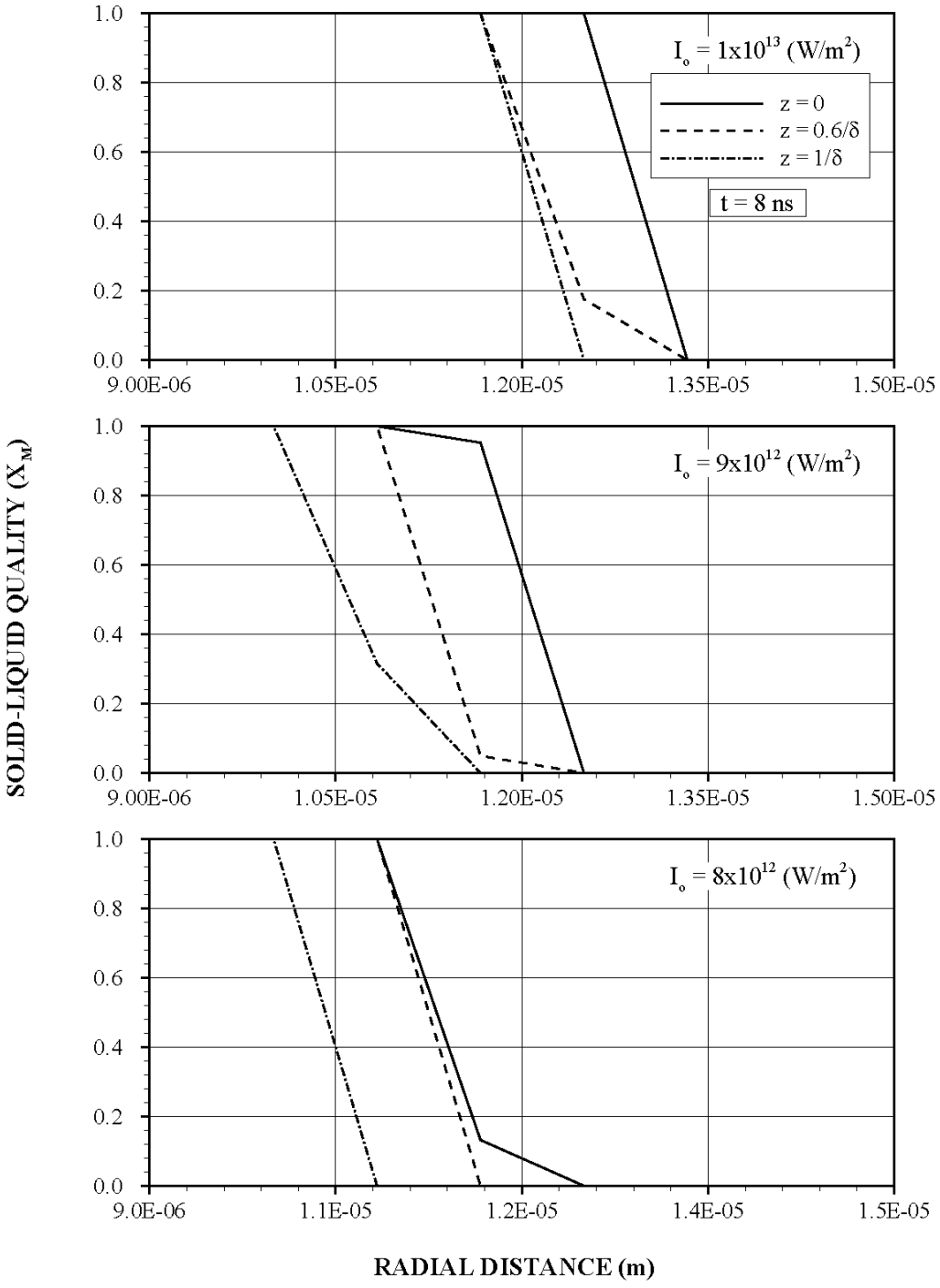

Figure 5.26 - Liquid-solid quality (x_m) along the radial distance at the instant of peak intensity for different laser pulse intensities and axial locations.

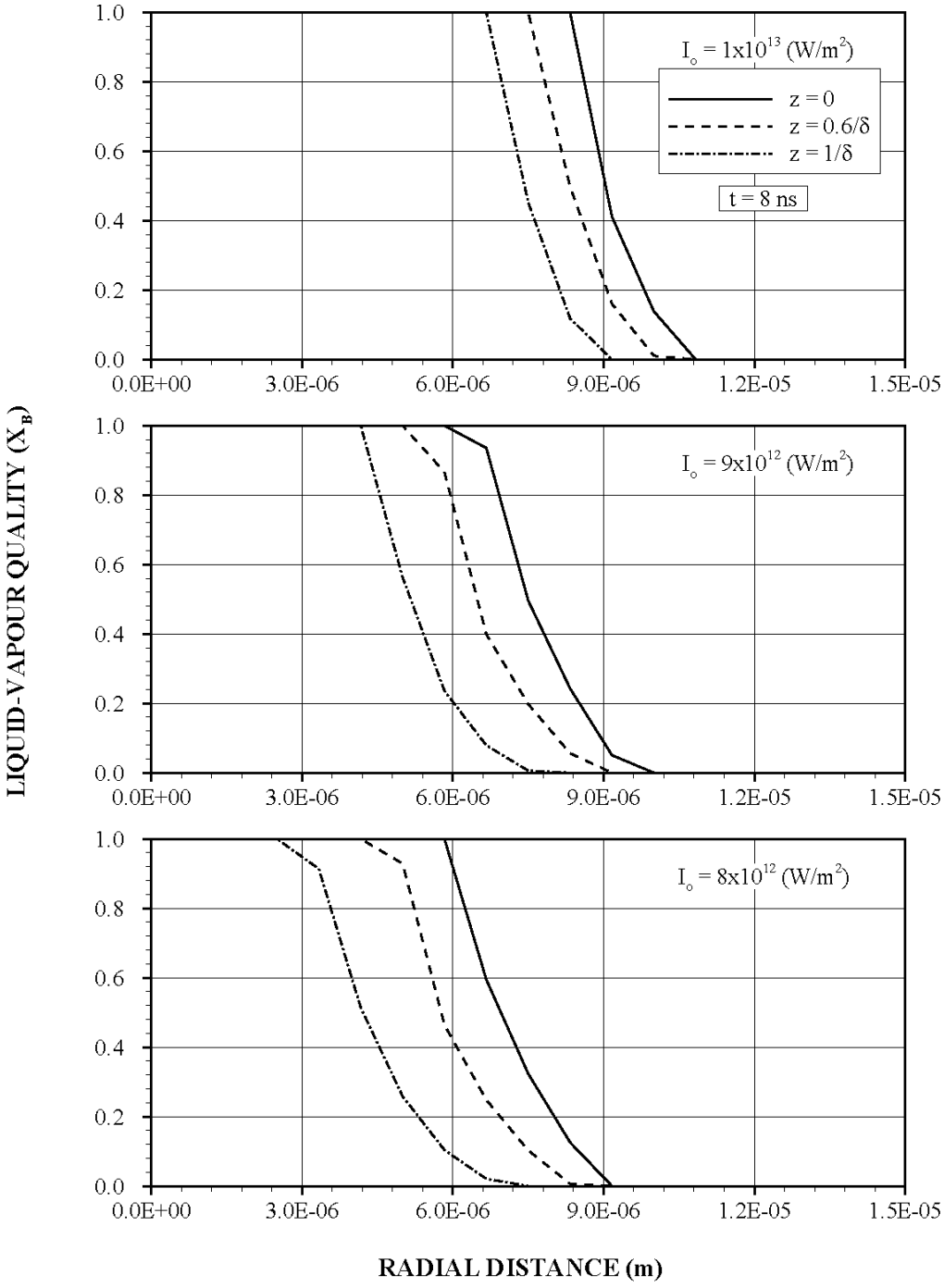

Figure 5.27 - Vapour-liquid quality (x_b) along the radial distance at the instant of peak intensity for different laser pulse intensities and axial locations.

T_m (K)	T_b (K)	ρ (kg/m^3)	Cp (J/kg/K)	k (W/m/K)	δ (1/m)	L_m (J/kg)	L_b (J/kg)
1811	3134	7860	420	63	$6.17x10^6$	247112	6213627

Table 5.1 - Material properties used in the simulations.

Peak Intensity (W/m^2)	Gaussian Parameter (1/m)	Nominal Pulse Length (ns)
$8x10^{12}$, $9x10^{12}$, $1x10^{13}$	120000	24

Table 5.2 - Laser pulse intensity used in the simulations.

5.2 Transiently Developing Jet in Relation to Laser Heating

The flow due to jet emanating from a laser produced cavity is considered and velocity, pressure and temperature fields are predicted numerically. Since the cavity formation is transient, a transient moving boundary problem is accommodated in the analysis. Laser produced cavity is assumed to be formed in the water ambient. This is the situation where the laser induced shock processing is being carried out. Consequently, the vapour emanating from the cavity expands into the water ambient. Since the thermophysical properties of the vapour front are not known and the equation of state for laser produced vapour is not formulated, two densities of vapour front are assumed. In addition, due to unknown equation of state for the vapour phase, the vapour front is assumed to be incompressible. Moreover, as the cavity recesses with time, the vapour-liquid front recesses the cavity with the same recession velocity. The selection of vapour front density is made 1/10 and 1/100 times of the liquid density. Table 5.3 gives the properties of the water and vapour front accommodated in the simulations.

Figure (5.28) shows the velocity contours in and around the cavity for four heating periods for jet density of 800 kg/m^3. It should be noted that the evaporation takes place after 1.8 ns from the laser pulse initiation. In the early heating period $(t = 6.54\,ns)$, jet expansion is more pronounced in the axial direction provided that the cavity diameter is small at cavity exit. The abrupt expansion of the jet into the stagnant ambient results in flow disturbance around the jet boundary. However, this expansion cannot generate a circulation cell next to the jet boundary i.e., it is the ambient density, which is high,

suppressing the circulation cell next to the jet boundary. Moreover, decay of radial momentum of the jet also contributes to the suppression of the circulation in this region. As the heating period progresses, jet expansion in the radial direction enhances, particularly in the front region of the jet. This can be observed from the velocity contour of $3.2\times10^{2}\ m/s$. Temporal expansion of the contour is more pronounced in the radial direction when comparing the jet behaviour at time durations of 7.74 ns and 8.34 ns. In this case, jet produced from the cavity remains almost at the same velocity. The high density fluid suppresses the axial velocity due to momentum conservation and radial velocity increases at the jet frontal region.

Figure (5.29) shows pressure contours corresponding to $800\,kg/m^{3}$ vapour density, in the jet for different heating durations. In the early heating period $(t = 6.54\,ns)$, pressure is build up in the cavity and the decay in radial momentum in the vicinity of the cavity results in high pressure generation in this region. This is particularly true for late heating periods. Pressure in the cavity reaches extremely high magnitude in the early heating period and as the heating progresses, jet production in the cavity enables the axial expansion of jet. This, in turn, lowers the pressure in the cavity. Although the centre of high pressure region is formed in the cavity slightly away from the symmetry axis, axial expansion of the jet does not get affected by this pressure centre. It should be noted that the recession of the cavity with time develops complex flow field in the cavity. However, at the outer edge of the jet, the flow behaviour is controlled by the high density fluid surrounding the jet. The magnitude of pressure in the cavity reaches as high as 26 GPa.

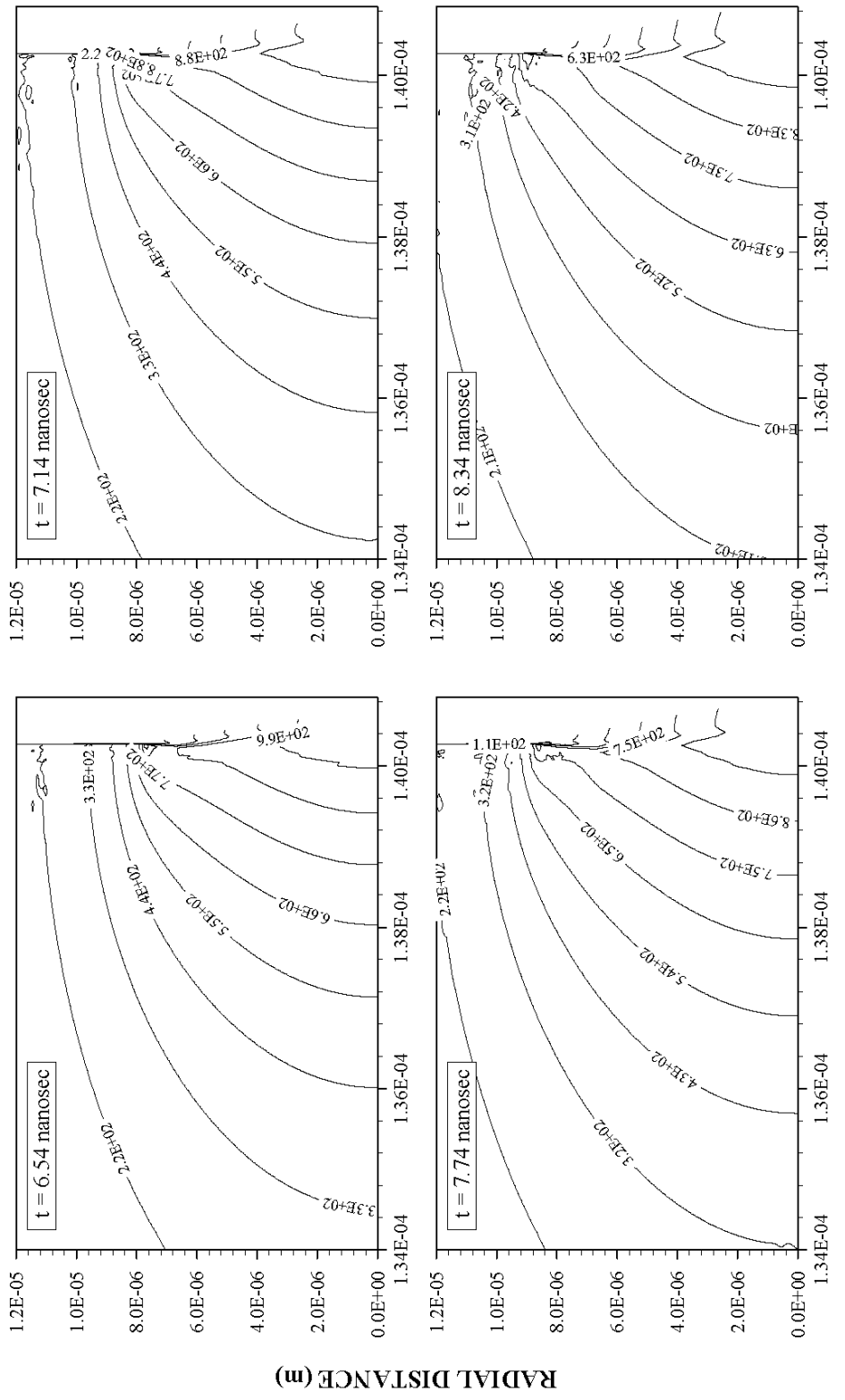

Figure 5.28 - Contour plots of velocity magnitude for three different heating durations for jet density $\rho = 800$ kg/m^3.

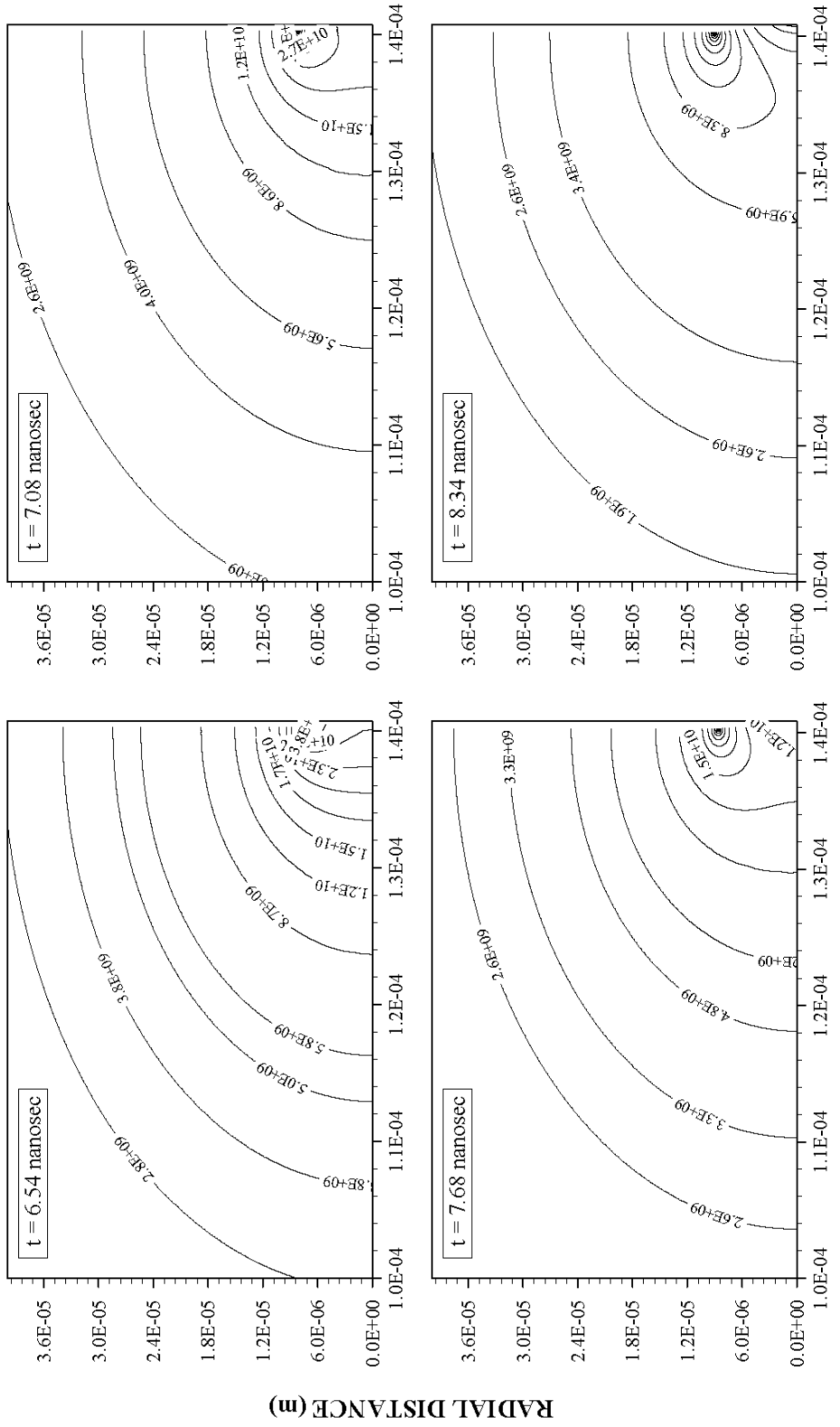

Figure 5.29 - Contour plots of pressure for three different heating durations for jet density $\rho = 800$ kg/m^3.

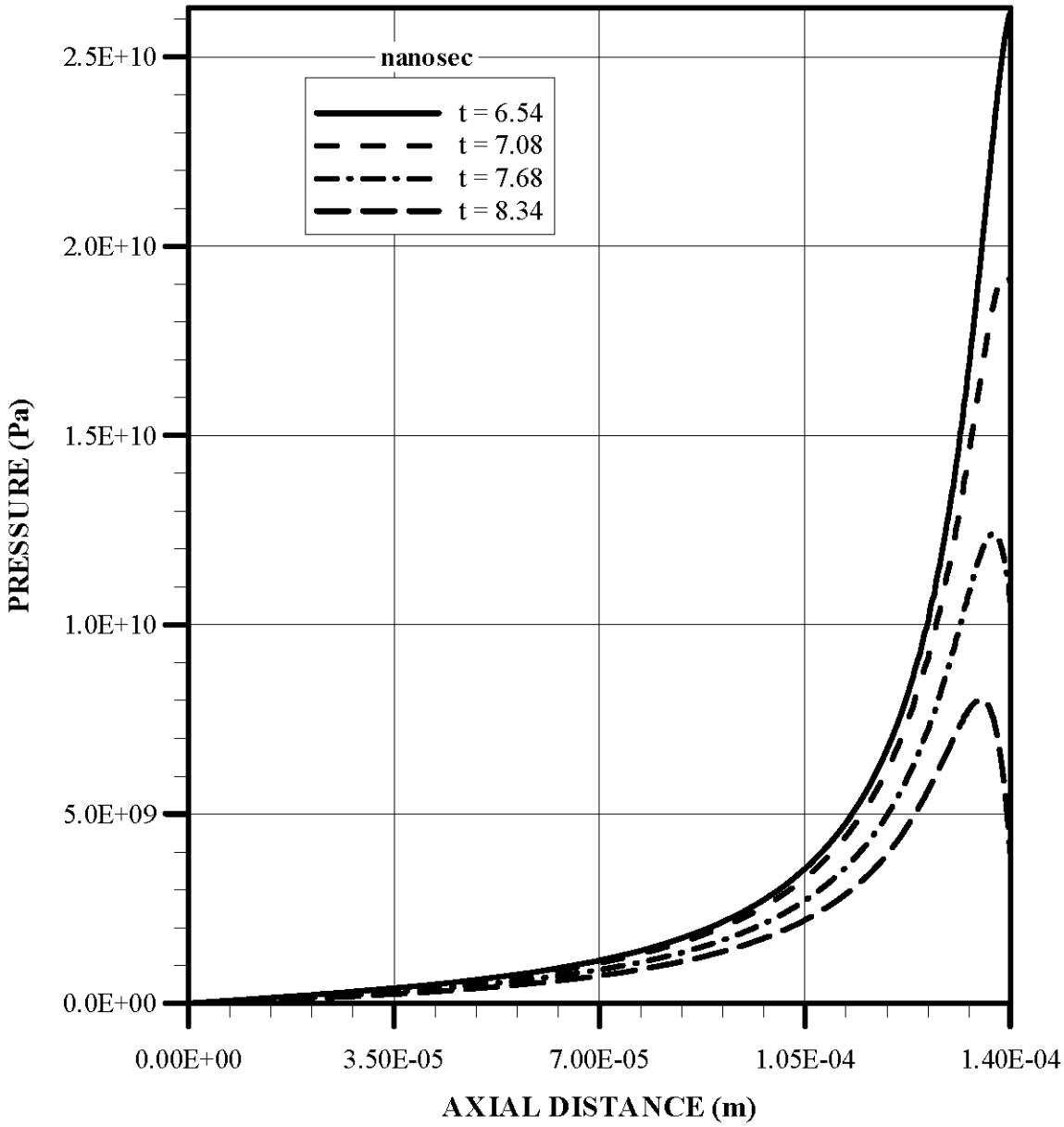

Figure 5.30 - Pressure distribution along the symmetry axis at different heating durations for jet density $\rho = 800$ kg/m^3.

Figure (5.30) shows pressure variation along the symmetry axis for different heating periods for jet density of 800 kg/m^3. The location of maximum pressure along the symmetry axis occurs away from the cavity wall. This is because of the recession of the cavity surface with time, i.e., cavity wall recesses opposite to the jet expansion creating the suction in the region of the cavity wall. This, in turn, lowers the pressure in this region. However, in the early heating period the cavity recession is less and the pressure builds up in the cavity. This results in excessive pressure generation in this region. Consequently, radial expansion of the jet in the jet frontal region reduces the pressure in this region. Consequently, jet expansion in the radial direction with progressing time results in decay of pressure in the jet.

Figure (5.31) shows velocity magnitude contours obtained for jet density of $50\,kg/m^3$ in and around the cavity for different heating durations. Since the mass flow rate for two cases $\left(\rho_{jet} = 800\,kg/m^3 \text{ and } \rho_{jet} = 50\,kg/m^3\right)$ is kept the same, lowering the jet density to $50\,kg/m^3$ results in high axial velocity of the jet emanating from the cavity. In the early heating period $\left(t = 6.54\,ns\right)$ the radial expansion of the jet is evident and as the time progresses jet penetration into a stagnant fluid does not enhances in the axial direction, which is particularly true for $\left(t = 8.34\,ns\right)$. Due to the high rate of fluid strain in the outer region of the jet and close to cavity edge, a circulation cell is formed next to jet boundary. This is more evident for heating periods $t \geq 7.74\,ns$. However, the radial expansion of the jet in the early periods can be attributed to the less axial momentum change in the frontal region of the jet; in which case, a pressure build up is resulted in this region.

Figure (5.32) shows pressure contours obtained for jet density $50\,kg/m^3$ for different heating periods. The radial expansion of the jet is evident in the early heating period. It is evident that next to the jet boundary particularly in the region of cavity edge, circulation cell is generated. Moreover, the detachment of the jet after emanating from the cavity is observed. This is more pronounced at late heating periods $(t \geq 7.74\,ns)$. This indicates that the initial acceleration of the jet is high and once the pressure increases in the frontal area of the jet, expands radially more than its axial component. However, continuous mass addition in the axial direction in the cavity, due to cavity recession, pushes the jet front penetrating into the surrounding fluid. This forms like a jet neck immediately above the cavity exit. Due to the rate of fluid strain, which is high in this region, forms a circulation cell in the vicinity of the jet neck. This appears as a detachment of jet front from the mainstream jet flow. This situation is also seen from figure (5.33), in which pressure variation along the symmetry axis is shown. Peak pressure occurs in the jet above the cavity exit and the locus of peak pressure moves along the axial direction as the time progresses. Moreover, as the time progresses, the magnitude of pressure reduces.

Figure (5.34) shows maximum pressure along the symmetry axis for two vapour front velocities. In the early heating period, the magnitude of maximum pressure is high and as

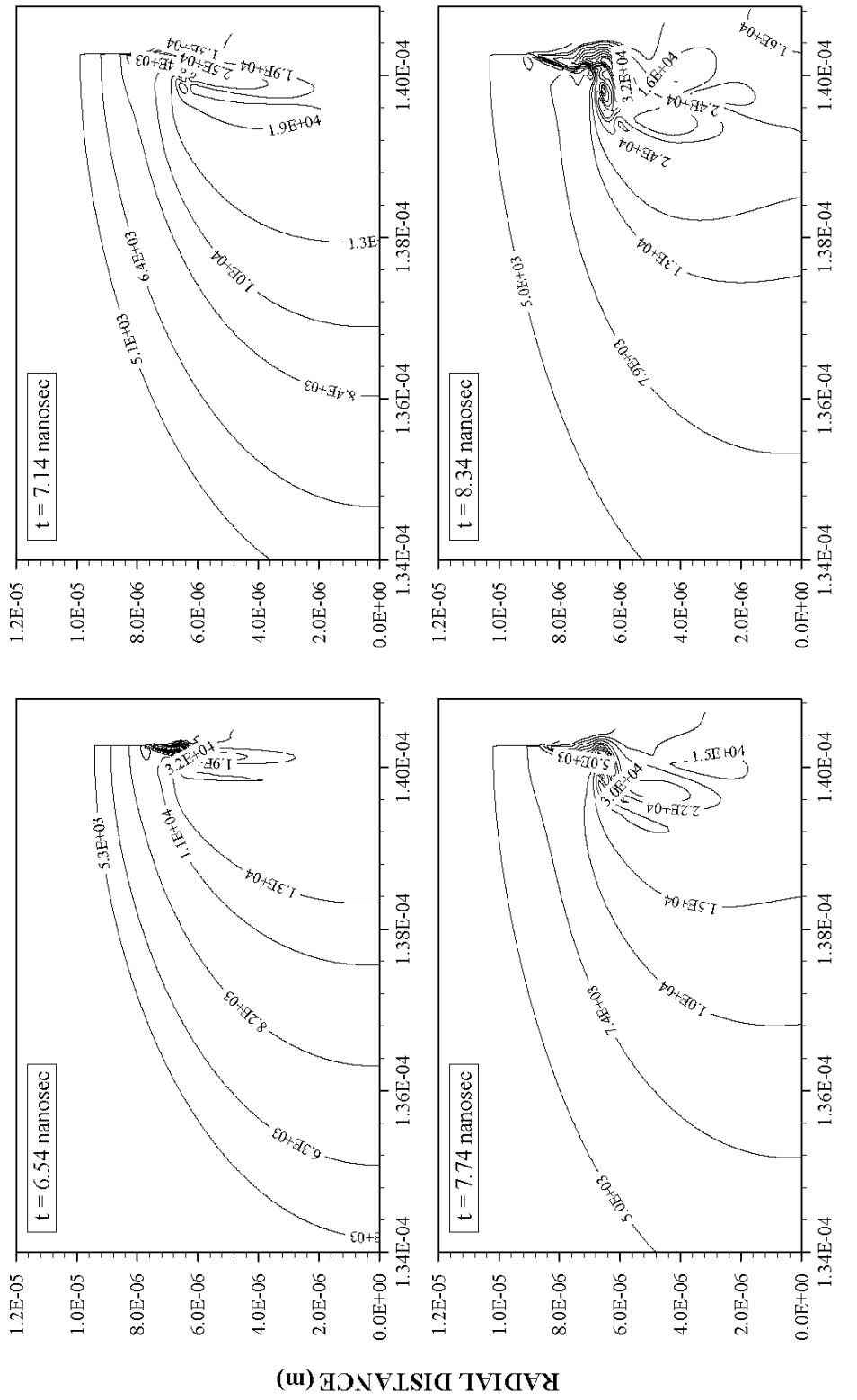

Figure 5.31 - Contour plots of velocity magnitude for three different heating durations for jet density $\rho = 50$ kg/m^3.

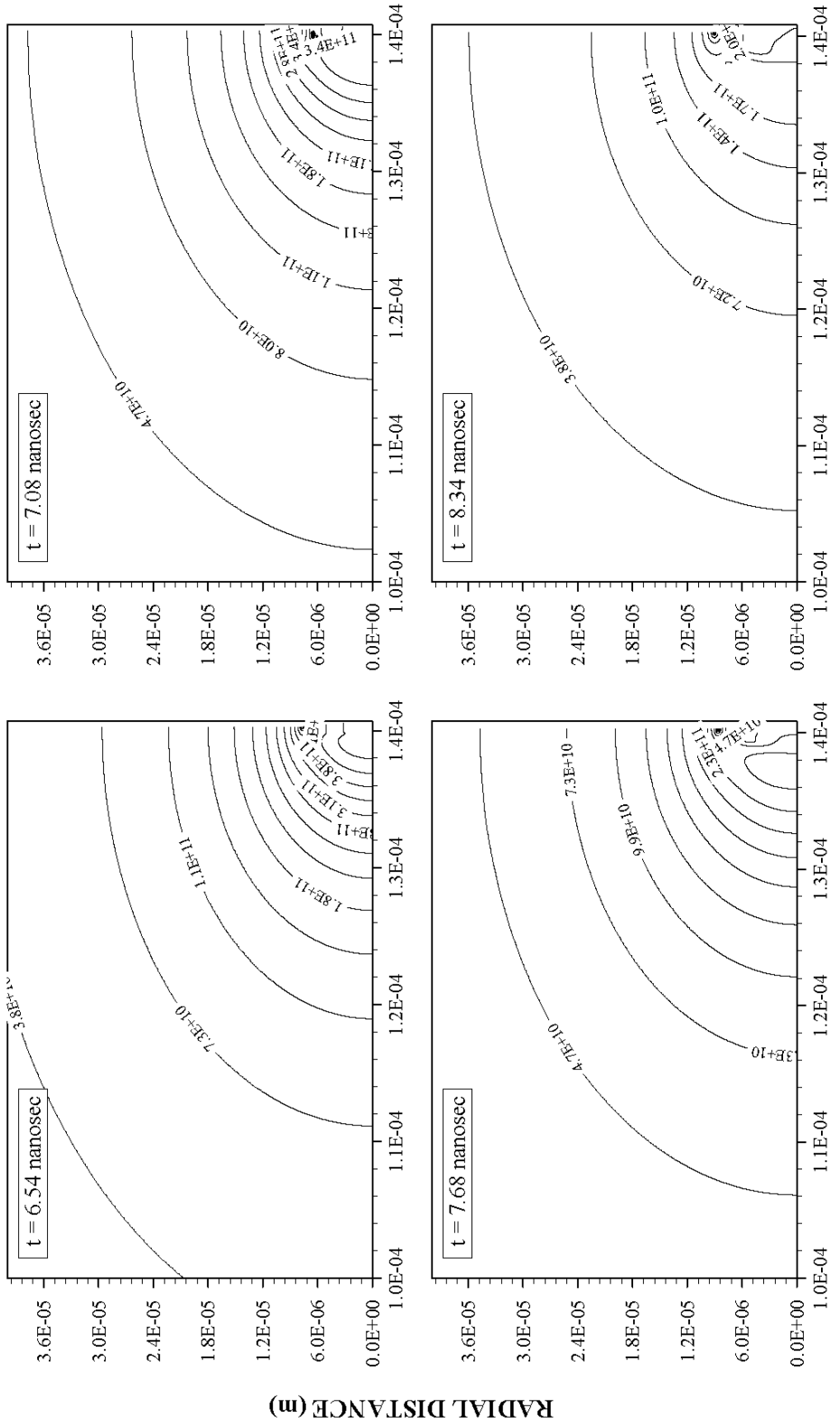

Figure 5.32 - Contour plots of pressure for three different heating durations for jet density $\rho = 50$ kg/m^3.

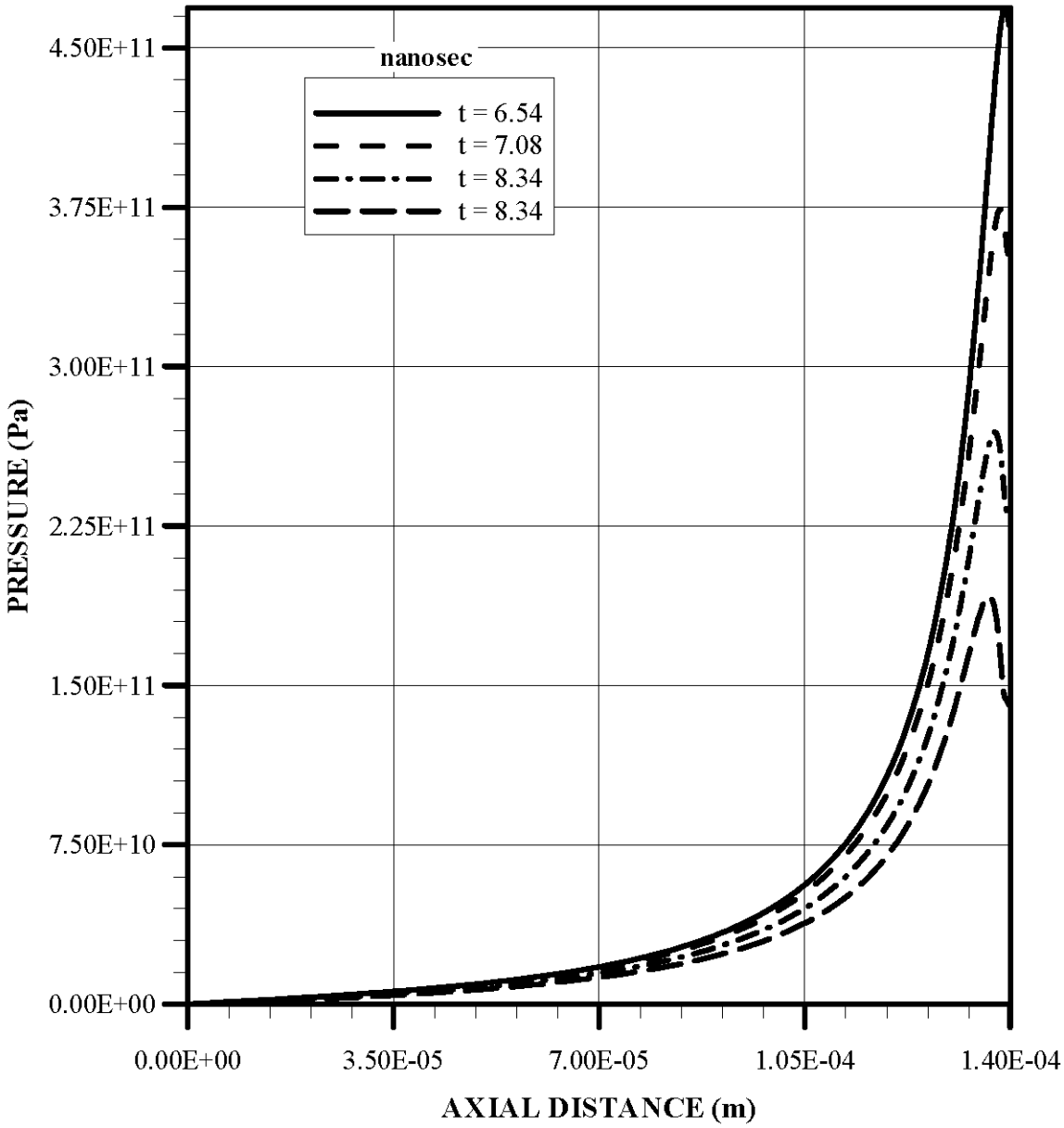

Figure 5.33 - Pressure distribution along the symmetry axis at different heating durations for jet density $\rho = 50$ kg/m^3.

the time progresses it reduces. The attainment of high pressure in the early heating period can be attributed to the recession velocity of the solid surface, which is high in the early heating period. In this case, solid surface recesses towards the solid bulk of the substrate material while vapour front expands opposite to the motion of the recessing solid surface. This in turn results in significant momentum change at vapour front-solid interface. Consequently, excessive pressure rise is generated at the interface, which is high in the early heating period.

Figure (5.35) shows the location of maximum pressure with time for two vapour front densities. The location of maximum pressure moves towards the cavity exit as the time progresses. This occurs because of the continuous jet production through recession of the melt surface (cavity wall recession). In addition, the cavity recesses opposite to the motion of jet and depth of cavity increases by time. In the case of low density, the location moves early in time, in the cavity due to momentum change with the surrounding fluid. It should be noted that the velocity of the jet emerging from the cavity wall is higher for low density fluid than that of high density fluid. Moreover, as time progresses further $\left(t \geq 7.74\, ns\right)$ change in the location of maximum pressure becomes small for low density fluid case.

Figure (5.36) shows dimensionless penetration depth $\left(Z_t / D\right)$ for two vapour front densities. Since the solid surface recesses, the cavity diameter extends with progressing time. Consequently the magnitude of Z_t / D is influenced by the cavity diameter.

Moreover, temporal expansion of cavity diameter is the same for both densities. The magnitude of Z_t/D attains high values in the early period and as the time progresses it decays gradually. This may be because of the both effects of expansion of cavity diameter and jet penetration in the early durations. However, when comparing the Z_t/D corresponding to two densities, high density results in more penetration of the jet in the early period than that of low density jet. This is because of high magnitude of pressure generated for high density fluid in the early period. Moreover, as the time progresses further, jet penetration into its surroundings becomes more for low density fluid than that corresponding to high density fluid. This is due to high velocity jet for low density fluid; in which case, jet momentum along the symmetry axis remains high resulting in high magnitude of jet penetration into stagnant fluid ambient.

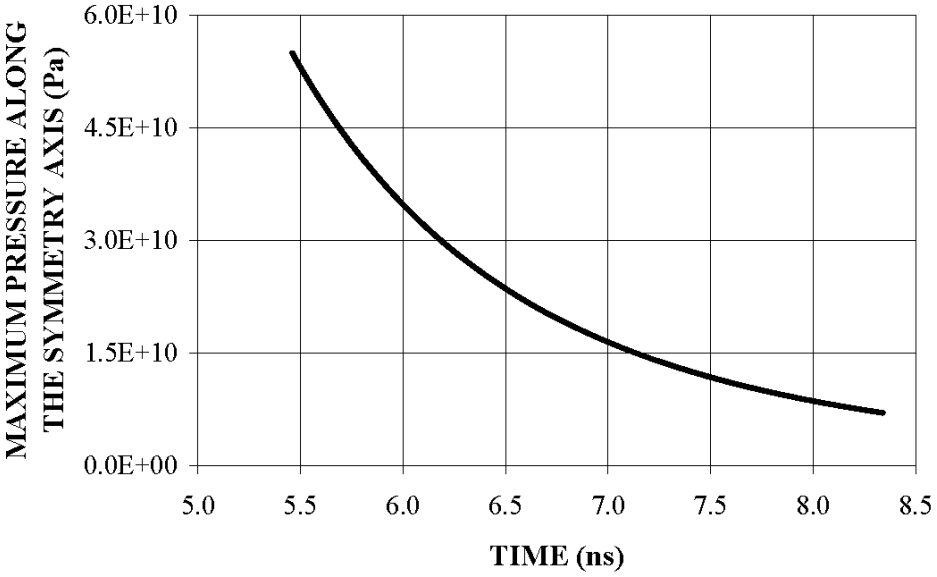

a) For jet density $\rho = 800$ kg/m^3.

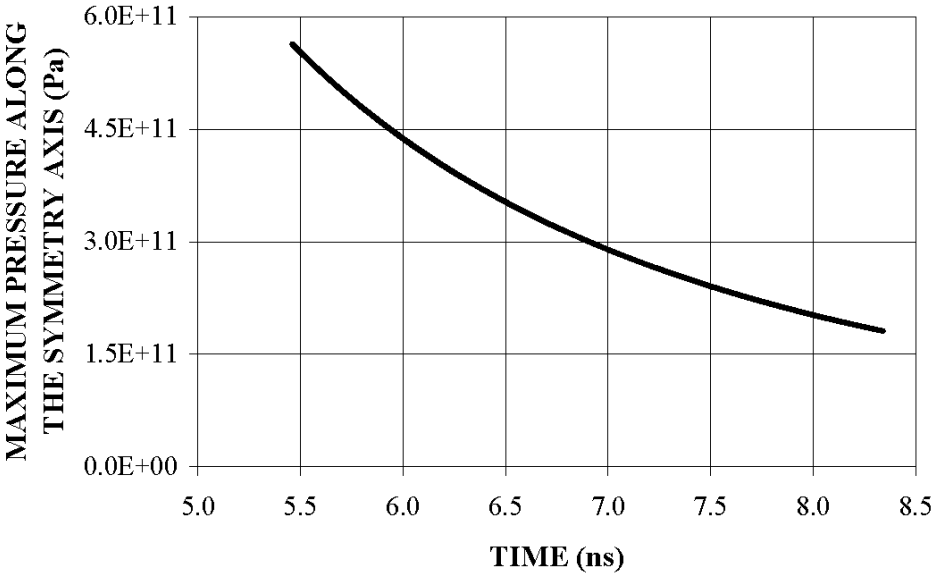

b) For jet density $\rho = 50$ kg/m^3.

Figure 5.34 - Maximum pressure along the symmetry axis with time for jet densities $\rho = 800$ kg/m^3 and $\rho = 50$ kg/m^3.

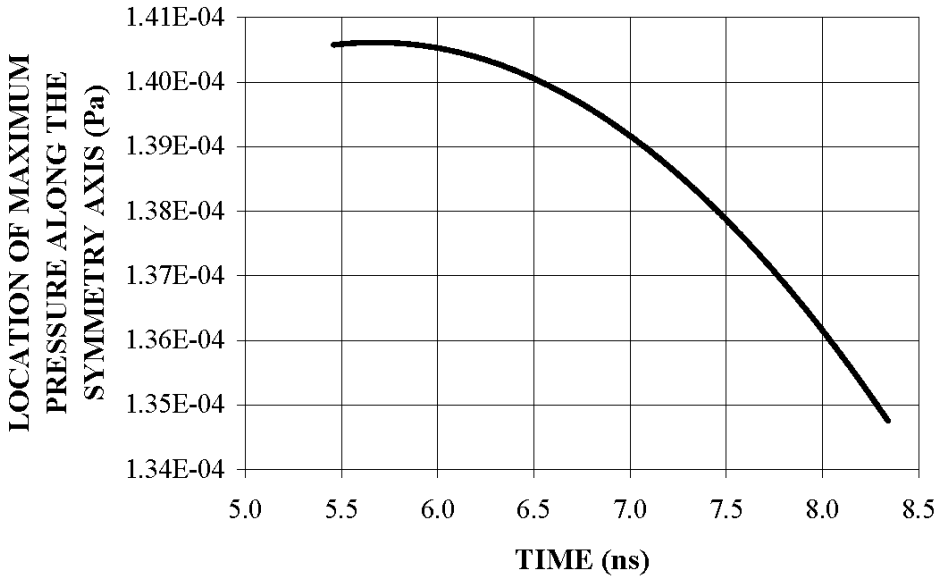

a) For jet density ρ = 800 kg/m^3.

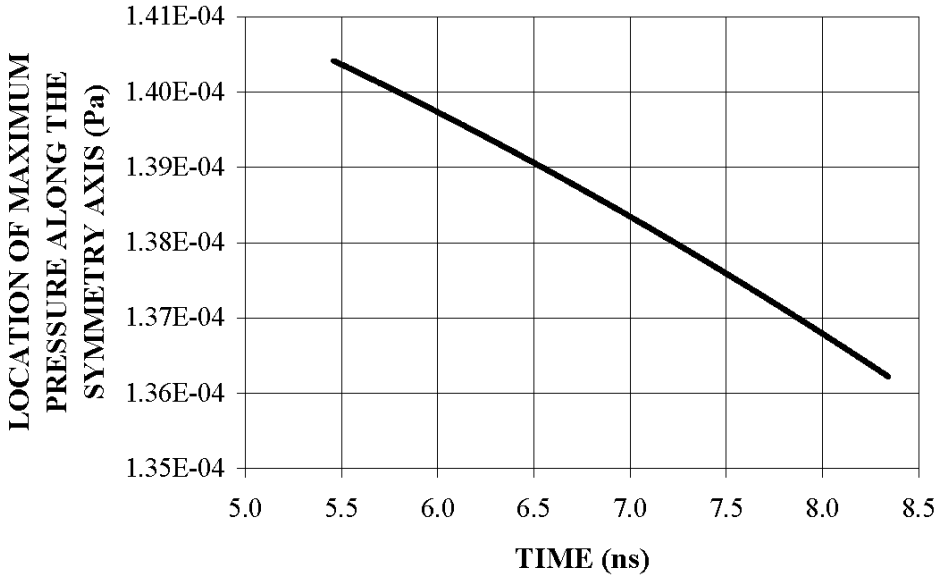

b) For jet density ρ = 50 kg/m^3.

Figure 5.35 - Location of maximum pressure along the symmetry axis with time for jet densities ρ = 800 kg/m^3 and ρ = 50 kg/m^3.

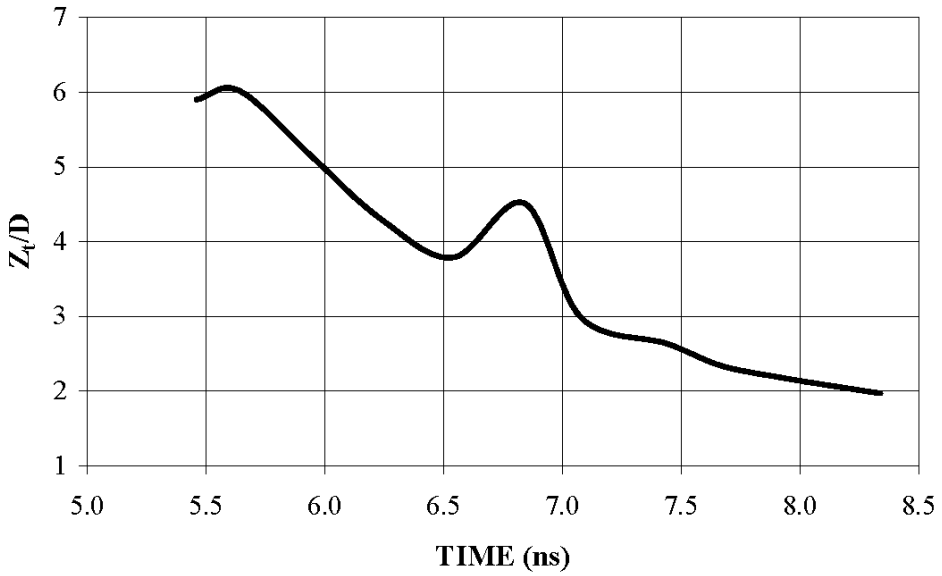

a) For jet density ρ = 800 kg/m^3.

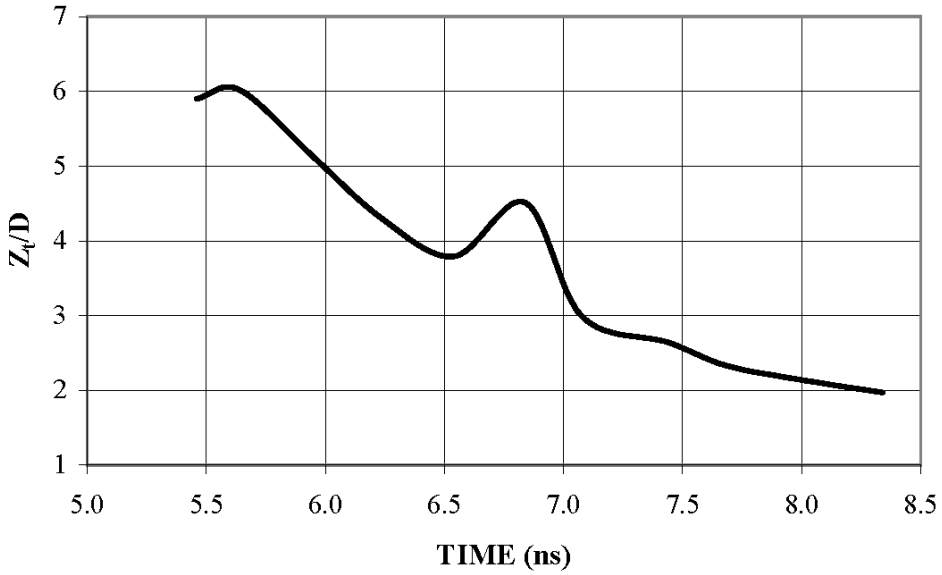

b) For jet density ρ = 50 kg/m^3.

Figure 5.36 - Dimensionless penetration depth (Z_t/D) for jet densities ρ = 800 kg/m^3 and ρ = 50 kg/m^3.

	Water	Water-Vapour
Density (kg/m^3)	998.2	50, 800
Viscosity (kg/m/s)	0.001003	$1.34x10^{-5}$
Mass Diffusivity (m^2/s)	$2.88x10^{-5}$	
Specific Heat Capacity (J/kg/K)	4182	2014
Thermal Conductivity (W/m/K)	0.6	0.0261
Molecular Weight (kg/kgmol)	18.0152	18.015

Table 5.3 - Properties of water and water-vapour used in the simulations.

CHAPTER 6

CONCLUSIONS

6.1 Laser Heating of the Substrate Material

Laser non-conduction heating of steel surface is considered and heating situation is modelled using an energy method. The mushy zones generated across solid-liquid and liquid-vapour phases are obtained for practical laser heating pulse. A numerical method using a control volume approach is introduced when predicting the temperature field in the substrate material. It is found that material response to laser heating pulse in the early heating period is different than that of late heating period. In this case the size of mushy zone across the solid-liquid interface becomes larger in the early heating period as compared to that corresponding to the late heating period, particularly in the surface region. Once the liquid layer thickness increases, the size of the mushy zone across the

solid-liquid interface remains almost the same with further progressing time. This occurs because of the rate of energy gain from the irradiated field and diffusional energy transport to this region from the liquid region, i.e. as the liquid depth increases, the energy gain, from the irradiated, across the solid-liquid mushy zone reduces significantly. Similar situation is observed for the mushy zone across the liquid-vapour mushy zone, provided that the location of both zones in the substrate material differs. Although energy absorbed by the substrate material is high at the free surface, high magnitude of latent heat of evaporation suppresses the cavity depth and the size of the liquid-vapour interface. The cavity depth size in the order of 1 μm below the workpiece surface occurs after 11 ns of the heating duration.

The temperature field and recession velocity of evaporating surface were also predicted. The predictions are compared with the one-dimensional analytical solutions as well as the experimental results. It is found that the mushy zone generated at solid-liquid interface is evident at some depth below the surface. The size of mushy zone changes in time and space. This is due to the energy gain by the substrate material, from the irradiated field via absorption, which is less at some depth below the surface and some radial distance away from the irradiated spot centre. The quality of liquid-vapour (x_b) changes sharply in the surface region while quality of solid-liquid (x_m) varies gradually away from the symmetry axis. The size of the cavity does not change significantly as the heating period progresses further $t > 19.5\,\text{ns}$, which is due to the temporal variation of laser pulse heating. The recession velocity of the evaporation front follows almost the temporal

behaviour of the laser heating pulse. This is more pronounced along the symmetry axis. Moreover, the recession velocity of the evaporating surface is higher in the region close to the symmetry axis then that corresponding to the region close to the edge of the irradiated spot. The predictions of cavity shape agree well with the experimental results. In addition, prediction of recessing liquid surface along the symmetry axis agrees well with the one-dimensional analytical model results.

Finally, the influence of laser pulse intensity on the evaporation and melting process is examined. It is found that laser pulse intensity has significant influence on the cavity size, particularly on cavity depth; in which case, small increase in laser power intensity enhances the cavity depth significantly. The recession velocities of the vapour-liquid and liquid-solid interfaces are high in the early heating period due to high rate of evaporation and melting in the early period. Once the melt depth increases, some amount of energy absorbed from the irradiated field is consumed by the super heating of the melt reducing the energy available at liquid-solid interface. As the time progresses, the radial extension of liquid-solid interface terminates due to the limited irradiated absorbed energy at some distance in the radial direction due to laser beam intensity distribution across the surface, which is Gaussian. The quality distribution varies almost linearly in the vapour-liquid mushy zone; however, it is rather gradual and non-linear in form, in the liquid-solid interface zone.

6.2 Transiently Developing Jet in Relation to Laser Heating

Jet emerging off a laser produced cavity is considered. Two densities of the jet resembling the laser produced vapour are accommodated in the analysis. A numerical method employing a control volume is accommodated to predict the flow characteristics. A moving mesh is employed to account for the transiently moving boundary problem due to cavity recession. It is found that the jet density has significant influence on the flow structure within and around the expanding jet. Since the mass flow rate emanating from the cavity is kept the same for both jet densities, jet with low density secures high velocity at cavity exit. This, in turn, results in formation of circulation cell next to the jet boundary immediately after the cavity exit.

The recoil pressure developed in the cavity is considerably high, provided that as time progresses, it reduces in the vicinity of the cavity due to cavity recession. Since the ambient fluid above the cavity exit has higher density than the jet, it suppresses the axial extension of the jet particularly at long durations. In this case, radial expansion of the jet in the frontal area results in jet neck just in the region of the cavity exit. This situation is attributed to the high velocity of the low density jet in the region at the cavity exit. The jet penetration is also influenced by the jet velocity and ambient fluid density. In this case, high density jet penetrates into the ambient fluid more than that corresponding to the low density jet.

NOMENCLATURE

A	Area (m^2)
a	Gaussian parameter (m)
CV	Control volume
Cp	Specific heat capacity (J/kg/K)
C	Various empirical constants in turbulence model
$cp_{1,2,3,4,5}$	Coefficients in the source term
D	Species diffusion coefficient (m^2/s), jet width (m)
F_j	Mass flux through the face 'j' ($kg/s/m^2$)
$F_{e,w,n,s}$	Mass flow rate through faces of the control volume (kg/s)
$f(r,t)$	Cavity profile equation
h	Convective heat transfer coefficient ($W/m^2/K$); Sensible enthalpy (J/kg)
I_o	Laser power intensity (W/m^2)
J_j	Total flux (convection plus diffusion) across face 'j' ($kg/s/m^2$ x $[\varphi]$)
$J_{e,w,n,s}$	Integrated total flux over the control volume face (kg/s x $[\varphi]$)
K	Turbulence kinetic energy (m^2/s^2)
k	Thermal conductivity (W/m/K)
k_t	Turbulent thermal conductivity (W/m/K)
L	Latent heat (J/kg)
nr	Number of divisions in the r- direction

nz	Number of divisions in the z- direction
$P_{e,w,n,s}$	Peclet number
Pr	Prandtl number
p	Pressure (Pa)
$\overline{p}$	Time-averaged pressure (Pa)
p'	Fluctuating component of mixture pressure (Pa)
$\overline{p}'$	Pressure correction (Pa)
$\overline{p}^*$	Guessed pressure (Pa)
r	Distance along the radial direction (m)
r_f	Reflectance
S	Source term (W/m^3)
Sc	Schmidt number
T	Temperature (K)
$\overline{T}$	Time-averaged temperature (K)
T'	Fluctuating component of temperature (K)
t	Time (s)
t_m	Time at which melting starts in the solid phase (s)
t_{sl}	Time at which solid-liquid mushy zone starts converting into the liquid phase (s)
t_b	Time at which evaporation starts in the liquid phase (s)
U	Energy content (J)

u	Velocity component (m/s), z- direction velocity (m/s)
$\bar{u}$	Time-averaged velocity component (m/s), Time-averaged z- direction velocity (m/s)
u'	Fluctuating component of z- direction velocity (m/s)
$\bar{u}'$	z- direction velocity correction (m/s)
$\bar{u}^*$	Guessed z- direction velocity (m/s)
$\forall$	Volume (m^3)
V	Velocity (m/s)
v	r- direction velocity (m/s)
$\bar{v}$	Time-averaged r- direction velocity (m/s)
v'	Fluctuating component of r- direction velocity (m/s)
$\bar{v}'$	r- direction velocity correction (m/s)
$\bar{v}^*$	Guessed z- direction velocity (m/s)
x	Quality
Y	Mass fraction in species transport model
$\bar{Y}$	Time-averaged mass fraction in species transport model
Z_t	Penetration depth (m)
zc	Depth of cavity (m)
z	Distance along the radial direction (m)

Greek symbols

α	Under-relaxation factor
δ	Reciprocal of absorption depth (m^{-1})
ε	Rate of dissipation equation (m^2/s^3)
Γ	Diffusion coefficient (kg/m/s)
μ	Molecular viscosity coefficient (kg/m/s)
μ_t	Turbulent viscosity coefficient (kg/m/s)
φ	Arbitrary variable
$[\varphi]$	Unit of arbitrary variable φ
ρ	Density (kg/m^3)
$\overline{\rho}$	Time-averaged density (kg/m^3)
ρ'	Fluctuating component of density (kg/m^3)
σ_K	Turbulent prandtl number for K
σ_ε	Turbulent prandtl number for ε

Subscripts

b	vapour-liquid mushy zone; boiling
eff	effective
I,J	indices used in grid staggering
i,j	arbitrary direction, indices used in grid staggering
l	liquid
max	maximum; maximum cavity radius
m	solid-liquid mushy zone; melting
N,S,E,W	nodes around a control volume
n,s,e,w	interface of a node to its north, south, east or west
o	initial value
p	time index
P,C	a typical node in the computational domain
ref	reference
s	solid, surface
t	turbulent
v	vapour

REFERENCES

[1] Shuja, S. Z., “Laser heating of a moving slab in the presence of an impinging gas jet: Influence of slab velocity,” Numerical Heat Transfer; Part A: Applications, Vol. 42, No. 7, pp. 757-775, 2002.

[2] Qiu, Taiqing; Tien, Chang-Lin; Shannon, Mark A.; Russo, Richard E., “Thermal and mechanical response of gold films during nanosecond laser-pulse heating,” Experimental Heat Transfer, Vol. 7, No. 3, pp. 175-188, 1994.

[3] Qiu, T. Q.; Tien, C. L., “Size effect on nonequilibrium laser heating of metal films,” American Society of Mechanical Engineers, Dynamic Systems and Control Division (Publication) DSC, Micromechanical Systems, Vol. 40, pp. 227-241, 1992.

[4] Yilbas, B. S.; Sami, M., “Thermal integration in laser pulse heating – a kinetic-theory approach,” Journal of Physics D: Applied Physics, Vol. 30, No. 22, pp. 3088-3095, 1997.

[5] Grigoropoulos, C. P.; Park, H. K.; Xu., X., “Modelling of pulsed laser irradiation of thin silicon layers,” International Journal of Heat and Mass Transfer, Vol. 36, No. 4, pp. 919-924, 1993.

[6] Yilbas, Bekir S.; Sami, M.; Danisman, K., “Laser successive pulse heating of a moving slab: A kinetic theory approach,” Japanese Journal of Applied Physics, Part 1: Regular Papers & Short Notes & Review Papers, Vol. 37, No. 4A, pp. 1855-1864, 1998.

[7] Yilbas, Bekir S.; Shuja, S. Z., “Laser heating of silicon: A kinetic theory approach,” Numerical Heat Transfer; Part A: Applications, Vol. 36, No. 6, pp. 563-584, 1999.

[8] Chen, J. K.; Beraun, J. E.; Grimes, L. E.; Tzou, D. Y., “Modelling of femtosecond laser-induced non-equilibrium deformation in metal films,” International Journal of Solids and Structures, Vol. 39, No. 12, pp. 3199-3216, 2002.

[9] Yilbas, B. S., “Laser short-pulse heating of Gold-Copper two-layer assembly: Thermo-elasto-plastic analysis,” Japanese Journal of Applied Physics, Part 1: Regular Papers and Short Notes and Review Papers, Vol. 41, No. 8, pp. 5226-5234, 2002.

[10] Naqavi, I. Z.; Yilbas, B. S.; Khan, Ovaisullah, “Laser heating of multilayer assembly and stress levels: Elasto-plastic consideration,” Heat and Mass Transfer/Waerme- und Stoffuebertagung, Vol. 40, No. 1-2, pp. 25-32, 2003.

[11] Oane, Mihai; Apostol, Ileana; Timcu, Adrian, “Temperature field modelling in laser heated metals for laser cleaning of surfaces,” Proceedings of SPIE – The International Society for Optical Engineering, Vol. 5227, pp. 323-328, 2003.

[12] Shao, D.; Mahajan, R. L., “Transient thermal modelling of pulsed laser irradiation of a low absorbing multilayer device using a 2D model,” Proceedings of the ASME Summer Heat Transfer Conference, Vol. 2003, pp. 79-86, 2003.

[13] Shen, Zhong-Hua; Zhang, Shu-Yi, “Laser heating of thin plate with time-dependent absorptance,” Microwave and Optical Technology Letters, Vol. 28, No. 5, pp. 364-367, 2001.

[14] Shuja, S, Z.; Yilbas B. S., “Gas-assisted laser repetitive pulsed heating of a steel surface,” Proceedings of the Institution of Mechanical Engineers, Part C: Journal of Mechanical Engineering Science, Vol. 212, No. 8, pp. 741-757, 1998.

[15] Shuja, S. Z.; Yilbas, B. S., “3-Dimensional conjugate laser heating of a moving slab,” Applied Surface Science, Vol. 167, No. 3, pp. 134-148, 2000.

[16] Jimenez Perez, J. L.; Sakanaka, P. H.; Algatti, M. A.; Mendoza-Alvarez, J. G.; Cruz Orea, A., “An improved three-dimensional model for growth of oxide films induced by laser heating,” Applied Surface Science, Vol. 175-176, pp. 703-708, 2001.

[17] Kapitskii, S. V.; Mashendzhinov, V. I.; Nikulin, D. A.; Semenov, V. N., "Numerical modelling of the natural convection of a compressible gas during laser heating," Teplofizika Vysokikh Temperatur, Vol. 26, No. 6, pp. 934-940, 1989.

[18] Handa, Sushil; Cielo, Paolo, "Transient thermoelastic modelling of laser-heated structures," ANSYS Conference Proceedings., Pittsburgh, PA, USA, Swanson Analysis Systems Inc., pp. 8.32-8.42, 1985.

[19] Yilbas, B. S., "Convergence of electron kinetic, two-temperature, and one-temperature models for laser short-pulse heating," Applied Physics A; Materials Science and Processing, Vol. 79, No. 7, pp. 1775-1782, 2004.

[20] Yilbas, B. S.; Shuja, S. Z.; Hashmi, M. S. J.; "A numerical solution for laser heating of titanium and nitrogen diffusion in solid," Journal of Materials Processing Technology, Vol. 136, No. 1-3, pp. 12-23, 2003.

[21] Tian, Weixue; Chiu, Wilson K. S., "Radiation modelling of stationary fused silica rods and fibers heated by CO_2 laser irradiation," Numerical Heat Transfer; Part A: Applications, Vol. 46, No. 2, pp. 115-130, 2004.

[22] Chen, Jinn-Kuen; Latham, W. P.; Beraun, J. E., “Axisymmetric modelling of femtosecond-pulse laser heating on metal films,” Numerical Heat Transfer, Part B: Fundamentals, Vol. 42, No. 1, pp. 1-17, 2002.

[23] Shuja, S. Z.; Yilbas, B. S.; Budair, M. O., “Modelling of laser heating of solid substance including assisting gas impingement,” Numerical Heat Transfer; Part A: Applications, Vol. 32, No. 3, pp. 315-339, 1998.

[24] Reich, Alton J.; Tham, Choon; Smith, Stan, “Computational modelling of laser induced heating,” American Society of Mechanical Engineers, Pressure Vessels and Piping Division (Publication) PVP, Computational Technologies for Fluid/Thermal/Structural/Chemical Systems with Industrial Applications – 2004, Vol. 491, No. 1, pp. 65-71, 2004.

[25] Yilbas, B. S., “Analytical solution for time unsteady laser-pulse heating of semi-infinite solid,” International Journal of Mechanical Sciences, Vol. 39, No. 6, pp. 671-682, 1997.

[26] Iwamoto, M.; Ye, M.; Grigoropoulos, C. P.; Grief, R., “Numerical analysis of pulsed laser heating for the deformation of metals,” Numerical Heat Transfer; Part A: Applications, Vol. 34, No. 8, pp. 791-804, 1998.

[27] Kalyon, M.; Yilbas, B. S., “Laser pulse heating: A formulation of desired temperature at the surface,” Optics and Lasers in Engineering, Vol. 39, No. 1, pp. 109-119, 2003.

[28] Shuja, S. Z.; Arif, A. F. M.; Yilbas, B. S., “Laser repetitive pulse heating of steel surface: A material response to thermal loading,” Journal of Manufacturing Science and Engineering, Transactions of the ASME, Vol. 124, No. 3, pp. 595-604, 2002.

[29] Tzou, Da Yu; Zhang, Yunsheng, “Lagging behaviour in the short-pulse laser heating on multi-layered metallic films,” American Society of Mechanical Engineers, Heat Transfer Division, (Publication) HTD, ASME Heat Transfer Division, Vol. 317-2, pp. 573-581,1995.

[30] Tokarev, Vladimir N.; Kaplan, Alexander F. H., “Analytical modelling of time dependent pulsed laser melting,” Journal of Applied Physics, Vol. 86, No. 5, pp. 2836-2846, 1999.

[31] Qiu, T. Q.; Tien, C. L., “Heat transfer mechanisms during short-pulse laser heating on metals,” American Society of Mechanical Engineers, Heat Transfer Division, (Publication) HTD, Transport Phenomena in Materials Processing and Manufacturing, Vol. 196, pp. 41-49, 1992.

[32] Liu, Zhi; Li, Ruxin; Yu, Wei; Zhang, Zhengquan; Xu, Zhizhan, “Heating of planar metal targets by ultrashort laser pulses,” Guangxue Xuebao/Acta Optica Sinica, Vol. 20, No. 10, pp. 1297-1304, 2000.

[33] Yilbas, B. S.; Shuja, S. Z.; Budair, M. O., “Nano-second laser pulse heating and assisting gas jet considerations,” International Journal of Machine Tools and Manufacture, Vol. 40, No. 7, pp. 1023-1038, 2000.

[34] Smith, Andrew N.; Norris, Pamela M.; Lee, Anthony S., “Theoretical determination of the laser induced damage threshold for ultrashort pulse heating of metal films,” American Society of Mechanical Engineers, Dynamic Systems and Control Division (publication) DSC, Microelectromechanical Systems (MEMS), Vol. 62, pp. 161-169, 1997.

[35] Yilbas, Bekir S.; Shuja, S. Z., “Laser short-pulse heating of surfaces,” Journal of Physics D: Applied Physics, Vol. 32, No. 16, pp. 1947-1954, 1999.

[36] Al-Nimr, M. A., “Heat transfer mechanisms during a short-duration laser heating of thin metal films,” International Journal of Thermophysics, Vol. 18, No. 5, pp. 1257-1268, 1997.

[37] Longtin, Jon P.; Tien, Chang-Lin, “Saturable absorption during high-intensity heating of liquids,” American Society of Mechanical Engineers (Paper), 95-WA/HT-50, 8 pp., 1995.

[38] Hosseini-Tehrani, P.; Eslami, M. R.; Shojaeefard, M. H., “Generalised thermoelastic analysis of layer interface excited by pulsed laser heating,” Engineering Analysis with Boundary Elements, Vol. 27, No. 9, pp. 863-869, 2003.

[39] Yilbas, B. S.; Shuja, S. Z., “Electron kinetic theory approach for sub-nanosecond laser pulse heating,” Proceedings of the Institution of Mechanical Engineers, Part C: Journal of Mechanical Engineering Science, Vol. 214, No. 10, pp. 1273-1284, 2000.

[40] Yilbas, B. S.; Kalyon, M., “Formulation of laser pulse heating: A closed form solution including heating and cooling cycles with pulse parameter variation,” Lasers in Engineering, Vol. 14, No. 3-4, pp. 213-228, 2004.

[41] Yilbas, B. S., “Electron kinetic theory approach – one- and three-dimensional heating with pulsed laser,” International Journal of Heat and Mass Transfer, Vol. 44, No. 10, pp. 1925-1936, 2001.

[42] Khan, Ovais U.; Yilbas B. S., “Laser heating of sheet metal and thermal stress development,” Journal of Materials Processing Technology, Proceedings of the International Conference on Advances, Vol. 155-156, No. 1-3, pp. 2045-2050, 2004.

[43] Yilbas, B. S.; Sahin, Ahmet Z.; Sami, M.; Coban, Ali; Bozdogan, R., “Study into laser heating of Ti-14Al-21Nb alloy to improve properties,” Optics and Lasers in Engineering, Vol. 23, No. 1, pp. 53-54, 1995.

[44] Tian, Weixue; Chiu, Wilson K. S., “Numerical modelling of CO_2 laser-heated moving glass rods,” American society of Mechanical Engineers, Heat Transfer Division, (Publication) HTD, Vol. 372, No. 5, pp. 25-32, 2002.

[45] Com-Nougue, J.; Kerrand, E., “Laser transformation hardening of Chromium steels: correlation between experimental results and heat flow modelling,” LIA (Laser Institute of America), Vol. 43, pp. 112-119, 1985.

[46] Yilbas, Bekir Sami, “Laser shortpulse heating of gold: Variable properties case,” International Journal of Heat and Mass Transfer, Vol. 46, No. 18, pp. 3511-3520, 2003.

[47] Grimes, M. K.; Rundquist, A.; Lee, Y.-S.; Downer, M. C., “Experimental identification of vacuum heating at femtosecond-laser-irradiated metal surfaces,”

IQEC, International Quantum Electronics Conference Proceedings, pp. 96-97, 1999.

[48] Yilbas, B. S.; Kalyon, M., “Analytical solution for pulsed laser heating process: Convective boundary condition case,” International Journal of Heat and Mass Transfer, Vol. 45, No. 7, pp. 1571-1582, 2002.

[49] Arnold, Douglas; Cartier, E., “Theory and modelling of laser-induced free-electron heating in wide-gap solids,” Proceedings of SPIE – The International Society for Optical Engineering, Vol. 1848, pp. 424-437, 1993.

[50] Chen, J. K.; Beraun, J. E.; Tham, C. L., “Investigation of thermal response caused by pulse laser heating,” Numerical Heat Transfer; Part A: Applications, Vol. 44, No. 7, pp. 705-722, 2003.

[51] Zhao, Jian; Sullivan, James; Zayac, John; Bernett, Ted D., “Thermophysical modelling of CO_2 laser-silica glass interaction,” American Society of Mechanical Engineers, Heat Transfer Division, (Publication) HTD, Vol. 374, No. 3, pp. 347-353, 2003.

[52] Brantov, A. V.; Bychenkov, V. Yu; Batischev, O. V.; Rozmus, W., “Nonlocal heat wave propagation due to skin layer plasma by short laser pulses,” Computer

Physics Communications, Proceedings of the 18th International Conference, Vol. 164, No. 1-3, pp. 67-72, 2004.

[53] Lu, Y. F., "Laser heating of substrate by multi-beam irradiation," Materials Research Society Symposium Proceedings, Vol. 279, pp. 705-710, 1993.

[54] Yilbas, B. S.; Arif, A. F. M., "Temperature and stress fields in silver due to laser picosecond heating pulse," Numerical Heat Transfer; Part A: Applications, Vol. 42, No. 6, pp. 623-646, 2002.

[55] Yilbas, B. S.; Faisal, M.; Shuja, S. Z.; Arif, A. F. M., "Laser pulse heating of steel surface and flexural wave analysis," Optics and Lasers in Engineering, Vol. 37, No. 1, pp. 63-83, 2002.

[56] Yilbas, Bekir Sami, "Entropy analysis and improved formulation of electron kinetic theory approach for laser short-pulse heating," Numerical Heat Transfer, Part B: Fundamentals, Vol. 45, No. 1, pp. 75-98, 2004.

[57] Yilbas, B. S., "Short-pulse laser heating of gold-chromium layers: Thermo-elasto-plastic analysis," Journal of Physics D: Applied Physics, Vol. 35, No. 11, pp. 1210-1217, 2002.

[58] Shuja, S. Z.; Yilbas, B. S., “Influence of gas jet velocity in laser heating - a moving workpiece case,” Proceedings of the Institution of Mechanical Engineers, Part C: Journal of Mechanical Engineering Science, Vol. 214, No. 8, pp. 1059-1078, 2000.

[59] Kozlov, V. P., “Local heating of a semiinfinite body by a laser source,” Inzhenerno-Fizicheskii Zhurnal, Vol. 54, No. 3, pp. 338-345, 1988.

[60] Jiang, Hongjun; Woodard, Paul, “Methodology of generic modelling as applied to energy coupling of CO_2 laser material interaction,” Optics and Lasers in Engineering, Vol. 43, No. 1, pp. 19-31, 2005.

[61] Zheng, X. J.; Zhou, Y. C.; Yan, X. H.; Nin, M. Z.; Yang, Z. Y., “Thermopiezoelectric response of a piezoelectric thin film due to a laser heating,” Mechanics and Material Engineering for Science and Experiments, pp. 271-274, 2003.

[62] Chen, J. K.; Beraun, J. E.; Tham, C. L., “Comparison of one-dimensional and two-dimensional axisymmetric approaches to the thermomechanical response caused by ultrashort laser heating,” Journal of Optics A: Pure and Applied Optics, Vol. 4, No. 6, pp. 650-661, 2002.

[63] Takahashi, Akihiko; Nishijima, Kiyoto, “Kinetic model of gas heating of laser-produced plasmas by CO_2 laser in atmospheric air,” Japanese Journal of Applied Physics, Part 1: Regular Papers & Short Notes & Review Papers, Vol. 37, No. 1, pp. 313-319, 1998.

[64] Shuja, S. Z.; Yilbas, B. S.; Arif, A. F. M., “Investigation into thermoelastic displacement of surfaces subjected to gas assisted laser-repetitive pulse,” Surface Engineering, Vol. 18, No. 1, pp. 37-45, 2002.

[65] Yilbas, Bekir Sami, “Laser short-pulse heating: Influence of laser power intensity on temperature fields,” Numerical Heat Transfer; Part A: Applications, Vol. 46, No. 3, pp. 255-275, 2004.

[66] Ho, Woei-Yun; Ma, Chunchi; Walser, Rodger M.; Becker, Michael F., “Nonequilibrium behaviour and defect diffusion in laser heating of semiconductors,” Proceedings of SPIE – The International Society for Optical Engineering, Vol. 1848, pp. 438-449, 1993.

[67] Shuja, S. Z.; Yilbas, B. S.; Budair, M. O., “Laser pulse heating of steel surfaces including impinging gas effect and variable properties,” International Journal of Numerical Methods for Heat and Fluid Flow, Vol. 12, No. 2-3, pp. 195-219, 2002.

[68] Grum, Janez; Sturm, Roman, “Calculation of temperature cycles, heating and quenching rates during laser melt hardening of cast iron,” Conference on Lasers and Electro-Optics Europe - Technical Digest, CWF63, pp. 195, 1996.

[69] Tian, Weixue; Chiu, Wilson K. S., “Temperature prediction for CO_2 laser heating of moving glass rods,” Optics and Laser Technology, Vol. 36, No. 2, pp. 131-137, 2004.

[70] Hoogers, G.; Papageorgopoulos, D. C.; King, D. A., “Strain-induced disordering of metal surfaces: Rapid laser heating of Rh{111} and Rh{332},” Surface Science, Vol. 310, No. 1-3, pp. 147-154, 1994.

[71] Yilbas, Bekir Sami; Sahin, Ahmet Z.; Davies, R., “Laser heating mechanism including evaporation process initiating laser drilling,” International Journal of Machine Tools & Manufacture, Vol. 35, No. 7, pp. 1047-1062, 1995.

[72] Yilbas, Bekir Sami, “Numerical approach to pulsed laser heating of semi-infinite aluminium substance,” Heat and Mass Transfer/Waerme- und Stoffuebertagung, Vol. 31, No. 4, pp. 279-282, 1996.

[73] Yilbas, B. S.; Al-Garni, A. Z., “Some aspects of laser heating of engineering materials,” Journal of Laser Applications, Vol. 8, No. 4, pp. 197-204, 1996.

[74] Cole, J. M.; Humphreys, P; Earwaker, L. G., “Melting model for pulsed laser heating of Silicon,” Vacuum, Vol. 34, No. 10-11, pp. 871-874, 1984.

[75] Mancini, R. C., “Hydrodynamic modelling of laser ablation,” Materials Research Society Symposium Proceedings, Vol. 285, pp. 63-68, 1993.

[76] Linford, Gary J., “Simulations of intracavity laser heating of particles,” Proceedings of SPIE – The International Society for Optical Engineering, Vol. 1415, pp. 196-210, 1991.

[77] Arif, A. F. M.; Yilbas, B. S., “Laser short pulse heating of copper: Thermo-elasto-plastic analysis,” Journal of Laser Applications, Vol. 16, No. 2, pp. 111-120, 2004.

[78] Zhvavyi, S. P.; Ivlev, G. D.; Gatskevich, E. I.; Sadovskaya, O. L., “Two beam laser heating and melting of GaAs crystal layers,” Proceedings of SPIE - The International Society for Optical Engineering, Vol. 4157, pp. 200-203, 2001.

[79] Jimenez Perez, J. L.; Sakanaka, P. H.; Algatti, M. A.; Mendoza-Alvarez, J. G.; Cruz Orea, A., “One-dimensional analytical model for oxide thin film growth on Ti metal layers during laser heating in air,” Applied Surface Science, Vol. 175-176, pp. 709-714, 2001.

[80] Yilbas, Bekir S.; Arif, A. F. M., “Laser short pulse heating and elastic-plastic wave generation,” Japanese Journal of Applied Physics, Part 1: Regular papers and Short Notes and Review Papers, Vol. 39, No. 10, pp. 5879-5888, 2000.

[81] Sami, Muhammad; Yilbas, B. S., “Kinetic theory approach for laser pulse heating process,” Optics and Lasers in Engineering, Vol. 24, No. 4, pp. 319-337, 1996.

[82] Kostyukov, I.; Rax, J.-M., “Collisional versus collisionless resonant and autoresonant heating in laser-cluster interaction,” Physical Review E, Vol. 67, No. 62, pp. 066405/1-066405/6, 2003.

[83] Kaplan, Alexander F. H., “Model of the absorption variation during pulsed laser heating applied to welding of electronic Au/Ni-coated Cu-leadframes,” Applied Surface Science, Vol. 241, No. 3-4, pp. 362-370, 2005.

[84] Kalyon, M.; Yilbas, B. S., “Closed form solution for exponentially decaying laser pulse heating: Evaporation at the surface,” Japanese Journal of Applied Physics, Part 1: Regular Papers and Short Notes and Review Papers, Vol. 41, No. 6A, pp. 3737-3746, 2002.

[85] Cote, P. J.; Todaro, M. E.; Kendall, G.; Witherell, M., “Gun bore erosion mechanisms revisited with laser pulse heating,” Surface and Coatings Technology, Vol. 163-164, pp. 478-483, 2003.

[86] Volkert, C. A.; Wuttig, M., “Modelling of laser pulsed heating and quenching in optical data storage media,” Journal of Applied Physics, Vol. 86, No. 4, pp. 1808-1816, 1999.

[87] Yilbas, B. S., “3-Dimensional laser heating model including a moving heat source consideration and phase change process,” Heat and Mass Transfer/Waerme- und Stoffuebertagung, Vol. 33, No. 5-6, pp. 495-504, 1998.

[88] Li, J. F.; Li, L.; Stott, F. H., “Comparison of volumetric and surface heating sources in the modelling of laser melting of ceramic materials,” International Journal of Heat and Mass Transfer, Vol. 47, No. 6-7, pp. 1159-1174, 2004.

[89] Mazhukin, V. I.; Nosov, V. V., “Mathematical modelling of nonequilibrium heating and melting of Si by Nd-YAG laser radiation at 1.06 μm,” Proceedings of SPIE - The International Society for Optical Engineering, Vol. 2713, pp. 236-247, 1996.

[90] Shen, Z. H.; Zhang, S. Y.; Lu, J.; Ni, X. W., “Mathematical modelling of laser induced heating and melting in solids,” Optics and Laser Technology, Vol. 33, No. 8, pp. 533-537, 2001.

[91] Yilbas, Bekir S.; Sami, M.; AbuAlHamayel, H. I., “3-dimensional modelling of laser repetitive pulse heating: A phase change and a moving heat source considerations,” Journal of Engineering and Applied Science, Vol. 34, No. 1-4, pp. 159-178, 1998.

[92] Yilbas, B. S., “Laser heating process and experimental validation,” International Journal of Heat and Mass Transfer, Vol. 40, No. 5, pp. 1131-1143, 1997.

[93] Bashenko, V. V.; Deich, A. Sh.; Karkhin, V. A.; Rimmer, I. S.; Safarevich, S. S., “Laser heating the surface of the workpiece in finish machining,” Fizika Obrabotki Materialov, Vol. 22, No. 5, pp. 511-515, 1988.

[94] Yilbas, Bekir S.; Sahin, Ahmet Z., “Heating mechanism in relation to the laser machining process,” Pramana - Journal of Physics, Vol. 41, No. 5, pp. 453-465, 1993.

[95] Yilbas, B. S.; Sami, M., “Three-dimensional laser heating including evaporation - a kinetic theory approach,” International Journal of Heat and Mass Transfer, Vol. 41, No. 13, pp. 1969-1981, 1998.

[96] Peng, T. C.; Mazumder, J., “Comparison of heat-transfer modelling for laser melting of Ti-Alloys,” Metallurgical Soc of AIME, Proceedings of a Symposium Held at the 113th AIME annual Meeting, Los Angeles, CA, USA, pp. 51-59, 1985.

[97] Koc, A.; Yilbas, B. S.; Koc, Y.; Said, S.; Gbadebo, S. A.; Sami, M., "Material response to laser pulse heating: a kinetic theory approach," Optics and Lasers in Engineering, Vol. 30, No. 3-4, pp. 327-350, 1998.

[98] Balandin, V. Yu.; Aleksandrov, L. N.; Dvurechenskii, A. V.; Kulyasova, O. A., "Interference effects at laser pulse heating of multilayer structures," Physica Status Solidi (A) Applied Research, Vol. 142, No. 1, pp. 99-105, 1994.

[99] Yilbas, B. S.; Naqvi, I. Z., "Laser heating including the phase change process and thermal stress generation in relation to drilling," Proceedings of the Institution of Mechanical Engineers, Part B: Journal of Engineering Manufacture, Vol. 217, No. 7, pp. 977-991, 2003.

[100] Dutta, Pradip; Sarkar, S.; Mohan Raj, P.; Chakraborty, S., "Three-dimensional computational modelling of momentum, heat and mass transfer in a laser surface alloying process," Numerical Heat Transfer; Part A: Applications, Vol. 42, No. 3, pp. 307-326, 2002.

[101] Kalyon, M.; Yilbas, B. S., "Analytical solution of laser evaporative heating process: Time exponentially decaying pulse case," Journal of Physics D: Applied Physics, Vol. 34, No. 22, pp. 3303-3311, 2001.

[102] Chung, Haseung; Das, Suman, “Numerical modelling of scanning laser-induced melting, vaporisation and resolidification in metals subjected to step heat flux input,” International Journal of Heat and Mass Transfer, Vol. 47, No. 19-20, pp. 4153-4164, 2004.

[103] Cho, J. Ray; Roberts, S. Mark; Reed, Roger C., “Process modelling for laser beam welding of Ti-6Al-4V,” Proceedings of SPIE - The International Society for Optical Engineering, Vol. 4831, pp. 192-196, 2002.

[104] Ye, Xiao-Hu; Chen, Xi, “Three-dimensional variable-property modelling of laser full-penetration welding characteristics,” Progress in Computational Fluid Dynamics, Vol. 2, No. 2-4, pp. 106-113, 2002.

[105] Coelho, Joao M. P.; Abreu, Manuel A.; Carvalho Rodrigues, F., “High-speed laser cutting of superposed thermoplastic films: Thermal modelling and process characterisation,” Optics and Lasers in Engineering, Vol. 42, No. 1, pp. 27-39, 2004.

[106] Fischer, P.; Romano, V.; Weber, H. P.; Karapatis, N. P.; Andre, C.; Glardon, R., “Modelling of near infrared pulsed laser sintering of metallic powders,” Proceedings of SPIE - The International Society for Optical Engineering, AIT’02 International Conference on Advanced Laser Technologies, Vol. 5147, pp. 292-298, 2003.

[107] Yagnik, S. K.; Olaner, D. R., “Surface temperature transients from pulsed laser heating of UO_2,” Journal of Nuclear Materials, Vol. 154, No. 2-3 7(I), pp. 253-262, 1988.

[108] McMasters, R. L.; Beck, J. V.; Dinwiddie, R. B.; Wang, H., “Accounting for penetration of laser heating in flash thermal diffusivity experiments,” Journal of Heat Transfer, Transactions ASME, Vol. 121, No. 1, pp. 15-21, 1999.

[109] Potente, H.; Korte, D.; Becker, F., “Laser transmission welding of thermoplastics: Analysis of the heating phase,” Annual Technical Conference, ANTEC, Conference Proceedings, Processing, Vol. 1, pp. 1022-1025, 1998.

[110] Wang, Yang; Ma, Li-Xin; Xie, Da-Gang; Wei, Sui-Xin, “Distribution of temperature fields for laser heating assisted cutting of ceramics,” Harbin Gongye Daxue Xuebao/Journal of Harbin Institute of Technology, Vol. 33, No. 6, pp. 785-788, 2001.

[111] Yilbas, B. S.; Shuja, S. Z., “Investigation of nitrogen diffusion during laser heating of titanium,” Surface Engineering, Vol. 16, No. 6, pp. 519-523, 2000.

[112] Min'ko, L. Y.; Chivel, Yuri A., "Metal surface defect formation arising by the laser heating," Proceedings of SPIE - The International Society for Optical Engineering, Vol. 2713, pp. 361-367, 1996.

[113] Tiwari, Pawan K.; Tripathi, V. K., "Model of laser-aided heating and evaporation of particles," Journal of Applied Physics, Vol. 92, No. 10, pp. 5680-5683, 2002.

[114] Sonti, N.; Amateau, M. F., "Finite-element modelling of heat flow in deep-penetration laser welds in aluminium alloys," Numerical Heat Transfer: An International Journal of Computation and Methodology; Part A: Applications, Vol. 16, No. 3, pp. 351-370, 1989.

[115] S. V. Patankar, Numerical Heat Transfer and Fluid Flow, Series in Computational Methods in Mechanics and Thermal Sciences, McGraw-Hill Book Company, 1980.

[116] H. K. Versteeg and W. Malalasekera, An introduction to Computational Fluid Dynamics, The Finite Volume Method, Longman Scientific and Technical, 1995.

[117] Yilbas, B. S.; Shuja, S. Z., "Laser non-conduction limited heating and prediction of surface recession velocity in relation to drilling," Proc Instn Mech Engrs, Part C: J. Mechanical Engineering Science, Vol. 217, pp. 1067-1076, 2003.

[118] Yilbas, B. S., Davies, R., Gorur, A., Yilbas, B. S., Begh, F., Kalkat, M., Akcakoyun, N., “Study into the measurement and prediction of penetration time during CO_2 laser cutting process,” Proc. Instn Mech. Engrs, Part B, Vol. 204, pp. 105-113, 1990.

VITA

Name: Saad bin Mansoor

Address: E-1, Block 17, Gulshan-e-Iqbal, Karachi, Pakistan.

Telephone: (00 92 21) 480 2157

Education: Received degree of Bachelor of Engineering (Mechanical) in April 2001, from NED University of Engineering & Technology, Karachi, Pakistan.

Served as lecturer at the Mechanical Engineering Department of NED University of Engineering & Technology, Karachi for an year.

Joined Mechanical Engineering Department at King Fahd University of Petroleum & Minerals, Dhahran, Saudi Arabia in September 2002 as Research Assistant.